UNIVERSITAT DE BARCELONA

On the out-of-equilibrium dynamics with tensor networks

Carlos Ramos Marimón

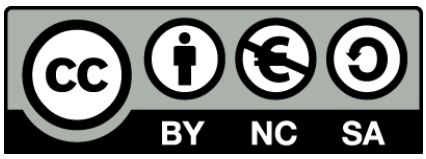

PhD thesis

ON THE OUT-OF-EQUILIBRIUM DYNAMICS WITH TENSOR NETWORKS

Carlos Ramos Marimón

Advisors
Dr. Luca Tagliacozzo and Dr. Stefano Carignano

Universitat de Barcelona

On the out-of-equilibrium dynamics with tensor networks

Memòria presentada per optar al grau de
doctor per la Universitat de Barcelona

Programa de doctorat en Física

Autor
Carlos Ramos Marimón

Directors
Dr. Luca Tagliacozzo i Dr. Stefano Carignano

Tutor
Prof. Joan Soto

Departament de física quàntica i astrofísica

Barcelona, maig de 2025

Universitat de Barcelona

List of publications

This thesis includes the content of (but it is not restricted to):

Carignano, S., Marimón, C. R., & Tagliacozzo, L. (2024). Temporal entropy and the complexity of computing the expectation value of local operators after a quench. Physical Review Research, 6(3), 033021.

Ramos-Marimón, C., Carignano, S., & Tagliacozzo, L. (2025). Pauli weight requirement of the matrix elements in time-evolved local operators: Dependence beyond the equilibration temperature. Physical Review B, 111(9), 094301.

Other studies in which I have participated during the Ph.D are:

Barcons Ruiz, D., Hesp, N. C., Herzig Sheinfux, H., Ramos Marimón, C., Maissen, C. M., Principi, A., ... & Koppens, F. H. (2023). Experimental signatures of the transition from acoustic plasmon to electronic sound in graphene. Science advances, 9(39), eadi0415.

Bou-Comas, A., Marimón, C. R., Schneider, J. T., Carignano, S., & Tagliacozzo, L. (2024). Measuring temporal entanglement in experiments as a hallmark for integrability. arXiv preprint arXiv:2409.05517.

Abstract: On the out-of-equilibrium dynamics with tensor networks

Keywords: Quantum dynamics, Many-body, Quantum information, Tensor networks

Quantum many-body dynamics is a vast field of physics at the intersection of statistical mechanics, condensed matter, quantum information, and computational physics. Understanding the time evolution of observable correlations—such as those involved in material responses—is both a milestone for technological advancement and a cornerstone for generating fundamental knowledge.

At the intersection of emergent collective behavior in many-body systems, quantum physics, and information theory lies the classical simulation of out-of-equilibrium phenomena. Without numerical tools, progress in disciplines that require heavy computations with high-dimensional vectors and matrices would be limited to purely analytical predictions and constrained by the available expertise and resources needed to build benchmarking experiments.

The goal of this thesis is to advance the classical simulation of quantum many-body systems using Tensor Networks. This technique has proven fruitful for predicting equilibrium ground states and thermal properties of one-dimensional systems, yet it still faces challenges when applied to out-of-equilibrium scenarios. In brief, the dynamics of experimentally accessible expectation values can be represented as a 2D Tensor Network, which must be contracted using iterative methods such as Time-Evolving Block Decimation. However, the memory and computational time required for these calculations—which reflect the methods' complexity—are known to grow exponentially with the simulated physical time in generic systems. This limitation is often referred to in the literature as the entanglement barrier.

This manuscript tackles the problem through the three inequivalent ways in which the 2D Tensor Network can be contracted.

In Chapter 3, we study how Schrödinger-picture contraction from the state edge of the network can be modified to improve the convergence of iterative contraction and reduce truncation errors in small systems. To this end, we explore physical decoherence in optimized bases and artificial generalized decoherence, finding that both alternatives

show promise for new protocols that overcome the entanglement barrier.

In Chapter 4, we explore Heisenberg-picture contraction from the observable edge, combining the concept of generalized decoherence with Pauli Weight truncation. By thoroughly characterizing the Pauli weight requirements to accurately describe the time evolution of local expectation values from initial product states, we conclude that truncating off-diagonal Pauli Weights is an effective scheme for simulating long-time dynamics—and we successfully implement it. We conclude with a spatial characterization of Pauli Weight spreading, bridging Tensor Network simulations and the field of operator hydrodynamics.

Finally, in Chapter 5, we focus on the transverse contraction of the 2D Tensor Network using the light-cone algorithm, analyzing its variants in terms of truncation strategies and convergence across different models. This leads to a systematic characterization of the method based on the integrability of the underlying Hamiltonians and single-spin noise models.

Resum: Estudi de la dinàmica fora de l'equilibri mitjançant xarxes tensorials

Paraules clau: Dinàmica quàntica, Molts cossos, Informació quàntica, Xarxes tensorials

La dinàmica quàntica de molts cossos és un camp extens de la física on convergeixen la mecànica estadística, la matèria condensada, la informació quàntica i la física computacional. Comprendre l'evolució temporal de les correlacions observables—com les implicades en la resposta dels materials—és tant una fita per al desenvolupament tecnològic com un pilar per a la generació de coneixement fonamental.

A la intersecció entre el comportament col·lectiu emergent dels sistemes de molts cossos, la física quàntica i la teoria de la informació, hi trobem la simulació clàssica de fenòmens fora de l'equilibri. Sense eines numèriques, el progrés en disciplines que requereixen càlculs intensius amb vectors i matrius d'alta dimensió es veuria limitat a prediccions purament analítiques i condicionat pels coneixements i recursos disponibles per construir experiments de referència.

L'objectiu d'aquesta tesi és fer avançar la simulació clàssica de sistemes quàntics de molts cossos mitjançant Xarxes Tensorials. Aquesta tècnica ha demostrat ser útil per predir estats fonamentals en equilibri i propietats tèrmiques de sistemes unidimensionals, però encara presenta reptes en escenaris fora de l'equilibri. En resum, la dinàmica dels valors esperats accessibles experimentalment es pot representar com una Xarxa Tensorial bidimensional, que s'ha de contreure amb mètodes iteratius com la Decimació de Blocs Depenent del Temps. Tanmateix, la memòria i el temps de càlcul requerits—que mesuren la complexitat dels mètodes—han demostrat créixer exponencialment amb el temps físic simulat en sistemes genèrics. Aquesta limitació és coneguda a la literatura com la barrera de l'entrellaçament.

Aquest manuscrit aborda el problema des de les tres maneres no equivalents en què es pot contreure una Xarxa de Tensor bidimensional.

Al Capítol 3 estudiem com es pot modificar la contracció segons la imatge de Schrödinger des de la vora de l'estat per tal de millorar la convergència de la contracció iterativa i reduir l'error de truncament en sistemes petits. Per aconseguir-ho, explorem la decoherència física en bases optimitzades i la decoherència generalitzada artificial,

trobant que ambdues alternatives són prometedores per desenvolupar nous protocols que superin la barrera del entrellaçament.

Al Capítol 4 explorem la contracció segons la imatge de Heisenberg des de la vora de l'observable, combinant el concepte de decoherència generalitzada amb la truncació del Pes de Pauli. Amb una caracterització exhaustiva dels requisits del Pes de Pauli per descriure amb precisió l'evolució temporal dels valors esperats locals des d'estats producte inicials, concloem que truncar els Pesos de Pauli fora de la diagonal és un esquema eficaç per simular dinàmiques, i el portem a la pràctica amb èxit. Finalitzem amb una caracterització espacial de l'expansió del Pes de Pauli, unint les simulacions amb Xarxes Tensorials amb el camp de la hidrodinàmica d'operadors.

Finalment, al Capítol 5 ens centrem en la contracció transversal de la Xarxa Tensorial bidimensional amb l'algorisme del con de llum, analitzant-ne variants pel que fa a estils de truncament i la seva convergència en diferents models. Això ens permet elaborar una caracterització sistemàtica del mètode segons la integrabilitat dels Hamiltonians subjacents i models de soroll d'espins individuals.

Table of Contents

List of Figures

1

Introduction

One of the most remarkable aims of modern physics is to understand and harness the rich phenomenology of many-body systems, which display a variety of properties in and out of equilibrium, arising from the cooperation of all their many classical or quantum constituents (Anderson (1972)). Despite powerful analytical techniques have been developed through years of research (Altland and Simons (2010); Coleman (2015)), in order to attain the ambitious goal of comprehending collective phenomena, it is clear that we need to go beyond pen and paper calculations.

The main alternative to deriving analytical expressions for both mainstream and exotic behaviors of complex systems is computational physics, which has as a main villain the exponential growth of the number of configurations in classical systems, and the dimension of the Hilbert space for their quantum counterparts, required for tracking physical quantities. Luckily (and after a lot of effort), numerical physicists have found ways to get around this obstacle which we dub the **curse of dimensionality**. The most prominent methods in this matter consist on (1) statistical sampling of the probability distributions of the system configurations through **Monte Carlo simulations**, available either in classical (Metropolis et al. (1953); Swendsen and Wang (1987); Wolff (1989)) or quantum (Ceperley (1995)) versions, and (2) dimensionality reduction with **Tensor Networks** for compressing high-dimensional vectors, matrices and higher rank objects.

In this thesis we will dive into the use of Tensor Networks for investigating a particular subset of the attractive features of quantum many-body physics: the dynamics. The excitement on such a specific topic can be understood by commenting on the many branching directions.

The first viewpoint we shall mention is the generation of knowledge and understanding of fundamental structures in physics. Quantum dynamics is connected to equilibrium physics through the concept of **dynamical phase transitions** (Heyl et al. (2013)). Such a link is vital for uncovering **universal scaling laws** in time-evolving systems, even if they are isolated and unitary, suggesting that non-equilibrium dynamics could be organized into structured phases like equilibrium matter does.

In the opposite extreme lie the application-oriented studies of quantum many-body systems. Using well-understood non-equilibrium phenomena for the construction of new technologies, like **nano-optoelectronic devices** (Koppens et al. (2011)), or controlling phases of matter that remained elusive at room temperature, like **photo-excited superconductivity** (Fausti et al. (2011)), are some of the main examples evidencing the science-assisted technological progress where dynamics is an underlying theme. Moreover, these studies positively feedback on the further development of fundamental understanding of condensed matter physics (Barcons Ruiz et al. (2023); Brahms et al. (2025)), being readily amenable for being studied with Tensor Networks (Zhang et al. (2025)).

In-between the two extreme approaches of knowledge-for-knowledge and engineering progress, there is an extensive zoo of lines of research focused on non-equilibrium phenomena, with potential to build new bridges among fields and open technological development avenues.

Historically, only the steady state properties of systems have been the main characters in these study of dynamics, which branched out from thermodynamics and statistical physics. It is natural then that counter-intuitive phenomena, like exceptions to thermalization, gathered all the attention as soon as they were detected in experiments. These violations of the settled notions of thermodynamics were manifest both in transitory times and after equilibration (if that would ever happen), sparkling new interest from the theory and application-oriented communities on a holistic level: the whole dynamics of the systems should be followed in order to understand what was going on.

These exotic behaviors with respect to mainstream thermalizing systems include:

- **Prethermalization**, corresponding to the existence of quasi-stationary states, where some but not all the observables have thermalized due to the presence of exact or approximate conservation laws (Berges et al. (2004)). This phenomenon was first experimentally detected with cold Bose gases trapped in 1D (Gring et al. (2012)), and it can be forced by external drivings (Abanin et al. (2015))

- **Quantum many-body scarring** (Serbyn et al. (2021)), consisting on the inability of the quantum state to escape a subspace of the Hilbert space, retaining a high degree of coherence that translates into persistent oscillations. This behavior was first observed in a Rydberg atom simulator (Bernien et al. (2017)), setting a prototypical model of constrained toy Hamiltonians which would be later studied theoretically in Turner et al. (2018a,b), and realized in other platforms, like cold atoms (Rauer et al. (2018)).

- **Many-body localization**, which avoids thermalization through memory of local correlations in space Schreiber et al. (2015)) and time (Bordia et al. (2017)), as shown in cold atom and trapped ion (Smith et al. (2016)) experiments.

Some advance in the form of experimental validation of these alternative dynamical trends of quantum systems was put forward with the avenue of **analog quantum simulators**, which were conceived as synthetic substitutes of classical computers (Feynman (1982)); despite that, they currently host a hybrid position in research, between constituting the hardware that *performs calculations*, and becoming the object of study themselves (like in Bezvershenko et al. (2021)), due to the faster development of the competitor they had tried to beat, our own laptops. Nevertheless, the extreme technical effort that culminated in the first quantum simulators encouraged the project of building **quantum computers** (Cirac and Zoller (1995)). The main platforms on top of which analog simulators have been built are:

- **Cold atoms** (Bloch et al. (2008, 2012)), which allowed for (1) the the detection of the **Mott-to-superfluid transition** in lattice bosons (Greiner et al. (2002)), (2) the observation of the **crossover** between the **Bose-Einstein condensation** and **Bardeen-Cooper-Schrieffer pairing** regimes (Bourdel et al. (2004)), (3) conducting the first instance of the breakdown of thermalization in low dimensions (Kinoshita et al. (2006)), (4) engineering new phases of matter like **droplets and stripes** (Cabrera et al. (2018)) and (5) constitute the core of new strategies for simulating **gauge theories**, with (Chisholm et al. (2022)) and without (Halimeh et al. (2025)) **topological terms**. Recent developments have allowed to track local properties of systems, being able to extract hydrodynamic information through **quantum gas microscopy** (Buob et al. (2024); Wienand et al. (2024)).

- **Rydberg atoms** (Saffman et al. (2010)), which leverage the **Rydberg blockade** and the strong long-range interactions between highly excited states to implement gate protocols. These atoms can be addressed individually with **optical tweezers** (Browaeys and Lahaye (2020)).

- **Trapped ions**, which promise the cleanest setups and longest coherences for simulating Ising models and quantum phase transitions (Blatt and Roos (2012)), frustration, long-range Hamiltonians and dynamical phase transitions (Monroe et al. (2021)).

- **Superconducting qubits** (Devoret and Schoelkopf (2013)), which have been able to simulate the evolution of small fermion systems (Barends et al. (2015)) and admit coupling with photonic waveguides (Gu et al. (2017)).

So, in all this *Mare Magnum* of interesting phenomena and curious platforms devised for their study, where the distinction between the former and the later blurs as research keeps establishing thousands of interconnections, where does this thesis stand? Well, as we commented earlier, we will stick to the use of laptops (and in many of the upcoming figures, clusters). In particular, we will devote the following $\mathcal{O}(10^2)$ pages to make the best out of existing Tensor Network structures for simulating the dynamics of extense quantum systems in 1D.

Tensor Networks are local factorizations of big vectors and matrices; in the context of quantum many-body systems, these objects represent the quantum state of a collective system and the operators acting on it. These decompositions have been breaking the mold since the invention of the main algorithm making use of them, the **Density Matrix Renormalization Group** (DMRG), used for determining the states with lowest energy of spin chains (Schollwöck (2011); White (1992)), a relevant piece of information for understanding low (or zero) temperature equilibrium phases of matter. In fact, DMRG even found its way beyond 1D, being able to predict classical thermodynamic properties for 2D magnets (Nishino (1995); Nishino and Okunishi (1996)). But our object of interest is the mutable world of dynamics, a very different beast.

Soon after the popularization of DMRG, other algorithms constructing on the basis of Tensor Networks where conceived to simulate the passage of time in quantum chains: **Time Evolving Block Decimation** (TEBD, Vidal (2004a)), time-DMRG (tDMRG, White and Feiguin (2004)), and some time later, a version of the **Time-Dependent Variational Principle** (TDVP, Haegeman et al. (2011)). Despite particular dynamics setups could be emulated easily, all these algorithms suffered from the same catch: nothing ensured that an efficient classical simulation of arbitrary setups could be done with finite memory and time resources.

The measure of complexity of these algorithms is the dimension of the biggest matrices in memory, the **bond dimension**. Such a quantity had been proven to be bound by a constant when DMRG was applied to gapped local Hamiltonians (Hastings (2007)); opposed to that, this dimension (and therefore the required memory to store the states, and time to perform any computation with them) grows exponentially with the simulated physical times for generic Hamiltonians. This huge problem, which receives the name of **the entanglement barrier** for reasons which will be explained throughout the thesis, restricts the extraction of information to short time simulations, in a setup (1D quantum lattices) where quantum coherence is expected to last much longer; thus a full picture of the transitory and equilibrated properties of the simulated systems is not accessible.

In this thesis we will explore different avenues for overcoming the entanglement barrier in 1D by building on the TEBD method. In Chapter 2 we give an overview on the simulation of quantum dynamics for 1D systems with Tensor Networks. Starting from basic concepts of quantum physics, we introduce closed and open system dynamics with an emphasis on thermalization. Shortly after, we introduce the diagrammatic notation from Tensor Networks, and use it to formulate the toy models tackled throughout the manuscript. Afterwards, the main strategies used for contracting the Tensor Network encoding the dynamics of states and observables are discussed, together with their respective measures of complexity.

In Chapter 3 we explore the first strategy: Schrödinger picture evolution of the quantum state, in the form of a density matrix. Inspired by DMRG, we try to gap the unitary evolution with the purpose of easing the convergence of TEBD. In order to do that, we use physical and artificial decoherence to retain local information accessible in experiments, finding in the process connections to the theory of classical stochastic systems. We end the discussion with simulations on small systems, where a combination of Tensor Networks and exact diagonalization is used to implement the protocols.

In Chapter 4 we export the decoherence ideas to the Heisenberg picture, where the evolving object is an observable, finding that we are generalizing the Pauli Weight truncation strategies proposed in recent works. We explore the regimes of applicability of a modified TEBD in which the truncation is performed in terms of coherence (orthogonal Pauli Weight) in the diagonal basis of the reference state, obtaining suggestive results for short-time simulations implying that not only the equilibration temperature of the reference state may play a role, but also its geometry. After an exhaustive study supporting the potential success of our method, we perform extensive simulations and benchmarks, concluding that the algorithm is suited for long-time evolution of non-integrable closed systems, with the equilibration temperature being the main factor of complexity. We end up the discussion by introducing Tensor Network strategies for studying the spatial components of the evolving observables, and link our insights on the complexity of our algorithm with operator spreading.

We conclude with Chapter 5 by making new efforts to understand the success of the transverse evolution strategy. As a main result, we upper bound the complexity of this strategy by the smallest complexity from the former Schrödinger and Heisenberg schemes. With the purpose of exposing and summarizing the results that other works have not explicitly shown, we simulate a variety of models and states with the light-cone algorithm and its different truncations.

2

Quantum Dynamics from the Tensor Network Lens

The central topic of this thesis is the numerical simulation of the out-of-equilibrium dynamics of quantum many-body systems through a particular family of classical methods compressing states and operators in the form of simple Tensor Networks. In this chapter we review the general expectations on what will occur to an extended quantum system under quantum quench conditions (either in isolated or open setups), followed by a summary of the Tensor Network language and the simplest algorithm (TEBD) deployed for dynamical simulations.

2.1 Overview on Quantum Dynamics.

In the first part of this chapter we introduce the main jargon to be used throughout the thesis, including a mixture of concepts from quantum physics, information theory and thermodynamics Nielsen and Chuang (2000), Breuer and Petruccione (2002).

2.1.1 Quantum States.

We will be describing spin-$1/2$ systems with **quantum states** $|\Psi\rangle$ or ρ. For 1D chains of L spins, the states may be represented by **state vectors** $\big|\Psi\big\rangle$ belonging to a Hilbert space $\mathscr{H}$ of dimension $D = 2^L$, or by **density matrices** ρ acting on it. Both alternatives can be written in terms of any basis spanning $\mathscr{H}$; for the sake of convenience, we will generically use the **computational basis**, for which each spin can be pointing up $|\uparrow\rangle := |0\rangle$ or down $|\downarrow\rangle := |1\rangle$; this allows for labeling each basis element with a binary string $\{\ell_i\}_{i=1}^{i=L}$ where $\ell_i = 0, 1$:

$$\big|\Psi\big\rangle = \sum_{\{\ell_i\}} c_{\{\ell_i\}} |\{\ell_i\}\rangle = \sum_{\ell_1 \ldots \ell_{\mathrm{L}}} c_{\ell_1 \ldots \ell_{\mathrm{L}}} |\ell_1 \ldots \ell_{\mathrm{L}}\rangle, \quad \text{or} \tag{2.1}$$

$$\rho = \sum_{\{\ell_i\},\{\ell_j\}} \rho^{\{\ell_j\}}_{\{\ell_i\}} |\{\ell_i\}\rangle\langle\{\ell_j\}| = \sum_{\ell_1,\ell'_1\ldots} \rho^{\ell'_1\ldots\ell'_{\rm L}}_{\ell_1\ldots\ell_{\rm L}} |\ell_1\ldots\ell_{\rm L}\rangle\langle\ell'_1\ldots\ell'_{\rm L}|. \tag{2.2}$$

In order to ensure the global normalization of the probability of being in a particular state, both representations come with constraints

$$\big\langle\Psi\big|\Psi\big\rangle = 1 \quad \text{and} \quad \mathrm{Tr}\{\rho\} = 1. \tag{2.3}$$

Any of these two options are suited to predict the expectation values of observable quantities, according to the distribution marked by the quantum superposition at hand. These observables are encoded by hermitian operators $O = O^\dagger$, and their expected values are extracted as

$$\langle O\rangle = \big\langle\Psi\big|O\big|\Psi\big\rangle \quad \text{or} \quad \mathrm{Tr}\{\rho\, O\}. \tag{2.4}$$

In order for these predictions to be real, the density matrix representation comes with the additional restriction of being hermitian $\rho = \rho^\dagger$.

Despite the restriction overhead, the density matrix can represent physical scenarios that simple vectors cannot. If one tries to reconcile both, vector and density matrix representations, it is clear that the connection between them is the equality $\rho = \big|\Psi\big\rangle\big\langle\Psi\big|$, i.e. the density matrix ρ is the projector onto the superposition $\big|\Psi\big\rangle$; this is the case for **pure states**, which are those where the quantum physics is the unique guilty of the uncertainty in measurable properties. Unlike that, a fully valid density matrix could be a normalized superposition of projectors $\sum_k w_k \big|\Psi_k\big\rangle\big\langle\Psi_k\big|$ with $\sum_k w_k = 1$, and includes an extra source of uncertainty on measures associated with statistics in the classical sense; states constructed as statistical mixtures are therefore called **mixed states**.

The direct measure to discern whether a state is purely quantum or not receives the name of **purity** $P = \mathrm{Tr}\{\rho^2\} = \sum_k w_k^2$, and ranges from 1 for completely pure states to $\frac{1}{D}$ for an equally weighted sum of D projectors. As an illustrative example, consider the states

$$\begin{aligned} \big|\Psi_1\big\rangle = \sqrt{\frac{1}{5}}|0\rangle + \sqrt{\frac{4}{5}}|1\rangle \longrightarrow \rho_1 =& \frac{1}{5}|0\rangle\langle 0| + \frac{4}{5}|1\rangle\langle 1| + \frac{2}{5}\Big(|0\rangle\langle 1| + |1\rangle\langle 0|\Big), \\ \rho_2 =& \frac{1}{5}|0\rangle\langle 0| + \frac{4}{5}|1\rangle\langle 1|. \end{aligned}$$

While the first state is pure, the second is mixed; for this example, the ρ_1 includes off-diagonal terms, which are called **coherences**, opposed to ρ_2, containing only diagonal terms or **populations**. The different names assigned to the diagonal/off-diagonal is related to their counterpart in classical statistical physics, where the uncertainty on a measure is nowhere related to quantum physics: populations are identified with probabilities w_k of the system being in a particular state $\big|\Psi_k\big\rangle$; this is the reason why fully diagonal density matrices are called **classical states** in an abuse of language. On the other hand, coherences correspond to interference effects, purely originating from the quantum nature of the systems. Note that the moduli of these off-diagonals change depending on the basis in which the state is written.

Typically, we are interested in observing quantities that are **local**, i.e. operators O_ℓ that can be only expressed as sums of terms acting on a finite support within a region ℓ, for example $\ell = \{\ell_1, \ell_2, \ell_3\}$. This opens the possibility to erasing the information from sites not belonging to ℓ, since the expectation value of O_ℓ will remain unaffected:

$$\begin{aligned}
\mathrm{Tr}\{\rho\, O_\ell\} &= \sum_{\{\ell_i,\tilde{\ell}_i\},\{\ell_j,\tilde{\ell}_j\}} \rho^{\{\ell_j,\tilde{\ell}_j\}}_{\{\ell_i,\tilde{\ell}_i\}} \big\langle \{\ell_j,\tilde{\ell}_j\}\big|O_\ell\big|\{\ell_i,\tilde{\ell}_i\}\big\rangle \overset{\{\tilde{\ell}_i\},\{\tilde{\ell}_j\}\notin\ell}{=} \\
&= \sum_{\{\ell_i,\tilde{\ell}_i\},\{\ell_j,\tilde{\ell}_j\}} \rho^{\{\ell_j,\tilde{\ell}_j\}}_{\{\ell,\tilde{\ell}_i\}} \delta_{\tilde{\ell}_i,\tilde{\ell}_j} \big\langle \{\ell_j\}\big|O_\ell\big|\{\ell_i\}\big\rangle = \\
&= \sum_{\{\ell_i,\tilde{\ell}_i\},\{\ell_j,\tilde{\ell}_j\}} \mathrm{Tr}_{L\backslash\ell}\Big\{\rho^{\{\ell_j,\tilde{\ell}_j\}}_{\{\ell_i,\tilde{\ell}_i\}}\Big\}\big\langle \{\ell_j\}\big|O_\ell\big|\{\ell_i\}\big\rangle = \mathrm{Tr}_\ell\Big\{\mathrm{Tr}_{L\backslash\ell}\{\rho\, O_\ell\}\Big\} \\
&:= \mathrm{Tr}_\ell\Big\{\rho_\ell\, O_\ell\Big\},
\end{aligned} \tag{2.5}$$

where in the last equality we have defined the **reduced density matrix** ρ_ℓ on the support ℓ as the partial trace of the degrees of freedom on its complement $L\backslash\ell$.

The former definition could be made in the first place because the Hilbert space factorizes between the physical sites of the chain, allowing for the separation $|\{\ell,\tilde{\ell}\}\rangle = |\{\ell\}\rangle \otimes |\{\tilde{\ell}\}\rangle$. In order to generically factorize a vector state into superpositions that take product form between a region ℓ and its complementary, one resorts to the **Schmidt decomposition**

$$\big|\Psi\big\rangle = \sum_k s_k \big|\Psi^\ell_k\big\rangle \otimes \big|\Psi^{L\backslash\ell}_k\big\rangle, \tag{2.6}$$

where the orthonormal **Schmidt vectors** $\big|\Psi^\ell_k\big\rangle$ representing ℓ and those representing its complement can be extracted, together with the superposition weights, from the **Singular Value Decomposition** (SVD) of the matrix with elements $[\, c\,]_{\{\ell_i\},\{\tilde{\ell}_i\}}$, built by reshaping the superposition component tensor $c_{\{\ell_i,\tilde{\ell}_i\}}$ by grouping the local degrees of freedom on ℓ into rows, and the rest into columns. To that goal, the SVD decomposes the reshaped component matrix as

$$c = \mathcal{U}\; s\; \mathcal{V}^\dagger = \sum_k \big|\Psi^\ell_k\big\rangle\; s^{(\ell)}_k\; \big\langle \Psi^{L\backslash\ell}_k\big|, \tag{2.7}$$

and the vectors referring to ℓ are the eigenvectors of $c\; c^\dagger = \mathcal{U}\; s\; \mathcal{V}^\dagger\; \mathcal{V}\; s\; \mathcal{U}^\dagger = \mathcal{U}\; s^2\; \mathcal{U}^\dagger$; conversely, those on the complement are the eigenvectors of $c^\dagger\; c$. This means that $\mathcal{U}$ contains the components of $\big|\Psi^\ell_k\big\rangle$ in its columns, and $\mathcal{V}^\dagger$ contains the components of $\big|\Psi^{L\backslash\ell}_k\big\rangle$ in its rows. Note that the number of non-zero eigenvalues $(s^{(\ell)}_k)^2$ will be equal to the smallest Hilbert space dimension between subsystems ℓ and its complement, imposing an **isometry** structure on the unitaries $\mathcal{U}$ and $\mathcal{V}^\dagger$, with respective dimensions $(2^{n_\ell}, 2^{n_{L\backslash\ell}})$ and $(2^{n_{L\backslash\ell}}, 2^{n_\ell})$. These isometries are full **unitaries** on the reduced Hilbert space $\mathcal{U}\mathcal{U}^\dagger = \mathbb{1}_{2^{n_\ell}}$ and $\mathcal{V}\mathcal{V}^\dagger = \mathbb{1}_{2^{n_\ell}}$, but **projectors** from the complement onto ℓ[1].

[1]These projectors are trimmed identities with 2^{n_ℓ} ones and $2^L - 2^{n_\ell}$ zeros, where the number of sites on each support is n_ℓ and $n_{L\backslash\ell}$.

This decomposition allows us to rebuild the reduced density matrix defined in 2.5 with the Schmidt vectors as

$$\rho_\ell = \sum_k (s_k^{(\ell)})^2 \left|\Psi_k^\ell\right\rangle\left\langle\Psi_k^\ell\right|, \tag{2.8}$$

allowing us to identify the **Schmidt coefficients** $(s_k^{(\ell)})^2$, for this particular system partition, as the eigenvalues of the reduced density matrices, and deduce their normalization condition $\sum_k (s_k^{(\ell)})^2 = 1$. It is possible that the number of non-zero Schmidt values is even smaller than 2^{n_ℓ}; the number of non-zero Schmidt values is the **Schmidt rank** $\mathfrak{R}$. If $\mathfrak{R} = 1$, then the state is perfectly **separable** (it takes the form of a tensor product) between ℓ and its complement, and the reduced states on both subsystems are pure; opposed to that, if $\mathfrak{R} > 1$ the reduced states are mixed, and the global state can not be exactly factorized into pure states describing each subsystem.

This is rephrased in terms of the **von Neumann entanglement entropy**[2]:

$$S_{\ell,L\setminus\ell} = -\mathrm{Tr}\{\rho_\ell \log \rho_\ell\} = -\mathrm{Tr}\{\rho_{\mathrm{L}\setminus\ell} \log \rho_{\mathrm{L}\setminus\ell}\} = -\sum_{k=1}^{\mathfrak{R}} (s_k^{(\ell)})^2 \log (s_k^{(\ell)})^2 := S_\ell, \tag{2.9}$$

which takes a minimum value 0 when the states are pure ($s_1 = 1$ and $s_{k>1} = 0$) and reaches a maximum value $\log(\mathfrak{R})$ for the **maximally mixed state** $\rho(\infty) = \frac{\mathbb{1}_{2^{\mathfrak{R}}}}{2^{\mathfrak{R}}}$ with dimension $\mathfrak{R}$ and minimal purity $P = \frac{1}{\mathfrak{R}}$, i.e. the state with a homogeneous distribution of Schmidt values $s_k = \frac{1}{\sqrt{\mathfrak{R}}}$. This last definition drives us to the following important conclusion: statistical mixture on a subsystem ℓ is indistinguishable from entanglement when the degrees of freedom out of ℓ are traced out.

Note that the von Neumann entanglement entropy is a particular case of the **Rényi entanglement entropies** in the limit $\alpha \to 1$

$$S_\ell^{(\alpha)} = \frac{1}{1-\alpha} \log\left(\mathrm{Tr}\{\rho_\ell^\alpha\}\right). \tag{2.10}$$

2.1.2 Quantum Evolution.

One can distinguish two main dynamical scenarios depending on the degrees of freedom that are explicitly accounted in the equations to be solved. When a part of the relevant degrees of freedom is integrated out in the form of source terms, we label the dynamics as **open**; conversely, if all degrees of freedom are accounted for, the dynamics is **closed**.

The particular setup we will be focusing on in this thesis is the **quantum quench**, consisting on preparing a system in some initial state $\rho(0)$, and evolving it with some Hamiltonian H or Liouvillian $\mathcal{L}$ inducing non-trivial dynamics.

[2] From here on we assume that the separation between ℓ and its complement is just a bipartition

2.1.2.1 Closed Systems.

Closed quantum dynamics represents perfectly isolated experimental conditions, being the most idealized setup for which any property of a system can be tracked. Despite it appearing to be the simplest scenario, the general quantum many-body closed dynamics is intractable through exact diagonalization, due to the immense dimensionality of the Hilbert space in which quantum states live.

For closed systems, we will be quenching from an initial pure state that must not be an exact eigenstate of the Hamiltonian ($\big[H, \big|\Psi(0)\big\rangle\big\langle\Psi(0)\big|\big] \neq 0$); this ensures that non-trivial dynamics will be induced. The trajectory of expectation values of observables is obtained by solving the **Schrödinger's equation**[3]

$$\frac{d}{dt}|\Psi(t)\rangle = -iH|\Psi(t)\rangle, \tag{2.11}$$

with formal solution

$$\big|\Psi(t)\big\rangle = e^{-iHt}\big|\Psi(0)\big\rangle = \sum_{\alpha} c_\alpha e^{-iE_\alpha t}|E_\alpha\rangle \quad \text{with} \quad c_\alpha = \big\langle E_\alpha\big|\Psi(0)\big\rangle. \tag{2.12}$$

The state is expressed in the H-eigenbasis $\{|E_\alpha\rangle\}_{\alpha=1}^{D}$, and each eigenvector is labeled by its associated eigenenergy E_α. In terms of the density matrix, Eq. 2.11 becomes the **von Neumann's equation**

$$\frac{d}{dt}\rho(t) = -i[H, \rho(t)], \tag{2.13}$$

and the solution for the evolution in terms of energy eigenstates and eigenvalues reads:

$$\rho(t) = e^{-iHt}\rho(0)e^{iHt} = \big|\Psi(t)\big\rangle\big\langle\Psi(t)\big| = \sum_{\alpha\beta} c_\alpha \bar{c}_\beta e^{-i(E_\alpha - E_\beta)t}|E_\alpha\rangle\langle E_\beta|. \tag{2.14}$$

The former expression contains redundant information, since both bra and ket are the conjugate transposed of each other. The operator that translates the initial state along time, $U_t = e^{-iHt}$, is a **unitary operator** $U_t U_t^\dagger = U_t^\dagger U_t = \mathbb{1}_D$ preserving the norm and purity of ρ, as they are invariant under unitary transformations. Despite the global evolution being unitary, reduced states behave as open systems, typically flowing towards statistical mixtures even for initially pure cases.

Despite the formal solution in Eqs. 2.11 and 2.13 does not provide exact information on the values of observables unless the Hamiltonian is diagonalized, it can be used to understand the fate of local observables for long evolution times. In particular, one would expect that any system thermalizes, reconciling quantum many-body physics with classical thermodynamics. In the following, we will distinguish between two subtypes of long-time dynamics: those relaxing to a thermal ensemble, and those escaping this expectation.

[3] Throughout this thesis we set the Planck's constant to 1.

2.1.2.2 Thermalization.

When studying the evolution of some expectation value of the local observable O_ℓ, the first question we may ask is whether it will **equilibrate**, meaning that $\langle O_\ell(t)\rangle$ will reach the vicinity of some stationary value O_ℓ^{stat} and stay close to it for the rest of the time. In this matter, different studies (Linden et al. (2009), Short (2011), Gogolin and Eisert (2016)) agree that in many-body quantum systems local observables do equilibrate, i.e. after some transitory time they acquire certain level of time translation symmetry: $\langle O_\ell(t)\rangle \simeq \langle O_\ell(t' > t)\rangle$ for $t, t' > t^{\text{eq}}$. On the level of quantum states, this means that for every subsystem ℓ there exists a well-defined limit (Calabrese (2024))

$$\lim_{t\to\infty} \rho_\ell(t) = \rho_\ell^{\text{equil}}. \tag{2.15}$$

Note that this statement holds for thermodynamically large systems, and for finite systems it is true for limited times before quantum recurrences occur: if v is some velocity related to the spread of correlations in the system, stationary values may be reached for $t < t^{\text{rec}} = \frac{L}{v}$, provided $t^{\text{equil}} < t^{\text{rec}}$.

Equilibration is already suggested by inspecting the expectation value of observables in the energy eigenbasis, in the spirit of Eqs. 2.12 and 2.14:

$$\begin{aligned}\langle O(t)\rangle &= \sum_{\alpha\beta} c_\alpha \bar{c}_\beta e^{-i(E_\alpha - E_\beta)t}\langle E_\beta|O|E_\alpha\rangle \\ &= \sum_\alpha |c_\alpha|^2 \langle E_\alpha|O|E_\alpha\rangle + \sum_{E_\alpha\neq E_\beta} c_\alpha \bar{c}_\beta e^{-i(E_\alpha - E_\beta)t}\langle E_\beta|O|E_\alpha\rangle \\ &= \sum_\alpha |c_\alpha|^2 O_{\alpha\alpha} + \sum_{E_\alpha\neq E_\beta} c_\alpha \bar{c}_\beta e^{-i(E_\alpha - E_\beta)t} O_{\alpha\beta},\end{aligned} \tag{2.16}$$

and after averaging for long times

$$\lim_{t\to\infty} \frac{1}{t}\int_0^t \langle O(t)\rangle \to \sum_\alpha |c_\alpha|^2 O_{\alpha\alpha} = \text{Tr}\{\rho_{\text{DE}}\, O\}, \tag{2.17}$$

where we have considered that the spectrum has no degeneracies (or at least there is a subextensive amount of them). This means that, in rather generic conditions, the quantum many-body systems are expected to relax to the **diagonal statistical ensemble** with respect to the Hamiltonian, defined as a mixture

$$\rho_{\text{DE}} = \sum_\alpha |c_\alpha|^2 |E_\alpha\rangle\langle E_\alpha|. \tag{2.18}$$

The main question then is whether such an ensemble is also thermal. The **microcanonical ensemble** for a system with expected total energy $\langle H\rangle$ is defined as the average over the $n_{\mathcal{W}}$ projectors over eigenstates, $|E_\alpha\rangle\langle E_\alpha|$, labeled by energies E_α within a differentially small window around $\langle H\rangle$, i.e.

$$\rho_{\text{micro}}\big(\langle H\rangle\big) = \frac{1}{n_{\mathcal{W}}} \sum_{E_\alpha\in\mathcal{W}} |E_\alpha\rangle\langle E_\alpha|, \tag{2.19}$$

with $\mathcal{W} = [\langle H\rangle - \delta E, \langle H\rangle + \delta E]$. Conversely, the **canonical ensemble**[4] state is defined by

$$\rho_{\text{cano}}(\beta) := \rho(\beta) = \frac{e^{-\beta H}}{\mathcal{Z}}, \quad \mathcal{Z} = \text{Tr}\{e^{-\beta H}\}. \tag{2.20}$$

For this later mixed state $\rho(\beta)$, the purity ranges from 1 when the **inverse temperature** $\beta = \frac{1}{T} \to \infty$ (corresponding to the pure ground state) to $\frac{1}{2^L}$ for the **infinite temperature ensemble**[5] for $\beta = 0$, $\rho(\beta = 0) = \frac{\mathbb{1}_{2^L}}{2^L}$.

The **thermalization** of an initial state with well-defined average energy density and subextensive energy fluctuations implies that its local observables will relax to the microcanonical (or equivalently canonical) predictions, and stay close to them for all times (Calabrese (2024)). This implies that for any subsystem ℓ the reduced states of the globally pure unitarily evolved state match the thermal reduced states after time average

$$\lim_{t\to\infty} \frac{1}{t} \int_0^t \rho_\ell(t) = \rho_\ell^{\text{equil}} = \rho_\ell(\beta), \tag{2.21}$$

where the inverse temperature β is derived from the conservation of energy

$$E = \langle H\rangle = \text{Tr}\{\rho(0)H\} = \text{Tr}\{\rho(t)H\} \overset{!}{=} \text{Tr}\{\rho(\beta)H\}. \tag{2.22}$$

In order for Eq. 2.21 to hold, several assumptions must be taken, since the predictions in the diagonal ensemble from Eq. 2.17 must match those of the thermal ensemble. For this connection, the study of **Random Matrix Theory** (RMT) was decisive (Deutsch (1991)), since ensembles of Gaussian random unitary/orthogonal matrices fulfill that:

- The value of averaged diagonal elements is independent from the eigenstate in which they are computed $O_{\alpha\alpha} = \overline{O}$.
- The absolute value of averaged off-diagonal elements $O_{\alpha\beta}$ is exponentially small in the dimension of the matrices. This result is due to the existence of sizeable hoppings between every pair of eigenvectors of the matrix, erasing any notion of locality.

This opens up a question: under which conditions do physical Hamiltonians of experimental interest share features with random matrices, such that their eigenstates display the same properties?

On a seminal work by Bohigas et al. (1984) it was proven that Hamiltonians whose gaps ω in the spectrum distribute according to the **Wigner-Dyson distribution**

$$p(\omega) \propto \omega^\beta e^{B_\beta \omega^2}, \quad \text{with} \quad \beta = 1, 2, \tag{2.23}$$

[4]Recall the equivalence between microcanonical, canonical and grand canonical ensembles in the thermodynamic limit.

[5]Note that the infinite temperature density matrix is also the maximally mixed one, and therefore we may use both ways to refer to it interchangeably.

fulfill the requirements to match RMT; the key is the vanishing probability of degeneracies, also dubbed **level repulsion**. These Hamiltonians are called **ergodic, chaotic** or **non-integrable**, where the later label arises as a counterpart for (Bethe Ansatz) **integrable** Hamiltonians, which can be diagonalized thanks to the presence of an extensive amount of conserved quantities $[\mathcal{I}_m, H] = 0$ for $m \propto L$.

Nevertheless, for random matrix ensembles the results after substituting the matrix elements in Eq. 2.17 boil down to the constant infinite temperature prediction, i.e. they lead to expectation values independent of the energy density (or conversely, temperature) of the initial state and the particular observable under study. This turns the focus onto extensions of RMT able to match the conditions that realistic quantities measured in experiments would demand.

Based on the conjecture that eigenstates of **ergodic** Hamiltonians are essentially random uncorrelated vectors, *Srednicki* formulated the **Eigenstate Thermalization Hypothesis** (ETH, Srednicki (1994, 1999)), proven in numerical experiments in Rigol et al. (2008), and substantiated in many later works (Polkovnikov et al. (2011), D'Alessio et al. (2016), Gogolin and Eisert (2016)).

The ETH is an ansatz for the matrix elements of few-body observables in energy basis, i.e. those O_ℓ with $n_\ell \ll n_{L\setminus\ell}$:

$$\langle E_\beta|O|E_\alpha\rangle = O_{\beta\alpha} = \overline{O}_{\alpha\beta} = O(\overline{E})\delta_{\alpha\beta} + e^{\frac{S(\overline{E})}{2}} f_0(\overline{E},\omega)R_{\alpha\beta}, \tag{2.24}$$

where all the functions featuring in Eq. 2.24 are smooth in their variables[6], the average energy $\overline{E} = \frac{E_\alpha + E_\beta}{2}$ and the gaps $\omega = E_\beta - E_\alpha$. The random variables $R_{\alpha\beta}$ are introduced to recover the results of random matrix theory, and fulfill either $\overline{|R_{\alpha\beta}|^2} = 1$ or $\overline{R^2_{\alpha\beta}} = 1$.

Eq. 2.24 solves the issues of RMT by introducing (D'Alessio et al. (2016)):

- Energy-dependent average diagonal elements $O(\overline{E})$.
- An **envelope function** $f_O(\overline{E},\omega)$ on top of the **Gaussian fluctuations** $e^{\frac{S(\overline{E})}{2}}$ (also dubbed **inverse effective Hilbert space dimension**). This prefactor is specific of the observable, the mean energy $\overline{E}$ and the gap ω. Within sufficiently narrow gaps where the envelope function is constant, the ETH reduces to the prediction of RMT; the threshold ω^* below which ETH becomes RMT receives the name of **Thouless energy** in diffusive systems. The importance of $f_0(\overline{E},\omega)$ roots in its connection with non-equal-time correlation functions, and therefore linear response theory.

Despite there is no true understanding on the regime of applicability of this Ansatz, it has been extensively tested for few-body observables, local or not. The only clear exceptions to it are pure eigenstates of the Hamiltonian (which have no experimental relevance).

[6] Note that the overline in $O_{\alpha\beta}$ means complex conjugation, while it refers to an average on top of E.

Integrable spin Hamiltonians lacking level repulsion do not escape the predictions of thermalization, but they rather relax to a **generalized Gibbs ensemble** (GGE), in the same spirit as the grand canonical one, including an extense family of conserved quantities (Vidmar and Rigol (2016)):

$$\rho_{\mathrm{GGE}}(\beta) = \frac{e^{-\beta H - \sum_m \lambda_m \mathcal{I}_m}}{\mathcal{Z}_{\mathrm{GGE}}}, \quad \mathcal{Z}_{\mathrm{GGE}} = \mathrm{Tr}\{e^{-\beta H - \sum_m \lambda_m \mathcal{I}_m}\}. \tag{2.25}$$

The construction of this ensemble is subtle, and has historically attracted much of attention (see for example the case of the integrable quantum Ising model, found to have an infinite set of conserved charges by Grady (1982), requiring truncation as in Fagotti and Essler (2013)). After all, every Hamiltonian has an exponential set of conserved quantities, the projectors over their eigenstates; nevertheless, only sufficiently local combinations of those may enter the ensemble. These local I_m^{loc} and **quasi-local** I_m^{qloc} quantities are characterized admitting a density description (Ilievski et al. (2016))

$$I_m^{\mathrm{loc}} = \sum_i (\rho_m^{\mathrm{loc}})_i, \quad I_m^{\mathrm{qloc}} = \sum_{ij} (\rho_m^{\mathrm{loc}})_i \, \mathcal{K}(j-i) \, (\rho_m^{\mathrm{loc}})_j, \tag{2.26}$$

where the kernel $\mathcal{K}(j-i)$ decays sufficiently fast to ensure extensivity of I_m^{qloc}.

In particular cases, some dynamics retain a high level of memory of the initial state even when the Hamiltonian is non-integrable, but these cases are also framed within the GGE (Gogolin et al. (2011)).

2.1.2.3 Open Systems.

An open quantum system is just a smaller part of a whole; following the dynamics of such a piece amounts to tracing out the rest of degrees of freedom that are irrelevant or just too complicated to track (Breuer and Petruccione (2002); Nielsen and Chuang (2000)); the exact equation describing their dynamics is still the von Neumann equation

$$\frac{d}{dt}\rho_\ell(t) = -i\mathrm{Tr}_{L/\ell}\big\{[H, \rho(t)]\big\}. \tag{2.27}$$

Nevertheless, the trace of part of the degrees of freedom could lead to a highly non-linear differential equation, which is not at all desirable. In order to overcome this caveat, many insights on how to model the degrees of freedom that are traced out, called **bath**, do help on the task of deriving a simpler linear differential equation.

The key for simplification is realizing that most bulk systems are in fact memoryless or **Markovian**; the precise physical conditions underlying this fact have been extensively studied, both analytically and experimentally, and are related to the decay of unequal time correlations in the bath[7]. This absence of memory allows to write a formal

[7] In this thesis we will not perform any microscopic derivation of the Markov, Born and rotating-wave typical approximations that are usually deployed for reaching the desired linear differential equations.

solution for the reduced density matrix evolution

$$\rho_\ell(t) = e^{\mathcal{L}t}\rho_\ell(0), \quad \text{with} \quad e^{\mathcal{L}(t_1+t_2)} = e^{\mathcal{L}t_1}e^{\mathcal{L}t_2}, \tag{2.28}$$

where the generator of time translations is the **Liouvillian** $\mathcal{L}$. This object is a **Completely Positive and Trace-Preserving map**[8] (CPTP), and reduces to $-i[H, \cdot\,]$ in the case of closed systems. As this object acts on both sides (indices) of the density matrix, it is usually alluded as super-operator.

The equation solved by 2.28 can be derived after differentiation by reorganizing the operators involving the partial trace on the unseen system into new operators acting only on the subsystem ℓ:

$$\frac{d}{dt}\rho(t) = \mathcal{L}\rho(t) = -i[\tilde{H}, \rho(t)] + \sum_k \gamma_k \Big(2L_k\rho(t)L_k^\dagger - \{L_k^\dagger L_k, \rho(t)\}\Big). \tag{2.29}$$

This is the **Liouville equation in Lindblad form**, and it generalizes the unitary evolution to cases with dissipation. While the first term on the rightmost hand side corresponds to Hamiltonian evolution, which may be renormalized by the trace of part of the system into a shifted/rescaled Hamiltonian $\tilde{H}$, the second term responds to loss processes, i.e. physical quantities *jumping* from the system to the bath and viceversa; this is the reason why the operators L_k inducing loss are called **jump operators**. There are as many of these operators as potential loss channels in the reduced/open dynamics, and the time scales for which these decays occur in the observables are functions of the rates γ_k.

The open system dynamics can be extremely rich, from cases in which any initially pure reduced density matrix ends up evolving into a fully mixed state, to cases in which an initially mixed state purifies Diehl et al. (2008); Verstraete et al. (2009). In-between the two extremes, thermalization can still occur. The simplest toy model replicating thermalization in open systems is that in which the reduced system is connected to a thermal bath with jump operators that effectively swap the states of the subsystem and the environment (Brun (2002)). Furthermore, interesting thermal phases may arise in open systems with continuously measured dynamics (Ladewig et al. (2022)).

[8] It maps density matrices to density matrices.

2.2 Quantum Dynamics in 1 Dimension with Tensor Networks.

The strategy that we will follow to simulate closed and open dynamics will be that of encoding all the involved vectors and matrices as Tensor Networks. **Tensor networks** (TNs) consist on factorizations of big tensors into (typically) smaller ones, such that when contracted the total number of indices and entries of the global object is preserved with high accuracy, but the required memory to save the decomposed version is much smaller (Orús (2014); Ran et al. (2020)); their main advantage, from a computational perspective, is such an ease in memory and computational costs for running algorithms that natively used expensive and intractable tensors.

2.2.1 Tensor Train Decompositions.

In order to address 1D spin systems, the TNs that we will be using have the shape of **Tensor Trains**[9] (TTs, rows of matrices coupled to the physical degrees of freedom). The tensors that we will be factoring will be superpositions of strings of single spin states, which will be recast as **Matrix Product States** (MPSs)

$$|\Psi\rangle = \sum_{\{\ell_i\}} c_{\{\ell_i\}} |\{\ell_i\}\rangle = \sum_{\{\ell\}} \mathrm{Tr}\{W_\Psi^{\ell_1} W_\Psi^{\ell_2} ... W_\Psi^{\ell_{L-1}} W_\Psi^{\ell_L}\} |\{\ell_i\}\rangle. \tag{2.30}$$

For the case of operators, we will express them in the basis of strings of single spin operators or **Pauli strings**, and factor them as **Matrix Product Operators** (MPOs)

$$\rho = \sum_{\{\ell_i\}} \mathrm{Tr}\{W_\rho^{\ell_1} W_\rho^{\ell_2} ... W_\rho^{\ell_{L-1}} W_\rho^{\ell_L}\} \{\sigma^{\ell_i}\}, \tag{2.31}$$

according to the local degrees of freedom of the underlying lattice. Note that in Eq. 2.30 the set of indices $\ell_i = 0, 1$ correspond to the physical single spin states $|0\rangle$ and $|1\rangle$, while for Eq. 2.31 they run over the squared dimension $\ell_i = 0, 1, 2, 3$, corresponding to single spin operators $\sigma^0 = \mathbb{1}_2,\ \sigma^1 = \sigma^x,\ \sigma^2 = \sigma^y,\ \sigma^3 = \sigma^z$. It is also possible to map the MPO representing an operator to an MPS by locally **folding** or **vectorizing** the bra and ket indices

$$\rho \cong |\rho\rangle = \sum_{\{i\}} \mathrm{Tr}\{W_\rho^{i_1} W_\rho^{i_2} ... W_\rho^{i_{L-1}} W_\rho^{i_L}\} |\{\sigma^i\}\rangle. \tag{2.32}$$

The terms 'Tensor Train' and 'Matrix Product' are clear when observing Eq. 2.30: the amplitudes in the superposition (once a set of indices $\{\ell_i\}$ is fixed to a bit string like

[9] Nevertheless, other geometries have been exploited: for 1D states, like ground states of critical systems (Vidal et al. (2003), Latorre et al. (2004), Vidal (2007b), Vidal (2008)), states with tree-like correlations (Shi et al. (2006)) and translationally invariant states (Vidal (2007a)); and 2D states, both in their finite (Verstraete and Cirac (2004)) and translationally invariant (Jordan et al. (2008)) versions.

01001011...) are factored as products of matrices; since the systems we will be dealing with are finite, W^{ℓ_1} and W^{ℓ_L} will be row and column vectors, respectively. We push the discussion on the physical cases for which MPS and MPO representations are efficient and accurate to Sec. 2.2.5.

The importance of the TT decomposition roots on the shape of the factor rectangular matrices W^{ℓ_i}, whose dimensions are $(\chi_{\mathrm{L}},\ \chi_{\mathrm{R}})$. Dimensions $\chi_{\mathrm{L/R}}$ are called the left/right **bond dimensions**; they indicate the number of complex entries needed to describe the underlying global tensor. For an MPS/MPO with constant $\chi_{\mathrm{L,R}} = \chi$, this number is polynomial in the extent of the chain $\mathcal{O}(L \cdot d\chi^2)$, where d is the number of single spin possible states or **physical dimension**. This is in contrast with the number of complex entries required to save in memory a generic quantum state in the Hilbert space, which is exponential with the size of the system $\mathcal{O}(d^L)$.

From a constructive viewpoint, MPS/MPOs describe sums of $d-$strings for which each number from 0 to $d-1$ correspond to some physically local tensor, and the rules for the strings appearing in the sum are indicated by the concatenation of W^{ℓ_i} (Perez-Garcia et al. (2007)). Therefore, reading the TT from left to right is equivalent to writing sums of *messages*. To clarify this point, we present the example of the extensive sum of interaction terms of some nearest-neighbor Hamiltonian, $\sum_{i=1}^{L-1} \sigma_i^\alpha \sigma_{i+1}^\alpha$; a TT decomposition from writing this superposition as messages is the following

$$
\begin{aligned}
W^{\ell_1} &= \begin{pmatrix} |0\rangle & |1\rangle & 0 \end{pmatrix} = \langle 0| \otimes |0\rangle + \langle 1| \otimes |1\rangle, \\
W^{\ell_i \neq \ell_1, \ell_L} &= \begin{pmatrix} |0\rangle & |1\rangle & 0 \\ 0 & 0 & |1\rangle \\ 0 & 0 & |0\rangle \end{pmatrix} = |0\rangle\langle 0| \otimes |0\rangle + |0\rangle\langle 1| \otimes |1\rangle + |1\rangle\langle 2| \otimes |1\rangle + |2\rangle\langle 2| \otimes |0\rangle, \\
W^{\ell_L} &= \begin{pmatrix} 0 \\ |1\rangle \\ |0\rangle \end{pmatrix} = |1\rangle \otimes |1\rangle + |2\rangle \otimes |0\rangle.
\end{aligned}
$$

In this example, the matrix forms contain physical vectors as entries representing the indices $\ell_i = 0, 1$; when written as tensors, the elements before the tensor product $\otimes$ respond to the non-zero entries in the matrices $W^{\ell_i=0,1}$. These parts of the tensor with at most χ **internal states** gives the rules of writing the message. For the case $L = 4$, contracting this tensor train yields the superposition of all strings with two neighboring $|1\rangle$ states:

$$|1100\rangle + |0110\rangle + |0011\rangle.$$

Note that in order to properly obtain the first and last messages, the boundary tensors W^{ℓ_1,ℓ_L} need to be designed to initiate and accept a set of strings. If W^{i_L} would have been $|0\rangle \otimes |1\rangle + |1\rangle \otimes |1\rangle + |2\rangle \otimes |0\rangle$, the message $|000\rangle$ would have been accepted and enlarged with the physical state $|1\rangle$.

The construction of the Hamiltonian interaction finishes by contracting the physical indices ℓ_i with a tensor setting the local operators; in this case, every time there is a state $|1\rangle$ we want to introduce a Pauli operator σ^α, so we contract the superposition of messages with $|0\rangle \otimes \mathbb{1}_2 + |1\rangle \otimes \sigma^\alpha$, yielding

$$\sigma^\alpha \sigma^\alpha \mathbb{1}_2 \mathbb{1}_2 + \mathbb{1}_2 \sigma^\alpha \sigma^\alpha \mathbb{1}_2 + \sigma^\alpha \sigma^\alpha \mathbb{1}_2 \mathbb{1}_2. \tag{2.33}$$

2.2.2 Diagramatic Notation.

In the context of TNs it is usual to depict the local factorizations with diagrams that put the contractions of indices from many tensors into simple, visual schemes. In Figs. 2.1 and 2.2 we resume how to represent quantum states, expectation values of operators and closed/open dynamics.

In Fig. 2.1 we describe the different alternatives for representing quantum states. A simple vector as $|\Psi\rangle$ is represented as a single shape (light green circle) with a single **physical leg** representing an uncontracted index running over its full dimension ($D = 2^L$ if it is a global state for the whole chain, or just $d = 2$ for the case of a single spin pure state).

In order to admit mixed states in the picture, we rather use density matrices ρ with two physical legs; despite usually the nature of the index (whether it acts on a vector space or on its dual) is usually left for the reader to understand from the context, we try to depict them coherently. Therefore, the left leg will correspond to the ket (column vectors with an index running over rows) and the right leg for the bra (row vectors with an index running over columns.

If the density matrix corresponds to a pure state, it can also be split into the two copies of the state $|\Psi\rangle$ and its dual $(|\Psi\rangle)^\dagger = \langle\Psi|$; conversely, if the state is mixed this separation is not possible, and a **virtual leg** disconnected from any observable appears between bra and ket, representing the **purification index**. It is more comfortable to bend the legs to be contracted with observables in order to have clearer diagrams; the expectation value corresponds to connecting either the density matrix or the two copies of the pure state to some hermitian operator (red circle), i.e. contraction is as simple as connecting shapes. Note that upon folding, the upper contraction is the ket and the lower one is the bra.

In order to introduce the tensor train decompositions representing MPOs we introduce the spatial dimension in the picture (assume a chain with $L = 5$); this requires playing a bit with perspective: the contraction between two shapes now is promoted to the contraction of two trains. The green train is the MPO representation of the density operator, with green spheres referring to local transfer tensors $W_\rho^{\ell_i}$ connected through the poles with the local ket (north) and bra (south) to the corresponding local transfer tensors of the observable (red spheres).

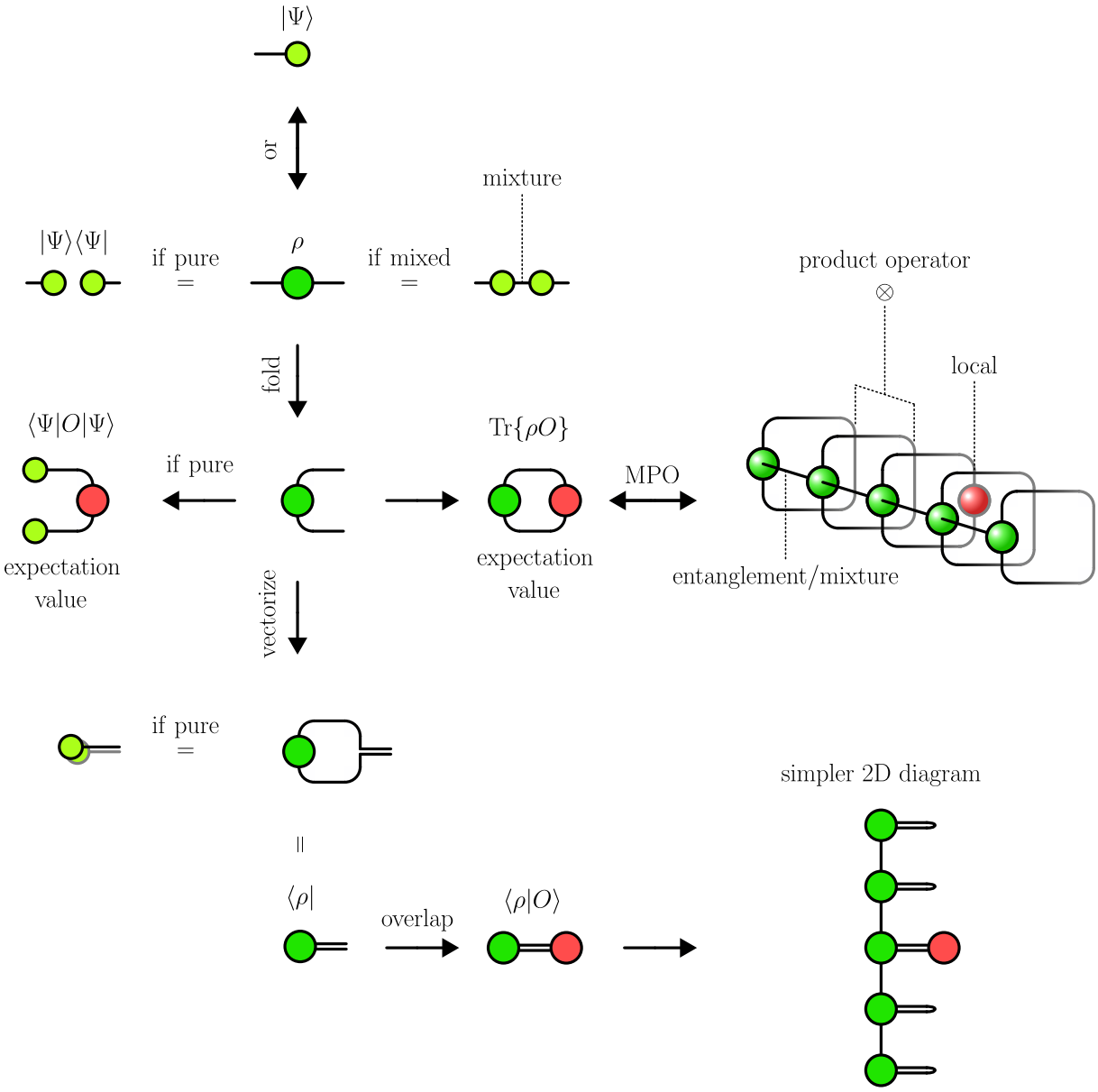

Figure 2.1: Tensor network diagrams for states and expectation values.. A state vector $|\Psi\rangle$ is represented as a shape (light green circle) with one leg/index, while a state matrix ρ (green circle) has two legs, which may correspond to the two copies of a pure state (bra and ket); if the state is mixed, an intern summation/contracted leg over the weighted projectors is introduced. An empty space represents the tensor product $\otimes$. The legs of the state can be folded for simplifying the diagrams when computing the trace with an operator, or even merged/vectorized into $\langle\rho|$; this procedure is helpful, since 3D diagrams like the tensor trace of two MPOs representing the expectation value of a local operator (red circle) can be recast as a 2D TN.

While the tensors corresponding to ρ are united by virtual legs of dimension χ representing the entanglement and mixture, the observable has no virtual legs; this is because it is a 1-spin observable, with the only non-trivial insertion σ^α in the middle of the chain.

The rest of sites are traced out (ket and bra are connected to each other), and this can be seen either as a partial trace producing the reduced density matrix in the middle of the system, or as the contraction with the local trivial observable $\mathbb{1}_2$; in other words, the depicted observable is a single Pauli string $\mathbb{1}_2\mathbb{1}_2\sigma^\alpha\mathbb{1}_2\mathbb{1}_2$.

Despite adding the spatial dimension in the plot was not dramatic for this simple example, graphical representation of dynamics with all the involved tensors and legs could be critical. In order to avoid this situation, we merge the ket and bra as a local vectorized Hilbert space of dimension d^2. Whenever we do this procedure, we will represent objects that are usually operators, like ρ and O, as vectors $\langle\rho|$ and $|O\rangle$, and their trace as the overlap. This allows us to represent TT states extended in space as simple 2D networks, rather than 3D diagrams.

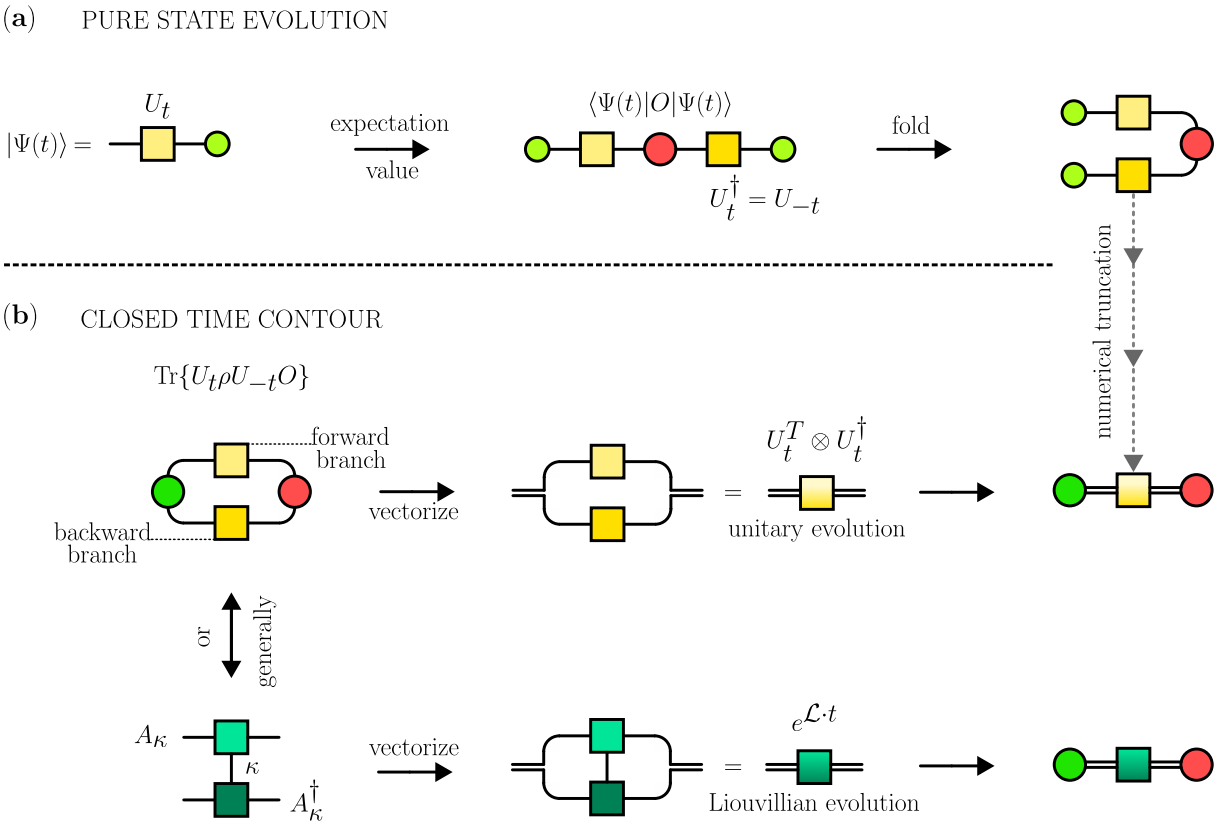

Figure 2.2: Tensor network schemes for quantum evolution. While **(a)** the dynamics of pure states just consists on applying the evolution U_t on the ket and U_{-t} on the bra, **(b)** the evolution of mixed states requires a closed time contour representation where either mixed states or observables couple the boundaries. Dissipation is represented as couplings along the evolution corresponding to the purification index κ. If vectorized, the contour representing both unitary dynamics $\langle\rho|U_t^T \otimes U_t^\dagger$ or non-unitary $\langle\rho|e^{\mathcal{L}\cdot t}$ reduce to a single row.

In Fig. 2.2 we introduce the objects involved in the dynamics of quantum states. For the case of pure states in (a) the only modification consists on acting with the evolution operator U_t on the ket and compute the conjugate transpose of it; for generic mixed states, closed unitary dynamics or open non-unitary dynamics is depicted in (b). Since the usual U_t is placed up in the evolving expectation value, we dub that branch of the diagram as the **forward contour/branch**[10]; conversely, the lower contracted leg contains $U^\dagger$, and receives the name of **backward contour/branch**.

Note that the two branches never couple in the case of unitary dynamics excepting on the right edge where the observable is placed, or if the initial state is mixed at the left edge. Since non-unitary dynamics involves a purification leg counting the number of different channel elements acting on the density matrix, the contour is zipped for this case (as many times as different channels are placed on it). Again, vectorization transforms the dynamics of systems with unspecified dimensionality into a single row of contracted tensors. The only subtlety of this last point roots on the matrices placed on the forward branch: they must be understood as transposed.

2.2.3 Spin Chain and Noise Models.

In this thesis we intend to test the regimes of applicability of existing and new homemade TN evolution algorithms; thus our benchmarks will restrict to spin chain toy models prepared in simple product states and evolved with well-known Hamiltonians and channels.

2.2.3.1 Uniform Spin Product States.

We will always quench from initially unentangled and uniform states. These **Product States** (PS) are parametrized by two angles $(\theta,\ \varphi)$ as

$$|\theta,\varphi\rangle = \left(\cos\left(\frac{\theta}{2}\right)|0\rangle + e^{i\varphi}\sin\left(\frac{\theta}{2}\right)\right)^{\otimes L}, \tag{2.34}$$

where L is the length of the chain. This parametrization allows for a representation on $\mathcal{S}_2$, called the **Bloch sphere**. In this representation, the eigenstates of the three 1-spin operators correspond to opposite poles of the sphere; by choosing the computational basis as the eigenbasis of σ^z, the north pole will correspond to $|0,0\rangle = |Z+\rangle = |0\rangle$, and the south pole to $|\pi,0\rangle = |Z-\rangle = |1\rangle$. On the equator, the 4 eigenstates of σ^x and σ^y will be placed at $\varphi = 0$ ($|X+\rangle = |+\rangle$), $\frac{\pi}{2}$ ($|Y+\rangle = |R\rangle$), π ($|X-\rangle = |-\rangle$) and $\frac{3\pi}{4}$ ($|Y-\rangle = |L\rangle$).

[10] This name is inherited from the Quantum Field Theory community.

This representation does also allow for depicting 1-spin mixed states. The main distinction with pure states from Eq. 2.34 is that the radius coordinate in the sphere will be used to represent their purity. For these simple states, the purity is connected to the expectation values of σ^α as

$$P = \frac{1}{2}\Big(1 + \sum_{\alpha=1}^{3} \langle\sigma^\alpha\rangle^2\Big), \tag{2.35}$$

such that the distance to the center of the Bloch sphere, where the infinite temperature state is, will be $R = 2P - 1 = \sum_{\alpha=1}^{3}\langle\sigma^\alpha\rangle^2$.

2.2.3.2 1D Nearest-Neighbour Hamiltonians.

The Hamiltonians that we present in the following have been extensively studied provided their locality, simplicity, symmetries and interesting physics. Before enumerating the Hamiltonians together with their basic lore and MPO representations, we remind the **Holstein-Primakov transformation** for spins $1/2$, allowing to trade spin degrees of freedom[11] by hard-core bosonic ones, i.e. a system that forbids multiple bosonic occupancy per site (Holstein and Primakoff (1940)):

$$\sigma_i^z = 2n_i - 1, \quad \sigma_i^+ = 2b_i^\dagger\sqrt{1-n_i}, \quad \sigma_i^- = 2\sqrt{1-n_i}\, b_i, \tag{2.36}$$

where the bosonic operators satisfy the local constraint $(b_i^{(\dagger)})^2 = 0$ ensuring a maximum population $\langle n_i\rangle \in \{0, 1\}$.

The first model we introduce is the **XY model**:

$$\begin{aligned} H_{\mathrm{XY}} &= \sum_i \left(\mathrm{J}_x\sigma_i^x\sigma_{i+1}^x + \mathrm{J}_y\sigma_i^y\sigma_{i+1}^y + g_x\sigma_i^x + g_z\sigma_i^z\right) \\ &\simeq 2\sum_i \Big[\mathrm{J}\Big((b_i^\dagger b_{i+1} + b_i b_{i+1}^\dagger) + 2\gamma(b_i^\dagger b_{i+1}^\dagger + b_i b_{i+1})\Big) + g_z n_i + g_x(b_i^\dagger + b_i)\Big], \end{aligned} \tag{2.37}$$

where we redefined the average coupling $\mathrm{J} = \frac{\mathrm{J}_x+\mathrm{J}_y}{2}$ and the **anisotropy** $\gamma = \frac{\mathrm{J}_x-\mathrm{J}_y}{\mathrm{J}}$. On each line the Hamiltonian was expressed in spin $1/2$ and hard-core boson language. The $\simeq$ sign is used to signal that the different expressions may differ by unobservable global shifts in energy.

This model, generically non-integrable, becomes integrable when the in-plane field g_x is turn off; in the integrable parameter space, the XY model can be exactly diagonalized through the **Jordan-Wigner** (mapping to fermions Jordan and Wigner (1928)) and **Bogoliubov** (incorporating the pairing terms that change the particle number by units of 2) transformations.

[11] Recall the connection between transverse local magnetizations and the rising and lowering operators $\sigma_i^\pm = \sigma_i^x \pm i\sigma_i^y$.

At the particular point where the anisotropy disappears, the pairing terms vanish, and the model acquires a **global** $U(1)$ **symmetry** (particle number conservation); since this is a fundamental difference for the physics of the system, we dub this particular point as the **XX model**.

By introducing an interaction in the remaining z-direction to the XY model we create the **XYZ** model:

$$H_{\mathrm{XYZ}} = \sum_i \left(\mathrm{J}_x\sigma_i^x\sigma_{i+1}^x + \mathrm{J}_y\sigma_i^y\sigma_{i+1}^y + \mathrm{J}_z\sigma_i^z\sigma_{i+1}^z + g_z\sigma_i^z + g_x\sigma_i^x\right), \tag{2.38}$$

which is non-integrable while $g_x \neq 0$. By eliminating the anisotropy between the $x-$ and $y-$ directions, we obtain the **XXZ model**:

$$\begin{aligned} H_{\mathrm{XXZ}} &= \sum_i \Big(\mathrm{J}(\sigma_i^x\sigma_{i+1}^x + \sigma_i^y\sigma_{i+1}^y + \Delta\sigma_i^z\sigma_{i+1}^z) + g_z\sigma_i^z + g_x\sigma_i^x\Big), \\ &\simeq 2\sum_i \left[\mathrm{J}\Big((b_i^\dagger b_{i+1} + b_i b_{i+1}^\dagger) + 2\Delta n_i n_{i+1}\Big) + \Big(g_z - \frac{\Delta\mathrm{J}}{2}\Big)n_i + g_x(b_i^\dagger + b_i)\right], \end{aligned} \tag{2.39}$$

which apart of being integrable for $g_x = 0$ via **Bethe Ansatz**, it is interacting due to the new density-density coupling between nearest sites, hosting a $U(1)$ symmetry in the same way as the XX model.

Finally, the simplest and most paradigmatic toy model we will be treating is the **Ising model**

$$H_{\mathrm{Ising}} = \sum_i (\mathrm{J}\sigma_i^z\sigma_{i+1}^z + g_z\sigma_i^z + g_x\sigma_i^x), \tag{2.40}$$

which breaks integrability through the longitudinal field g_z; in the $g_z = 0$ limit the purely transverse field Ising model enjoys a $\mathbb{Z}_2$ symmetry, and it can be mapped to free fermions through the Jordan-Wigner transformation.

Since the focus of this thesis is the simulation of quantum many body systems in challenging regimes where TN descriptions fail, we turn our attention to generic non-integrable points of the former Hamiltonians. In particular, we will extensively study the Ising Hamiltonian at $\{\mathrm{J} = -1,\ g_x = -1,\ g_z = -0.5\}$. Since chaotic models are expected to drive the quench dynamics towards local thermalization, we present in Fig. 2.3 the equilibration temperature map for uniform PS sampled from the Bloch sphere. Such a temperature is fixed by the energy density in the thermodynamic limit

$$h_{\mathrm{Ising}}(\mathrm{J} = -1,\ g_x = -1,\ g_z = -0.5) = -\cos^2(\theta) - \sin(\theta)\cos(\varphi) - \frac{1}{2}\cos(\theta), \tag{2.41}$$

and Eq. 2.22. In Ch. 4 we will explore in depth the connection between the equilibration temperature of initial states and the complexity of simulating the Heisenberg dynamics of local observables, and in Ch. 5 we will find similar suggestive results in the transverse picture.

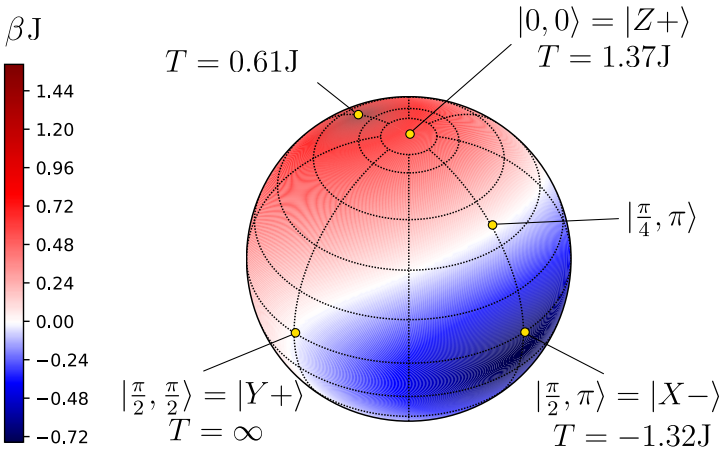

Figure 2.3: Equilibration temperature map for the non-integrable Ising model at point $\{\mathrm{J} = -1,\ g_x = -1,\ g_z = -0.5\}$. The interplay between the ferromagnetic interaction, seeking the alignment of the neighboring spins, and the local fields, trying to orient the system along $|X+\rangle$ and $|Z+\rangle$ respectively, produces an interesting map of equilibration temperatures. The diverging color scale ranges from dark-red for increasing positive β, to dark-blue for decreasing negative β. The minimum positive temperature corresponds to the minimal energy PS pointing to some direction halfway $|X+\rangle$ and $|Z+\rangle$; crossing a white line of infinite temperature states that strongly overlap with eigenstates on the middle of the spectrum, a region of inverted population states opens, with coldest[a] state close to being counter-aligned with $|X+\rangle$.

[a]This state should actually be addressed as the hottest, if we recall basic thermodynamics: negative temperature systems tend to donate much more heat than positive temperature ones.

2.2.3.3 MPO Forms.

The different Hamiltonians presented in the former section can be compactly written as MPOs with small constant bond dimension.

For XY and XX models the bond dimension is $\chi = 4$, and the transfer tensor is:

$$W_{\mathrm{XY}} = \begin{pmatrix} \mathbb{1}_2 & \mathrm{J}_x\sigma^x & \mathrm{J}_y\sigma^y & g_x\sigma^x + g_z\sigma^z \\ 0 & 0 & 0 & \sigma^x \\ 0 & 0 & 0 & \sigma^y \\ 0 & 0 & 0 & \mathbb{1}_2 \end{pmatrix}, \tag{2.42}$$

with left and right boundaries $[W_{\mathrm{XY}}^{\ell_1}]_i = [W_{\mathrm{XY}}]_{1,i}$, and $[W_{\mathrm{XY}}^{\ell_{\mathrm{L}}}]_i = [W_{\mathrm{XY}}]_{i,4}$ respectively.

For XYZ and XXZ models the bond dimension is $\chi = 5$:

$$W_{\mathrm{XYZ}} = \begin{pmatrix} \mathbb{1}_2 & \mathrm{J}_x\sigma^x & \mathrm{J}_y\sigma^y & \mathrm{J}_z\sigma^z & g_x\sigma^x + g_z\sigma^z \\ 0 & 0 & 0 & 0 & \sigma^x \\ 0 & 0 & 0 & 0 & \sigma^y \\ 0 & 0 & 0 & 0 & \sigma^z \\ 0 & 0 & 0 & 0 & \mathbb{1}_2 \end{pmatrix}, \tag{2.43}$$

with left and right boundaries $[W^{\ell_1}_{\mathrm{XYZ}}]_i = [W_{\mathrm{XYZ}}]_{1,i}$, and $[W^{\ell_{\mathrm{L}}}_{\mathrm{XYZ}}]_i = [W_{\mathrm{XYZ}}]_{i,5}$.

Finally, for the Ising model the bond dimension is $\chi = 3$:

$$W_{\mathrm{Ising}} = \begin{pmatrix} \mathbb{1}_2 & \mathrm{J}_z\sigma^z & g_x\sigma^x + g_z\sigma^z \\ 0 & 0 & \sigma^z \\ 0 & 0 & \mathbb{1}_2 \end{pmatrix}, \tag{2.44}$$

with $[W^{\ell_1}_{\mathrm{Ising}}]_i = [W_{\mathrm{Ising}}]_{1,i}$, and $[W^{\ell_{\mathrm{L}}}_{\mathrm{Ising}}]_i = [W_{\mathrm{Ising}}]_{i,3}$.

2.2.3.4 Lindblad Equations.

Weak dissipation in quantum systems can be viewed as a probabilistic measurement, and it plays a central role in the development of fault-tolerant quantum computers (Nielsen and Chuang (2000), Breuer and Petruccione (2002),Preskill (2018),Krantz et al. (2019)). Consider the case of a 1-spin in state $\rho(t)$ measured with probability P; the state $\rho(t+\delta t)$ will be a mixture between the undisturbed state and the resulting one after the measure: $(1-P)\rho(t) + P\rho_{\mathrm{meas.}}$. The measured $\rho_{\mathrm{meas.}}$ coincides with the diagonal ensemble $\rho_{\mathrm{DE},O}$ of the measured observable O; for example, if the measured quantity is a local magnetization σ^α, with eigenstates $|\sigma^\alpha_\pm\rangle$, then $\rho_{\mathrm{meas.}} = \sum_s |\sigma^\alpha_s\rangle\langle\sigma^\alpha_s|\rho|\sigma^\alpha_s\rangle\langle\sigma^\alpha_s| = \sum_s P_s|\sigma^\alpha_s\rangle\langle\sigma^\alpha_s|$, where P_s is the probability of any of the $s = 0, 1$ outcomes. This process, representing the non-filtering measure of observables, or equivalently that of forgetting the outcomes, can be recast as a channel.

The action of such a quantum channel can be represented as

$$\varepsilon_{\mathrm{flips}}(P)[\rho] = \left(1 - \frac{P}{2}\right)\rho + \frac{P}{2}\sigma^\alpha\rho\sigma^\alpha, \tag{2.45}$$

and receives different names depending on α:

- For $\alpha = z$ the channel is called **phase flip, dephasing** or **decoherence**, since it decays in different levels the off-diagonal terms of a density matrix. For a single spin, the coherences are multiplied by a factor $1 - P$. Weak decoherence is achieved in the limit $P \to 0$, while full decoherence corresponds to $P \to 1$, projecting the state onto the diagonal basis of σ^z. This means that after the channel the representation of the 1-spin (reduced) state on the Bloch sphere will decay towards the axis connecting $|0\rangle$ and $|1\rangle$.

- For $\alpha = x$ the channel is called **bit flip**, and acts on all elements of single spin states by equilibrating the populations; the case of $\alpha = y$ has a hybrid effect, and for that reason it is called **bit-phase flip**. After the channel, the representation of the 1-spin reduced state on the Bloch sphere will decay towards the axes connecting $|+\rangle$ and $|-\rangle$, or $|R\rangle$ and $|L\rangle$, respectively.

Another important channel in the context of quantum computing is the **depolarizing channel**, which corresponds to the equal action of the phase, bit and bit-phase flips:

$$\begin{aligned}\varepsilon_{\text{depol}}(P)[\rho] &= \Big(1-\frac{P}{2}\Big)\rho + \frac{P}{2}\frac{1}{3}\sum_{\alpha}\sigma^{\alpha}\rho\sigma^{\alpha} \\ &= (1-P)\rho + P\mathbb{1}_2,\end{aligned} \tag{2.46}$$

corresponding to substituting the state by the infinite temperature one with probability P. This channel contracts any state on the Bloch sphere towards its center.

A synthesized form for the channels represented by Eqs. 2.45 and 2.46 can be written by introducing the probabilities p_α of measuring σ^α:

$$\varepsilon_{\text{gen. depol}}(P, p_x, p_y)[\rho] = \Big(1-\frac{P}{2}\Big)\rho + \frac{P}{2}\sum_{\alpha} p_\alpha \sigma^{\alpha}\rho\sigma^{\alpha}, \quad \text{with} \quad \sum_{\alpha} p_\alpha = 1. \tag{2.47}$$

It reduces to the usual depolarization for the isotropic case $p_\alpha = \frac{1}{3}$, and to the flip channels in the maximally anisotropic cases $p_\alpha = 1$.

Since we will be interested in the weak measurement limit $P \to 0$ of positive evolution in Lindblad form (as in Eq. 2.29), we impose the scaling $P = \gamma L \delta t$[12], where the 1-spin rate γ is introduced as an experimental parameter. Combining this continuous time version of the channel and the spin Hamiltonians used for coherent evolution, we reach the following Lindblad type equations:

$$\frac{d}{dt}\rho(t) = -i[H, \rho(t)] + \gamma \sum_{k=1}^{3}\Big(2L_k\rho(t)L_k^\dagger - \{L_k^\dagger L_k, \rho(t)\}\Big), \tag{2.48}$$

with jump operators

$$L_k = \sum_i L_{i,k}, \quad L_{i,k} = \sqrt{\frac{p_k}{4}}\sigma_i^k. \tag{2.49}$$

The solution for the local dynamics of these equations will be addressed in Ch. 4 and 5.

Since dynamics is generated by the interplay of unitary dynamics (imaginary exponents) and erasure from dissipation (real exponents), we expect that any non-zero rate of measurement will decay any initial states towards the infinite temperature ensemble on the level of 1 spin: the coherent part of the Lindblad equation will scramble information away from the diagonal, and the channel will always erase a part of the off-diagonal with respect to some σ^α. This point will become clearer when rewriting the channels in Pauli string language (Sec. 4.2.2, Eq. 4.15).

[12] This scaling avoids issues with the separabilty of the channel when discretizing time (Wolf and Cirac (2008)).

2.2.4 TEBD and Evolution Pictures.

After introducing the physical models to be studied, we jump into describing the algorithms for simulating dynamics with TNs. The key algorithm over which we will elaborate is the Time Evolving Block Decimation for finite systems (Vidal (2004b)). In order to run it, we need to represent exponentials of the operators that translate states in time, $e^{-iH\delta t}$ and $e^{\mathcal{L}\delta t}$.

2.2.4.1 Trotterization.

The usual procedure for computing the exponential of a sum of non-commuting operators like $\exp\{\sum_i(\sigma_i^z\sigma_{i+1}^z+\sigma_i^x)\}$ involves finding its eigenvalues and eigenvectors. This task is completely out of our reach for more than ~ 16 spins.

In seminal works, Trotter and Suzuki (Suzuki (1976); Trotter (1959)) conceived a way to approximate the exponential of such a sum in terms of the exponentials from each of the different terms. For the Hamiltonians and channels presented in Sec. 2.2.3, the non-commuting terms are local fields and nearest-neighbor interactions acting along orthogonal axes. The key of the Trotter-Suzuki decomposition lies in the sequential action of exponentials of each term, which include factors weighting their time of action. These weights can be complex and were derived in Suzuki (1976).

In order to approximate the exponential of the Hamiltonians/Lindbladians appearing in Sec. 2.2.3 we can group the addenda in many ways; the simplest corresponds to form 3 non-commuting families: a set of Hamiltonian terms acting on the even bonds, another on the odd bonds, and one last term containing all the local fields and dissipation (actually, we could reduce this number to 2 by absorbing half of the local terms on each bond, but for practical reasons it is clearer to construct the evolution tensors by separating the unitary and non-unitary parts.). From these families, the ones inducing coherent evolution are[13]

$$\mathcal{L}_{\text{even, odd}} = -i\sum_i\sum_\alpha\left(\mathrm{J}_\alpha\sigma_i^\alpha\sigma_{i+1}^\alpha+\frac{g_\alpha}{2}\sigma^\alpha\right),\quad \text{for}\quad \mathrm{mod}_2(i)=0\quad\text{or}\quad \mathrm{mod}_2(i+1)=0. \tag{2.50}$$

For a small time step δt, the first order Trotter-Suzuki decomposition is

$$e^{\mathcal{L}\delta t}\simeq\varepsilon_{\text{g.depol.}}(\delta t)e^{\mathcal{L}_{\text{odd}}\delta t}e^{\mathcal{L}_{\text{even}}\delta t}, \tag{2.51}$$

which incurs in an error of order $\mathcal{O}(\delta t^2)$. This means that using this decomposition for a total time $t=N\delta t$ accumulates an error of order $\mathcal{O}(N\delta t^2)\sim\mathcal{O}(t\delta t)$; thus for a time step $\mathcal{E}\delta t=0.1$ we expect an accumulated error of order $\mathcal{O}(10^{-1})$, after a total time $\mathcal{E}t\simeq\mathcal{O}(1)$; $\mathcal{E}=\sqrt{\mathrm{Tr}\{h^\dagger h\}}$ is the Frobenius norm of the energy density.

[13] The terms corresponding to the edges of the system must account for the full local fields on those sites, requiring the removal of the $\frac{1}{2}$ prefactor before the g_α's.

This can be improved by shifting to the second order decomposition, involving the symmetric factorization

$$e^{\mathcal{L}\delta t} \simeq \varepsilon_{\text{g.depol.}}\left(\frac{\delta t}{2}\right) e^{\mathcal{L}_{\text{odd}}\frac{\delta t}{2}} e^{\mathcal{L}_{\text{even}}\delta t} e^{\mathcal{L}_{\text{odd}}\frac{\delta t}{2}} \varepsilon_{\text{g.depol.}}\left(\frac{\delta t}{2}\right), \tag{2.52}$$

which thank to the properties unveiled in Suzuki (1976), is valid until third order in δt, introducing an error $\mathcal{O}(\delta t^3)$; thus for the same time step $\mathcal{E}\delta t = 0.1$, an error $\mathcal{O}(10^{-1})$ is not accumulated until time $\mathcal{E}t \simeq \mathcal{O}(10)$.

The resulting approximation for the time evolution without dissipation is graphically depicted as in Fig. 2.4 (b), where the full exponential tensor is approximated by the first order Trotter-Suzuki as a **brick-wall-circuit**. This brick-wall can be further recast into a single layer MPO by splitting the 2-body gates through SVD decompositions, and grouping all the terms on a single site, as it is always more efficient to sweep through the system one time when contracting the local tensors than twice.

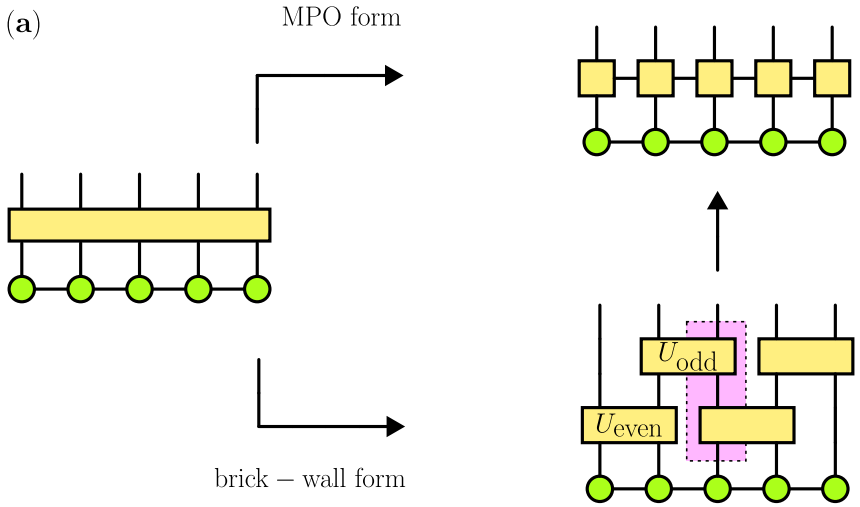

Figure 2.4: Exact and approximate TN representation of exponentials of Hamiltonians. For nearest-neighbor interactions, the evolution operator for a time step δt can be represented to some order in the Trotter-Suzuki factorization. While some simple Hamiltonians (like Ising) admit exact MPO forms for interaction terms, as depicted in **(a)**, others are amenable for even-odd partitions of the interactions, which can be later recast as an MPO (like XY or XYZ)

In some cases, the algorithms make use of the translational and reflection invariance. For obtaining local tensors fulfilling these symmetries, we can resort to:

- The **Pirvu's** (Pirvu et al. (2010)) **translationally invariant MPO formulation of the exponential** of interaction terms: for a set of commuting interaction terms, like $\mathrm{J}_z\sigma_i^z\sigma_{i+1}^z$ in the Ising model, an exact formulation of the exponential can be constructed with $\chi = 2$ and transfer tensors specified by

$$W^{\ell_i=0} = \begin{pmatrix} \cos(\delta t) & 0 \\ 0 & -\sin(\delta t) \end{pmatrix}, \quad W^{\ell_i=1} = \begin{pmatrix} 0 & \sqrt{i\sin(\delta t)\cos(\delta t)} \\ \sqrt{i\sin(\delta t)\cos(\delta t)} & 0 \end{pmatrix}. \tag{2.53}$$

  This exact form can be extended to next-to-nearest neighbor interactions and higher local dimensions $d > 2$, since the recipe to construct it only relies on the commutation of the terms acting on different bonds.

- The **Autonne-Takagi** (Chebotarev and Teretenkov (2014)) **reflection symmetric decomposition of matrices**: in Sec. 2.2.4.3 we will describe an algorithm that can be optimized by profiting the reflection symmetry of the underlying state and Liouvillian. Therefore, a decomposition of any matrix (including gates and environments described in Sec. 2.2.5 during truncation of MPS/MPOs) becomes particularly relevant. Given some complex symmetric matrix $\mathfrak{M} = \mathfrak{M}^T$, there exists a decomposition $\mathcal{Q}\,\mathfrak{M}_{\text{diag}}\,\mathcal{Q}^T$ where $\mathcal{Q}$ is a unitary matrix[14] and $\mathfrak{M}_{\text{diag}}$ is a diagonal of real numbers. To obtain this decomposition, we resort to the SVD of $\mathfrak{M}$:

$$\begin{aligned} \mathfrak{M} &= \mathcal{U}s\mathcal{V}^\dagger = \overline{\mathcal{V}}s\mathcal{U}^T = \mathfrak{M}^T \\ \mathcal{U}^\dagger(\mathcal{U}s\mathcal{V}^\dagger)\overline{\mathcal{U}} &= \mathcal{U}^\dagger(\overline{\mathcal{V}}s\mathcal{U}^T)\overline{\mathcal{U}} \\ s\mathcal{V}^\dagger\overline{\mathcal{U}} &= s\mathcal{U}^\dagger\overline{\mathcal{V}} \\ s\mathcal{Z}^T &= \mathcal{Z}s, \quad \text{with} \quad \mathcal{Z} = \mathcal{Z}^T \quad \text{and} \quad \overline{\mathcal{Z}} = \mathcal{Z}^\dagger \end{aligned} \tag{2.54}$$

  Since conjugation with $\mathcal{Z}$ preserves the singular value spectrum, we conclude that $\mathcal{Z} = \mathcal{Z}^T$ and $[s, \mathcal{Z}] = 0$. Therefore, for non-degenerate s, any power $\mathcal{Z}^\lambda$ is a diagonal of phases for $\lambda \in \mathbb{R}$, while it acquires a block-diagonal structure when a singular value repeats. This allows for a symmetric decomposition of $\mathfrak{M}$:

$$\begin{aligned} \mathfrak{M} &= \mathcal{U}s\mathcal{V}^\dagger = \mathcal{U}s\mathcal{V}^\dagger\overline{\mathcal{U}}\mathcal{U}^T = \mathcal{U}s\mathcal{Z}\mathcal{U}^T = \mathcal{U}s^{\frac{1}{2}}s^{\frac{1}{2}}\mathcal{Z}^{\frac{1}{2}}\mathcal{Z}^{\frac{1}{2}}\mathcal{U}^T \\ &= \mathcal{U}s^{\frac{1}{2}}\mathcal{Z}^{\frac{1}{2}}s^{\frac{1}{2}}\mathcal{Z}^{\frac{1}{2}}\mathcal{U}^T = (\mathcal{U}s^{\frac{1}{2}}\mathcal{Z}^{\frac{1}{2}})(\mathcal{U}s^{\frac{1}{2}}\mathcal{Z}^{\frac{1}{2}})^T, \end{aligned} \tag{2.55}$$

  giving thus a clear recipe to split gates in a reflection-symmetric way.

Although not used in this thesis, other optimizations of the trotterized evolution can be found in Zaletel et al. (2015) and Barthel and Zhang (2020).

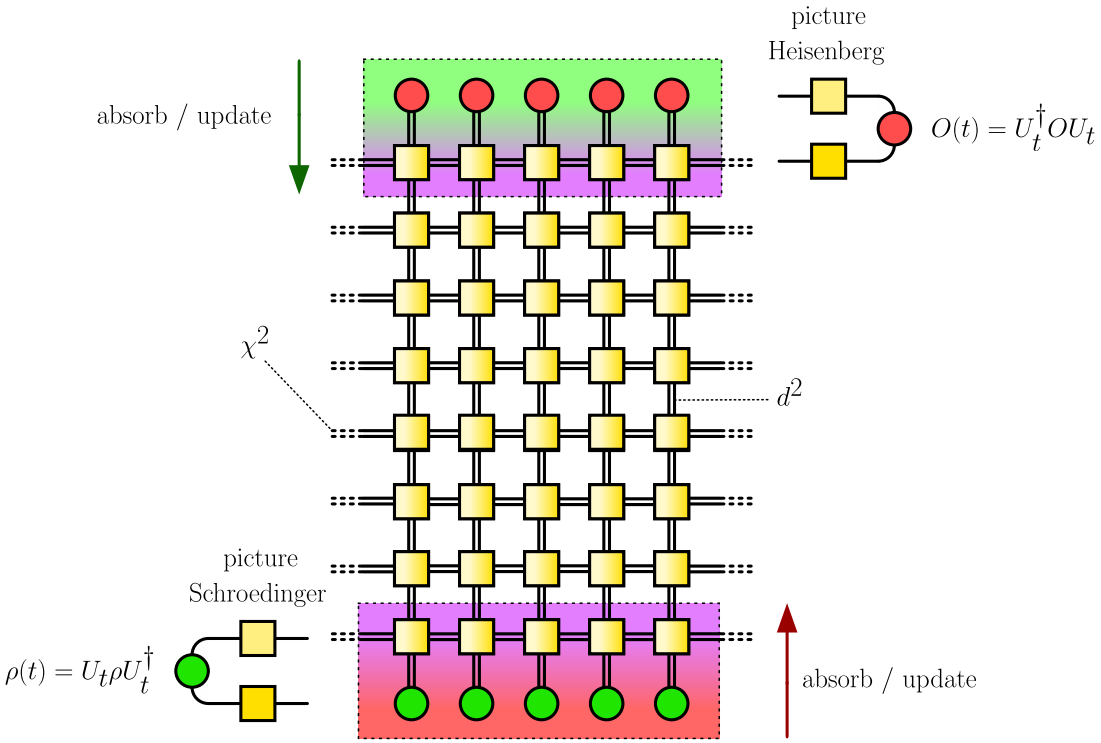

Figure 2.5: Dynamics in 1D with TNs corresponds to contracting a 2D TN. In order to determine the dynamics of arbitrary observables for a particular initial state, the network is contracted from the state edge (Schrödinger picture), while contraction from the opposite operator edge determines an observable which can be overlapped with any initial state (Heisenberg picture). The update process implies absorbing local evolution tensors along the vertical, which increases the bond dimensions by a factor χ^2 on the dynamic MPO, requiring a truncation scheme.

2.2.4.2 States and Operators: Space-like TEBD.

Once we have built local tensors representing both the initial state and the evolution operator, we can start contracting the network depicted in Fig. 2.5. Instead of evolving just the forward branch, which is equivalent to keeping the state $|\Psi(t)\rangle$ in vector form (Vidal (2004b), White and Feiguin (2004), Daley et al. (2004a), Orús and Vidal (2008)), we will evolve the vectorized state $\langle\rho(t)|$ (Zwolak and Vidal (2004)) and the vectorized operator $|O(t)\rangle$ (Hartmann et al. (2009), Pižorn et al. (2014)).

This corresponds to merging two copies (up to a change in sign in the time argument) of the evolution tensors, rendering the problem of determining dynamics of a 1-dimensional quantum chain into that of contracting a 2-dimensional TN as in Fig. 2.5, with physical dimension d^2 (along the columns) and virtual dimension χ^2 (along the rows).

[14]Note that this decomposition is not necessarily equal to the eigen-decomposition $\mathcal{Q}\mathfrak{M}_{\text{diag}}\mathcal{Q}^{-1}$.

Upon picking an edge of the depicted 2-dimensional TN to start the contraction, we will be working either in the **Schrödinger picture** (updating the state density matrix $\langle\rho(t)| \to \langle\rho(t+\delta t)|$ as in Ch. 3) or in **Heisenberg picture** (update a particular observable $|O(t)\rangle \to |O(t+\delta t)\rangle$ as in Ch. 4).

The rationale behind contraction is to update locally the row of tensors representing the changing object by absorbing a single layer of MPO evolution; i.e. the physical indices are contracted, and the local dimensions of the tensors in the evolving MPO change as

$$(\chi_{\mathrm{L}}(t),\ d^2,\ \chi_{\mathrm{R}}(t)) \to (\chi_{\mathrm{L}}(t+\delta t),\ d^2,\ \chi_{\mathrm{R}}(t+\delta t)) = (\chi^2\chi_{\mathrm{L}}(t),\ d^2,\ \chi^2\chi_{\mathrm{R}}(t)).$$

Naturally, if $\chi \geq 2$ for the unfolded gates, each update layer roughly multiplies the weight in memory by a factor $\chi^4 = 16$, demanding a truncation step that reduces the bond dimensions to a lower value. The growth of this bond dimension is the main drawback of this algorithm, called the **Time Evolving Block Decimation** (TEBD). The details on how the bond dimension is controlled are left for Sec. 2.2.5, where we will connect the complexity of contracting the network with a variety of entropies.

The use of Schrödinger or Heisenberg picture has not more relevance than the targeted physics: if the aim is to understand how all different observables change in time for a particular initial state, then Schrödinger picture is the most appropriate election; on the other hand, if the goal is to study a particular observable for different physical states, then Heisenberg picture must be picked.

2.2.4.3 Time-like TEBD.

Despite Schrödinger and Heisenberg pictures have been extensively used in the literature, not only for numerical strategies but specially with analytical purposes, the 2D representation of quantum chain dynamics as a TN contraction opens the window for a new strategy: the **transverse picture contraction**, introduced in the seminal works Bañuls et al. (2009); Müller-Hermes et al. (2012b).

The rationale behind it may be confused with a simple alternative, but it unveils a rich structure on the dynamics, from the cancellation of traced quasi-particles to the existence of Trotter-Suzuki and physical light cones. In Fig. 2.6 we present the same TN representing the dynamics, this time of a single site observable; the evolution MPOs are cast into a brick-wall shape for later explanatory convenience. The object to be updated this time is the MPS representing a column, or in physical terms, the history of 1, 2 or more spins (depending on the trotterization); note that some gates must be split, advisably with the symmetric decomposition from Eq. 2.55. The evolution step then consists on transversely absorbing columns of tensors, in the same way as for space-like TEBD, with the same issues on bond dimension growth.

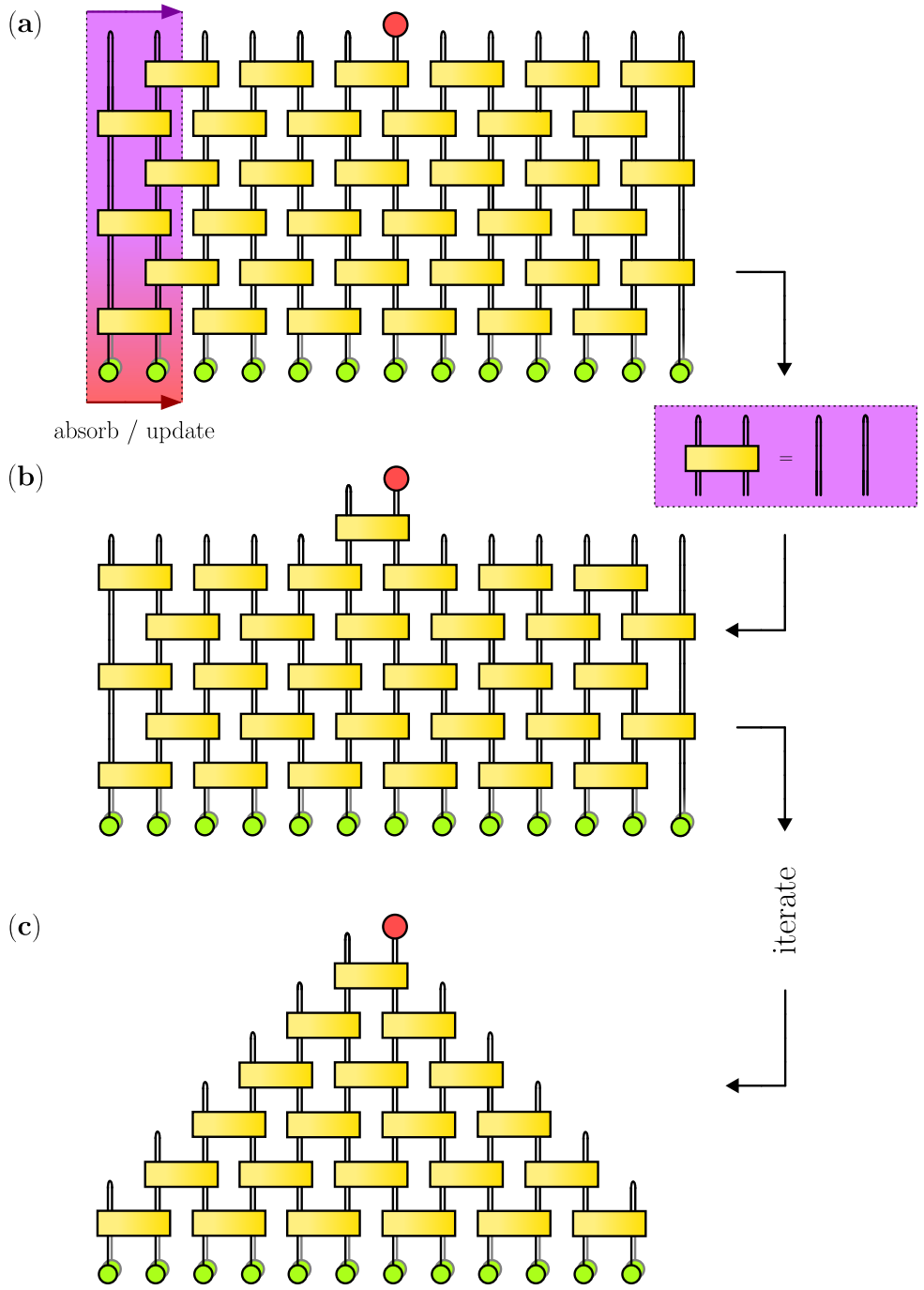

Figure 2.6: Reducing the folded TN representing 2-spin observables into a Trotter light cone. **(a)** The spin chain dynamics can be computed by contracting from the side (vertical edges). On each step, one column of evolution tensors related to the history of a small block of spins is absorbed. **(b)** With the use of unitarity of trotterized gates, the layers disconnected from non-trivial operators (Pauli matrices) in the observable edge can be traced out. **(c)** Iterating this procedure a Trotter-Suzuki light-cone pyramid TN emerges.

This scheme allows for a nice optimization, presented in Frías-Pérez and Bañuls (2022)[15]: note that all the observable sites with trivial folded identities $|\mathbb{1}_2\rangle$ connect local gates and their inverses between the forward and backward contours. This simplifies the TN as in Fig. 2.6, using the highlighted (purple box) unitarity relation, eliminating a row of tensors excepting those connected to the non-trivial insertion $|\sigma^\alpha\rangle$. The procedure shall be iterated until a **Trotter-Suzuki light-cone** structure emerges.

This light-cone shape allows for an efficient way of updating the evolving spin-block history MPS, or for convenience, **time MPS** (tMPS). For one step in time δt, the pyramid in Fig. 2.6 only contains two layers of 2-spin gates, and a tMPS of length 1 is constructed; in order to retrieve the local observables for time $2\delta t$, the operator edge of the tMPS is closed with a folded identity, and two more columns with length 2 are contracted with the tMPS of the former step. This procedure is clarified in Fig. 2.7: the evolving tMPS always corresponds to one of the halves of the 2D TN (now triangular thank to the light-cone structure), split from the bonds where the local observables will be connected. For generic systems, we can define the left $\langle\mathcal{L}(t)|$ and right $|\mathcal{R}(t)\rangle$ tMPSs, with growing length $\frac{t}{\delta t}$. The overlap of both objects produces the reduced density matrix of the represented spin block:

$$\langle\mathcal{L}(t)|\mathcal{R}(t)\rangle = \rho_2(t). \tag{2.56}$$

The reader shall note that the use of bra and ket overlap is an abuse of notation, since the outcome is not a scalar, but a matrix (the physical legs of the upmost tensors remain open). This allows for the computation of any 2-spin observable

$$\langle\mathcal{L}(t)|\sum_k O_k^{(1)}Q_k^{(2)}|\mathcal{R}(t)\rangle = \langle\sum_k O_k^{(1)}Q_k^{(2)}(t)\rangle, \tag{2.57}$$

as in the bottom of Fig. 2.7.

The scheme used in Figs. 2.6 and 2.7 is just one particular realization of the transverse contraction algorithm. It is though extremely flexible, and admits various optimizations depending on the targeted physics:

- The depicted setup is amenable for describing first order trotterized dynamics of XY and XYZ models, with initial states that can be homogeneous (as in Eq. 2.34), random $\bigotimes_i |\theta_i, \varphi_i\rangle$, or domain-wall like $\bigotimes_{i<\frac{L}{2}} |\theta_\mathrm{L}, \varphi_\mathrm{L}\rangle \bigotimes_{i>\frac{L}{2}} |\theta_\mathrm{R}, \varphi_\mathrm{R}\rangle$ (appealing for simulations of transport through impurities and Kondo physics, as in Kloss et al. (2023); Thoenniss et al. (2023b)).
- The purely reflection-symmetric case with homogeneous Lindbladians and states only requires keeping in memory $\langle\mathcal{L}(t)|$, which shall be overlapped with itself. This will be our case of study in Ch. 5.

[15] Apparently submitted on the same date and journal by Lerose et al. (2023).

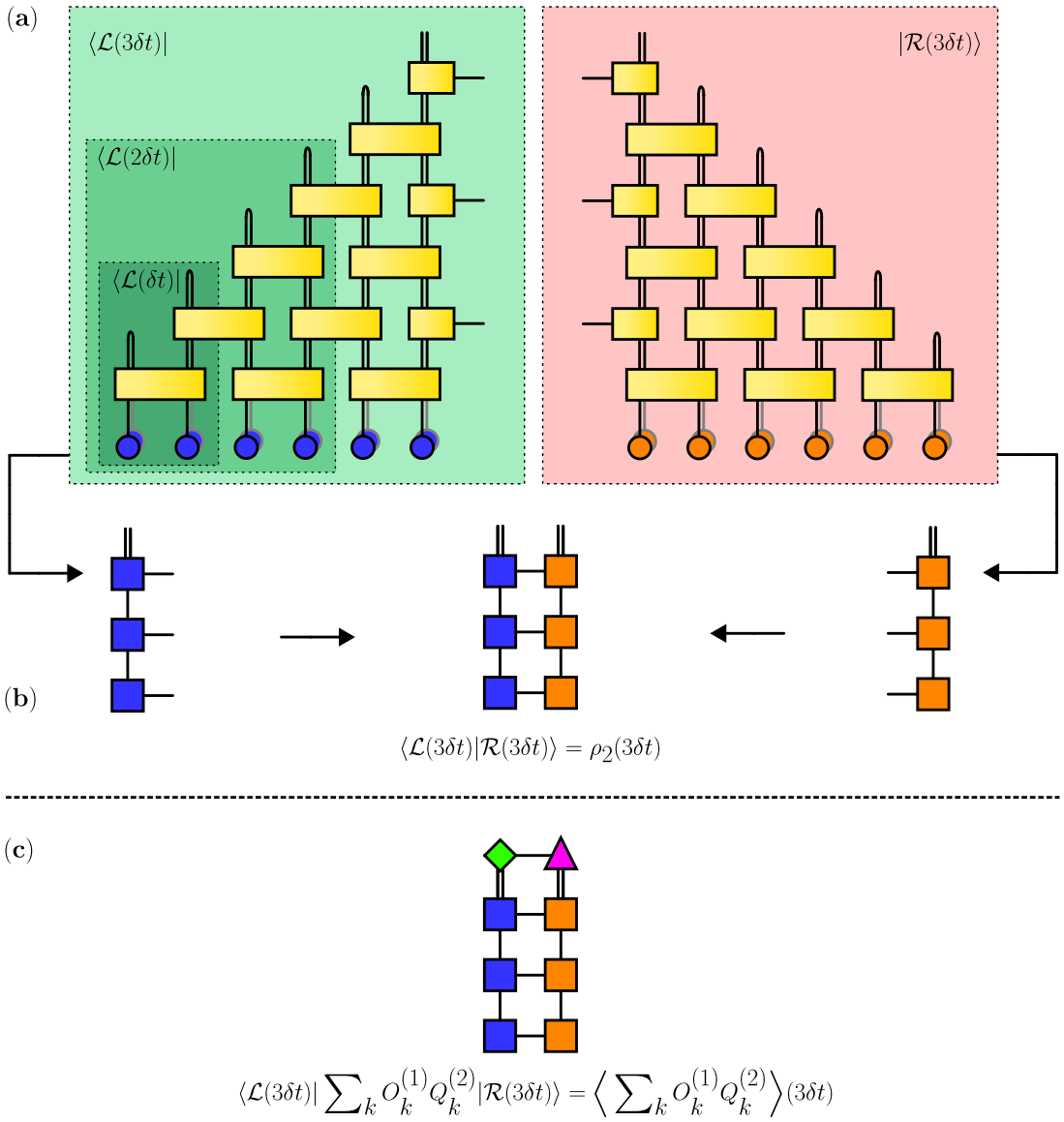

Figure 2.7: Trotterized light-cone growth and use. **(a)** The growth procedure for the tMPS on the left and right of the pyramid consist on the absorption of tensor columns of increasing length according to the times being represented. **(b)** Each half of the pyramid can be recast as an MPS with an open physical leg, which when overlapped with the other half yields the reduced density matrix of a 2-spin block. **(c)** With the reduced density matrix representation, the expectation value of any 2-spin observable can be computed.

- Simple models with only one type of interactions admit the translationally invariant form from Pirvu et al. (2010), reducing the number of columns to be absorbed per time step to 1 rather than 2.
- Any correlator between different local observables placed at different times and positions can be computed by introducing columns of length $\frac{t}{\delta t}$ between $\langle\mathcal{L}(t)|$ and $|\mathcal{R}(t)\rangle$, turning the network into a Meso-American pyramid.

- Initial translationally invariant thermal states (Zwolak and Vidal (2004), Orús and Vidal (2008)) lead to further simplifications, since exact evolution leaves them unperturbed; in the case of infinite temperature, the trotterized evolution close to the state edge also simplifies, leading to a tilted pillow TN (Frías-Pérez and Bañuls (2022)).

- Further use of the physical bounds for the propagation of correlations like the **Lieb-Robinson bound** on the velocity of wave-packets (Lieb and Robinson (1972)) can be used to narrow down the Trotter-Suzuki light-cone to a **physical-cone**, such that its contraction differs from the full one by exponentially suppressed corrections.

From the physical point of view, this contraction method acquires a meaning as the so-called bath (see Sec. 2.1.2.3) of the system, since it represents the degrees of freedom that are traced-out (in our case, the rest of the spins in an infinite chain in contact with the 2-spin block in which observables are inserted). This receives the name of **Feynman-Vernon Influence Functional** (IF, Feynman and Vernon (1963)), as pointed out by Lerose et al. (2021a,b); Sonner et al. (2021), where the authors *rediscovered* the transverse contraction, and applied it to simple and solvable kicked models in the vicinity of self-dual points.

For a nice review on the transverse contraction method and its complexity, we refer the readers to Cerezo-Roquebrún et al. (2025).

2.2.5 Measuring the Complexity of Encoding States and Operators as MPS/MPOs.

So far we have presented the update procedures for the different contraction styles of the network, and delayed the discussion on how to compress the bond dimension of the evolving MPSs until now. The truncation procedure is related with entropies, measuring entanglement in the case of pure states.

2.2.5.1 Pure State Entanglement Entropies.

In order to reduce the increasing dimensionality of the MPS/MPOs featuring in the TEBD algorithm, we invoke to the **Eckart-Young Theorem** (Eckart and Young (1936)). On the level of a single matrix $\mathfrak{M}$ with rank $\mathfrak{R}$, this theorem tells us that its best low-rank approximation $\mathfrak{M}_{\text{trunc}}$ with $\mathfrak{R}' \leq \mathfrak{R}$ consists on the truncation of its lowest singular values:

$$\mathfrak{M} = \mathcal{U}\ s\ \mathcal{V}^{\dagger} \quad \rightarrow \quad \mathfrak{M}_{\text{trunc}} = \mathcal{U}_{\text{trunc}}\ s_{\text{trunc}}\ \mathcal{V}^{\dagger}_{\text{trunc}}, \tag{2.58}$$

where $\mathfrak{R}$ is the length of s (the number of non-zero singular values before truncation), and $\mathfrak{R}_{\text{trunc}}$ is the length of s_{trunc}. In order to match the new size of s_{trunc}, the dimensions of the isometries $\mathcal{U}$ and $\mathcal{V}^\dagger$ must be projected down to the subspace with $\mathfrak{R}_{\text{trunc}}$ highest singular values, becoming $\mathcal{U}_{\text{trunc}}$ and $\mathcal{V}^\dagger_{\text{trunc}}$. This truncation minimizes the erasure of Frobenius norm of the matrix $||\mathfrak{M}||_2$, which is reduced by an amount equal to the sum of squared discarded singular values

$$\epsilon = ||\mathfrak{M} - \mathfrak{M}_{\text{trunc}}||_2 = \sum_{k=\mathfrak{R}_{\text{trunc}+1}}^{\mathfrak{R}_{\text{trunc}}} s_k^2. \tag{2.59}$$

In the case of a TN, where several sub-tensors are connected by contraction, the norm of the network must be concentrated around a tensor or a contracted index[16]. Such a procedure receives the name of **isometrization** (Evenbly), and the tensor/index where the norm is accumulated becomes a **center of orthogonality**. This procedure can be carried out in multiple equivalent ways for MPS/MPO:

- Through QR decomposition of local tensors followed by reabsorption of the R matrix in the next tensor.
- Through SVD decomposition and reabsorption of $s\ \mathcal{V}^\dagger$ or $\mathcal{U}\ s$ in the next tensor.
- Through **gauge fixing**, i.e. introducing $A\ A^{-1}$ on the bonds, such that one of the matrices isometrizes the tensor on one side, and the other pulls its norm to the next one.

The use of either of the options depends on the information that we need to access.

Importantly enough, for pure states, the rank reduction has a direct connection with the normalization of the state; we explain this through Fig. 2.8. In (a) we see the tensor network computation of the norm $\langle\Psi|\Psi\rangle$ for a state on a chain of length $L = 5$, and in (b) its isometrization on the second bond (starting from the left). The set of isometries[17] connected to the left of the orthogonality center correspond to the Schmidt vector $|\Psi_k^{\text{L}}\rangle$, while the converse is true for the right hand side. If the norm is recomputed in this form, it is easy to see that $\langle\Psi|\Psi\rangle = \sum_k s_k^2$. Therefore the rank reduction in any bond is translated in norm loss in the global pure state $\langle\Psi|\Psi\rangle - \langle\Psi_{\text{trunc}}|\Psi_{\text{trunc}}\rangle = \epsilon$.

At the same time, truncation of singular values on a bond is the same as the truncation of the eigenvalues of two matrices: $\mathcal{M}_{(3,4,5)}$ and $\mathcal{M}_{(1,2)}$, depicted in (c), which correspond to $\sum_k |\Psi_k^{\text{L}}\rangle s_k^2 \langle\Psi_k^{\text{L}}|$ and $\sum_k |\Psi_k^{\text{R}}\rangle s_k^2 \langle\Psi_k^{\text{R}}|$, respectively. These matrices differ just by an isometry from the reduced density matrices at each side, $\rho_{(1,2)}$ and $\rho_{(3,4,5)}$, as

[16] When we refer to an index as a center of orthogonality we are slightly abusing language; what we really mean is that we generate a diagonal matrix in a bond, containing the list of singular values of the bipartition across that index.

[17] Note that the isometries are represented by triangular tensors that point towards the center of orthogonality.

depicted in (c). Therefore the eigenspectrum of $\mathcal{M}_{(3,4,5)}$ and $\rho_{(1,2)}$ is the same, and rank reduction corresponds also to norm loss in the reduced density matrices:

$$\mathrm{Tr}\{\rho_\ell - \rho_{\ell,\mathrm{trunc}}\} = \epsilon = \mathrm{Tr}\{\rho_{\ell\backslash L} - \rho_{\ell\backslash L,\mathrm{trunc}}\},$$

and depurification in case of initially pure reduced states.

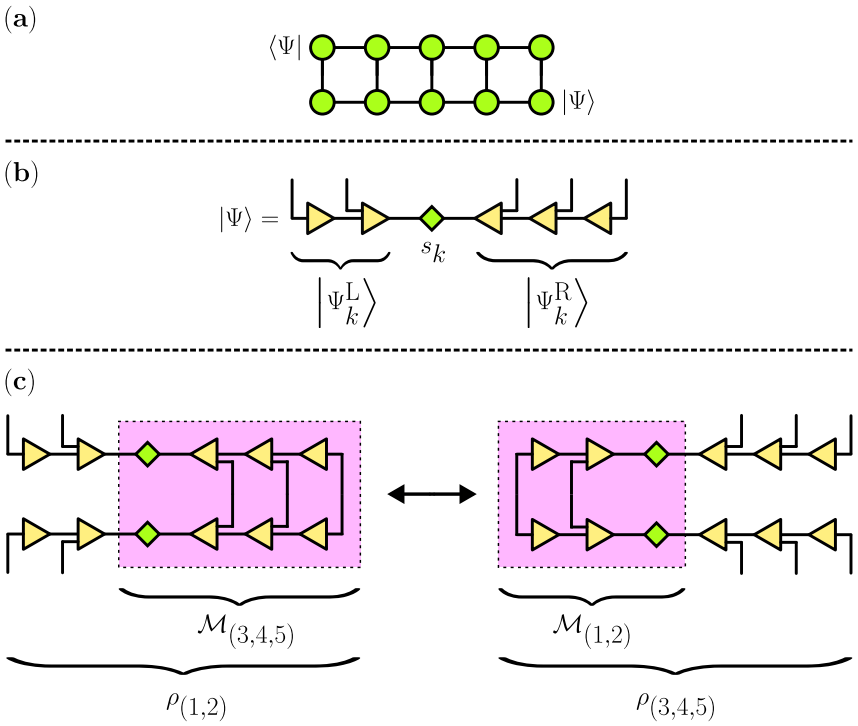

Figure 2.8: Truncating a state vector. (a) The norm of a state represented by an MPS is the zipper of two copies of $|\Psi\rangle$; (b) upon isometrizing the state by setting a particular bond as a center of orthogonality, it can be seen (c) that the eigenvalues of the reduced density matrices of the subsystems separated by such a bond coincide with s_k^2.

After understanding the procedure on how to reduce the bond dimension of the evolving states, we face the following question: how much are we allowed to reduce the dimensionality $\chi_\ell = \mathfrak{R}_\ell$ of a particular bond $(\ell, \ell\backslash L)$, such that the incurred error ϵ_ℓ (or its sum over all bonds $\epsilon = \sum_\ell \epsilon_\ell$) at a particular time in the global normalization is held constant?

This question was first answered *in the context of equilibrium physics*, i.e. which χ_ℓ was required to represent a state as L grew, rather than t. The results were summarized for a quantity intimately related to χ_ℓ, the entanglement entropy S_ℓ defined in Eq. 2.9. Note that the eigenvalues s_k^2 of the reduced density matrices of left ℓ and right $\ell\backslash L$ subsystems with respect to a particular bond $(\ell, \ell\backslash L)$ enter in the definition S_ℓ.

The entanglement entropy S_ℓ measures how informative the eigenvalue distribution $\{s_k^2\}$ is, being maximal $S_\ell^{\max} = \log \mathfrak{R}_\ell$ for infinite temperature reduced states, for which all the eigenvalues are equal. This means that the upper bound in entropy is controlled by the rank of the reduced density matrices ρ_ℓ, or conversely, by the bond dimension χ_ℓ across bond $(\ell, \ell \backslash L)$. When the tail of $\{s_k^2\}$ is trimmed, the entropy is also truncated in the same way as the norm. For small singular values, the function $-x \log x \simeq x$, giving

$$S_\ell - S_{\ell,\text{trunc}} \simeq \sum_{k=\mathfrak{R}_{\text{trunc}+1}}^{\mathfrak{R}} s_k^2 = \epsilon.$$

This means that, if the exact entropy was proven to grow linearly with length ℓ for particular systems and quenches, the required bond dimensions $\chi_\ell = \mathfrak{R}_\ell$ to keep ϵ fix would grow accordingly as $\chi_\ell \propto e^{\alpha \ell}$ to ensure that the truncated entropy is closed to the exact one by ϵ. This worst-case scenario receives the name of **volume law** entanglement growth, in reference to how entropy scales with the length of the subsystem ℓ; in order to represent volume law states with fixed accuracy, an exponential amount of computational resources would be required.

In the opposite scenario, if S_ℓ was constant with ℓ, so would be χ_ℓ. This is the **area law** of entanglement (in 1D the *perimeter* of ℓ has constant extension). For intermediate cases, the bond dimension shall grow polynomially, which translates into a logarithmic behavior of S_ℓ. Schuch et al. (2008) concluded that the cases in which χ_ℓ grow sub-exponentially are adequate for numerical simulation:

- The main physical instances of area law states are the ground states (and low excited ones) of gapped local Hamiltonians; this result explained the success of DMRG (White (1992)), as studied by Verstraete and Cirac (2006) in solvable models, and formalized by Hastings (2007).
- The logarithmic excursions on top of the area law of the entropy were first detected for critical integrable Conformal Field Theories by Vidal et al. (2003) and Calabrese and Cardy (2004). This violation of the constant behavior of S_ℓ is connected to the gapless spectrum of the underlying Hamiltonian at the critical point.

As for non-equilibrium physics, i.e. how S_ℓ scales with t in a quench scenario, Calabrese and Cardy (2005) generalized their former study (Calabrese and Cardy (2004)) to incorporate the time dependence, finding that in their integrable model $S_\ell \propto t$. More instances of a volume law for dynamics were found ever since, including interacting integrable (Alba and Calabrese (2017)) and non-integrable models (Kim and Huse (2013)); the later proved that the entanglement would spread faster than energy, which is expected to spread diffusively in chaotic systems.

This despairing results elevated the simulation of generic dynamics scenarios to a challenging task: many algorithms have been developed in order overcome the computational issues posed by the linear growth of entropy out-of-equilibrium, gathered under the umbrella term of **the entanglement barrier**.

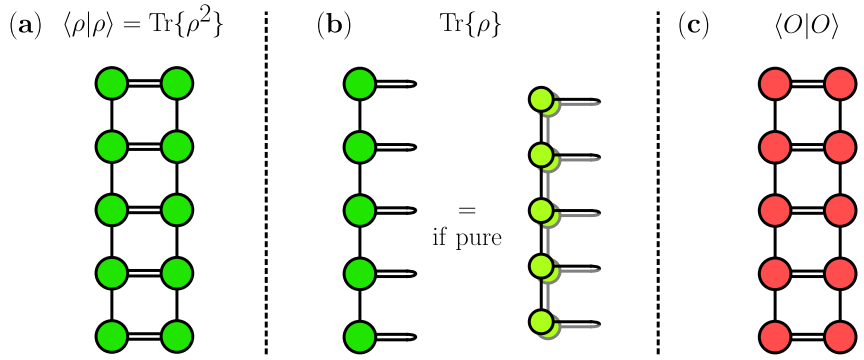

Figure 2.9: Truncating operators. (a) The norm over which the folded density matrices are truncated is their purity. (b) Only the contraction of ρ with $\mathbb{1}_{2^L}$ corresponds to the probability normalization of the state, which decouples in two disconnected layers for the pure case. (c) The norm of observables is not bounded between 0 and 1.

2.2.5.2 Operator Space *Entanglement* Entropies.

When dealing with global density matrices, the measure of computational complexity inherits the mathematical expression of the von Neumann entropy,

$$\mathrm{OSEE}_\ell = -\sum_k s_k^2 \log s_k^2, \tag{2.60}$$

which stands for Operator Space Entanglement Entropy; despite the name, this object is only related to the entanglement entropy for density matrices of pure states, as derived by Dubail (2017), fulfilling that

$$\mathrm{OSEE}_\ell(|\Psi\rangle\langle\Psi|) = 2S_\ell(|\Psi\rangle). \tag{2.61}$$

For mixed states, this measurable[18] quantity confuses entanglement with mixture, so it is not a proper entanglement witness. Nevertheless, we use it heavily in numerical studies. Its truncation impacts the norm of the vectorized object (recall that the bra and ket indices of local tensors in MPO can be folded and merged, generating an MPS with squared physical dimension), which in this case is the purity $P = \langle\rho|\rho\rangle = \mathrm{Tr}\{\rho^2\}$ (see Fig. 2.9(a)). This has an uncontrolled effect on the norm of the state, which corresponds to closing the physical legs with folded identities $|\mathbb{1}_2\rangle$, as in Fig. 2.9(b). The same definition shall be applied to observables, and the truncation may be performed over their norm $\langle O|O\rangle$.

The behavior of the OSEE for density matrices is different depending on whether the systems are at equilibrium or out-of-equilibrium; in the later case, it depends on the integrability of the underlying Hamiltonian inducing the evolution:

[18] By using several replicas of the state, as specified in Dubail (2017) and inspired by Hastings et al. (2010) and Islam et al. (2015).

- The OSEE is bounded for (Generalized) Gibbs equilibrium states (irrespectively of the underlying integrability), as found numerically by Žnidarič et al. (2008a). At the critical point, Dubail (2017) found that the upper bound of the OSEE for a CFT only grows logarithmically with β.
- For evolving density matrices (Schrödinger picture) that were initially pure, Žnidarič et al. (2008a) and Dubail (2017) found that OSEE should grow linearly at short times. Nevertheless, knowing that the quenched state should equilibrate locally, Dubail (2017) argued and derived analytically for a free fermion model that OSEE should fall back to its thermal equilibrium bound.
- For evolving density matrices that were initially thermal, Prosen and Žnidarič (2007) determined numerically a (sub-)linear growth of χ_ℓ (area law) for high temperature initial states evolved with integrable models, and exponential for low temperatures (volume law); opposed to that, for states with any initial temperature, non-integrable Hamiltonians would drive their OSEE always to follow a volume law.

Unlike density matrices, the OSEE of relevant local observables in MPO form can only be judged out-of-equilibrium. In such a matter, *Prosen et al.* exhaustively explored all possible behaviors of Heisenberg picture observables under different Hamiltonians:

- Prosen and Žnidarič (2007) also found that local operators evolved by integrable Hamiltonians may be recast as exact MPS with low bond dimension (like the σ^x operator for the integrable Ising model, which is an MPS with $\chi = 4$); such a dimension is related to the **fermionic index**[19] of the observable. For observables with infinite index, χ_ℓ would grow linearly, leading to an OSEE that follows an area law for some quantities and violates it logarithmically for others. Global sums of local observables were found to increase the growth rate of χ_ℓ from constant to linear, and from linear to super-linear (but sub-exponential), respectively.
- When non-integrable perturbations are introduced, the OSEE follows a volume law, as confirmed by Prosen and Pižorn (2007a) for the Ising model and by Pižorn and Prosen (2009a) for the XY model.
- On top of that, Prosen and Pižorn (2007a) established that at the critical point of integrable Hamiltonians, the OSEE increases logarithmically with time, but later Pižorn and Prosen (2009a) found that introducing weak disorder would trigger saturation from logarithmic to area law. This promoted the study of OSEE for Hamiltonians displaying Many-Body Localization, which was found again to display a logarithmic growth in time (Žnidarič et al. (2008b)).

To conclude this section, we want to note that the OSEE has been also studied for the evolution operators U_t themselves in chaotic (volume law OSEE, Dubail (2017); Zhou and Luitz (2017)), Anderson-localized (bounded OSEE, Dubail (2017)) and Many-Body-Localized (logarithmic OSEE, found by Bardarson et al. (2012) and explained by an

[19] Half the number of fermionic operators after Jordan-Wigner transformation.

effective dephasing identified by Serbyn et al. (2013)) Hamiltonians. To the best of our knowledge, the only case where OSEE has been studied with Liouvillian dynamics is that of Wellnitz et al. (2022), where it was found bounded, except if an extra symmetry was imposed on the Liouvillian, leading to volume law growth.

2.2.5.3 *Time Entanglement* Entropy.

In the same style as for folded density and observable operators, the compression of the tMPS introduced in the transverse contraction in Sec. 2.2.4.3 also relies on a quantity, which in an abuse of language has been also dubbed **Time Entanglement Entropy** (TEE[20]), despite also carrying information on mixture across unequal times. This is an umbrella term, since each new article that pops up working on TEE slightly redefines it; therefore, instead of writing about generalized-generalized-generalized time entanglement measures, we will refer to TEE as the measure of complexity for particular realizations of the transverse folding algorithm.

The first study concerning the difficulty of contracting the 2D evolution network from the transverse direction was carried out by Müller-Hermes et al. (2012a); on it, the authors were concerned about the effect of folding the network (merging forward and backward directions and effectively squaring the index dimensions) on the complexity of the contraction. Their definition of TEE is again the von Neumann entropy, but for an MPS representing the trajectory of a single spin (the leftmost or rightmost columns of the 2D network). This seminal work did not include the light-cone simplification allowing for the iterative growth of the tMPS, but the results for the behavior of TEE is expected to be exactly the same as with the light-cone trick, since gate cancellation should still occur under the hood.

Based on simple transport models of non-interacting entangled pairs that spread ballistically, they argued that for integrable models that can be mapped to free particles, the folding should cancel out the entanglement when connecting the forward and backward contours through the traces on the operator edge. Through simulations, they proved that the maximum TEE scaling with total time $\mathrm{TEE}_{\max}(t, T-t)$ for the initial fermionic Fourier vacuum changed from volume to area law upon folding the integrable evolution. This could be explained by the trace cancellation of counter-propagating entangled particles on the operator edge of the network. When adding non-integrable perturbations, the advantage of folding was blurred, since deep in the non-integrable regime, the maximal TEE for the folded strategy surpassed the unfolded one.

Some time later, Lerose et al. (2021a) applied the same algorithm to simulate **kicked Floquet dynamics**[21] close to the **perfect dephaser point**, where OSEE grows the fastest, connecting the tMPS with the Feynman Vernon IF; they found that the tMPS looks like

[20] Maybe, since OSEE included the information on the object we are referring to, it would make sense to call it Bath-TEE or BTEE.

[21] Similar to a first-order Trotter-Suzuki evolution but setting $\delta t = 1$.

a PS along time. They confirmed their numerical results with analytical solutions of self-consistency bath equations at solvable, infinite temperature instances (Lerose et al. (2021b)). In a follow-up, the same authors studied the same models with non-integrable perturbations, and MBL Hamiltonians where disorder average was required (Sonner et al. (2021)); in all cases they reported area law (folded) TEE or sublinear growth. Their subsequent works found the same results on slightly modified models: Kloss et al. (2023); Lerose et al. (2023); Thoenniss et al. (2023a,b).

Giudice et al. (2022) carried similar studies for the kicked XXZ, targeting the question on whether integrable interactions violate the area law found in former works. The result was positive, yielding a logarithmic increase of the maximum TEE as the model deviated from the **self-dual point** (point where exchanging spatial indices of the local evolution by temporal indices renders the evolution unaffected).

More analytical derivations were performed by Foligno et al. (2023), who focused on random brick-wall and dual-unitary circuits, but generalized the tMPS to correspond to cutting the 2D TN with an angle; in particular, exact solutions in the thermodynamic limit for the TEE of tilted tMPS could be found in the solvable dual-unitary examples. Interestingly, they did not only study the von Neumann entropy, but also Rényi entropies with $\alpha > 1$. Their study reported a generic volume law behavior for the random circuit case and the purely transverse strategy on self-dual circuits; in the later case, $\alpha > 1$ grew sublinearly for any tilt of the tMPS. Overall, this extensive study found once more that the tMPSs have large overlaps with PS and that few singular values decaying slowly contain most of the norm of the contraction. In order to perform their derivations, they connected the TEE with the OSEE through the ranks and purities of Schrödinger picture evolved density matrices, and concluded that TEE can be an indicator for dynamical chaos, by distinguishing integrable Hamiltonians from their non-integrable generalizations.

In a similar spirit as this last work, Yao and Claeys (2024) studied self-dual unitary circuits with and without presence of measurements, finding that in the measurement-free regime the entanglement has a volume law peak (like Dubail (2017) found for OSEE in a CFT), while for sufficiently high rate of measurements the TEE follows an area law characterized by diffusive propagation of entanglement versus the ballistic spreading of the volume phase.

2.2.6 The Goal of this Thesis.

In the present manuscript we dedicate three different chapters to tackle each one of the strategies for contracting the 2D TN representing the dynamics of local observables.

On the Schrödinger and Heisenberg pictures (Chapters 3 and 4 respectively) we try to find suitable generalizations of TEBD implementing the reduction from volume law pure evolving states/operators to the area law of their thermal counterparts. As such, the present thesis connects with the work of Surace et al. (2019), where the algorithm proposed by Dubail (2017) was implemented for fermionic quadratic Hamiltonians. In the course of this thesis, a continuation of *Surace et al.*'s work by Frías-Pérez et al. (2024) was published, where the authors identify long-range entanglement beyond the support of local density matrices, and transform it into mixture, managing to tame the entanglement barrier in Schrödinger picture.

On the transverse picture, our purposes are more humble, and we focus on filling the summary table hereunder for different Hamiltonian and dissipation models.

Contraction	**Evolving Hamiltonian**	$\langle\rho(t=0)\|$ **or** $\|O(t=0)\rangle$	**OSEE Law after Quench**
Schrödinger	Integrable	Pure	Volume
		High Temperature Thermal ($\mathcal{E}\beta \ll 1$)	Log
		Low Temperature Thermal ($\mathcal{E}\beta \gg 1$)	Volume
	Integrable Critical (CFT)	Pure	Volume ($\mathcal{E}t \ll 1$) and Area ($\mathcal{E}t \gg 1$)
	Non-integrable	Pure/Thermal	Volume
Heisenebrg	Integrable	Local	Area (finite-index) Log (∞-index)
		Global	Log
	Integrable Critical (CFT)	Local	Log
	Non-integrable	Local	Volume
	MBL	Local	Log

3

Explorations in the Schrödinger Picture: a take on Decoherence and Classical Stochastic Systems

In this chapter we present a set of initial ideas explored at the beginning of this thesis. Since its contents belong to a brainstorming period, the pipeline we describe here may not look obvious or straightforward, but rather branching and detached from the concept of entanglement barrier. Nevertheless, the order in which the results are presented faithfully represents our original attempts of improving TEBD, and how they were crucial for the later studies carried out in Ch. 4. Therefore, we hope you receive the following discussion as an enjoyable dance of open-ended ideas.

When a quantum system is evolved in time, the operation that is performed numerically is that of iteratively applying the imaginary exponential of the Hamiltonian H on the vector $|\Psi\rangle$ that encodes the initial state

$$|\Psi(t)\rangle = e^{-itH}|\Psi(t=0)\rangle = \prod_{n=1}^{N} \left(e^{-i\delta t H}\right)^n |\Psi\rangle, \tag{3.1}$$

therefore, any time evolution method that divides the unitary operator $U_t = e^{-itH}$ in $N = \frac{t}{\delta t}$ numerical steps is effectively a power method. Normally, such a method would gradually project the initial state onto the dominant eigenspace of the operator that is applied, conditioned on the fact that there exists a gap in the eigenvalue spectrum.

In particular, we are usually interested on operators with two well separated leading eigenvalues, like for Euclidean time evolution, corresponding to Eq. 3.1 with $\delta t = -i\delta\tau$; the resulting one-step-operator $e^{-\delta\tau H}$ is used as an alternative to DMRG, iteratively projecting initial states onto the ground state of gapped local Hamiltonians.

Opposed to that, unitary evolution presents modulus 1 eigenvalues, given by the

imaginary exponents of the eigenenergies of H: $\{e^{-itE_1},\ e^{-itE_2},\ ...e^{-itE_{2^L}}\}$. This reasoning holds for the closed unitary evolution of any initial density matrix, pure or mixed, which is time-translated by the superoperator $U_t[\ \cdot\ ]U_t^\dagger$. By vectorizing the latter, we observe that the eigenvalues of such a folded operator are also phases, taking as arguments all the possible differences of energies $\{e^{-i(E_m-E_n)}\}_{m,n=1}^{2^L}$.

From this power method perspective, opposed to DMRG and Euclidean time TEBD, real time TEBD for the simulation of unitary dynamics can not be efficiently tackled unless a gap is introduced in the spectrum of the evolution operator[1]. In this chapter, we devote ourselves to exploring the many ways in which such a gap can be induced while accurately retrieving physically sensible quantities.

3.1 Introducing Gaps in the Unitary Evolution with Tensor Networks.

Our core idea in this chapter is to open a gap in the spectrum of the unitary evolution while minimally disturbing the natural flow of quantum dynamics. In the process, many complications may (and will) arise.

3.1.1 Step 1: Introducing Full Decoherence.

In order to introduce a gap, we recall the TN structure of quantum systems subject to dissipation in Sec. 2.1.2.3. In those settings, decay channels like depolarization or decoherence involve the coupling between the forward and backward contours. The simplest coupling one can think about is a generalized identity, also dubbed as **copy tensor** by the TN community. For our later purposes, we introduce here the 3- and 4-legged copy tensors,

$$\left[\mathbb{1}_2^{(3)}\right]_{ijk} = \delta_{ijk} = \delta_{ij}\delta_{jk}, \quad \left[\mathbb{1}_2^{(4)}\right]_{ijkl} = \delta_{ijkl} = \delta_{ij}\delta_{jk}\delta_{kl}, \tag{3.2}$$

where $\left[\mathbb{1}_2^{(2)}\right] = \delta_{ij}$ is the Kronecker tensor for 2 indices with entries $\delta_{i=j} = 1$ and $\delta_{i\neq j} = 0$. The graphical representation of these tensors is shown in Figs. 3.1 (b) and (c).

[1] Sometimes this is not even the case, since open system dynamics poses other types of problems; in particular, when dealing with condensed matter impurity models, some researchers choose to perform unitary evolution on the impurity + leads system rather than finding the effective positive evolution in order to reduce the model bias, introducing problematic overheads in the computations.

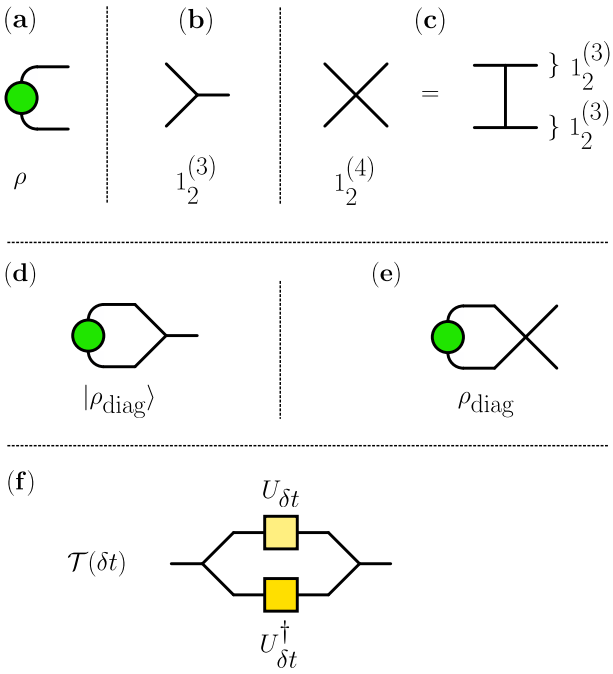

Figure 3.1: Density matrices, copy tensors and gapped evolution superoperators. The coupling between bra (forward contour) and ket (backward contour) legs of a density matrix ρ **(a)** is a crucial component of dissipative dynamics. This can be done introducing a copy tensor (generalized identity) with 3 **(b)** or 4 legs **(c)**; the 4-legged identity can be decomposed as the contraction of two 3-legged identities. Upon connecting these copy tensors to the density matrix, we extract its diagonal in the form of a vector **(d)**, or as a matrix **(e)** whose off-diagonal elements have been set to 0. When operating with 3-legged copy tensors on superoperators like the closed unitary evolution, we generate positive doubly stochastic transfer matrices **(f)** whose entries correspond to the modulus squared of either the forward or backward branches.

If we now connect $\mathbb{1}_2^{(3)}$ or $\mathbb{1}_2^{(4)}$ to an initial density matrix, we retrieve the vector of its diagonal in the first case, as in Fig. 3.1 (d), or a fully **incoherent/classical density matrix** in the second case, as in Fig. 3.1 (e); both resulting objects are equivalent representations of the same normalized probability distribution:

$$\left[|\rho_{\text{diag}}\rangle\right]_k = \sum_{ij} \delta_{ijk}\rho_{ij} = \rho_{kk}, \quad \left[\rho_{\text{diag}}\right]_{kl} = \sum_{ij} \delta_{ijkl}\rho_{ij} = \rho_{kl}\delta_{kl}. \tag{3.3}$$

At this point, we note that an identity coupling between the forward and backward contours (or bra and ket indices) leads to the erasure of the off-diagonal terms of the quantum states, amounting to a total decoherence[2]; given this correspondence, we will use interchangeably the names copy tensor and **full decoherence superoperator** for addressing the index connecting the bra and ket contours.

[2]In fact, this operation eliminates the off-diagonal of any matrix, but such an erasure acquires the meaning of decoherence in the context of quantum states.

Complete decoherence dissipates information, and it may be introduced along the evolution to induce the cherished gap on the evolution superoperator $U_t[\,\cdot\,]U_T^\dagger = U \otimes \overline{U}$; as an experiment, we sandwich $U_{\delta t} \otimes \overline{U}_{\delta t}$ with a pair of 3-legged copy tensors, and study the resulting **transfer operator** $\mathcal{T}(\delta t)$:

$$\begin{aligned}\big[\mathcal{T}(\delta t)\big]_{kl} &= \sum_{ijmn} \delta_{ijk}[U_{\delta t}]_{mi}[U_{\delta t}^\dagger]_{jn}\delta_{lmn} = \\ &= \sum_{ijmn} \delta_{ijk}[U_{\delta t}]_{mi}[U_{\delta t}]_{nj}^*\delta_{lmn} = \big|[U_{\delta t}]_{kl}\big|^2.\end{aligned} \tag{3.4}$$

Note that the resulting matrix is **doubly stochastic** or bistochastic, i.e. both its rows and columns contain only positive entries and add up to 1. This will allow us to later interpret a modified closed time-contour TN with interspersed decoherences in terms of classical stochastic systems in Sec. 3.1.3.

Specializing for the case of a single spin Hamiltonian, we can readily check whether a gap appeared in the new $\mathcal{T}(\delta t)$: the infinitesimal evolution $U_{\delta t}$ takes the form $\mathbb{1}\cos(\delta t) - i\sin(\delta t)\mathbf{n}(\theta,\phi)\boldsymbol{\sigma}$, where $\mathbf{n}(\theta,\phi) = (\sin(\theta)\cos(\phi), \sin(\theta)\sin(\phi), \cos(\theta))$ is some parametrization on the $\mathcal{S}_2$ sphere of the axis around which the spin will precess. The eigenvalues of $\mathcal{T}(\delta t)$ are $\lambda_1 = 1$ and $\lambda_2 = \cos^2(\delta t) + \sin^2(\delta t)\cos(2\theta)$, leading to a gap of order δt^2.

With this simple example we successfully conclude that the simple recipe of introducing copy tensors in the evolution induces a gap on the evolution superoperator, transforming it into a positive transfer matrix. This transfer matrix will act on the diagonal of the initial density matrix $|\rho_{\text{diag}}\rangle$, depicted in Fig. 3.1 (d), transforming it into another valid classical density matrix: $\mathcal{T}(\delta t)|\rho_{\text{diag}}(0)\rangle = |\rho_{\text{diag}}(\delta t)\rangle$.

Despite this small success, the process of opening a gap erased potentially important information on both the initial state and the evolution superoperator, and thus we should not expect that a modified dynamics with total decoherences placed between each time step will yield any faithful representation of the original dynamics.

In fact, even if we rewrite an arbitrary initial diagonal density matrix $|\rho_{\text{diag}}(0)\rangle = (\alpha, 1-\alpha)$ (for some $\alpha \in [0,1]$) in the eigenbasis of the transfer operator, constituted by $|\lambda_1\rangle = \frac{1}{\sqrt{2}}(1,1)$ and $|\lambda_2\rangle = \frac{1}{\sqrt{2}}(1,-1)$, it takes the form of $|\rho_{\text{diag}}(0)\rangle = \frac{1}{\sqrt{2}}|\lambda_1\rangle + \frac{2\alpha-1}{\sqrt{2}}|\lambda_2\rangle$. The iterated action of the transfer matrix on such a state yields

$$\begin{aligned}|\rho(n\delta t)\rangle = \mathcal{T}^n(\delta t)|\rho_{\text{diag}}(0)\rangle &= \frac{1}{\sqrt{2}}|\lambda_1\rangle + \lambda_2^n\frac{2\alpha-1}{\sqrt{2}}|\lambda_2\rangle \\ &\overset{n\to\infty}{\longrightarrow} \frac{1}{\sqrt{2}}|\lambda_1\rangle = \frac{1}{2}(1,\ 1) = |\rho(\beta=0)_{\text{diag}}\rangle,\end{aligned} \tag{3.5}$$

leading to the distribution associated to an infinite temperature density matrix $\rho(\beta = 0)$ and a complete loss of information.

In general, we expect this result to hold for an arbitrary number of spins: the proposed scheme is equivalent to a complete decoherence after each time step δt, and since any Hamiltonian including both local terms and interactions will scramble the information away from the diagonal with a rate specified by the hopping terms, the copy tensors will iteratively erase this information, converging sooner or later to the infinite temperature ensemble.

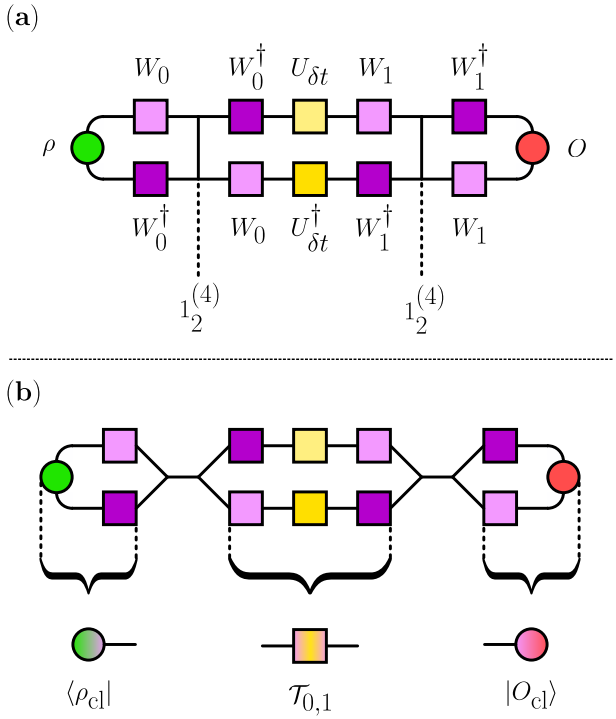

Figure 3.2: Closed time contour with chosen basis complete decoherences. **(a)** The usual closed system dynamics may be modified by introducing copy tensors after every numerical step in order to induce a gap; such a decoherence may be implemented in a particular basis W_m. **(b)** Using the correspondence between 4-legged and 3-legged copy tensors, we can split the contour into smaller contours and map each mini-loop within the graph into vectors and matrices. This maps the closed system evolution into a classical stochastic process where an initial vector of probabilities $\langle \rho_{\rm cl}|$ (which is the diagonal of the initial quantum density matrix written in W_0 basis) is evolved through a set of transfer matrices $\mathcal{T}_{m-1,\,m}$ until the overlap with the classical observable (diagonal of O in W_N basis) at the end of the contour is made. Note that the upper branch on the diagrams corresponds to the bra of the density matrix, which has been folded; therefore, all the matrices featuring in such branch need to be read as transposed matrices.

3.1.2 Step 2: Selecting a Basis.

So far we have seen that it is possible to induce a gap in the evolution. Despite that, we need an extra level of flexibility that allows us to find an optimal modified dynamics, retrieving either a locally stationary state resembling that of the unitary evolution, or the correct observables for sufficiently long times.

The solution for the lack of flexibility is tied to the way in which copy tensors $\mathbb{1}_2^{(3,4)}$ act: as we have interpreted earlier, applying them on a density matrix produces total decoherence and, as such, these objects are not basis covariant. Coherence entries in a density operator (or off-diagonal in arbitrary matrices) are mixed with the diagonal through rotations, and thus the erasure of copy tensors depends on the prescription chosen to distinguish between diagonal and off-diagonal elements, i.e. the basis in which the state is written. This means that we can introduce rotations on tensor legs and shift to a basis in which we prefer to lose coherence; afterwards, we can proceed to fully decohere, and back-rotate to the original basis, as we depict in Fig. 3.2 (a).

Thus, we introduce the copy tensors in the contour dressed by chosen rotations W_m at each time step as in Fig. 3.2; the new sequence of $N+1$ rotations (where $N = \frac{t}{\delta t}$) is labeled by $\{W_m\}_{m=0}^{m=N}$. Upon selecting each W_m, we could map the closed dynamics to a classical equivalent, mediated by positive transfer operators. The m-th transfer operator in this modified time contour will now include the $(m-1, m)$-th changes of basis

$$\left[\mathcal{T}_{m-1,\,m}(\delta t)\right]_{kl} = \left|\left[W_{m-1}^{\dagger} U_{\delta t} W_m\right]_{kl}\right|^2, \tag{3.6}$$

as represented in Fig. 3.2 (b) for a contour with a single time step. Note that the matrix $\mathcal{T}_{m-1,\,m}(\delta t)$ acts as $\langle \rho_{\mathrm{cl}}\big((m-1)\delta t\big)|\mathcal{T}_{m-1,\,m}(\delta t) = \langle \rho_{\mathrm{cl}}(m\delta t)|$, updating the probability distribution on the former basis W_{m-1}. The choice of writing it as an application from bra to bra is just made to match the scheme in Fig. 3.2 (b).

The net transfer operator encoding the full gapped evolution after N time steps now reads

$$\mathcal{T}(N\delta t) = \prod_{m=0}^{N-1} \mathcal{T}_{m-1,\,m}(\delta t), \tag{3.7}$$

mapping the diagonal of the initial state $\langle \rho_{\mathrm{cl}}| = \langle \rho_{\mathrm{diag}}(0)|$, written in the basis specified by W_0, onto a new classical state $\langle \rho_{\mathrm{cl}}(t)|$ to be overlapped with the diagonal of an observable O, written in basis W_n as $|O_{\mathrm{cl}}\rangle$ (see Fig. 3.2 (b)).

After including a new set of rotations for extra tuning, now we can find the optimal set of changes of basis correctly reproducing the dynamics in our spin chains. At this stage the first question that may rise is whether there exists an exact solution for such an optimization problem. The answer to this question is affirmative, and it can be extracted directly from the graphical representation in Fig. 3.2 (a). If we want to preserve the information of any observable (either local or non-local) for all times, the

rotations W_m must diagonalize whichever density matrix came from the former step, before the coupling between forward and backward branches erases the off-diagonal. This solution thus requires the following set of rotations

$$\Big\{W_0 = \mathcal{B},\ W_1 = U_{\delta t}^{\dagger}\mathcal{B}, ...W_N = U_{N\delta t}^{\dagger}\mathcal{B}\Big\}, \tag{3.8}$$

where $\mathcal{B}$ is the transformation that diagonalizes the initial state as $\mathcal{B}\rho(0)\mathcal{B}^{\dagger} = \rho_{\text{diag}}(0)$; recall that W_m act on the bra index of the density operator, so the forward/upper branches on Fig. 3.2 (a) need to be understood as the transpose of the matrices featuring on it.

Despite the simplicity of this solution, we run into problems when constructing the transfer operator: by plugging Eq. 3.8 into Eq. 3.6 we get the trivial result $\mathcal{T}_{m-1,\,m} = \mathbb{1}_{2^L}\ \forall\ m$. Therefore the exact solution is also a gapless and useless one. On top of that, it would require finding the exact evolution by diagonalizing both the full Hamiltonian and the initial density matrix, which is everything we want to avoid, a prohibitive task for systems larger than $L \sim \mathcal{O}(10)$.

3.1.3 The Stochastic-Quantum Correspondence.

In the process of introducing a gap in the evolution, we have proposed a recipe for mapping the closed unitary dynamics of a many-body quantum system to that of a classical stochastic system where the evolving object is a probability distribution. In this section we analyze the elements of the stochastic-quantum correspondence in the spirit of D'Alessio et al. (2016) (5.1.1) and Barandes (2023a,b).

Following Fig. 3.2 (b), we identify $\langle\rho_{\text{cl}}|$ as the row vector encoding the **standalone probabilities** p_i of populating a set $\mathcal{C} = 1, 2, ...2^L$ classical configurations. Therefore the populations of the density matrix, which are basis dependent, correspond to the probabilities p_i of occurrence of each system configuration.

If the initial quantum state is a PS, the space of configurations at time $t = 0$ will coincide with the bit strings specified by the computational basis for which the initial state is diagonalized. In other words, there is a rotation W_0 taking the form of a set of single spin rotations fixing the quantization axis for a system with unentangled spins, pointing in arbitrary directions

$$W_0 \quad \text{s.t.} \quad W_0 \bigotimes_{\ell=0}^{L} |\theta_\ell, \varphi_\ell\rangle = \bigotimes_{\ell=0}^{L} |0\rangle = |0...0\rangle. \tag{3.9}$$

In this case we can easily interpret $\mathcal{C}$ as the collection of all possible strings generated by spin flips with respect to this reference state. All these bit strings are in one-to-one correspondence with the string labeling the computational basis defined by W_0.

Moving on to how the (row) vector of probabilities may evolve in time, we introduce the **stochastic map** $\Gamma(0,t)$, that linearly mixes the probabilities of populating each classical state (vector entries) for any time as $p_j(t) = \sum_{i=1}^{2^L} p_i(0)\Gamma_{ij}(0,t)$. Such a map is the matrix of **conditional probabilities** $\Gamma_{ij}(0,t) = p(i,0|j,t)$ of the system being in state j at time t, given the fact that it was initialized in state i. Since this matrix contains probabilities, all its entries are positive, and the probability normalization imposes a column- and row-wise sum to 1 for $\Gamma(0,t)$ in the form $\sum_j \Gamma_{ij}(0,t) = 1$.

In our discussion, the stochastic map corresponds to the accumulated transition matrix $\mathcal{T}(N\delta t) := \Gamma(N\delta t)$ defined in 3.7. Due to the way in which we introduced the transfer matrices as evolving differentially in time, the construction ensures map divisibility (Wolf and Cirac (2008)) as $\mathcal{T}(t,0) = \mathcal{T}(t,t')\mathcal{T}(t',0)$ with $0 \leq t' \leq t$ and $\mathcal{T}$ a smooth function of time. Importantly enough, the sandwiched unitary evolution between basis rotations contains the roots of the conditional probabilities in the map $\Gamma(t', t'+\delta t)$:

$$p(i,t'|j,t'+\delta t) = \left| W_{\frac{t'}{\delta t}} U_{\delta t} W_{\frac{t'}{\delta t}+1} \right|^2. \tag{3.10}$$

Note that after short times the quantum state will be entangled, and no simple interpretation in terms of a basis of PS (bit strings) will be available for the classical configurations. The meaning of the configurations in $\mathcal{C}$ will change with time, and a clear interpretation of what each represents comes by measuring observables.

In general stochastic systems, observable quantities are encoded as time-dependent random variables $A(t)$, taking on different values $a_i(t)$ for each configuration i; in our full decoherence picture, the vector $|O_{\text{cl}}\rangle$ contains these values $a_i(t)$ allowing for physical interpretation of the time dependent configurations. This time dependence is tied to the last rotation $W_{N=\frac{t}{\delta t}}$.

The closed modified time-contour is nothing else than the expectation value of a time dependent random variable, induced from whichever hermitian operator O is being measured, and a time dependent entangled basis W_N; that is the reason why it takes the form of the inner product between the evolved classical probability distribution $\langle \rho_{\text{cl}}(N\delta t)|$ and the vector of $a_i(t)$ values on each state of the random variable at a given time, $|O(N\delta t)\rangle$:

$$\langle O(N\delta t)\rangle = \langle \rho_{\text{cl}}(0)|\mathcal{T}(0,N\delta t)|O_{\text{cl}}(N\delta t)\rangle = \langle \rho_{\text{cl}}(N\delta t)|O_{\text{cl}}(N\delta t)\rangle. \tag{3.11}$$

3.2 Tuning the Classically-Mapped Evolution to Preserve the Local Physics.

The problem at hand acquired the form of mapping the closed quantum unitary evolution to a classical gapped evolution, with a time-dependent transfer operator. Since the exact solution of the modified closed time-contour through chosen basis decoherences turns out to yield a trivial transfer operator, we shift our focus onto finding an approximate solution.

3.2.1 Where is the Local Physics?

As formerly motivated in Ch. 2, local observables are believed to witness the thermalization in challenging non-integrable many-body quantum systems, turning them into interesting quantities to be simulated. From the numerical viewpoint, thermalization can be used to test the efficiency with which new methods reach the long time regime, since they are believed to stabilize around thermal values; these thermal values can be easily estimated with exact diagonalization calculations, that converge already for small system sizes ($L \sim \mathcal{O}(10)$), constituting a nice guide to the eye for the soundness of our numerical experiments. This brings us to add an extra constraint on the time-dependent transfer operator: it must correctly reproduce the local physics (expectation values of few-site operators).

For such an endeavor we first need to determine where the relevant local information is hidden within the quantum state at hand. We do this through an example: if we compute the correlation $\sigma_1^x \sigma_2^z \sigma_4^y$ in a spin chain of length $L = 4$, we obtain

$$\begin{aligned}
\mathrm{Tr}\{\rho\, \sigma_1^x \sigma_2^z \sigma_4^y\} &= \mathrm{Tr}\Big\{ \sum_{\{\ell\},\{\ell'\}} \rho^{\ell_1' \ell_2' \ell_3' \ell_4'}_{\ell_1 \ell_2 \ell_3 \ell_4}\, \sigma_1^x \sigma_2^z \sigma_4^y\, |\ell_1, \ell_2, \ell_3, \ell_4\rangle\langle \ell_1', \ell_2', \ell_3', \ell_4| \Big\} \\
&= \mathrm{Tr}\Big\{ \sum_{\{\ell\},\{\ell'\}} \rho^{\ell_1' \ell_2' \ell_3' \ell_4'}_{\ell_1 \ell_2 \ell_3 \ell_4}\, i(-1)^{\ell_2+\ell_3+1}\, |\ell_1+1, \ell_2, \ell_3+1, \ell_4\rangle\langle \ell_1', \ell_2', \ell_3', \ell_4'| \Big\} \\
&= \sum_{\{\ell\},\{\ell'\}} \rho^{\ell_1' \ell_2 \ell_3' \ell_4'}_{\ell_1 \ell_2 \ell_3 \ell_4}\, i(-1)^{\ell_2+\ell_3+1} \delta_{\ell_1+1,\ell_1} \delta_{\ell_2,\ell_2'} \delta_{\ell_3+1,\ell_3'} \delta_{\ell_4,\ell_4'} \\
&= \sum_{\{\ell\}} i(-1)^{\ell_2+\ell_3+1} \rho^{\ell_1+1,\ell_2,\ell_3+1,\ell_4}_{\ell_1 \ell_2 \ell_3 \ell_4}.
\end{aligned}$$

The last line reduced the computation to the use of a subset of the entries in the density matrix, in particular those corresponding to the off-diagonal elements representing 2-spin-flips in computational basis.

Conversely, correlations implying a number $n^{\perp}$ of Pauli matrices drawn from the subset $\{\sigma^x,\ \sigma^y\}$ make use of density matrix entries relative to $n^{\perp}$-spin-flips, while observables with arbitrary $n^{\parallel}$ matrices of the type σ^z will only overlap with the entries resting on the diagonal. In general, computing an observable involving n Pauli matrices requires the extraction of elements from both the diagonal (populations) and the off-diagonal (coherences) up to n-spin-flips in computational basis.

The former paragraph can be rephrased in the following way: retrieving the local physics from a state represented by a density matrix only requires a limited amount of coherence; if we are interested in observables with non-trivial support clustered on ℓ sites, at most $(n \leq \ell)-$spin-flips (in computational basis) will participate in the expectation value. This simplification occurs thanks to the trace connecting the bra and the ket.

This brings us to aim for a decoherence scheme that protects the populations, a policy which is also attractive from the norm preservation viewpoint, and the coherences associated to few spin flips in computational basis. Inheriting the strategy of the exact solution in Sec. 3.1.2, we would like to diagonalize at each numerical time step the subspace of the density matrix involving all these entries. In order to do so, we design a projector in the form of an MPO, which is able to select the wanted information out of the state.

3.2.1.1 Recursive Relation for Coherence Projectors.

In the following, we will learn how to retrieve the off-diagonal entries corresponding to n-spin-flips from density matrix. For a single spin, this can be done by introducing an insertion σ^x in between the 3-legged copy tensors connecting the upper and lower contours, as illustrated in Fig. 3.3 (a). Following this prescription, the off-diagonal is extracted as

$$\begin{aligned}\left[\rho^{1-\text{flip}}_{\text{off}-\text{diag}}\right]^{n}_{l} &= \sum_{\ell_1,k,\ell_1',m} \delta_{\ell_1,k,l}\ \rho^{\ell_1'}_{\ell_1}\ [\sigma^x]_{k,m}\ \delta_{\ell_1',m,n} \\ &= \sum_{\ell_1,k,\ell_1',m} \delta_{\ell_1,k,l}\ \rho^{\ell_1'}_{\ell_1}\ \delta_{k+1,m}\ \delta_{\ell_1',m,n} = \rho^{n}_{l}\delta_{l,n+1},\end{aligned} \tag{3.12}$$

where we made use of σ^x being an anti-diagonal of ones. In a similar way, for a 2-spin density matrix the σ^x can be introduced either in the first or in the second site; a similar calculation as that on 3.12 proves that if the non-trivial insertion is placed in the first site, then the retrieved matrix contains only the terms associated to 1-spin-flip of the first spin in computational basis, as in Fig. 3.3 (b):

$$\begin{aligned}\left[\rho^{1-\text{flip}-\text{1st}}_{\text{off}-\text{diag}}\right]^{n,s}_{l,q} &= \sum_{\ell_1,k,p,\ell_1',m,r} \delta_{\ell_1,k,l}\ \delta_{\ell_2,p,q}\ \rho^{\ell_1',\ell_2'}_{\ell_1,\ell_2}\ [\sigma^x]_{k,m}\ \delta_{p,r}\ \delta_{\ell_1',m,n}\ \delta_{\ell_2',r,s} \\ &= \rho^{n,s}_{l,q}\ \delta_{l,n+1}\ \delta_{q,s}.\end{aligned} \tag{3.13}$$

Conversely, if placed on the second site, the insertion yields the 1-flip coherences for the second spin. Naturally, by adding both matrices $\rho^{1-\text{flip}-\text{1st}}_{\text{off}-\text{diag}}$ and $\rho^{1-\text{flip}-\text{2nd}}_{\text{off}-\text{diag}}$ containing

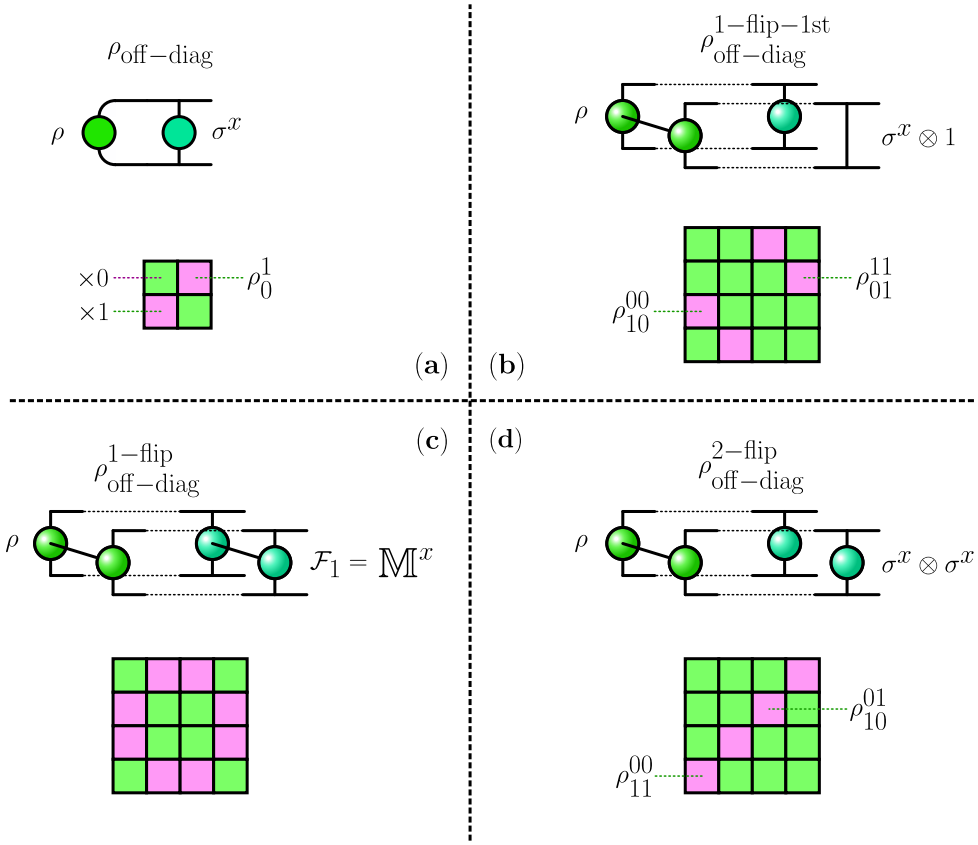

Figure 3.3: Illustrating coherence projectors. **(a)** For a single spin density matrix, connecting the forward and backward branches with a σ^x insertion projects out the diagonal elements, retrieving a matrix that only contains the coherence. **(b)** In the case of a 2-spin density matrix, we could input the insertion either on the first or in the second spin. If we include it on the first spin only, and fully decohere the second spin, then we select those entries corresponding to the first one flipping. **(c)** If we want all the off-diagonal terms participating on the single spin observables, then we introduce the transverse magnetization distributing σ^x in both sites. **(d)** Finally, the 2-flip terms can be obtained by introducing two σ^x.

the 1-flip coherences for the first and the second spins yields all 1-spin-flip entries in the system. This is equivalent to introducing an insertion between the forward and backward copy tensors of the complete density matrix with the shape $\sigma^x\mathbb{1} + \mathbb{1}\sigma^x$. For systems of arbitrary size, the insertion $\mathcal{F}_1$ retrieving all 1-spin-flips coincides with the transverse magnetization operator $\mathbb{M}^x = \sum_\ell \sigma^x_\ell$. This operator can be represented as an MPO, as in Fig. 3.3 (c); we will explain how to do it in the next Sec. 3.2.1.2.

Once we found how to retrieve the 1-spin-flip terms, we can aim for a higher number of flips. For example, the case of 2-spin-flip terms in a 2 spin density matrix requires inserting $\sigma^x\sigma^x$ as in Fig. 3.3 (d):

$$\begin{aligned}\left[\rho^{2-\text{flip}}_{\text{off}-\text{diag}}\right]^{n,s}_{l,q} &= \sum_{\ell_1,k,p,\ell_1',m,r} \delta_{\ell_1,k,l}\ \delta_{\ell_2,p,q}\ \rho^{\ell_1',\ell_2'}_{\ell_1,\ell_2}\ [\sigma^x]_{k,m}\ [\sigma^x]_{p,r}\ \delta_{\ell_1',m,n}\ \delta_{\ell_2',r,s} \\ &= \rho^{n,s}_{l,q}\ \delta_{l,n+1}\ \delta_{q,s+1}.\end{aligned} \tag{3.14}$$

It is clear now that addressing all the 2-spin-flips in an arbitrary large system requires generating all the distributions of a pair of σ^x; for any size L we can construct all of them with $\mathcal{F}_1$:

$$\mathcal{F}_1\mathcal{F}_1 = \underbrace{\sum_{\ell_1,\ell_2=\ell_1} \sigma^x_{\ell_1}\sigma^x_{\ell_2}}_{\text{overlapping sites}} + \underbrace{\sum_{\ell_1,\ell_2\neq\ell_1} \sigma^x_{\ell_1}\sigma^x_{\ell_2}}_{\text{non-overlapping sites}} = L\mathbb{1} + 2\mathcal{F}_2. \tag{3.15}$$

In the first sum of Eq. 3.15 the σ^x's overlap on the same site, generating an identity; this occurs L times out of a total number of L^2 terms. The second sum generates al pairs of non-overlapping σ^x's; since each arrangement is generated twice due to non-distinguishability upon permuting the σ's, $\mathcal{F}_2$ arises with a prefactor 2.

For an arbitrary number n of flips, the product $\mathcal{F}_1\mathcal{F}_{n-1}$ yields a sum with $L\cdot\binom{L}{n-1}$ addenda (L from $\mathcal{F}_1$ and $\binom{L}{n-1}$ from $\mathcal{F}_{n-1}$). Out of the whole sum, $(n-1)\cdot\binom{L}{n-1}$ terms will arise from cancellations, consequence of the σ^x from $\mathcal{F}_1$ overlapping with any of the σ^x's present in the terms from $\mathcal{F}_{n-1}$. All these terms with canceling σ^x will belong to $\mathcal{F}_{n-2}$, which contains $\binom{L}{n-2}$ addenda. On the other hand, the rest of $\Big(L-(n-1)\Big)\cdot\binom{L}{n-1}$ products yield terms with a number n of σ^x, distributed trough the system, belonging to $\mathcal{F}_n$. Therefore, the product $\mathcal{F}_1\mathcal{F}_{n-1}$ can be used to obtain the next $\mathcal{F}_n$ recursively

$$\mathcal{F}_1\mathcal{F}_{n-1} = \frac{(n-1)\binom{L}{n-1}}{\binom{L}{n-2}}\mathcal{F}_{n-2} + \frac{(L-n+1)\binom{L}{n-1}}{\binom{L}{n}}\mathcal{F}_{n-2} = (L-n+2)\mathcal{F}_{n-2} + n\mathcal{F}_n. \tag{3.16}$$

This brings us to the recursion relation

$$\mathcal{F}_n = \frac{1}{n}\Big[\mathcal{F}_1\mathcal{F}_{n-1} - (L-n+2)\mathcal{F}_{n-2}\Big] \quad \text{with} \quad \mathcal{F}_0 = \mathbb{1}_{2^L} \quad \text{and} \quad \mathcal{F}_1 = \mathbb{M}^x, \tag{3.17}$$

which is useful for constructing the projectors $\sum_{m=0}^{n}\mathcal{F}_m$ onto few-flip-coherence spaces for small systems that we can solve with exact diagonalization. Despite that, a TN generalization will be at hand for larger systems.

3.2.1.2 Few-Flip Projector in MPO Form.

The operators $\mathcal{F}_n$ distributing a number n of σ^x matrices can be readily obtained by designing an MPO that generates strings with n insertions, and selects in the end boundary those that we are interested in. To do so, the tensor in our first site takes the simple form

$$\begin{pmatrix} \mathbb{1}_2 & \sigma^x & 0 & \cdots & 0 & 0 & 0 \end{pmatrix}, \tag{3.18}$$

corresponding to either starting from the 0-th internal state without insertion, or the first one with already one σ^x. After this first tensor, the following $L-2$ bulk transfer tensors acting on the chain take the form

$$\begin{pmatrix} \mathbb{1}_2 & \sigma^x & 0 & \cdots & 0 & 0 & 0 \\ 0 & \mathbb{1}_2 & \sigma^x & \cdots & 0 & 0 & 0 \\ 0 & 0 & \mathbb{1}_2 & \cdots & 0 & 0 & 0 \\ \vdots & \vdots & \vdots & \ddots & \vdots & \vdots & \vdots \\ 0 & 0 & 0 & \cdots & \mathbb{1}_2 & \sigma^x & 0 \\ 0 & 0 & 0 & \cdots & 0 & \mathbb{1}_2 & \sigma^x \\ 0 & 0 & 0 & \cdots & 0 & 0 & \mathbb{1}_2 \end{pmatrix}, \tag{3.19}$$

and they include $n+1$ internal states: one state for the empty string purely constructed with $\mathbb{1}_2$, and n states counting the number of inserted σ^x.

Depending on which information is to be accepted, we close the MPO chain with a boundary vector:

$$\text{(a)} \begin{pmatrix} \sigma^x \\ \mathbb{1}_2 \\ 0 \\ \vdots \\ 0 \\ 0 \\ 0 \end{pmatrix} \quad \text{(b)} \begin{pmatrix} 0 \\ \sigma^x \\ \mathbb{1}_2 \\ \vdots \\ 0 \\ 0 \\ 0 \end{pmatrix} \quad \text{(c)} \begin{pmatrix} \mathbb{1}_2 + \sigma^x \\ \mathbb{1}_2 + \sigma^x \\ \mathbb{1}_2 \\ \vdots \\ 0 \\ 0 \\ 0 \end{pmatrix} \quad \text{(d)} \begin{pmatrix} \mathbb{1}_2 + \sigma^x \\ \mathbb{1}_2 + \sigma^x \\ \mathbb{1}_2 + \sigma^x \\ \vdots \\ \mathbb{1}_2 + \sigma^x \\ \mathbb{1}_2 + \sigma^x \\ \mathbb{1}_2 + \sigma^x \end{pmatrix}, \tag{3.20}$$

Option (a) retains the 1-spin-flips only, so it corresponds to an MPO representation of $\mathcal{F}_1$, while (b) accepts the 2-flips ($\mathcal{F}_2$). If we also want to retain the diagonal (combining Eqs. 3.3 and 3.12), then we choose (c), equivalent to applying $\sum_{m=0}^{2} \mathcal{F}_m$. Generally, if we want to retrieve the entries participating in the local physics until n-spin observables ($\sum_{m=0}^{n} \mathcal{F}_m$) we use (d).

The MPO language allows for higher flexibility. For example, if we were interested on short-range coherence in computational basis (flipping an entire cluster neighbouring of spins) the bulk tensor is almost equal, but as soon as the first insertion is detected, the internal state is only allowed to progress until reaching a number n of σ^x insertions; this is achieved by annihilating the diagonal elements excepting the first and the last:

$$\begin{pmatrix} \mathbb{1}_2 & \sigma^x & 0 & \cdots & 0 & 0 & 0 \\ 0 & 0 & \sigma^x & \cdots & 0 & 0 & 0 \\ 0 & 0 & 0 & \cdots & 0 & 0 & 0 \\ \vdots & \vdots & \vdots & \ddots & \vdots & \vdots & \vdots \\ 0 & 0 & 0 & \cdots & 0 & \sigma^x & 0 \\ 0 & 0 & 0 & \cdots & 0 & 0 & \sigma^x \\ 0 & 0 & 0 & \cdots & 0 & 0 & \mathbb{1}_2 \end{pmatrix}. \tag{3.21}$$

3.2.2 Retaining the Local Physics.

Now that we have developed the tools needed to filtrate the *low coherence* subspaces (in the sense of few-spin-flips in computational basis), we adjust the rotations W_m to both induce a gap and retain the local thermalizing physics.

For small system sizes, we can still make use of ED packages. ED would have been required if the exact solution in Eq. 3.8 would have been of any use; now, we will make use of it to find an approximate solution for small systems. Following the same rationale as in Sec. 3.1.2, we follow the scheme depicted in Fig. 3.2 (b) from left to right, and observe that any information that we wish to keep on the left of a total decoherence should be diagonal in order to survive the information loss.

Since we are interested on a low coherence subspace rather than in the full set of observables, *we propose to diagonalize such a subspace, following the intuition that this procedure may be close to solving the optimization problem of finding the best rotations that retain local physics*. In first place, we split the density matrix at a given time into the wanted local entries and the unimportant non-local entries:

$$\rho_n^{\mathrm{loc}}(t) = \sum_{m=0}^{n} \mathcal{F}_m\big\{\rho(t)\big\}, \quad \rho_n^{\mathrm{nloc}}(t) = \sum_{m=n+1}^{L} \mathcal{F}_m\big\{\rho(t)\big\}, \tag{3.22}$$

where we use the notation $\mathcal{F}_m\{\cdot\}$ to indicate that an insertion $\mathcal{F}_m$ between bra and ket copy tensors was applied on the argument (the density operator).

After performing the split, we use ED to find the rotation $\mathcal{B}_m^{\mathrm{loc}} = W_{m=\frac{t}{\delta t}}$ bringing $\rho_n^{\mathrm{loc}}(t)$ to diagonal form. Once we found the W_m, we note that part of $\rho_n^{\mathrm{nloc}}(t)$ may also flow to the diagonal, so actually the decoherence will keep more information than the one below n-spin coherence.

Dropping the time dependence for clarity, for every step we have:

$$W_m\,\rho\,W_m^\dagger = \mathcal{B}_m^{\rm loc}\,\rho\,\mathcal{B}_m^{\rm loc\,\dagger} = \mathcal{B}_m^{\rm loc}\,\rho^{\rm loc}\,\mathcal{B}_m^{\rm loc\,\dagger} + \mathcal{B}_m^{\rm loc}\,\rho^{\rm nloc}\,\mathcal{B}_m^{\rm loc\,\dagger} = \tilde{\rho}^{\rm loc}_{\rm diag} + \tilde{\rho}^{\rm nloc}_{\rm diag} + \tilde{\rho}^{\rm nloc}_{\rm offdiag}\,, \tag{3.23}$$

and the total decoherence erases the part of non-local correlations that was not saved by W_m, that is $\tilde{\rho}^{\rm nloc}_{\rm offdiag}$:

$$\tilde{\rho}^{\rm loc}_{\rm diag} + \tilde{\rho}^{\rm nloc}_{\rm diag} + \tilde{\rho}^{\rm nloc}_{\rm offdiag} \quad\longrightarrow\quad \tilde{\rho}^{\rm loc}_{\rm diag} + \tilde{\rho}^{\rm nloc}_{\rm diag} + \cancel{\tilde{\rho}^{\rm nloc}_{\rm offdiag}}\,. \tag{3.24}$$

Now, the back-rotation $W_m^\dagger$ will restore the entries referring to the local physics until n spins on their respective off-diagonal locations, but the non-local information $\tilde{\rho}^{\rm nloc}_{\rm diag}$ that was saved may now flow into any entry, yielding the modified density matrix:

$$\tilde{\rho} = \mathcal{B}^{\rm loc\,\dagger}\,(\tilde{\rho}^{\rm loc}_{\rm diag} + \tilde{\rho}^{\rm nloc}_{\rm diag})\,\mathcal{B}^{\rm loc} = \rho^{\rm loc} + \tilde{\tilde{\rho}}^{\rm nloc} = \underbrace{(\rho^{\rm loc} + \delta\rho^{\rm loc})}_{\text{into local observables}} + \tilde{\tilde{\rho}}^{\rm nloc}_{\rm offdiag}. \tag{3.25}$$

Therefore, this procedure introduces two errors in the observables:

- **Error I**: it is the deviation $\delta O(t)$ induced in the local observable $O(t)$ at the time $t = m\delta t$ in which the decoherence step is performed; it corresponds to the expectation value of $\delta\rho^{\rm loc} = \tilde{\tilde{\rho}}^{\rm nloc}_{\rm diag}$:

  $$\tilde{O}(t) = {\rm Tr}\{\tilde{\rho}(t)\,O\} = {\rm Tr}\Big\{\Big(\rho^{\rm loc}(t) + \delta\rho^{\rm loc}(t) + \tilde{\tilde{\rho}}^{\rm nloc}_{\rm offdiag}(t)\Big)\,O\Big\} = O(t) + \delta O(t) + 0. \tag{3.26}$$

  As such, *this error is a measure of how good is our proposal of diagonalizing the subspace below n-spin-flips for preserving the local observables*.

- **Error II**: it is the error induced on the future prediction of $O(t)$, due to the total decoherence steps performed at former times $t' < t$. It is therefore consequence of both, $\delta\rho^{\rm loc}(t)$ and $\tilde{\tilde{\rho}}^{\rm nloc}_{\rm offdiag}(t)$.

In order to gauge how good the procedure of diagonalizing the local subspaces is, we need to address both types of error. The error I can be estimated directly from the shift in the observable at every step due to full decoherence; it can be obtained by computing the expectation value before and after the bra-ket coupling in Fig. 3.2 (a). The simplest way of checking the error II is by direct comparison of the exact observable (which can only be computed for small systems) and the decoherent one.

The numerical tests checking the impact of these errors on local observables will be set aside until Sec. 3.4, where we will compare our procedure with the generalized decoherence scheme which we introduce in the next section.

3.3 Generalized Decoherence.

Rather than facing the complicated task associated with finding the optimal rotations diagonalizing the local projections of the density matrices, in this section we propose a more general framework with which we can induce a gapped evolution.

3.3.1 Designing Soft Threshold Decoherers.

Instead of rotating the state towards an optimized basis in which the density matrix completely loses coherence, we may directly erase it in computational basis by inserting a modified version of the coherence projectors $\mathcal{F}_n$ inserted between copy tensors. We call this new scheme generalized decoherence, and present it in Fig. 3.4, which deviates from 3.2 by:

- The rotations are set to the identity $W_m = \mathbb{1}_{2^L} \; \forall \; m$, since we want to avoid the complexity of finding variationally the rotations for arbitrarily long chains.
- Instead of a full decoherence, we introduce an insertion between bra and ket copy tensors of the form $\sum_{m=0}^{L} \mathcal{C}_m \mathcal{F}_m$, where $\mathcal{C}_m$ are constants smaller or equal than 1.

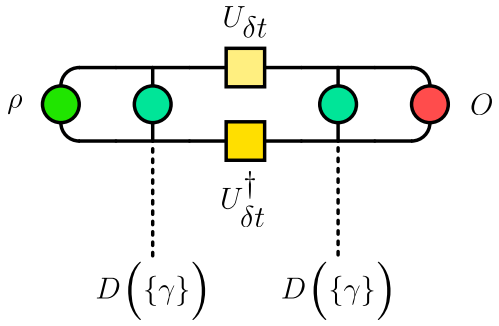

Figure 3.4: Generalized decoherence scheme. In order to generate a gap while avoiding prohibitive ED, a modification of the forward-backward couplings is proposed; it involves inserting a weighted sum of coherence projectors between copy tensors. This TN structure implements a generalized decoherence $D(\{\gamma\})$ parameterized by the $\{\gamma\}$ decay rates.

This new circuit has the effect of applying a mask $\sum_{m=0}^{L} \mathcal{C}_m \mathcal{F}_m$ entry-by-entry on the density matrix. After the action of the generalized decoherence step, every entry corresponding to $m-$spin-flips in computational basis will get multiplied by $\mathcal{C}_m$. This procedure has the following nice properties:

- It induces a gap as soon as some $\mathcal{C}_m$ is smaller than 1, since the information on the $m-$spin-flip entries is being partially erased.
- It does not require the step of storing the information on the diagonal through rotations, since one can tune the C_m's to affect only non-local observables.

For example, the case $C_{m\leq 1} = 1$ and $C_{m>1} < 1$ would leave the 1 spin reduced density matrix intact, since no entry relative to 1 site observables would be modified; in other words, there is no type I error in single spin observables (as introduced in the total decoherence explanation in Sec. 3.2.1).

Following the same rationale, the case $C_{m\leq 2} = 1$ and $C_{m>2} < 1$ is an energy preserving gapped evolution for the case of nearest-neighbor Hamiltonians, since at most 2-spin-flips are required to compute the energy density.

- The insertion that acts as a mask $\sum_{m=0}^{L} \mathcal{C}_m \mathcal{F}_m$ admits a compact MPO expression if the C_m's decay exponentially given a threshold $m = n$. The bulk and the accepting boundary tensors are:

$$\begin{pmatrix} \mathbb{1}_2 & \sigma^x & 0 & \cdots & 0 & 0 & 0 \\ 0 & \mathbb{1}_2 & \sigma^x & \cdots & 0 & 0 & 0 \\ 0 & 0 & \mathbb{1}_2 & \cdots & 0 & 0 & 0 \\ \vdots & \vdots & \vdots & \ddots & \vdots & \vdots & \vdots \\ 0 & 0 & 0 & \cdots & \mathbb{1}_2 & \sigma^x & 0 \\ 0 & 0 & 0 & \cdots & 0 & \mathbb{1}_2 & \sigma^x \\ 0 & 0 & 0 & \cdots & 0 & 0 & \mathbb{1}_2 + e^{-\gamma}\sigma^x \end{pmatrix} \quad \text{and} \quad \begin{pmatrix} \mathbb{1}_2 + \sigma^x \\ \mathbb{1}_2 + \sigma^x \\ \mathbb{1}_2 + \sigma^x \\ \vdots \\ \mathbb{1}_2 + \sigma^x \\ \mathbb{1}_2 + \sigma^x \\ \mathbb{1}_2 + e^{-\gamma}\sigma^x \end{pmatrix}, \tag{3.27}$$

  which add a penalty $e^{-\gamma}$ every time that a new σ^x is read by the MPO above the **coherence threshold** n. This translates in weights of the form $\mathcal{C}_{m\leq n} = 1$ and $\mathcal{C}_{m>n} = e^{-(m-n)\gamma}$.

This list of attractive features invites us to explore the use of the generalized decoherence scheme, avoiding the need of ED for arbitrary sizes. In the following, we will stick to the use of the MPO from Eq. 3.27.

3.3.2 Unphysicality of Generalized Decoherence.

In this section we prove that the MPO introduced in Sec. 3.3.1 is not a physical channel; as a consequence, it will map the state to an unphysical object. This means that no truncation scheme or filter affecting only a subset of the off-diagonal terms will be adequate to perform density matrix dynamics in purified form[3]. With this purpose we will make a constructive proof, starting from single spin channels inducing decoherence. In the following, we will try to build a physical channel that respects a subset of coherences and attacks the rest of the off-diagonals.

[3]For information on purified evolution schemes, see Daley et al. (2004b), Barthel et al. (2009), Feiguin and Fiete (2010), Enss and Sirker (2012), Karrasch et al. (2012), Barthel (2013), Tiegel et al. (2014), Karrasch et al. (2015), Binder and Barthel (2015), Kennes and Karrasch (2016) and Werner et al. (2016).

In order to do that, we recall the form of the single spin decoherence channel Π_{deco} as summarized in Sec. 2.1.2.3. The Kraus operators $\sqrt{1-\frac{P}{2}}\mathbb{1}$ and $\sqrt{\frac{P}{2}}\sigma^z$ (or any combination of diagonal matrices) introduce a decay in the off-diagonals of the single spin density matrix by multiplying the coherences by $1-P$, which can be recast as $e^{-\gamma\delta t}$ for $P=\gamma\delta t$ being the probability of measurement. A many-body channel inducing decays on the off-diagonals of the density matrix may be constructed with these single spin decoherences.

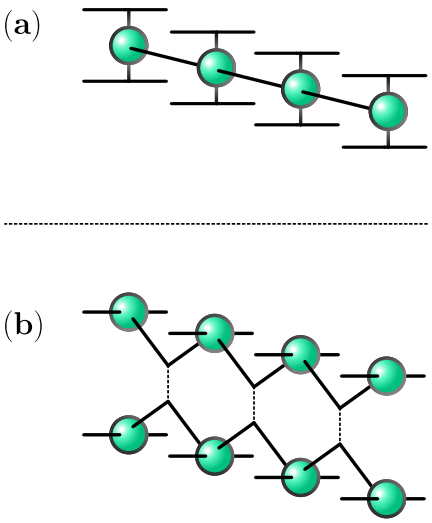

Figure 3.5: Generalized decoherence vs many-body channel decoherence. By design, selecting which entries of the density matrices will be affected and which not can be written in MPO form by introducing the sum of weighted $\mathcal{F}_n$'s in between copy tensors as in **(a)**. Nevertheless, if one would like to work with a fully positive density matrix along evolution, then a purified form like the one in **(b)** with the shape of a channel would be handy. Despite the shape shown in **(b)** is not the only purification scheme that we can propose, it allows us to build comprehensible channels by distributing single spin channels. In this case, the purification legs ensure that the virtual states between local tensors are equal both in the forward and backward contours.

3.3.2.1 Simplest Entangled Many-body Decoherence Channel.

The simplest entangled many-body channel destroying off-diagonal information is the one distributing $\varepsilon_{\text{deco}}$ on all sites of the chain, such that the list of Kraus operators A is

$$A \in \{\sqrt{\alpha}\mathbb{1}...\mathbb{1},\ \sqrt{\beta}\mathbb{1}\sigma^z\mathbb{1}...\mathbb{1},\ ...,\ \sqrt{\beta}\mathbb{1}...\mathbb{1}\sigma^z\mathbb{1}...\mathbb{1},\ ...,\ \sqrt{\beta}\mathbb{1}...\mathbb{1}\sigma^z\mathbb{1}\}, \tag{3.28}$$

with $\alpha,\ \beta > 0$. This channel admits a simple MPO form for both elements acting on the bra and the ket, provided the virtual states are matched through copy tensors (see Fig. 3.5):

$$\begin{pmatrix}\mathbb{1} & \sigma^z\end{pmatrix}, \quad \begin{pmatrix}\mathbb{1} & \sigma^z \\ 0 & \sigma^z\end{pmatrix}, \quad \begin{pmatrix}\sqrt{\alpha}\mathbb{1}+\sqrt{\beta}\sigma^z \\ \sqrt{\beta}\mathbb{1}\end{pmatrix}. \tag{3.29}$$

We would like to optimize the channel by selecting the values of α and β leaving the 1-spin-flip coherence unperturbed. The normalization of the channel requires that

$$\sum_{m=1}^{1+n_{\rm nt}} A_m A_m^\dagger = A_1 A_1^\dagger + \sum_{m=2}^{1+n_{\rm nt}} A_m A_m^\dagger = (\sqrt{\alpha})^2 + n_{\rm nt}(\sqrt{\beta})^2 = \alpha + L\beta = 1, \tag{3.30}$$

where $n_{\rm nt}$ is the number of strings in the set of channel elements with non-trivial form (those distributing σ^z); in this case, we distribute one Pauli matrix on L sites, so

$$n_{\rm nt} = \binom{L}{1} = L. \tag{3.31}$$

The action of $A_{m>1}$ placing the channel at position n on an arbitrary density matrix element is

$$\sqrt{\beta}\mathbb{1}...\mathbb{1}\sigma_n^z\mathbb{1}...\mathbb{1}|\ell_1,...\ell_n,...\ell_L\rangle\langle\ell'_1,...\ell'_n,...\ell'_L|\sqrt{\beta}\mathbb{1}...\mathbb{1}\sigma_n^z\mathbb{1}...\mathbb{1} = \beta(-1)^{\ell_n+\ell'_n}|\ell_1,...\ell_n,...\ell_L\rangle\langle\ell'_1,...\ell'_n,...\ell'_L|,$$

and the full action of the channel reads

$$\sum_{m=1}^{1+n_{\rm nt}} A_m|\ell_1,...\ell_n,...\ell_L\rangle\langle\ell'_1,...\ell'_n,...\ell'_L|A_m^\dagger = \left(\alpha + \beta\sum_{n=1}^{L}(-1)^{\ell_n+\ell'_n}\right)|\ell_1,...\ell_n,...\ell_L\rangle\langle\ell'_1,...\ell'_n,...\ell'_L|.$$

The factor $(-1)^{\ell_n+\ell'_n}$ is different from 1 when any of the pairs ℓ_n and ℓ'_n is different; in particular, for a 1-spin-flip coherence entry, only one of the pairs will be different, leading to a factor $\alpha + \beta(L-1)\cdot(+1) + \beta\cdot(-1) = (\alpha+\beta L) - 2\beta = 1 - 2\beta$. Now, we impose that no 1-spin-coherence is affected by setting $1-2\beta = 1$, leading to the trivial channel with $\alpha = 1$ and $\beta = 0$; thus we conclude that this toy channel instance fails to allow for selective or generalized decoherence, unless there is no channel at all.

3.3.2.2 Next-to-simplest Entangled Many-body Decoherence Channel.

We could nevertheless try a more involved channel, including also $L-1$ elements of the form $\sqrt{\gamma}\mathbb{1}...\mathbb{1}\sigma^z\sigma^z\mathbb{1}...\mathbb{1}$:

$$A \in \{\sqrt{\alpha}\mathbb{1}...\mathbb{1},\ ...,\ \sqrt{\beta}\mathbb{1}...\mathbb{1}\sigma^z\mathbb{1}...\mathbb{1},\ ...,\ \sqrt{\gamma}\mathbb{1}...\mathbb{1}\sigma^z\sigma^z\mathbb{1}...\mathbb{1},\ ...\}, \tag{3.32}$$

with normalization condition $\alpha + L\beta + (L-1)\gamma = 1$ for $\alpha,\ \beta,\ \gamma > 0$, and MPO form

$$\begin{pmatrix}\mathbb{1} & \sigma^z & \sigma^z\end{pmatrix}, \quad \begin{pmatrix}\mathbb{1} & \sigma^z & 0\\ 0 & \mathbb{1} & \sigma^z\\ 0 & 0 & \mathbb{1}\end{pmatrix}, \quad \begin{pmatrix}\sqrt{\alpha}\mathbb{1} + \sqrt{\beta}\sigma^z\\ \sqrt{\beta}\mathbb{1} + \sqrt{\gamma}\sigma^z\\ \sqrt{\gamma}\mathbb{1}\end{pmatrix}. \tag{3.33}$$

This channel acts on 1-spin-flips as $1-2(\beta+2\gamma)$, and a trivial action would imply setting $\beta=-2\gamma$, which is not possible since β and γ must be positive by construction. Note that protecting any coherence always involves a minus sign in front of some of the weights of the channel elements. Even if we combined all possible strings distributing an arbitrary amount of σ^z's along the chain, the result would be the same.

Therefore we conclude that any many-body decoherence channel will attack all the off-diagonal terms with a textured decay below 1; the only flexibility allowed in the problem is that of peaking the decay on particular off-diagonal entries, but it will never be possible to fully save that information with a physical channel.

As a consequence, we note that the program of generalized decoherence is a purely numerical scheme, which will produce unphysical density matrices. Since it will not break hermiticity or normalization by design, we already tease that the issue with this method will be that of generating unphysical negativity (appearance of negative eigenvalues in the density matrix itself). This problem will be illustrated in Sec. 3.4.5.2.

3.4 Numerical Explorations with Total and Generalized Decoherence.

In this section we will study the aforementioned schemes for a small system that we can exactly diagonalize. We will use a chain with $L=10$ sites and induce dynamics under the non-integrable Ising Hamiltonian (Eq. 2.40) with periodic boundary conditions and parameters $\{\mathrm{J}=-1,\ g=-1,\ h=-0.5\}$ and $\{\mathrm{J}=-0.625,\ g=-1,\ h=-0.125\}$ for ordered and disordered phases respectively.

3.4.1 Type I Error in Total Decoherence.

The first check we perform is the impact of total decoherence on an observable at a given time. Recall the discussion from Sec. 3.2.2, where we concluded that parasitic non-local components of correlations that where simultaneously diagonalized by the rotation protecting the local information could shift observables as specified by Eq. 3.26.

We evaluate this shift by comparing the predictions of single spin observables before and after the total decoherence; we choose the initial state $|0,\ 0\rangle$ and quench within the ordered phase with $|\mathrm{J}|\delta t=0.1$; the results we obtained are general for all other states and phases that we have studied. In Fig. 3.6 we plot the type I error shifts for all three projections of the magnetization.

We observe a common qualitative behavior in the mistakes introduced by the decoherence procedure:

- When the decoherence eliminates all information except that close to the diagonal (where the distance is measured in spin flips), the state converges to the infinite temperature density matrix, and all the observables decay exponentially to 0. This is the case when only the 2-spin-flip coherence is retained (red lines).

- When enough coherence is kept, the deviation induced by rotation, decoherence and back-rotation appears to reach an approximately steady value (the lower the threshold n, the sooner, following $t^{\text{steady}}_{n=4} < t^{\text{steady}}_{n=6} < t^{\text{steady}}_{n=8}$). We stress that such a value is not constant but rather a slow tail, as we clearly detect for $n = 4$ (violet curves) if we compare the curve with the underlying grid in the plot.

  These quasi-steady shifts fall clearly below typical precision thresholds ($\leq 10^{-3}$).

- For increasing n, the observable shift reduces, as we would expect from diagonalizing almost the full density matrix before decoherence destroys the off-diagonal information.

We conclude that if n is big enough, the imprecision induced at a given time is negligible, *and our proposal of diagonalizing the subspace containing the information on observables of n spins is numerically accurate with small error*. Nevertheless, it is still necessary to understand whether the information loss modifies or not the later dynamics, and whether such a change will be coherent with the ETH.

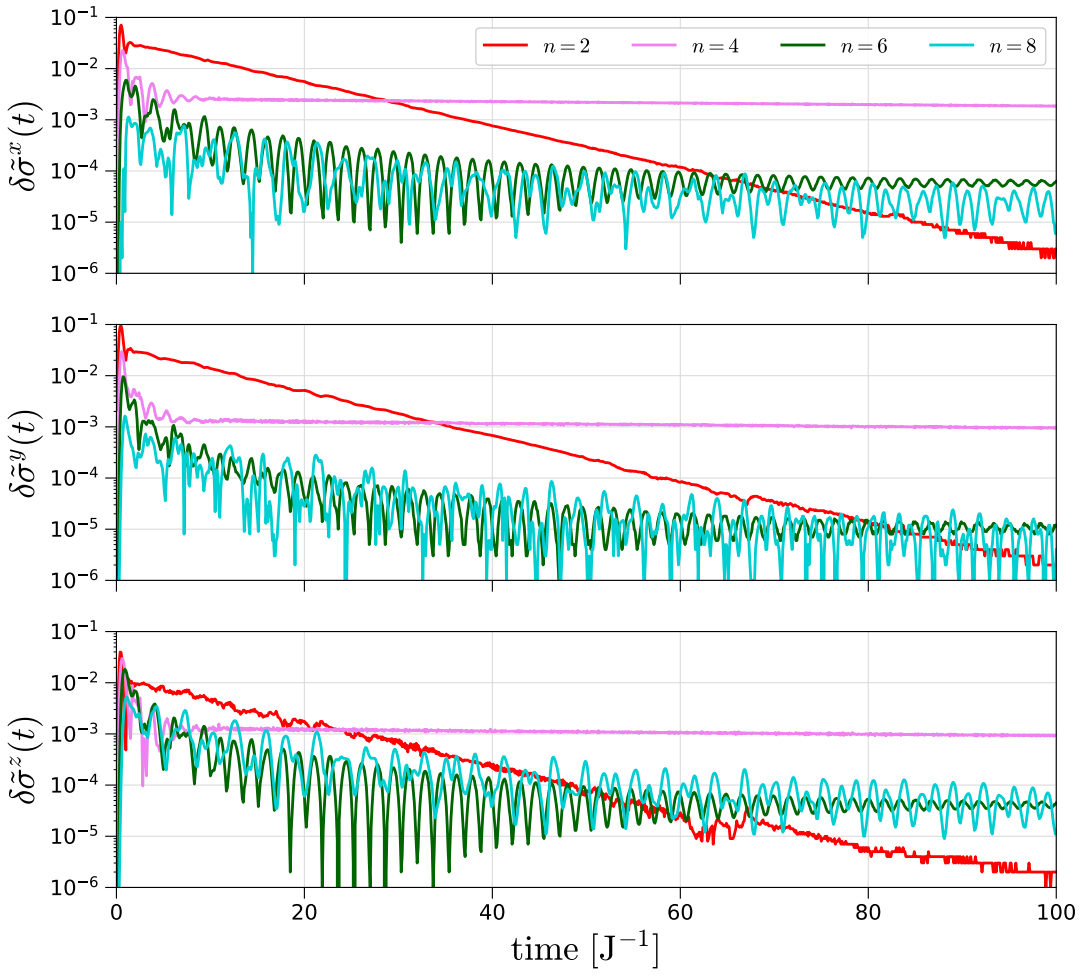

Figure 3.6: Type I error in local observables with full decoherence for varying thresholds. In each panel we compare the values of the local magnetizations and average energy for the initial state $|0,\ 0\rangle$ and numeric time step $|\mathrm{J}|\delta t = 0.1$. In all the cases, the increase on the protected coherence reduces the error introduced by parasitic non-local correlations surviving the decoherence process. Interestingly, the case $n = 2$ (red) shows an exponential decay in time, which we attribute to the convergence to infinite temperature of the underlying state, as shown in Fig. 3.7. Opposite to that $n = 4,\ 6,\ 8$ (violet, dark green and cyan respectively) appear to stabilize after long enough time in a hierarchical manner: the higher the n, the later the stabilization and the lower its value.

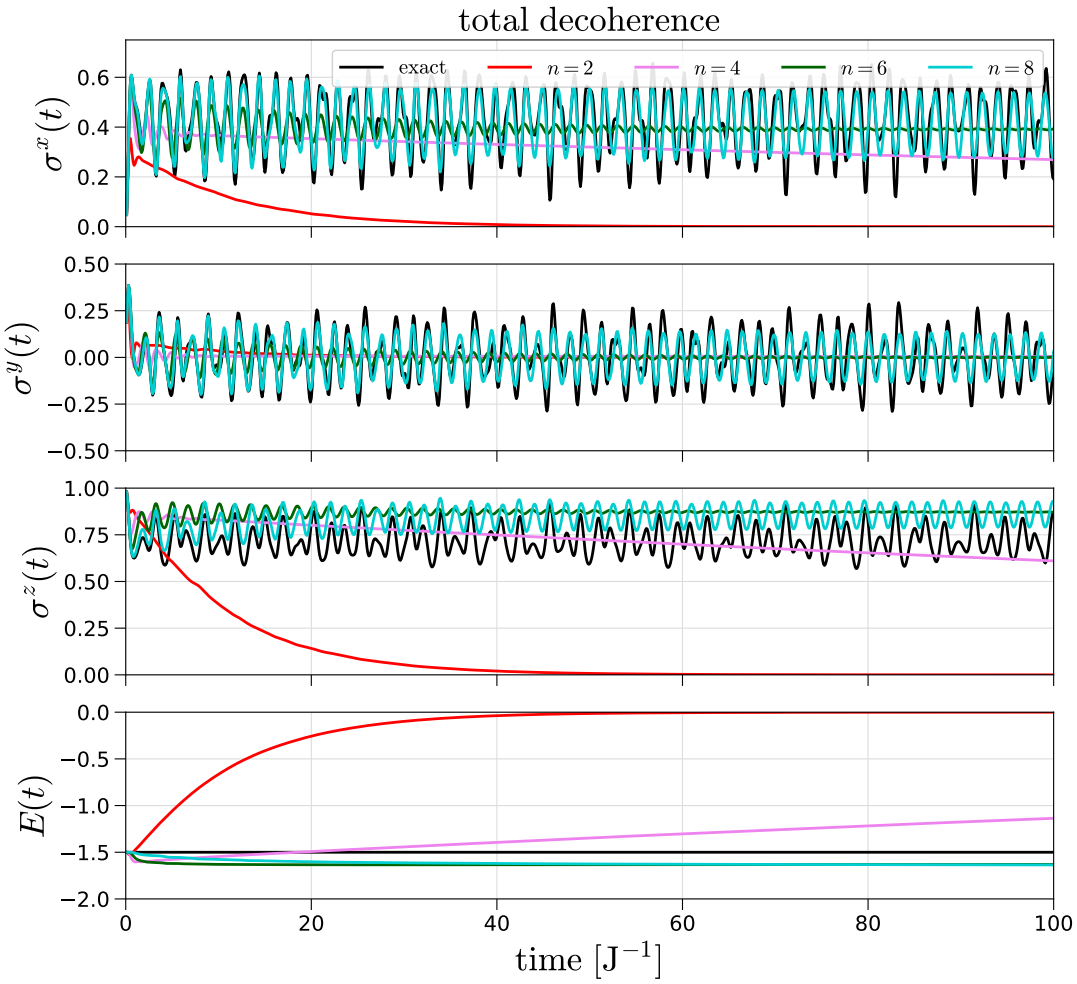

Figure 3.7: Predicting local observables with full decoherence and varying coherence thresholds. In each panel we compare the values of the local magnetizations and average energy for the initial state $|0,\ 0\rangle$ and numeric time step $|\mathrm{J}|\delta t = 0.1$. In all the cases, the increase on the protected coherence improves the prediction of the observable; while for $n = 2$ (red) the full decoherence at each step drifts the values towards infinite temperature predictions, for intermediate $n = 4,\ 6$ (violet and dark green, respectively) the observables appear to reach non-zero stable values approaching the time-averaged exact observable (black). For higher $n = 8$ (cyan) the predictions reproduce the fluctuations around the mean value with correct periodicity, though with damping. Notoriously, the energy is not preserved by any of the n values below L.

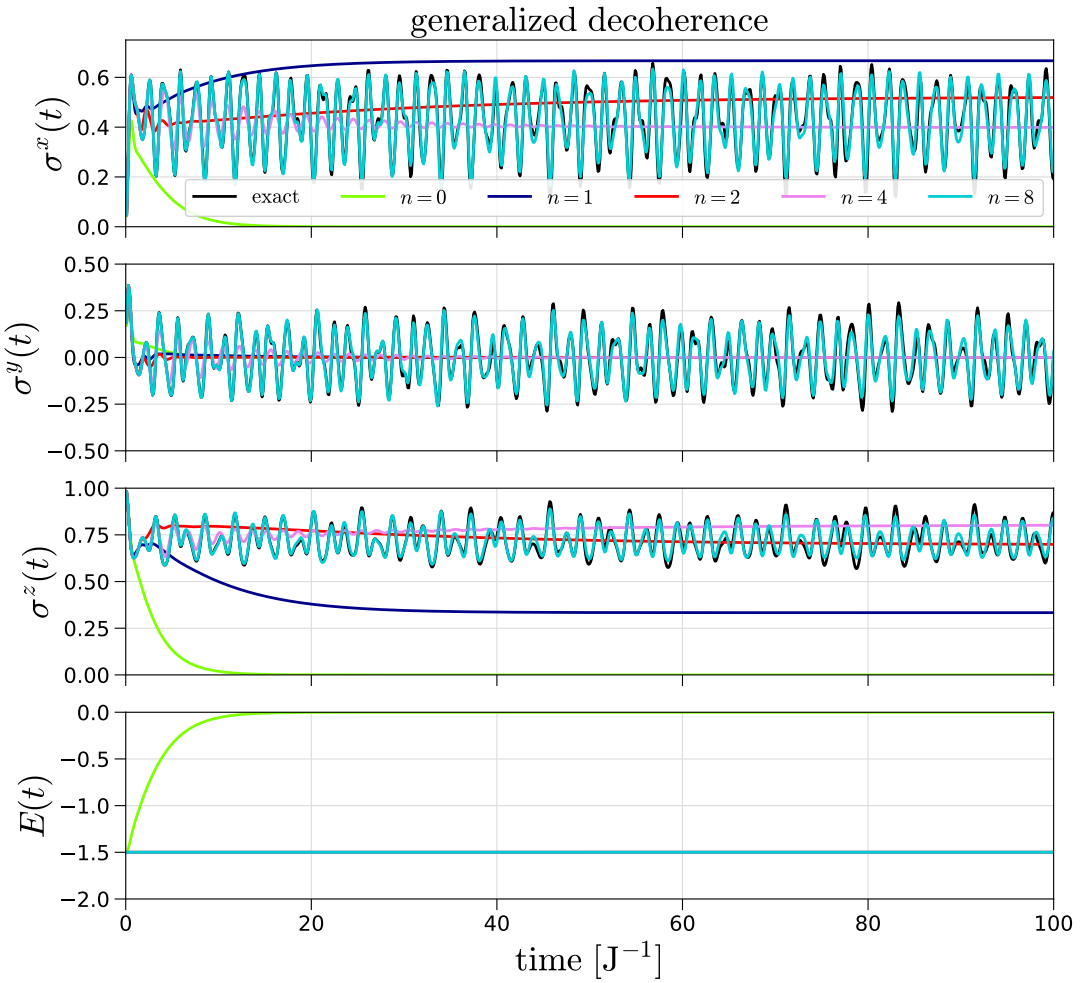

Figure 3.8: Predicting local observables with generalized decoherence and varying coherence thresholds. In each panel we compare the values of the local magnetizations and average energy for the initial state $|0,\ 0\rangle$ and numeric time step $|J|\delta t = 0.1$. In all the cases, the increase on the protected coherence improves the prediction of the observable; in this setting any $n > 0$ yields finite stationary values after short time, which approach to the time averaged observable of the exact dynamics as n crosses intermediate values 1 (dark blue), 2 (red), 4 (violet). As for full decoherence, higher n yield predictions that appropriately reproduce the fluctuations around the mean value with the correct periodicity but with some damping, but in this case the energy is preserved after $n \leq 1$, since the only off-diagonal term in the Hamiltonian is the transverse field $g\sigma^x$.

3.4.2 Dependence of Local Observables on Coherence Truncation: Type II Error.

Here we compare the effect of truncating coherence either with a hard cutoff (full decoherence) or with a soft threshold (generalized decoherence), focusing on the effect on later predictions. To do so, we compare the results for different values of the computational basis coherence threshold n with the exact predictions for all magnetization projections and the energy. The chosen initial state is $|0,\ 0\rangle$, and we quench within the ordered phase with $|\mathrm{J}|\delta t = 0.1$.

3.4.2.1 Comparing Total vs Generalized Decoherence.

In Fig. 3.7 we present the results for complete decoherence. As already noted in Sec. 3.4.1, $n = 2$ (red line) brings the state to the infinite temperature density matrix, inducing a decay in all the expectation values. From $n = 4$ (violet line) on, the behavior of the expectation values starts improving compared to the exact prediction (black line). Interestingly, the average total energy

$$E(t) = \frac{1}{L}\mathrm{Tr}\{\rho(t)H\}, \tag{3.34}$$

is clearly constant for $n = 6$ (dark green line) and $n = 8$ (cyan line), though slightly shifted; for these two cases, the former achieves a steady value close to the time average for both σ^x and σ^y while failing for σ^z, and the latter is able to catch fluctuations around the time average with an extra amplitude damping. The discrepancy between the decoherent observable $\sigma^z(t)$ and the exact one suggests that the order parameter in the ordered phase may require long-range coherence ($n > 8$) to be accurately reproduced for long times.

For thee sake of comparison, we turn to generalized decoherence in Fig. 3.8. As a first impression, we note that the quality of the results improved considering similar cutoffs of coherence. In this case, the absence of rotations guarantees the absence of type I error and the preservation of observables with support on density matrix entries corresponding to less than n flips.

The reduced disturbance of generalized decoherence is clearly reflected by the average total energy $E(t)$ of the system, which remains constant as soon as $n \geq 1$: recall that our quantization axis is z, so the unique off-diagonal term of the Hamiltonian is the local transverse field $g\sigma^x$, inducing single spin flips. The energy preservation comes with a faster stabilization in n of steady nonzero values of the predicted observables: even for $n = 1$ (dark blue line), the x- and z- magnetizations display a constant value that approaches the time averaged one as n increases (see $n = 2$ in red and $n = 4$ in violet).

This is a relevant result, since it can be read as the fact that stationary values are only related to low-coherence subspaces, and they are attained within short time windows. This seems to connect with the ETH (Sec. 2.1.2.2), which expects an exponentially reduced contribution from coherence in the energy eigenbasis for thermal local observables; despite our decoherence occurs in fully local computational basis, the coherence in the entangled energy eigenbasis may be similar enough such that upon destroying it we induce a decay towards the right thermal values.

With respect to the fluctuations around the time average value of the different observables, $n = 8$ (cyan line) is able to catch them almost exactly, except for a small amplitude damping. Such a decay of the fluctuations is already teased for $n = 2$ and $n = 4$, leading us to conclude that there is a damping time induced by generalized decoherence increasing with the threshold as $t^{\text{damp}}_{n=2} < t^{\text{damp}}_{n=4} < t^{\text{damp}}_{n=8}$.

The hierarchy of damping times and improvement of the results as n increases is related to the hierarchy of equations of motion for the different entries of the density matrix: consider the evolution of an arbitrary entry $\rho^{\ell'_1,\ell'_2\ldots\ell'_L}_{\ell_1,\ell_2\ldots\ell_L}$ from the von Neuman Eq. 2.13:

$$\frac{d\rho^{\ell'_1,\ell'_2\ldots\ell'_L}_{\ell_1,\ell_2\ldots\ell_L}(t)}{dt} = -i\Big[H\rho(t) - \rho(t)H\Big]^{\ell'_1,\ell'_2\ldots\ell'_L}_{\ell_1,\ell_2\ldots\ell_L}, \tag{3.35}$$

where a nearest neighbor Hamiltonian can at most induce 2 spin flips through the interaction term in some computational basis. This means that the time variation of any entry at a given time depends on all the density matrix entries that are 0, 1 or 2 flips away of the entry, i.e. those whose local tensor index lists $\{\ell_1, \ell_2\ldots\ell_L\}$ and $\{\ell'_1, \ell'_2\ldots\ell'_L\}$ differ by at most 2 indices. This explains the reason why the accuracy improves as we truncate n further away from the single spin observables, and invites us to revisit the impact of decoherence in slightly non-local observables.

3.4.2.2 Convergence Towards the Thermal Ensemble.

With the goal of understanding whether other not-so-local correlations yield sensible results using the different decoherence schemes, we compare the time-averaged reduced decoherent density matrices for blocks of contiguous spins with support $\ell = 3,\ 4,\ \text{and}\ 5$ with the respective thermal density matrices, computed as $\rho(\beta) = \frac{e^{-\beta H}}{\mathcal{Z}}$. We evolve the initial state $|0\rangle = |0,0\rangle$ in steps of $|\mathrm{J}|\delta t = 0.1$ with the mixed field Ising Hamiltonian at parameter point $\mathrm{J} = -1,\ g = -1,\ h = -0.5$ and equilibration inverse temperature is $\mathrm{J}\beta_0 = 0.75$, obtained as specified by Eq. 2.22 for $L = 10$.

$$\langle\rho^{\ell}_{\text{deco}}\rangle_t = \frac{1}{t}\int_0^t \text{Tr}_{L-\ell}\{\rho_{\text{deco}}(s)\}\, ds \tag{3.36}$$

In Fig. 3.9 we compare the results for total and generalized decoherence. As a guide for the eye, the exact result is plotted in dashed black, as a measure of how much a subsystem is able to thermalize by itself for sizes 3 to 5. We observe that despite the

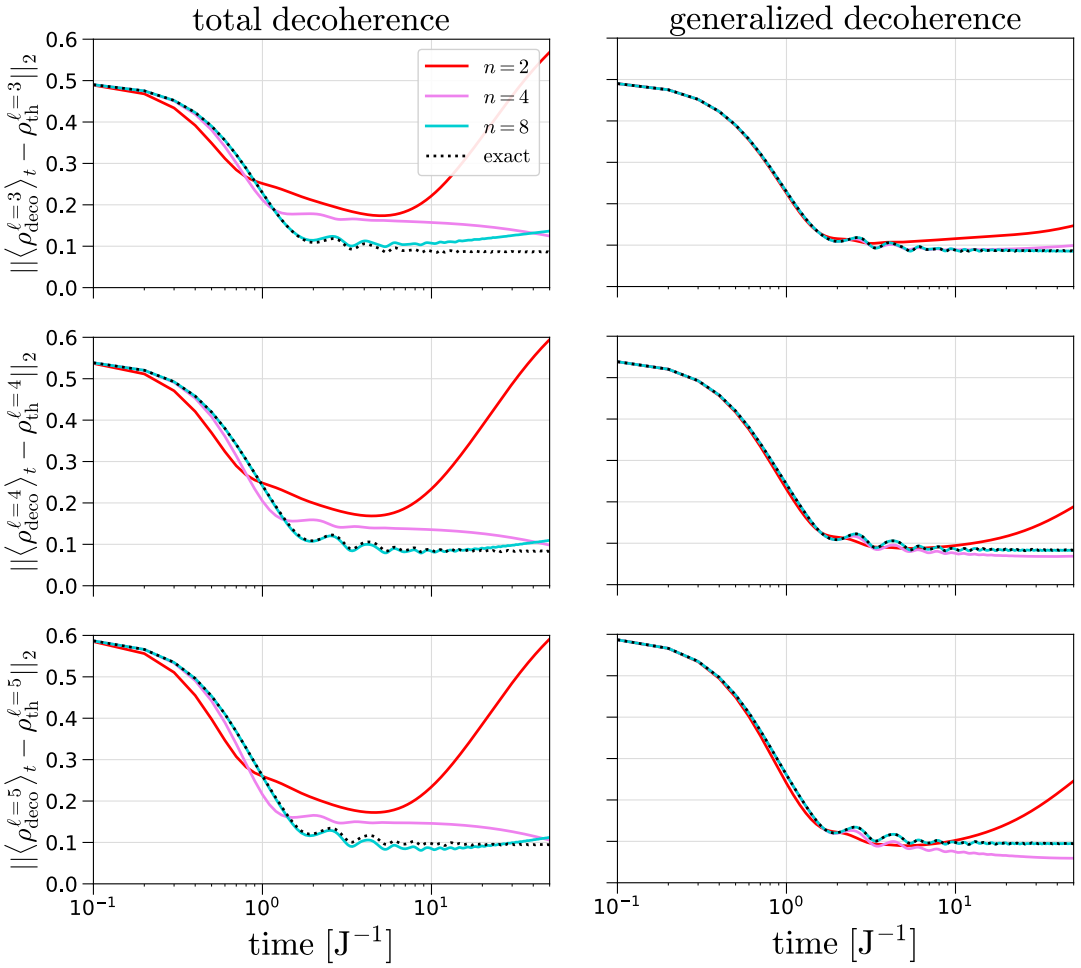

Figure 3.9: Fröbenius distance between time-averaged decoherent reduced density matrices and thermal states. The distances are computed for spin blocks of size 3 to 5 (first to third rows) and different decoherence thresholds $n = 2$ (red lines), 4 (violet) and 8 (cyan); the exact approach to the thermal state is depicted in dashed black for each block size. In the 6 subplots we see how the exact dynamics approaches within times $\mathcal{O}(\mathrm{J}^{-1})$ the thermal regime despite the simulation is run for size $L = 10$. For both modes of decoherence, $n = 2$ fails to reproduce the local physics and after a dip in the distance starts detaching from the right observables as the state converges towards a wrong state; this effect is much worse for total decoherence (left column) than for generalized decoherence (right panel). Intermediate cutoffs like $n = 4$ keep the time-averaged reduced density matrices close to their thermal prediction, even closer than the exact value for the case of generalized decoherence. The case $n = 8$ sticks better to the exact result, again performing much better for a soft threshold (right) than for a hard one (left).

system is small, the state is able to display a fast thermalization regime within times $\mathcal{O}(|\mathrm{J}|^{-1})$, followed by a slow tail (which in the large L limit may correspond to the hydrodynamic relaxation).

Compared to the exact result, the decoherent versions of the dynamics display a variety of regimes depending on the style and the chosen threshold. For $n = 2$ (red lines), we detected in Fig. 3.7 that the state heats and drifts towards the infinite temperature ensemble when the coherence cutoff is hard, while it appears to stabilize (at least for single spin observables) for soft cutoff decoherence in Fig. 3.8; this behavior appears to persist in the case of the reduced density matrices: despite both styles of dissipative evolution display a dip in the Fröbenius distance to the thermal states, the later evolution drifts far away in both cases. The deviation in the case of generalized decoherence is smaller, as we could already detect in Fig. 3.8.

For the case of $n = 4$ (violet lines) there is an interesting phenomenon occurring for the soft threshold: the distance with the thermal state is smaller than that achieved by the exact evolution. This means that an intermediate soft threshold is able to thermalize the finite system better than its self-capabilities. This does not occur for the hard cutoff, still retrieving Fröbenius distances between the cases $n = 2$ and $n = 8$ (cyan lines).

The fact that $n = 4$ can boost the thermalization process may be connected to the finite extent of the system, and we could expect that longer chains would relax even stronger in the exact case, leading to no actual improvement; nevertheless, it could also happen that this truncation scheme is actually easing the way towards equilibration, since the intensity of decoherence is weak enough to not alter the process of thermalization, but strong enough to destroy system-wide coherence, preventing revivals that keep observables away from their thermal value.

Finally, on the opposite regime of erasure strength the simulations with $n = 8$ stick close to the exact results. While the case of total decoherence still detaches from the thermal state for long times, the generalized decoherence evolution overlaps almost exactly with the coherent evolution. This result once more suggests that generalized decoherence could be a powerful candidate to simulate long time evolution for bigger systems.

3.4.3 Dependence of Local Observables on δt.

Since we are perturbing the evolution of the system by introducing dissipation (physical or not) with frequency $\frac{1}{\delta t}$, we expect that for lower rates the dynamics will remain almost unperturbed. Here we check that this intuition is correct both for total and generalized decoherence schemes by fixing the value of the threshold to $n = 4$, which appeared to be optimal in the former study of Sec. 3.4.2.2.

In Fig. 3.10 we establish this comparison for the three projections of magnetization by displaying the time averaged distances between the exact and the decoherent observable:

$$\langle \varepsilon(\sigma^\alpha) \rangle_t = \frac{1}{t} \int_0^t |\sigma^\alpha(s) - \sigma^\alpha_{\text{deco}}(s)|\, ds = \frac{1}{n_{\text{steps}}} \sum_{m=0}^{n_{\text{steps}}} |\sigma^\alpha(m\delta t) - \sigma^\alpha_{\text{deco}}(m\delta t)|, \tag{3.37}$$

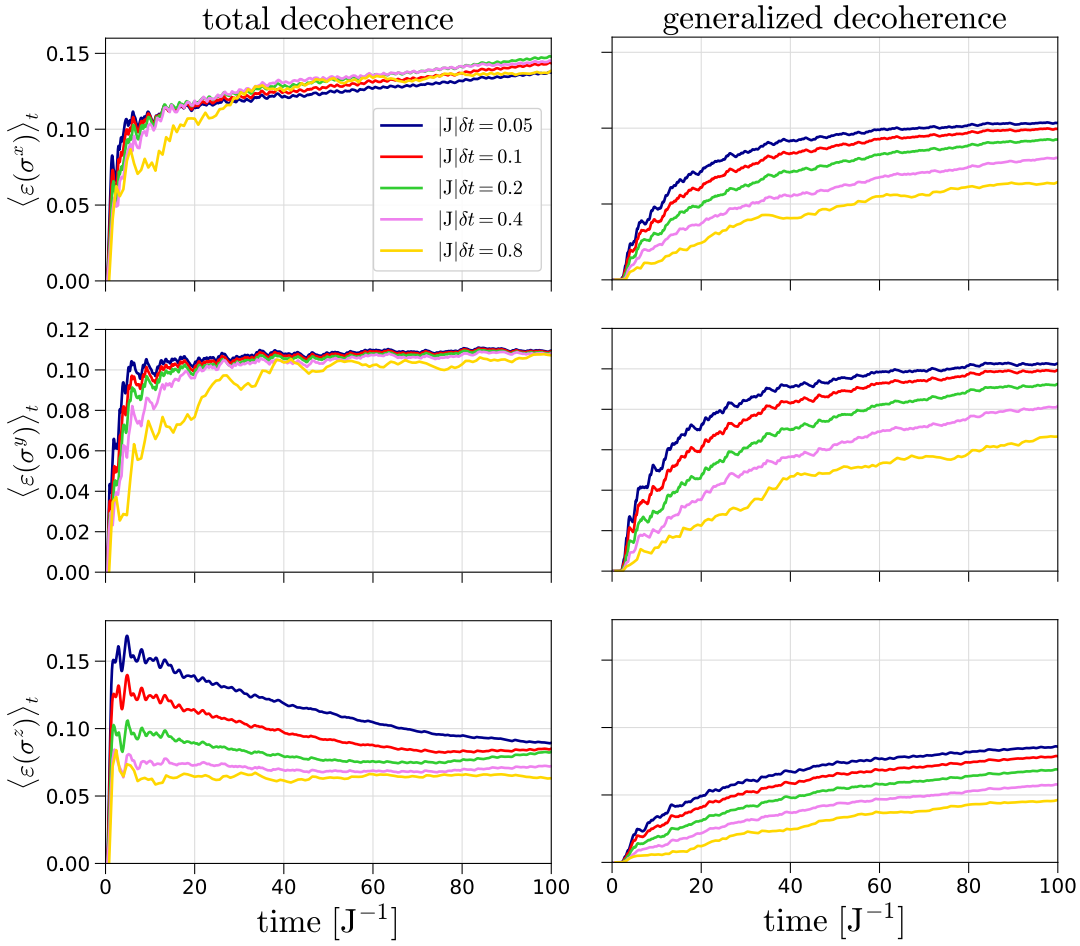

Figure 3.10: Influence of the frequency of decoherence in the single spin observable accuracy. For an initial state $|0,\ 0\rangle$ and fixed $n = 4$, we check the impact of the frequency of the operation that opens the gap for the three local magnetizations. With this purpose, we plot the time-averaged difference between the decoherent observables and the exact ones. While for full decoherence the improvement on the integrated distance becomes only visible on σ^z (third row), the generalized decoherence scheme shows a consistent reduction of the mistake in the observables as δt grows from 0.05 (dark blue) to 0.8 (yellow).

which is a much cleaner measure of the deviation due to decoherence than the direct difference of observables.

In the left column of Fig. 3.10 we show the results for full decoherence and, except for the third row displaying the observable $\sigma^z(t)$, there seems to be not much of a difference on increasing the time step δt with respect to $|\mathrm{J}|^{-1}$. The different curves for time steps 0.05 (dark blue), 0.1 (red), 0.2 (green), 0.4 (violet) and 0.8 (yellow) bunch up and saturate to a slowly increasing time-averaged deviation with time for $\sigma^{x,y}(t)$.

In contrast, the right column includes the results for generalized decoherence, which consistently yield smaller errors as $|\mathrm{J}|\delta t$ increases. Even for the highest frequency of $\frac{1}{0.05} = 20$ dissipations per $|\mathrm{J}|^{-1}$ step, the accumulated time-averaged error introduced for single spin observables is consistently smaller if compared to the hard threshold case.

We thus conclude that generalized decoherence scheme is more controlled in terms of preservation of reduced density matrices than its full decoherence counterpart.

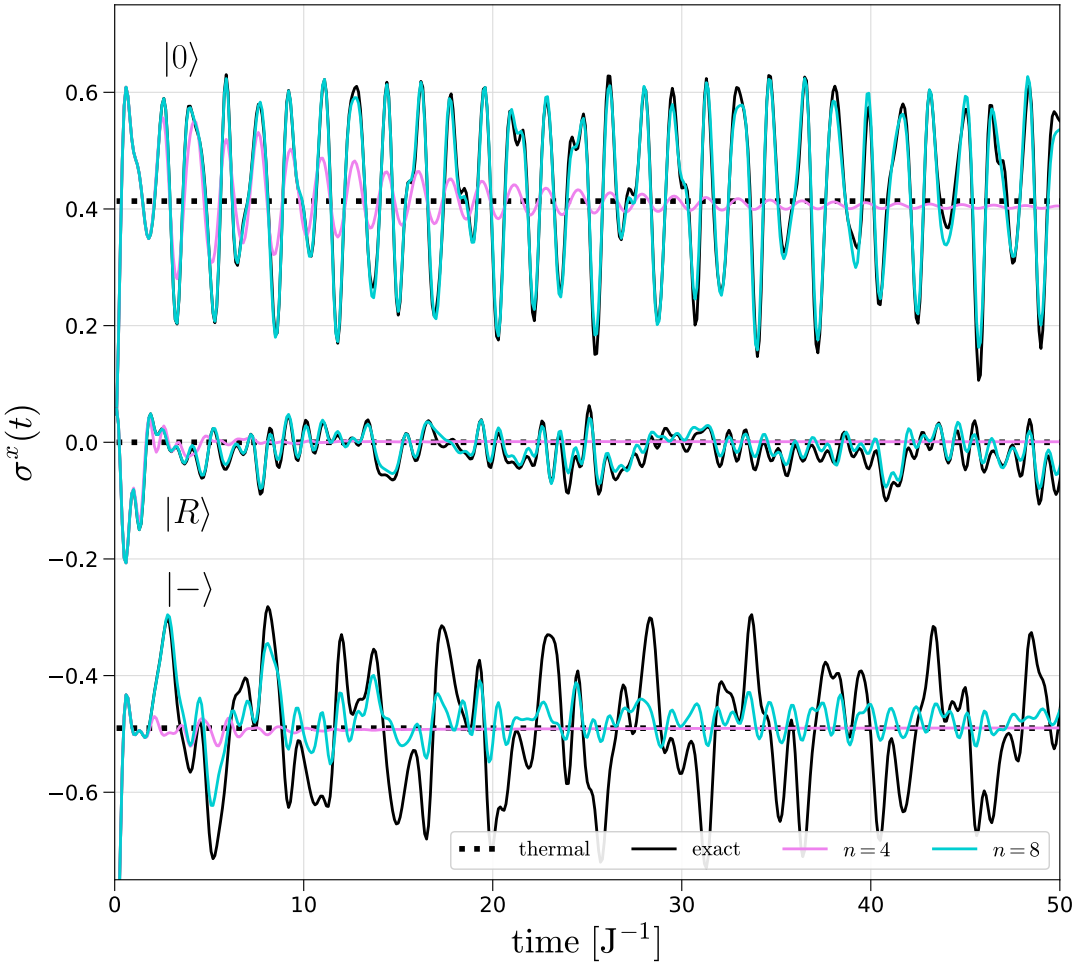

Figure 3.11: Transverse magnetization of different initial states under generalized decoherence with ferromagnetic Hamiltonian. We use the observable σ^x as a witness of different thermalization regimes and check whether the performance the generalized decoherence protocol varies among them within the ordered phase. While $|0\rangle$ (weakly thermalizing) and $|R\rangle$ (strongly thermalizing) yield good results, by converging to their thermal values for intermediate decoherence $n = 4$ (violet lines) and displaying coherent fluctuations close to the exact result for $n = 8$ (cyan line), the state $|-\rangle$ yields inconclusive results. On one side $n = 4$ is able to capture the thermalization of the magnetization, while $n = 8$ runs short, implying that such a state requires system-wide coherence to be accurately represented.

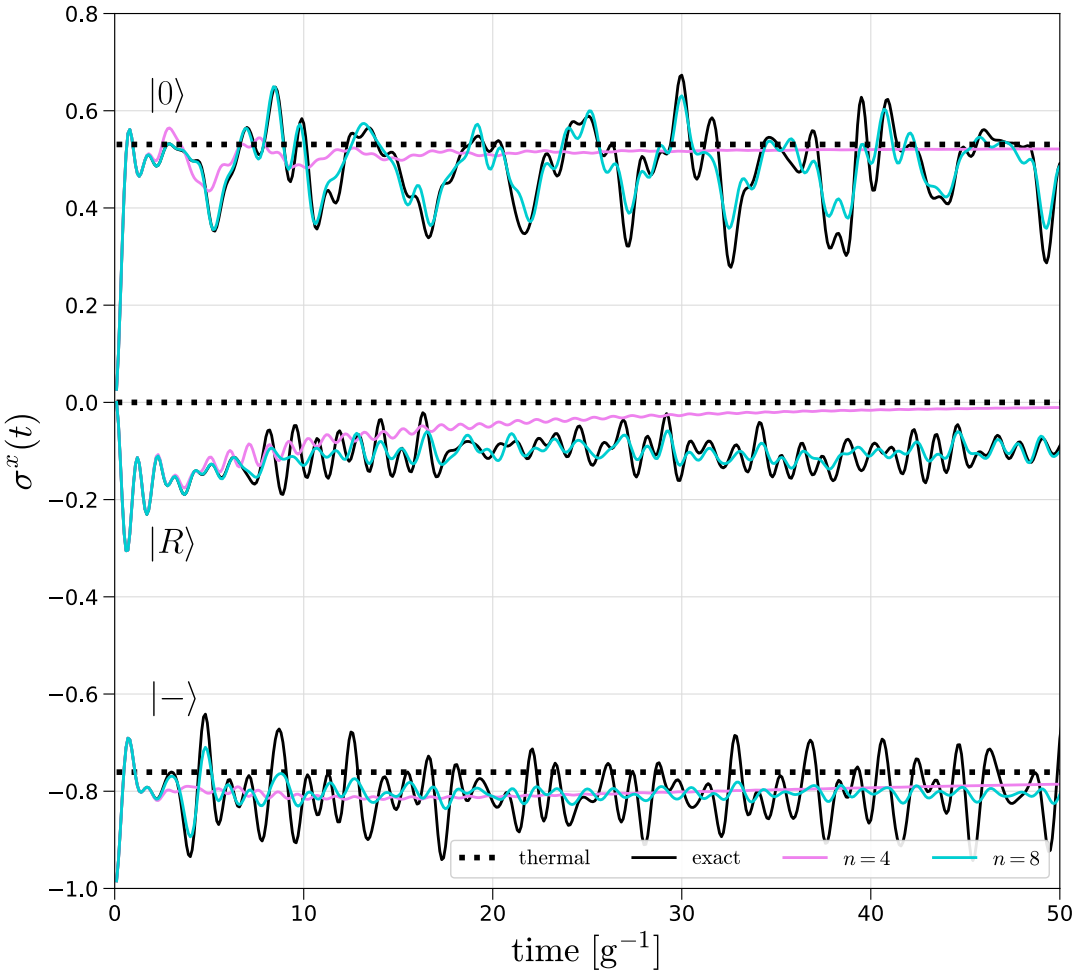

Figure 3.12: Transverse magnetization of different initial states under generalized decoherence with paramagnetic Hamiltonian. We use the observable σ^x as a witness of different thermalization regimes and check whether the performance the generalized decoherence protocol varies among them within the disordered phase. While $|0\rangle$ yields good results, by converging to its thermal values for intermediate decoherence $n = 4$ (violet lines) and displaying damped coherent fluctuations close to the exact result for $n = 8$ (cyan line), the states $|R\rangle$ and $|-\rangle$ yield inconclusive results. On one side $n = 4$ is able to capture the thermalization of the magnetization for $|R\rangle$, while it stays biased for $|-\rangle$. On top of that, $n = 8$ works well to describe the coherent fluctiations of $|R\rangle$, but runs short for $|-\rangle$, just as in the ordered phase.

3.4.4 Comparing Different Thermalization Regimes.

In the following we focus on the use of generalized decoherence, that apparently works better for the prediction of observables, and compare the results for different initial states and parameter regimes of the Hamiltonian; we will be studying the transverse magnetization $\sigma^x(t)$ with time step $|\mathrm{J}|\delta t$ (ordered) or $|g|\delta t$ (disordered) equal to 0.1.

The rationale behind this is that of understanding whether states associated to different thermalization regimes receive a similar impact from this artificial decoherence. We will study three initial states: $|0\rangle = |0, 0\rangle$, $|R\rangle = |\frac{\pi}{2}, \frac{\pi}{2}\rangle$ and $|-\rangle = |\frac{\pi}{2}, \pi\rangle$.

3.4.4.1 Ordered Phase.

In order to test the quenches with a Hamiltonian with ordered ground state we select the set of parameters $\mathrm{J} = -1,\ g = -1,\ h = -0.5$. At this point in parameter space, the initial states should thermalize locally with temperatures $|\mathrm{J}|\beta_0 = 0.75$, $|\mathrm{J}|\beta_R = 0$ and $|\mathrm{J}|\beta_- = -0.69$. This combination of Hamiltonian and initial states was already studied in Bañuls et al. (2011), where the authors identified $|0\rangle$ as weakly thermalizing, $|R\rangle$ as strongly thermalizing and $|-\rangle$ as a potential non-thermalizing state (despite in a later study, Yang et al. (2020) used spectral properties of the thermal ensemble to conclude that it does).

In Fig. 3.11 we plot the results for $n = 4$ (violet lines) and $n = 8$ (cyan lines) together with the exact observables (black lines) and the thermal values (black dashed lines); the later were estimated by exact diagonalization for size $L = 10$. As aforementioned, the results improve when n increases, but interestingly the lower $n = 4$ is already able to force the observables to their thermal value. This is curious, since thermalization usually becomes evident in the thermodynamic limit, but the generalized decoherence appears to unveil its value for intermediate thresholds in a system with only 10 spins.

While the three states display the correct convergence to the thermal value for $n = 4$, the fluctuations requiring higher coherence are retrieved satisfactorily only for $|0\rangle$ and $|R\rangle$. This is curious, since the problematic state $|-\rangle$ is the same that appeared to not thermalize when studied with transverse contraction methods in Bañuls et al. (2011), though here the issue is different. While we are able to force the magnetization in the state to converge to the right thermal value, the fluctuations appear to be extremely difficult to catch even for $n = 8$. Despite we do not have a full explanation for this phenomenon, we suspect that a study of the structure of state $|-\rangle$ in terms of Jordan-Wigner fermions may explain its requirement of long-range coherence.

3.4.4.2 Disordered Phase.

In order to test the quenches with a Hamiltonian with disordered ground state we select the set of parameters $\mathrm{J} = -0.625,\ g = -1,\ h = -0.125$, for which the initial states should thermalize locally with temperatures $|g|\beta_0 = 0.66$, $|g|\beta_R = 0$ and $|g|\beta_- = -1.40$.

We did not find any reference quenching within the non-integrable disordered phase, so we do not really know whether we should expect similar trends or not given the same three initial states. In fact, we identify again $|0\rangle$ as the state for which the decoherence works the best, with the x-magnetization converging to its thermal value $\sigma^x_{\mathrm{th},0} = 0.53$ for $L = 10$ when $n = 4$ (violet line); damped fluctuations commensurate with the exact

oscillations are attained with $n = 8$ (cyan line).

Opposed to $|0\rangle$, the states $|R\rangle$ and $|-\rangle$ appear to behave worse; nevertheless, we shall read the results carefully: these simulations are run for a small chain, and revivals from system-wide coherence may prevent the system to comfortably thermalize. This could be the case for $|R\rangle$, since $n = 4$ is able to converge the magnetization to 0 as it should, but $n = 8$ sticks close to the exact coherent result, implying that the protocol is still working within the small size regime for this state.

For $|-\rangle$ the reasons for worse performance of the protocol may be related with that mentioned in Sec. 3.4.4.1. On top of that, the thermal values obtained for $L = 10$ may converge slower for this state than for the other two, since $\sigma^x_{\text{th},0}(L = 10) = -0.76$ but in the simulation it appears to converge to -0.8.

3.4.5 Concluding Remarks.

In this section we offer a summary analyzing the strengths and weaknesses of each of the schemes presented through the chapter.

3.4.5.1 Physicality and Interpretability of Total Decoherence.

The total decoherence scheme is a valid procedure which chooses at each time step some basis in which coherence will be completely lost. As such, it corresponds to finding the average over measured density matrices in the entangled basis $\mathcal{B}^{\text{loc}}$. By construction, the disturbing object introduced in the closed time-contour is a valid quantum channel that admits an interpretation, and gives a prescription for implementing the stochastic-quantum correspondence.

These virtues open the path for future works, where we would like to extend this program for bigger systems and interpret the classically mapped probability distributions and transfer operators in terms of classical transport toy models.

On the bad side, it is unclear how easy is to optimally find the bases in a regime of sizes where ED is a prohibitive task. Also, the results retrieved for small systems already seem uncontrolled as compared to those obtained for generalized decoherence.

3.4.5.2 Accuracy and Unphysicality of Generalized Decoherence.

Opposed to the full decoherence scheme, generalized decoherence can not even be represented as a weak measurement protocol, since no channel can be engineered to leave a subset of the density matrix entries untouched. This involves that after each application the state becomes less and less physical, transforming itself into a mere numerical object that correctly approximates the local observables.

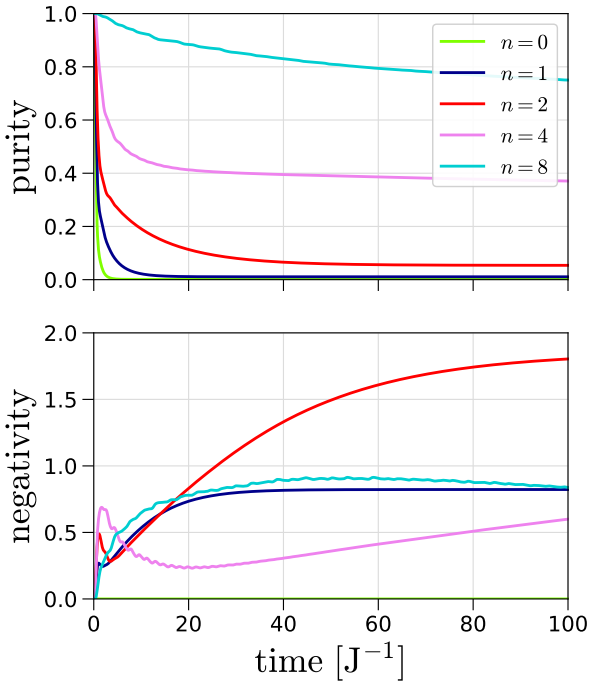

Figure 3.13: Depurification and unphysicality of the generally decohered density matrix. The quench used for illustrative purposes is that of state $|0\rangle$ in the ordered phase and $|J|\delta t = |J|^{-1}\gamma = 0.1$. The generalized decoherence scheme not only depurifies the density matrix (as any gapped operation would be expected to do) as shown in the upper panel, but also introduces negative eigenvalues in the operator, rendering it unphysical. There seems no not be any correlation between the threshold n for soft decoherence and the amount of negativity arising in the diagonal.

We illustrate the negativity generation together with the depurification of the physical state through generalized decoherence for the example of state $|0\rangle$ evolved in the ordered phase. While an increasing coherence threshold has a clearly smaller impact on the purity of the state, as displayed in the upper panel, the sum of negative eigenvalues generated by this process in the density matrix appears to be uncontrolled and not following any trend with n.

Despite that, generalized decoherence may not be an extremely bad policy, since many studies have used a TEBD-like update of the density matrix, incurring into the generation of negative eigenvalues: Verstraete et al. (2004), Prosen and Pižorn (2007b), Prosen and Pižorn (2008), Žnidarič et al. (2008a), Žnidarič et al. (2008b), Prosen and Žnidarič (2009), Pižorn and Prosen (2009b), Benenti et al. (2009), Žnidarič (2011), Jesenko and Žnidarič (2011), Prosen and Žnidarič (2012), Kliesch et al. (2014), Pižorn et al. (2014), Cui et al. (2015), Mascarenhas et al. (2015), Marzolino and Prosen (2016).

Importantly enough, both type I and II errors appeared to be very well controlled for small system sizes, inviting us to explore the method for longer systems. This

extension can be easily implemented with TNs, since the decoherer admits a simple MPO form. On top of that, energy conservation and any of its m-th powers is guaranteed as soon as the soft threshold fulfills $n \geq 2m$.

3.5 Outlook in the Schrödinger Picture.

In this chapter we have explored a method to introduce a gap in the Schrödinger evolution of the density matrix without erasing information relevant for the accurate representation of local observables.

In future works, we would like to further explore the connection between the chosen basis total decoherence and classical stochastic systems, which could reveal interesting reformulations of quantum dynamics. In particular, it could be interesting to understand how the elements of the rotating entangled basis look in terms of local observables; intuitively it would make sense that these vectors are characterized by magnetizations with broadening gaussian profiles, centered around particular sets of sites. Such a behavior would be a workhorse to establish a connection between the transport of quantum systems and diffusion in the corresponding classical system.

With respect to generalized decoherence, the results obtained in this chapter only prove that a decoherence scheme can generate a gap in the evolution while keeping the local observables faithful to their true values. Nevertheless, in the full TN picture there is one more question which shall be answered: whether the decoherence policies are able to control the growth of OSEE in Schrödinger picture. We will try to answer to this question in the following Ch. 4.

Halfway between using full and generalized decoherence, it could be interesting to design physical channels like those introduced in Secs. 3.3.2.1 and 3.3.2.2 to peak in particularly unnecessary density matrix entries, and aim at a zero-noise-extrapolation of the predictions. Such a scheme would be susceptible to be represented in purified form, avoiding the issue of unphysical negativity generation.

4

Explorations in the Heisenberg Picture: Orthogonal Pauli Weight Truncation

In the last Chapter we explored how erasing coherence on density matrices of small systems could lead to accurate long time results for local observables; nevertheless, the fact that generalized decoherence is not a quantum channel induced unphysical states. In this Chapter we switch to the Heisenberg picture, and combine what we have learned on the erasure of the off-diagonal elements of operators with insights on operator spreading to conceive an improved version of TEBD, the DecoAOE, which proves to yield consistent results with other methods achieving long-time evolution.

4.1 A Review on Pauli Weight Truncation in the Heisenberg Picture.

The main objective of developing alternative algorithms run on TN structures is to find suitable changes in the different parts of the existing ones, such that caveats like the entanglement barrier dissappear. For the case of Heisenberg evolving operators, the main measure of complexity was introduced in Ch. 2.2.5, and it is the OSEE. It turns out that a modification of the TEBD introduced by Rakovszky et al. (2022) for accurately obtaining transport coefficients of infinite temperature non-integrable systems is intimately related to our generalized decoherence strategy.

Their prescription, dubbed **Dissipation Assisted Operator Evolution** (DAOE) was specially designed for computing correlations of conserved quantities, like the energy density h, at different times

$$\langle h_{\ell_i}(0) h_{\ell_j}(t) \rangle_{\rho(\beta=0)} = \langle \rho(0) | \left[h_{\ell_i} \otimes \mathbb{1}_{2^L} \right] | h_{\ell_j}(t) \rangle, \tag{4.1}$$

These correlations enter the calculation of diffusion coefficients. In order to obtain such quantities $\langle h_{\ell_i}(0) h_{\ell_j}(t \to \infty) \rangle_{\rho(\beta=0)}$, it is required to compute the Heisenberg evolution of a local operator, calculation that suffers from the entanglement barrier of the OSEE. DAOE is an extension of TEBD that approximates $|h_{\ell_j}(t)\rangle$ by a truncated operator $|\tilde{h}_{\ell_j}(t)\rangle$ in terms of the **Pauli Weight** (PW) ω, i.e. the number of Pauli matrices contained in each basis element of the superposition.

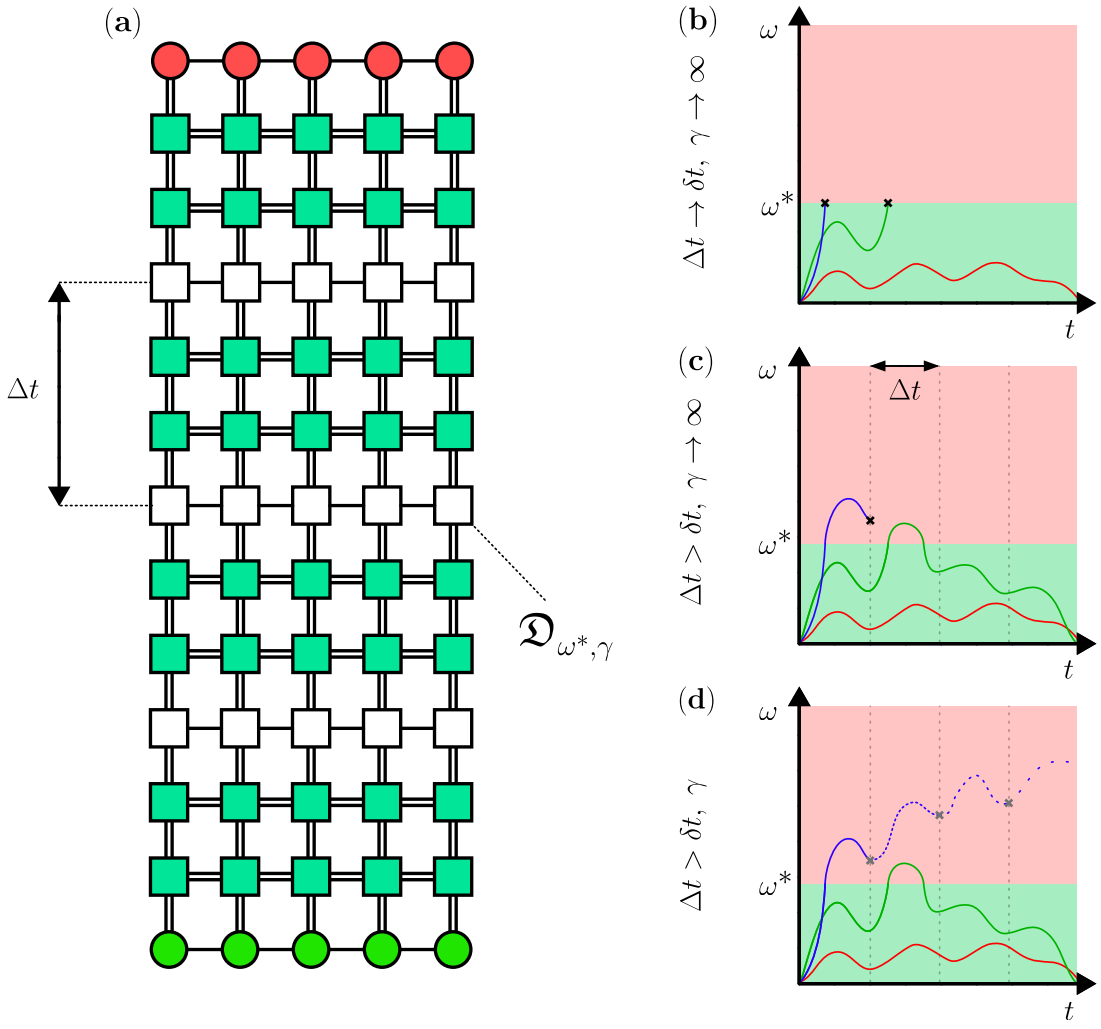

Figure 4.1: Pauli Weight truncation in the folded evolution. **(a)** The DAOE method introduces a dissipator $\mathfrak{D}_{\omega^*,\gamma}$ with period Δt, interspersed with the normal Liouvillian evolution. **(b)** If at every step in time all the strings with PW above the threshold ω^* are erased, then all the trajectories with PW growing beyond it will never have the opportunity to contribute; **(c)** opposed to that, if the period of erasure is wider, then some trajectories are allowed to perform excursions above the threshold, given that they are back on the retained subspace before the erasure. **(d)** The softest version corresponds to partially erasing the strings beyond ω^* through a decay factor, in such a way that they can still contribute, though with suppression factors.

Inspired by the memory matrix formalism and their previous results on diffusive hydrodynamics arising on locally random unitary circuits with and without conservation laws (Rakovszky et al. (2018); von Keyserlingk et al. (2018)), *Rakovzsky et al.* understood that heavy components of the $|h_{\ell_j}(t)\rangle$ superposition in terms of PW ($\omega \gg 1$) should not play a significant role on the long term dynamics. This can be understood by focusing on the state with which $[h_{\ell_i} \otimes \mathbb{1}_{2^L}]\,|h_{\ell_j}(t)\rangle$ is overlapped in Eq. 4.1, the infinite temperature $\propto \mathbb{1}_{2^L}$; it is an operator string with $\omega = 0$. Such an overlap cancels out all the components with any PW by orthogonality. Therefore at the moment in time in which the correlation is evaluated, only the superposition component along the identity is relevant.

This does not mean that the PW is completely irrelevant, since the evolution with nearest-neighbor Hamiltonians mixes $\omega = 0$ strings with $\omega = 1, 2$ strings; in fact, each weight ω is connected with $\omega \pm 1$ at first order of trotterization in δt. Thus, heavier strings at any point in time may affect the $\omega = 0$ component that is targeted at infinite temperature for future times. The process in which heavy strings develop light components with $\omega = 0, 1, 2$ is dubbed **operator backflow** in the literature.

The proposal of DAOE is to substitute the evolving Heisenberg operator by another one with PW dissipation à la Floquet:

$$|\tilde{O}(t)\rangle = e^{\mathcal{L}(t-N\Delta t)}\left[\mathfrak{D}_{\omega^*,\gamma}\, e^{\mathcal{L}\Delta t}\right]^N |O(t)\rangle, \tag{4.2}$$

where the normal Liouvillian evolution $e^{\mathcal{L}\Delta t}$ is interrupted with period Δt to introduce a dissipator $\mathfrak{D}_{\omega^*,\gamma}$ (an almost-projector) with the MPO form

$$W_{\mathfrak{D}}^{\ell_i\neq\ell_1,\ell_L} = \begin{pmatrix} |\mathbb{1}_2\rangle\langle\mathbb{1}_2| & \mathcal{P}_{\rm c}^{(1)} & 0 & \cdots & 0 & 0 & 0 \\ 0 & |\mathbb{1}_2\rangle\langle\mathbb{1}_2| & \mathcal{P}_{\rm c}^{(1)} & \cdots & 0 & 0 & 0 \\ 0 & 0 & |\mathbb{1}_2\rangle & \cdots & 0 & 0 & 0 \\ \vdots & \vdots & \vdots & \ddots & \vdots & \vdots & \vdots \\ 0 & 0 & 0 & \cdots & |\mathbb{1}_2\rangle\langle\mathbb{1}_2| & \mathcal{P}_{\rm c}^{(1)} & 0 \\ 0 & 0 & 0 & \cdots & 0 & |\mathbb{1}_2\rangle\langle\mathbb{1}_2| & \mathcal{P}_{\rm c}^{(1)} \\ 0 & 0 & 0 & \cdots & 0 & 0 & |\mathbb{1}_2\rangle\langle\mathbb{1}_2| + e^{-\gamma}\mathcal{P}_{\rm c}^{(1)} \end{pmatrix},$$

$$W_{\mathfrak{D}}^{\ell_1} = \begin{pmatrix} |\mathbb{1}_2\rangle\langle\mathbb{1}_2| & \mathcal{P}_{\rm c}^{(1)} & 0 & \cdots & 0 & 0 & 0 \end{pmatrix}, \qquad W_{\mathfrak{D}}^{\ell_L} = \begin{pmatrix} \mathbb{1}_4 \\ \mathbb{1}_4 \\ \mathbb{1}_4 \\ \vdots \\ \mathbb{1}_4 \\ \mathbb{1}_4 \\ |\mathbb{1}_2\rangle\langle\mathbb{1}_2| + e^{-\gamma}\mathcal{P}_{\rm c}^{(1)} \end{pmatrix}, \tag{4.3}$$

where $\mathcal{P}_{\rm c}^{(1)} = \Sigma_\alpha |\sigma^\alpha\rangle\langle\sigma^\alpha|$ is the projector onto the subspace of 1-spin operators with $\omega = 1$, and $\mathbb{1}_4 = |\mathbb{1}_2\rangle\langle\mathbb{1}_2| + \Sigma_\alpha |\sigma^\alpha\rangle\langle\sigma^\alpha|$.

The virtual dimension of this MPO is $\omega^* + 1$, and a decay rate γ parametrizes the dissipation $e^{-\gamma}$, introduced on the strings surpassing the maximal PW allowed, ω^*. This dissipator reads strings and multiplies them by a penalty every time that a *word* has more characters from the set $\{\sigma^\alpha\}$ than a threshold ω^*. The attentive reader may have already detected the connection with generalized decoherence (see Eq. 3.27).

In Fig. 4.1 we depict the modified TN evolution that intersperses PW truncation in (a) with period Δt, and the qualitative PW trajectories of components in the evolving operator. In panel (b), we depict what occurs if the period is synchronized with the trotterization time step and the decay is infinite: in this case, the dissipator coincides with a projector onto the subspace with $\omega \leq \omega^*$, and at every step the strings surpassing the threshold (green and blue trajectories) are killed. For panel (c), the period Δt is greater than δt (similar to a Floquet circuit, in an abuse of language), and violations of the PW threshold are allowed, so more trajectories (green) eventually converge to the $\omega = 0$ components contributing to the correlator. If the decay rate is finite, as in panel (d), only trajectories that stay a for times longer than Δt beyond the threshold ω^* are suppressed by a decay factor; such a factor is correlated with how much the PW of the string surpasses the threshold. Therefore, these strings still have the opportunity to contribute, though with a penalty.

Importantly enough, DAOE manages to control the growth of the OSEE, and renders the long term simulations of the Heisenberg dynamics feasible. The rationale behind it is the truncation of the dimension of the evolving superposition: DAOE introduces a soft dimension cutoff, which after long times retains only components with short strings. Since the number of singular values across the middle bipartition of the MPS chain is upper bounded by the dimension of the space in which the superposition lives, the OSEE is expected to saturate with the use of polynomial resources. For a cutoff ω^*, the highest number of singular values on a bond is upper bounded by the dimension[1] $\mathfrak{D}_{\text{bound}}$ of the subspace with $\omega \leq \omega^*$:

$$\mathfrak{D}_{\text{bound}} = \sum_{\omega=0}^{\omega^*} 3^\omega \binom{L}{\omega} . \tag{4.4}$$

We insist that this is only an upper bound for the dimension required by local operators, since they present the light-cone structure explained in Sec. 2.2.4.3, and L in Eq. 4.4 shall be replaced by the width of such a cone.

Despite the success of DAOE, the follow-up studies guaranteeing its validity (von Keyserlingk et al. (2022), Yoo et al. (2023), White (2023), Yi-Thomas et al. (2024)) and its extension to fermionic Hamiltonians (Lloyd et al. (2024), Kuo et al. (2024)), all these studies have been restricted to infinite temperature initial states.

[1] Note that for $\omega^* = L$ this dimension reduces to the full dimension of the squared Hilbert space 4^L using the definition of the binomial coefficient.

No understanding on whether it is applicable to arbitrary initial states has been developed so far, and sufficient arguments were given to foresee its failure in integrable systems (Rakovszky et al. (2018, 2022)). In the following section, we try to cover this gap by understanding the regime of applicability of DAOE for initial thermal and product states, and propose a modification of DAOE, which we dub DecoAOE.

4.2 Pauli Weight Characterization of Heisenberg Dynamics.

One of the main goals of the present Chapter is to understand whether cropping the components of the evolving Heisenberg operator superpositions is in fact accurate for general conditions, far from the idealized ones presented in former works. In order to understand this, we will focus on two types of initial states: mixed thermal states and pure Product States (PS).

4.2.1 Taking Thermal States with Finite β as a Reference.

The dynamics of any observable is trivial for thermal states of the same Hamiltonian which induces evolution. Despite that, after trotterization of the evolution operator the steadiness of these states could fail, since the local gates commute only approximately with the full Hamiltonian. On top of that, if the evolving object is an operator instead of the state itself, then no notion of commutation with the Hamiltonian simplifying the dynamics is even present. In terms of the folded Pauli string basis, a thermal state can be expanded as an infinite sum

$$\langle e^{-\beta H}| \propto \langle \mathbb{1}_2| \ + \ \beta\langle H| \ + \ \frac{\beta^2}{2}\langle H^2| \ + \ ... \tag{4.5}$$

Note that for nearest-neighbour Hamiltonians, $\langle H^n|$ contains strings with PW $\omega \leq 2n$; this means that the strings with $\omega = 2n,\ 2n+1$ in the thermal state superposition are weighted by β^n. By extension, the overlap with the evolving operator is a sum of terms weighted by inverse temperature powers and the Fröbenius norm $\mathcal{E} = \sqrt{\mathrm{Tr}\{h^2\}}$ of the energy density:

$$\begin{aligned} \langle e^{-\beta H}|O(t)\rangle &\propto \beta\langle H|O(t)\rangle \ + \ \frac{\beta^2}{2}\langle H^2|O(t)\rangle \ + \ ... \\ &\simeq \sum_{\omega>1}(\beta\mathcal{E})^n C_\omega(t), \end{aligned} \tag{4.6}$$

where C_ω is some time-dependent coefficient encoding the overlap of superpositions with equal Pauli weights. Note that local spin operators are traceless in the typical Pauli matrix convention, and this property is maintained along evolution, eliminating the $\omega = 0$ component.

The addenda in Eq. 4.6 are suppressed thus for $\beta\mathcal{E} < 1$ (high temperature regime), while they gain relevance if $\beta\mathcal{E} \geq 1$ (low temperatures). This implies that DAOE could perform well for temperatures above $|T| > \mathcal{E}$. From this perspective, it may appear that high temperature thermal states are simpler to simulate (if their Heisenberg dynamics would make any sense) than low temperature states.

4.2.2 Taking Product States as a Reference.

The discussion gets more interesting for non-stationary, unentangled initial states, like PS (this Section elaborates on the results published in Ramos-Marimón et al. (2025)). Opposed to thermal states, there is no parameter a priori guaranteeing that heavy strings will not be required in the expectation value. In the folded basis, they read

$$\begin{aligned}\langle\rho(\theta,\varphi)| &= \frac{1}{2^L}\Big(\langle\mathbb{1}| + \sin\theta\big(\cos\varphi\langle\sigma^x| + \sin\varphi\langle\sigma^y|\big) + \cos\theta\langle\sigma^z|\Big)^{\otimes L} \\ &= \frac{1}{2^L}\Big(\langle\mathbb{1}| + \langle\sigma^{\parallel}|\Big)^{\otimes L},\end{aligned} \tag{4.7}$$

where all the terms with $\omega = 1$ can be grouped into a **parallel Pauli matrix**[2] $\sigma^{\parallel}$; we dub it in this way, since on the level of a single spin, the rotation relating $\sigma^{x,y,z}$ with $\sigma^{\parallel}$ is the same which diagonalizes the PS, and therefore the one indicating the direction of the global magnetization in a homogeneous initial state[3]. In order to complete the new Pauli basis, we define the two **orthogonal Pauli matrices** through the relations

$$\langle\sigma^{\parallel}|\sigma^{\perp,\alpha}\rangle = 0 \quad \text{for} \quad \alpha = 1, 2. \tag{4.8}$$

With these definitions, it becomes clear that the overlap of a Heisenberg evolving operator with such a PS filters out any component containing a $\sigma^{\perp,i}$. This motivates us to split the PW into two different components: a parallel PW $\omega^{\parallel}$ and an orthogonal $\omega^{\perp}$ one, counting the number of $\sigma^{\parallel}$ and $\sigma^{\perp}$ on a string, respectively; both components add up to the original PW as $\omega = \omega^{\parallel} + \omega^{\perp}$. Then, for a given initial state with a particular parallel basis, we can split the evolving superposition into **contributing** $|O^{\mathrm{c}}(t)\rangle$ and **non-contributing** $|O^{\mathrm{nc}}(t)\rangle$ superpositions:

$$|O(t)\rangle = |O^{\mathrm{c}}(t)\rangle + |O^{\mathrm{nc}}(t)\rangle, \quad \text{s.t.} \quad \langle\rho(\theta,\varphi)|O^{\mathrm{nc}}(t)\rangle = 0. \tag{4.9}$$

Note the similarity with the infinite temperature state overlap treated in DAOE: the only component of the Heisenberg operator with a coefficient which will eventually feature in the expectation value is the contributing one, characterized by $\omega^{\perp} = 0$ rather

[2] We drop the reference to the angles (θ, φ) for which this matrix is defined for simplicity, since the state is translationally invariant within the extent of the chain.

[3] Note that a site-dependent rotation can also be defined, but then the reference to the angles defining the parallel basis for each spin should be kept.

than $\omega = 0$. As soon as a string includes an *error* or orthogonal insertion $\sigma^{\perp}$, its overlap with the state will cancel by orthogonality, no matter how much parallel PW it includes. We can summarize this in the following way: the contributing superposition is that containing only parallel PW, so it is characterized by $\omega^{\parallel} \geq 0$, while the non-contributing superposition may contain any parallel PW, but at least one orthogonal Pauli matrix, i.e. its PW fulfills that $\omega^{\parallel} \geq 0$ and $\omega^{\perp} \geq 1$.

Interestingly enough, we realize that if one could diagonalize an arbitrary initial state, such a change of basis would always let us define the contributing superposition as that containing only elements spanning the diagonal after the rotation. In this sense, once the basis bringing the initial state to the diagonal is found, truncating orthogonal PW amounts to eliminating coherence on the evolving operator in such particular basis; this decoherence is fixed by the initial state. The distinction between contributing and non-contributing parts is the starting point for our analysis on the validity of PW truncation, and it suggests a simple change of the DAOE strategy for arbitrary PS, as depicted in Fig. 4.2.

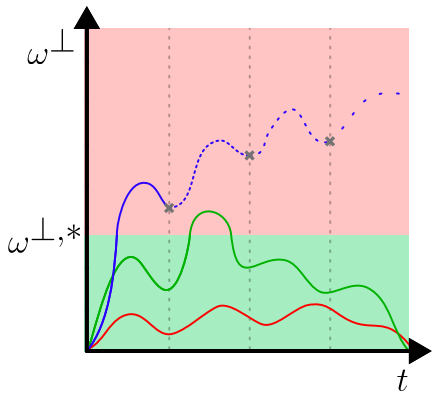

Figure 4.2: Orthogonal PW truncation. The picture of dissipating trajectories with PW surpassing a threshold can be extended to non-diagonal states, like arbitrary PS, by substituting the generic PW ω by the orthogonal/off-diagonal one $\omega^{\perp}$.

In order to perform such a splitting, we introduce the following projectors on the level of single spins:

- The projector onto the subspace with any kind of PW:

$$\mathcal{P}_{\omega}^{(1)} = \sum_{\alpha} |\sigma^{\alpha}\rangle\langle\sigma^{\alpha}|.$$

- The projector onto the contributing components

$$\mathcal{P}_{\mathrm{c}}^{(1)} = |\mathbb{1}_2\rangle\langle\mathbb{1}_2| + |\sigma^{\parallel}\rangle\langle\sigma^{\parallel}| = |\mathbb{1}_2\rangle\langle\mathbb{1}_2| + \mathcal{P}_{\omega^{\parallel}}^{(1)},$$

  which contains the projector onto only parallel Pauli matrices. Note that this object is the same as the full decoherence for a single spin: it is a projector onto the diagonal!

- The projector onto the perpendicular Pauli matrices

$$\mathcal{P}^{(1)}_{\omega^\perp} = \sum_\alpha |\sigma^{\perp,\alpha}\rangle\langle\sigma^{\perp,\alpha}|,$$

  corresponding to a pair of copy tensors with one σ^x insertion coupling the forward and backward contours, then vectorized: it is $\mathcal{F}_1$ for one spin!

Using these single spin projectors we can construct projectors for the operators on the chain; while the contributing projector $\mathcal{P}^{\rm c}$ is a simple product:

$$|O^{\rm c}(t)\rangle = \mathcal{P}^{\rm c}|O(t)\rangle \quad \text{with} \quad \mathcal{P}^{\rm c} = \bigotimes_{\ell=1}^{L} W^{(\ell)}_{\rm c} \quad \text{and transfer} \quad W^{(\ell)}_{\rm c} = \mathcal{P}^{(1)}_{\rm c}, \tag{4.10}$$

the non-contributing projector acquires a non-trivial bond dimension, associated with detecting the event of an orthogonal Pauli featuring in the string

$$W^{(\ell)}_{\rm nc} = \begin{pmatrix} \mathcal{P}^{(1)}_{\rm c} & \mathcal{P}^{(1)}_{\omega^\perp} \\ 0 & \mathbb{1}_4 \end{pmatrix}. \tag{4.11}$$

The first checks that we will perform consist on studying **superposition norm**, computed through the overlaps

$$o^{\rm c}(t) = \langle O^{\rm c}(t)|O^{\rm c}(t)\rangle, \qquad o^{\rm nc}(t) = \langle O^{\rm nc}(t)|O^{\rm nc}(t)\rangle, \qquad o^{\rm c}(t) + o^{\rm nc}(t) = 1, \tag{4.12}$$

and its Pauli Weight resolved versions $o^{\rm c}_\omega(t)$ and $o^{\rm nc}_\omega(t)$ defined by

$$\begin{aligned} o^{\rm c}(t) &= \sum_\omega \langle O^{\rm c}(t)|\mathcal{P}_\omega|O^{\rm c}(t)\rangle = \sum_\omega o^{\rm c}_\omega(t), \\ o^{\rm nc}(t) &= \sum_\omega \langle O^{\rm nc}(t)|\mathcal{P}_\omega|O^{\rm nc}(t)\rangle = \sum_\omega o^{\rm nc}_\omega(t). \end{aligned} \tag{4.13}$$

where we introduced the projector onto the subspace with PW ω

$$W^{(\ell\neq 1,L)}_\omega = \begin{pmatrix} |\mathbb{1}\rangle\langle\mathbb{1}| & \mathcal{P}^{(1)}_\omega & 0 & \cdots & 0 & 0 & 0 \\ 0 & |\mathbb{1}\rangle\langle\mathbb{1}| & \mathcal{P}^{(1)}_\omega & \cdots & 0 & 0 & 0 \\ 0 & 0 & |\mathbb{1}\rangle\langle\mathbb{1}| & \cdots & 0 & 0 & 0 \\ \vdots & \vdots & \vdots & \ddots & \vdots & \vdots & \vdots \\ 0 & 0 & 0 & \cdots & |\mathbb{1}\rangle\langle\mathbb{1}| & \mathcal{P}^{(1)}_\omega & 0 \\ 0 & 0 & 0 & \cdots & 0 & |\mathbb{1}\rangle\langle\mathbb{1}| & \mathcal{P}^{(1)}_\omega \\ 0 & 0 & 0 & \cdots & 0 & 0 & |\mathbb{1}\rangle\langle\mathbb{1}| \end{pmatrix}, \tag{4.14}$$

$$W^{(1)}_\omega = \begin{pmatrix} |\mathbb{1}_2\rangle\langle\mathbb{1}_2| & \mathcal{P}^{(1)}_\omega & 0 & \cdots & 0 & 0 & 0 \end{pmatrix}, \quad W^{(L)}_\omega = \begin{pmatrix} 0 \\ 0 \\ 0 \\ \vdots \\ 0 \\ \mathcal{P}^{(1)}_\omega \\ |\mathbb{1}_2\rangle\langle\mathbb{1}_2| \end{pmatrix},$$

which is an MPO with bond dimension $\chi = \omega + 1$.

In Fig. 4.3 we study $o^{\mathrm{c}}_{\omega}(t)$ and $o^{\mathrm{nc}}_{\omega}(t)$ for the transverse magnetization σ^x evolved with the Ising model at the point $\{\mathrm{J} = -1,\ g = -1,\ h = -0.5\}$ for different initial states and with channel decoherence. To analyze the differences across varying initial states, we pick $|0, 0\rangle$ and $|\frac{9\pi}{10}, 0\rangle$; conversely, for determining the impact of channel dissipation, we introduce decoherence with measurement rates $\gamma|\mathrm{J}| = 1.25,\ 10$ on the first state. The resulting picture can be analyzed at different levels:

- The **non-contributing norms** $o^{\mathrm{nc}}_{\omega}(t)$, depicted in dotted curves for $\omega = 1,\ 2,\ 4,\ 6$ (blue, red, violet and darkgreen, respectively), display a similar behavior for all the sub-panels: $\omega = 1,\ 2$ always dominate the short time-scales, since the initial operator contains just $\omega = 1$ strings at $t = 0$, and they transmit their norm towards higher weights. Heavier strings are synthesized by the Hamiltonian evolution, and their norm rises from 0, peaking at particular times (indicated with triangles for $\omega = 4,\ 6$), to later pass their norm to the next weight. The times $t^{\mathrm{nc,peak}}_{\omega}$ at which these non-contributing superpositions peak are ordered by ω as $t^{\mathrm{nc,peak}}_{\omega} < t^{\mathrm{nc,peak}}_{\omega+1}$ for $\omega > 2$.

- The **contributing norms** $o^{\mathrm{n}}_{\omega}(t)$ are depicted in solid lines, and can be split into two families for all panels: one with $\omega \leq 2$ (blue and red), containing most of the contributing norm (again, a consequence of the initial operator having $\omega = 1$) and decaying slowly, and another with $\omega > 2$ (green, violet, yellow, darkgreen), synthesized as the time passes and fast decaying.

  The difference between rates of decay may be explained in terms of the hydrodynamics of evolving operators, as proposed in Gopalakrishnan et al. (2018); Khemani et al. (2018): the conservation of energy imposes constraints on superpositions of strings with the same PW as those present in the Hamiltonian ($\omega \leq 2$ for nearest-neighbor models), forcing a slow hydrodynamic/diffusive spreading of their norm with respect to higher powers of the Hamiltonian.

- While the non-contributing part looks similar in the first column (0 dissipation rate), the converse is not true for the contributing parts: for $|0, 0\rangle$ the two lowest PWs dominate the superposition, and display a gap of a bit more of an order of magnitude with the contributing norms of heavier strings; on the other hand, for $|\frac{9\pi}{10}, 0\rangle$ only $\omega = 2$ dominates, and the gap with $\omega = 1$ is more than an order of magnitude, while the gap with heavier strings is more than two orders of magnitude.

- In presence of weak dissipation (upper panel, right column) the hierarchy of norms and rates of relaxation remains unaltered, but for strong dissipation (lower panel, right column) all norms decay exponentially. This means that the evolving operator is drifting towards the $\omega = 0$ component (similar to the infinite temperature case for Schrödinger picture evolution).

- Such a result is natural, as it can be understood by rewriting the channel from Eq. 2.47 in the folded Pauli basis:

$$\begin{aligned} \varepsilon_{\text{gen. depol}}|\mathbb{1}_2\rangle &= |\mathbb{1}_2\rangle, \\ \varepsilon_{\text{gen. depol}}|\sigma^\alpha\rangle &= \big[1 - P(1-p_\alpha)\big]|\sigma^\alpha\rangle \overset{P\to 0}{\simeq} e^{-\gamma\,(1-p_\alpha)\,\delta t}\,|\sigma^\alpha\rangle, \end{aligned} \tag{4.15}$$

  where it can be seen that single spin dissipation is equivalent to dissipation of different Pauli matrices. For the particular case of decoherence ($p_z = 1$), $\sigma^{x,y}$ get a decay $1 - P$, while σ^z is left invariant, as expected for a channel which dissipates just the off-diagonals.

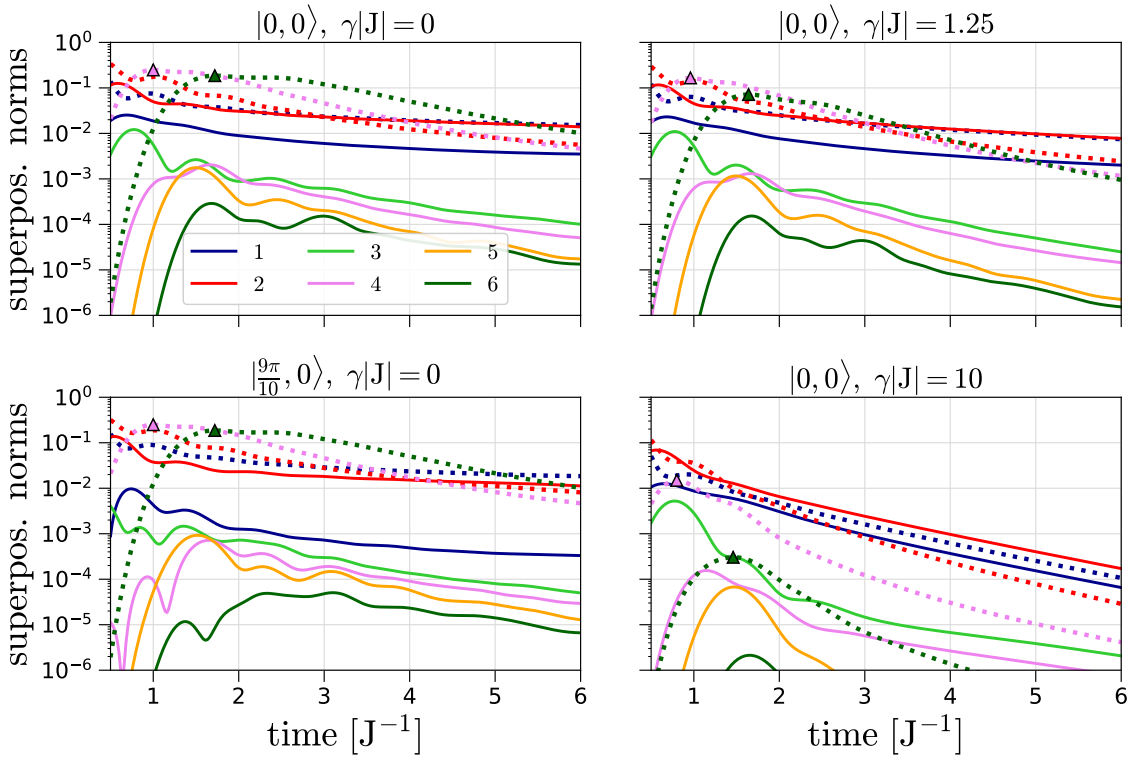

Figure 4.3: Contributing and non-contributing superposition norms.. The simulations were run for the non-integrable Ising model at $\{\mathrm{J} = -1,\ g = -1,\ h = -0.5\}$, without (right column) and with (left column) single spin decoherence. The TEBD parameters were $L = 32$, $|\mathrm{J}|\delta t = 0.02$ and $\chi = 384$; errorbars correspond to the difference with simulations at half the maximal bond dimension $\chi' = \frac{\chi}{2}$.

Profiting from the former calculation, we can make a small detour, and take a look at the OSEE of each superposition; this information could make us understand where the complexity of the simulation is originating from in Heisenberg picture. In Fig. 4.4 we present these results for the same states and channels as in Fig. 4.3.

Interestingly, in all cases the volume law for the OSEE of the total superposition $|O\rangle$ (solid purple curve) is slightly smaller than that of the non-contributing superposition $|O^{\mathrm{nc}}\rangle$ (dotted green curve). Opposed to that, the contributing superposition shows an area law, implying that if this superposition could be generated without taking into account the orthogonal strings, the Heisenberg evolution simulation would be classically efficient.

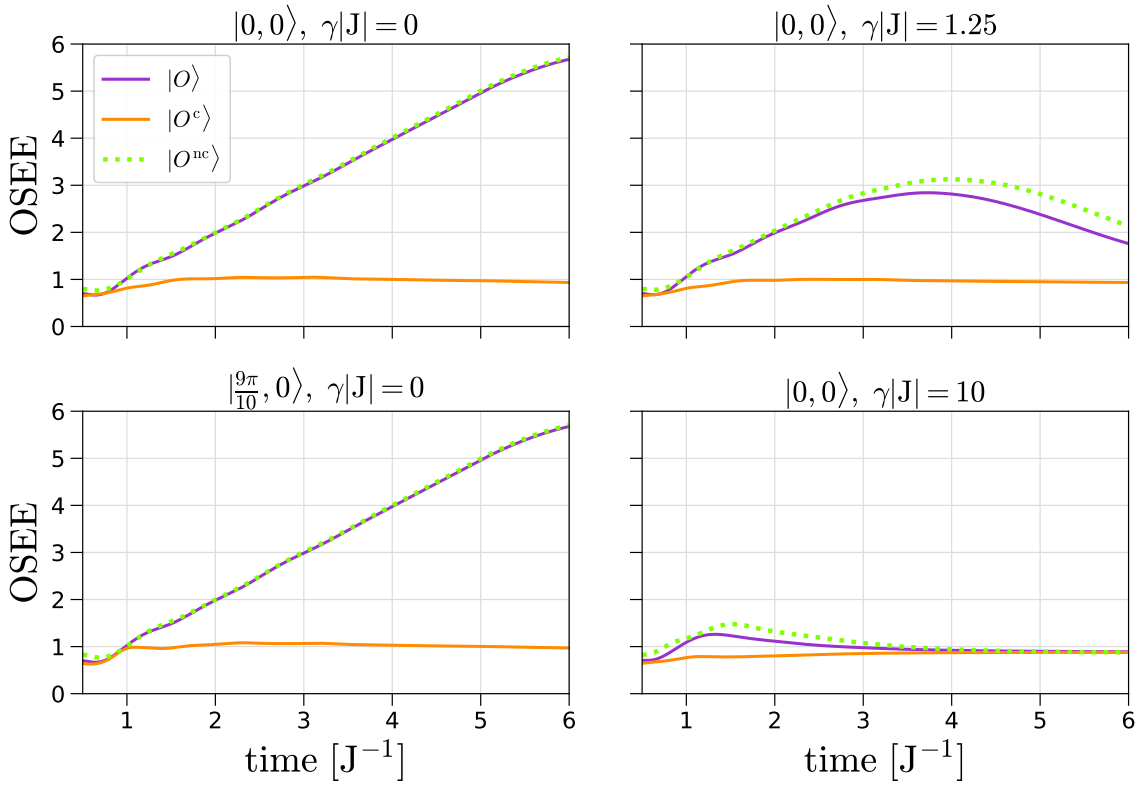

Figure 4.4: OSEE from contributing and non-contributing superpositions. The simulations were run for the non-integrable Ising model at $\{\mathrm{J}=-1,\ g=-1,\ h=-0.5\}$, without (right column) and with (left column) single spin decoherence. The TEBD parameters were $L=32$, $|\mathrm{J}|\delta t=0.02$ and $\chi=384$; errorbars correspond to the difference with simulations at half the maximal bond dimension $\chi'=\frac{\chi}{2}$.

Remarkably, the cases with channel dissipation (right column) naturally tame the OSEE growth. Again, from Eq. 4.15 this is related to the introduction of a soft upper bound on the Pauli string superposition dimension, which forbids the Schmidt rank at each bipartition to grow uncontrollably. This same conclusion was derived for random circuits subject to 2-spin depolarization by Noh et al. (2020).

From these preliminar results, it may appear that heavy contributing strings do not play an important role in the observable dynamics; nevertheless, the fact that there is a suppressed norm deposited into the subspaces with high parallel PW does not mean that in the overlap with the state the contributions will remain small. In fact, different phases in the coefficients of the different strings may lead to constructive interferences that could change the picture.

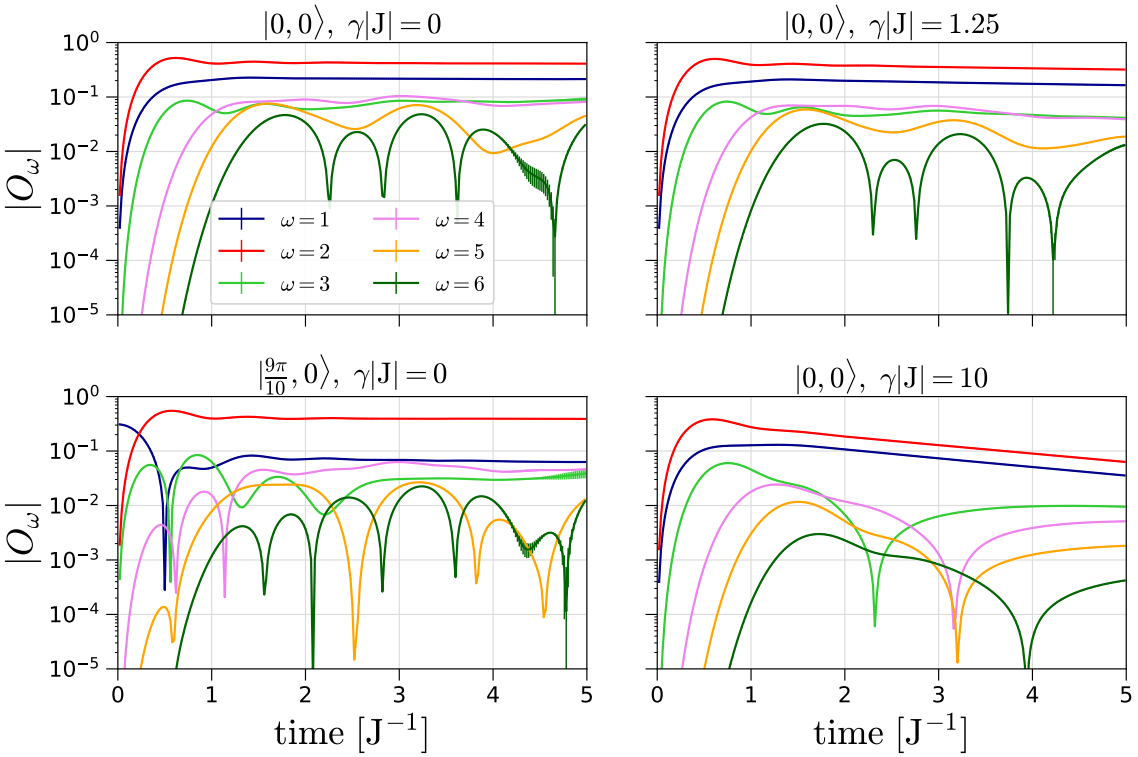

Figure 4.5: PW-resolved contributions. The simulations were run for the non-integrable Ising model at $\{\mathrm{J}=-1,\ g=-1,\ h=-0.5\}$, without (right column) and with (left column) single spin decoherence. The TEBD parameters were $L=32$, $|\mathrm{J}|\delta t=0.02$ and $\chi=384$; errorbars correspond to the difference with simulations at half the maximal bond dimension $\chi'=\frac{\chi}{2}$.

4.2.2.1 Pauli-Weight-resolved Contributions.

With the purpose of clearing out the doubts on whether interference in the expectation value computations may alter the former results, we study the **PW-resolved overlaps** with same conditions as in Figs. 4.3 and 4.4; these overlaps are defined by

$$O(t)=\langle\rho(\theta,\varphi)|O(t)\rangle=\sum_\omega\langle\rho(\theta,\varphi)|\mathcal{P}_\omega|O^c(t)\rangle=\sum_\omega O_\omega(t), \tag{4.16}$$

and we compute them in Fig. 4.5. The results can be summarized as follows:

- As we had feared, the contributions from heavy strings, whose norm was suppressed by several orders of magnitude, is eventually contributing even to order $\mathcal{O}(10^{-2})$ in the observable.

- The light subspaces stabilize, in the sense of damping their oscillating contributions to either constant or non-periodic curves, much faster than the heavy subspaces. Again, there appears to exist a hierarchy, imposed both by the fact that the initial operator has $\omega = 1$ and by the Hamiltonian being nearest-neighbor (mixing components among subspaces $\omega \pm 1$).

  Interestingly, the stabilized components start constructing the stationary value on top of which the heavy components introduce oscillations. This means that, if the observable is meant to thermalize (as for the simulated non-integrable point), the thermal value arises as the sum of stabilized values of the O_ω's, and the fluctuations around it are related to the ever-expanding heavy subspaces, which keep passing their norm to heavier strings, as seen in Fig. 4.3. We will come back to this point in Sec. 4.4, where we will center or study on the operator spreading itself.

- The results were computed for a system of size $L = 32$, $|\mathrm{J}|\delta t = 0.02$ and two different bond dimensions $\chi = 192,\ 384$. The errorbars represent the difference between the plotted values ($\chi = 384$) and those with stronger truncation ($\chi = 192$). It is clear from the upper left panel that contributions with more error due to TEBD-style truncation are ones from heavy subspaces. This means that, at least at short times, TEBD truncation may only introduce an extra damping on the fluctuations, but it will not drift the time-averaged values.

  Despite that, we are well-aware that TEBD fails at longer times, e.g. by breaking the energy conservation; this points towards the fact that, at short times, light strings are concentrated in a subspace of small dimension and explain stationary values. At longer times, this light string superposition competes with that of the fluctuating heavy subspaces to occupy the allowed dimensionality in the MPS. Classical TEBD truncation does not distinguish between subspaces, so it eventually fails yielding stable values.

- On top of the overall trend evidencing the increasing the role of heavy subspaces, we still detect the same distinctive features for each panel. State $|0,0\rangle$ requires heavier subspaces to reach an accuracy in the predictions of order $\mathcal{O}(10^{-1})$ (until $\omega = 4$), while $|\frac{9\pi}{10}, 0\rangle$ requires only $\omega = 2$ (note that $\omega = 1$ is suppressed by an order of magnitude). Furthermore, introducing increasing dissipation (right column) alters the contributions, starting from the heavier subspaces (upper panel), until the lightest ones (lower panel). Small dissipation lifts the errors introduced by TEBD on heavier subspaces (at least for these short time simulations), and strong dissipation decays all subspaces, as already pointed out in Fig. 4.3.

- The difference of PW required by the sum of overlaps in order to yield accurate results *could be related to the equilibration temperature of the initial states*: while $|0,0\rangle$ locally converges to a lower temperature ensemble with $\beta|\mathrm{J}| = 0.7522$ (fixed by Eq. 2.22), state $|\frac{9\pi}{10},0\rangle$ equilibrates to a higher temperature $\beta|\mathrm{J}| = 0.3120$ (roughly twice the temperature of the former). As we saw in Sec. 4.2.1, higher temperature states were prone to suppress heavy PW contributions through temperature, while low temperature states were not.

These results invite us to think that there could be a difference between the complexity of simulating different states, according to the amount of (parallel) PW required to accurately computing their time evolution in the Heisenberg picture. Such a difference could be provoked by: (1) the geometry of the state, or (2) by its average energy (fixing its equilibration temperature). An extensive study on this matter will be carried out in Sec. 4.2.2.3.

On top of that, we are almost ready to extend DAOE to a version truncating orthogonal PW, which we expect to work well for (potentially high temperature-) states, like $|\frac{9\pi}{10},0\rangle$. This generalization will be studied in Sec. 4.3, but before that, we need to make sure that the backflow from non-contributing subspaces ($\omega^{\perp} > 0$) to contributing ones ($\omega^{\perp} = 0$) is not an issue.

4.2.2.2 Backflow Study.

With the goal of understanding whether backflow could hinder an extension of DAOE based on orthogonal PW truncation, we study to which extent the non-contributing subspaces can generate contributions at later times. In order to do that, we localize the times $t_{\omega^\perp}^{\mathrm{nc,peak}}$ of maximum norm of a non-contributing subspace (indicated by the triangle markers in Fig. 4.3), project out the subspaces with higher orthogonal PW than some fixed amount, and keep evolving to study the overlap with the state. This is summarized by the following backflow expression:

$$O_{\omega^\perp}^{\mathrm{bck}}(t) = \langle \rho(\theta,\varphi)| \left[\, \mathcal{U}(t - t_{\omega^\perp}^{\mathrm{nc,peak}}) \otimes \overline{\mathcal{U}}(t - t_{\omega^\perp}^{\mathrm{nc,peak}}) \,\right] \mathcal{P}_{\omega^\perp} \, |O(t_{\omega^\perp}^{\mathrm{nc,peak}})\rangle, \tag{4.17}$$

where the projector over the subspace with less or equal orthogonal PW than $\omega^\perp$ is an MPO of bond dimension $\omega^\perp + 1$:

$$W_{\omega^\perp}^{i_\ell \neq i_1, i_L} = \begin{pmatrix} \mathcal{P}_{\mathrm{c}}^{(1)} & \mathcal{P}_{\omega^\perp}^{(1)} & 0 & \cdots & 0 & 0 & 0 \\ 0 & \mathcal{P}_{\mathrm{c}}^{(1)} & \mathcal{P}_{\omega^\perp}^{(1)} & \cdots & 0 & 0 & 0 \\ 0 & 0 & \mathcal{P}_{\mathrm{c}}^{(1)} & \cdots & 0 & 0 & 0 \\ \vdots & \vdots & \vdots & \ddots & \vdots & \vdots & \vdots \\ 0 & 0 & 0 & \cdots & \mathcal{P}_{\mathrm{c}}^{(1)} & \mathcal{P}_{\omega^\perp}^{(1)} & 0 \\ 0 & 0 & 0 & \cdots & 0 & \mathcal{P}_{\mathrm{c}}^{(1)} & \mathcal{P}_{\omega^\perp}^{(1)} \\ 0 & 0 & 0 & \cdots & 0 & 0 & \mathcal{P}_{\mathrm{c}}^{(1)} \end{pmatrix}, \tag{4.18}$$

$$W_{\omega^\perp}^{i_1} = \begin{pmatrix} |\mathbb{1}_2\rangle\langle\mathbb{1}_2| & \mathcal{P}_{\omega}^{(1)} & 0 & \cdots & 0 & 0 & 0 \end{pmatrix}, \quad W_{\omega^\perp}^{i_L} = \begin{pmatrix} \mathbb{1}_4 \\ \mathbb{1}_4 \\ \mathbb{1}_4 \\ \vdots \\ \mathbb{1}_4 \\ \mathcal{P}_{\omega}^{(1)} \\ |\mathbb{1}_2\rangle\langle\mathbb{1}_2| \end{pmatrix},$$

The reader may note the accepting right boundary filtering out strings beyond $\omega^\perp$.

The results for the same set of states and dynamics from Figs. 4.3, 4.4 and 4.5 are presented in Fig. 4.6. For the first column, we observe that backflow into the contributing space is of the same order for strings with $\omega^\perp = 4$ and 6 in both panels, but the magnitude of it is around 10 times bigger in $|0,0\rangle$ (upper panel) than in $|\frac{9\pi}{10},0\rangle$. This reinforces the idea that some states (apparently the high temperature ones) require less (parallel) PW for their simulation, versus others which receive strong backflow from orthogonal components.

For the case of dissipative dynamics in the right column, the *difficult state* $|0,0\rangle$ becomes easier in terms of PW by opening a gap between the backflow from $\omega^\perp = 4$ and 6 (upper panel), which gets clearly defined upon increasing the measurement rate (lower panel).

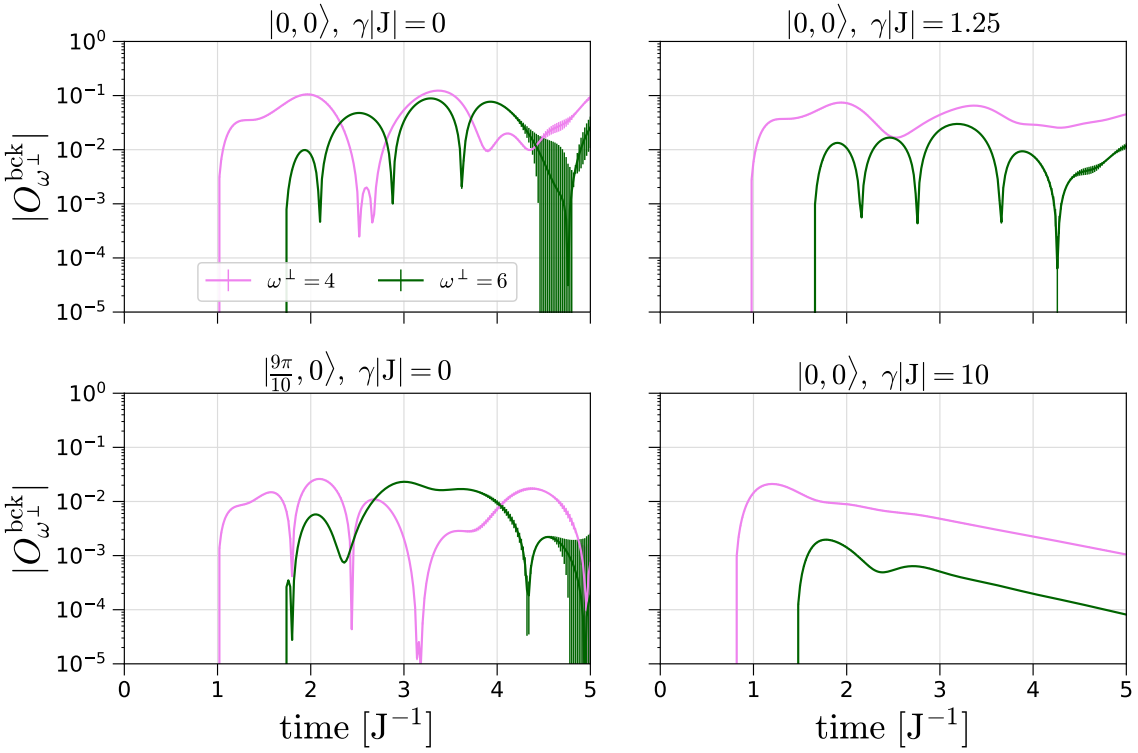

Figure 4.6: Backflow from contributing and non-contributing superpositions. The simulations were run for the non-integrable Ising model at $\{\mathrm{J}=-1,\ g=-1,\ h=-0.5\}$, without (right column) and with (left column) single spin decoherence. The TEBD parameters were $L=32$, $|\mathrm{J}|\delta t=0.02$ and $\chi=384$; errorbars correspond to the difference with simulations at half the maximal bond dimension $\chi'=\frac{\chi}{2}$.

4.2.2.3 Temperature Dependence of Complexity from Short Time Unitary Evolution.

In this section we try to understand whether the equilibration temperature of a particular initial state is related to the amount of parallel PW required for accurate simulations. Since checking the PW-resolved contributions for every combination of initial states and operators can be tedious and inefficient, we define a quantity that serves as a measure of such complexity; it will let us perform a systematic comparison of the specific matrix elements of the evolved operator selected by the initial states through a single quantifier.

With the aim of defining such a quantity, we introduce a few concepts. In first place, the **truncated observable** until PW ω

$$O^{\mathrm{acc}}_{\omega}(t)=\sum_{n=0}^{\omega}O_n(t), \tag{4.19}$$

such that the exact observable reads $O(t)=O^{\mathrm{acc}}_{L}(t)$, and its absolute distance to the exact observable

$$d_\omega(t)=|O(t)-O^{\mathrm{acc}}_{\omega}(t)|. \tag{4.20}$$

We want to define a probability distribution representing the information on the relative sizes of each contribution per PW subspace, so we define a normalization

$$\mathcal{N}_{\omega*}(t) = \sum_{\omega=0}^{\omega*} d_\omega(t). \tag{4.21}$$

The probability distribution corresponds to the normalized distances for al weights ω below a maximum ω^*, set by our limited simulation resources[4]:

$$p_{\omega,\omega^*}(t) = \frac{d_\omega(t)}{\mathcal{N}_{\omega*}(t)}. \tag{4.22}$$

These definitions allow us to characterize the distribution of normalized distances with an **Operator Weight Entropy** (OWE)

$$\mathrm{OWE}(t) = -\sum_{\omega=0}^{\omega*} p_{\omega,\omega^*}(t) \log_2 p_{\omega,\omega^*}(t). \tag{4.23}$$

Given the cumulative definition of p_{ω,ω^*}, we need to carefully consider the possible behaviors of OWE across time. For example, an expectation value that is accurately represented by a finite ω^* for arbitrarily late times be characterized by an OWE that saturates after the initial growth. Opposed to that, a linearly increasing OWE would only be obtained by an expectation value described by many Pauli strings with PW exceeding ω^*, since only in that case p_{ω,ω^*} would be flat.

With illustrative purposes, we show a sample of all these quantities in Fig. 4.7, again for the operator σ^x. On each panel, the histogram of distribution $p_{\omega,\omega^*}(t)$ is printed across-time, e.g. a vertical cut may contain an 80% of blue ($\omega = 1$), meaning that $p_{1,\omega^*}(t_{\mathrm{cut}}) = 0.8$. Such a representation allows us to understand the evolution of the relative relevance of the different subspaces contributing to the observable. The panels correspond to the unitary evolution of states $|0,0\rangle$ and $|\frac{9\pi}{10},0\rangle$, with the same Hamiltonian that has been used throughout the sections. As insets we show the OWE on the left, and the distances for weights 2 (red), 4 (violet), 6 (darkgreen), 8 (cyan) and 10 (orange) on the right.

The difference between the upper panel and the lower one is again clear: state $|0,0\rangle$ requires much more PW, as already concluded in former sections, appreciably requiring strings of weight 10 before $|\mathrm{J}|t = 5$, while state $|\frac{9\pi}{10},0\rangle$ is dominated by $\omega = 1$, and tiny amplitude oscillations are added on top by heavier subspaces. The offset of $p_{\omega,12}(t)$ for both states is different, and this is due to the way the evolution generates contributing strings: while state $|0,0\rangle$ is completely orthogonal to σ^x at initial times, $|\frac{9\pi}{10},0\rangle$ is not, and components with $\omega = 2$ are quickly generated.

[4]Recall that the bond dimension of the projectors onto the subspace with PW ω scales as $\omega + 1$; in our simulations, we will restrict to $\omega^* = 12$ and short times. Nevertheless, the fact that the absolute distances approach to 0, as required by the condition $d_{\omega=L}(t) = 0$ ensures that this truncated estimation will be representative of the exact result.

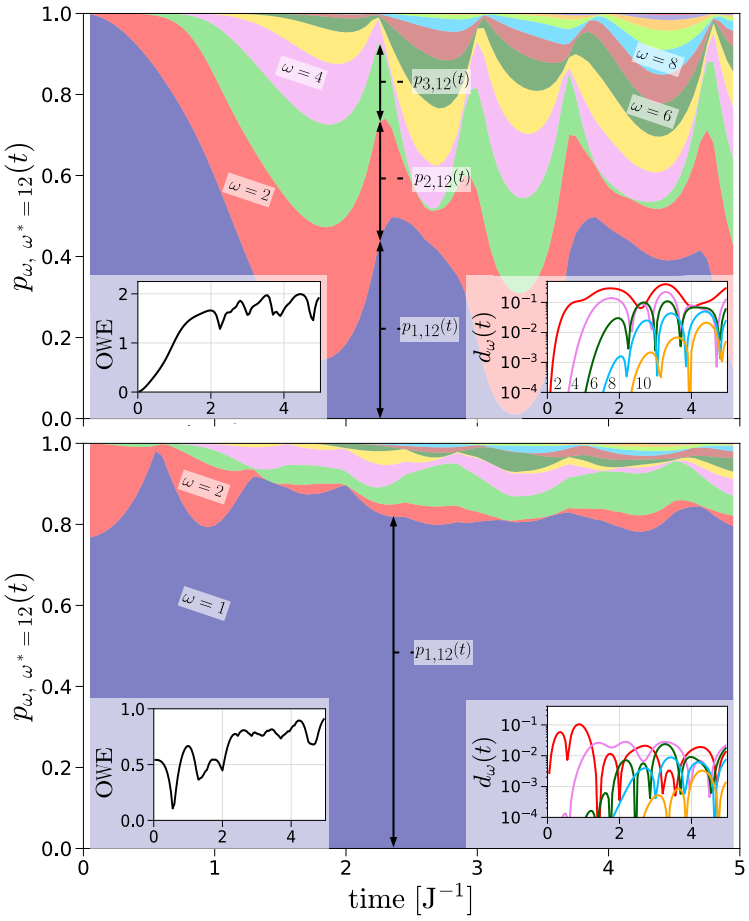

Figure 4.7: Evolution of the normalized distance distribution.The simulations were run for the non-integrable Ising model at $\{\mathrm{J} = -1,\ g = -1,\ h = -0.5\}$. The TEBD parameters were $L = 32$, $|\mathrm{J}|\delta t = 0.02$ and $\chi = 384$; errorbars correspond to the difference with simulations at half the maximal bond dimension $\chi' = \frac{\chi}{2}$.

The convergence to the exact observable as more and more PW is included in the accumulated sum of truncated observables is visible in the right insets, specially for state $|0, 0\rangle$. On the other hand, the OWE evolution for both states appears to be somewhere in between saturating and linearly growing, at least for the studied times; the difference between sizes points again towards the fact that the upper state is harder to simulate than the second.

No saturation to the maximum entropy $\log_2 12 \simeq 3.58$, marked by the maximal allowed resources, is reached in the simulated times. It is important to note that the OWE is a pessimistic measure for the PW required for given accuracies of expectation values, since it does not account for the potential cancellation between O_ω and $O_{\omega+1}$.

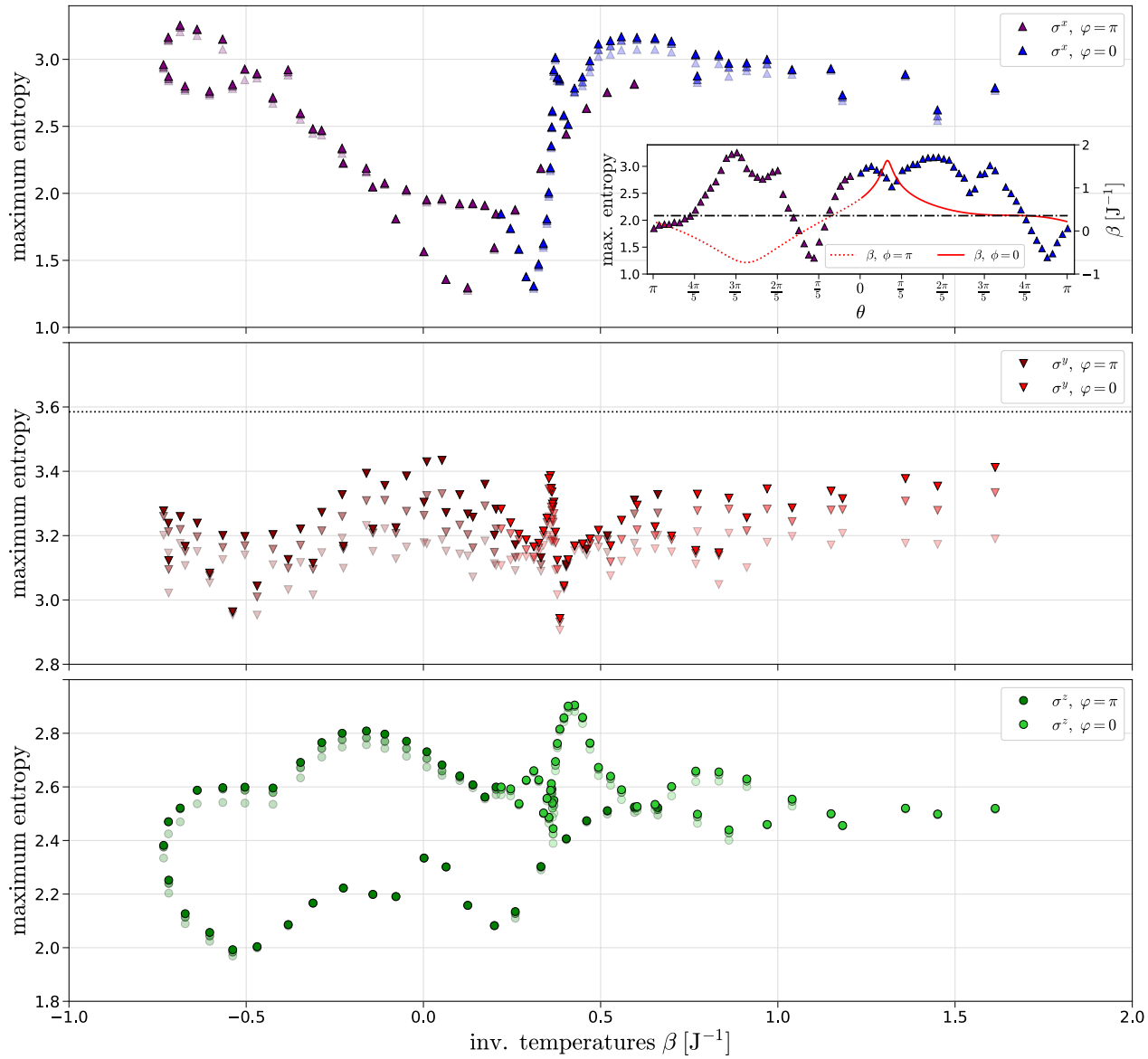

Figure 4.8: Maximum OWE in short time simulations for different combinations of operators and initial states. The simulations were run for the non-integrable Ising model at $\{J = -1,\ g = -1,\ h = -0.5\}$. The TEBD parameters were $L = 32$, $|J|\delta t = 0.02$ and $\chi = 384$; errorbars correspond to the difference with simulations at half the maximal bond dimension $\chi' = \frac{\chi}{2}$.

After this example, we are ready to carry out extensive simulations for several observables and states. In Fig. 4.8 we present the maximum OWE found in the time window [0, 5] in terms of the inverse temperature β to which the states are expected to relax. Calculations were carried for the three components of the spin magnetization, and were states sampled from a sagital cut of the Bloch sphere, containing $|0\rangle$, $|-\rangle$, $|1\rangle$ and $|+\rangle$.

In the first panel, the results for σ^x are also accompanied by an inset where the maximum OWE and the inverse temperatures are displayed versus the polar angle parameterizing the states. The blue markers correspond to initial states with positive $\langle\sigma^x(0)\rangle$, while purple markers correspond to negative $\langle\sigma^x(0)\rangle$. The 3 shades of each marker correspond to the calculations for $\omega^* = 10, 11$ and 12; when the shades collapse into a single marker, it means that the maximal bond dimension set in the simulations was able to properly represent the normalized distance distribution.

From this panel alone, it may look clear that the influence of temperature may not be decisive on the complexity of the simulation, at least for the short times that have been simulated. This can be seen by comparing the values of the maximum OWE on a vertical cut for different states. Nevertheless, the inset suggests that local minima of the maximum OWE occur near maxima of $|\beta|$, as it can be seen in the windows $[\frac{3\pi}{5}, \frac{2\pi}{5}]$ for $\varphi = \pi$ and $[0, \frac{\pi}{5}]$ for $\varphi = 0$. On top of this, we could loosely identify an inverse temperature region $[-0.5, 0.5]$ in the main panel where the maximum OWE drops.

The second panel contains the same results for σ^y, and signatures of the same drop in the maximum OWE are also visible in the inverse temperature window $[0, 0.5]$. Overall, this observable appears to be more difficult to predict by truncating Pauli weight, as the values of the OWE approach the upper bound allowed by our computational resources of 3.58 for almost all states. On top of this, convergence issues in ω are evidenced by the splitting of the three shades of the markers.

Finally, the third panel displays the results for σ^z, which also contains signatures of a complexity drop in the inverse temperature window $[0, 0.5]$. Opposed to σ^x, showing strong fluctuations in the maximum OWE, and σ^y, with high complexity for almost all states, σ^z shows an average complexity. It appears to be the easiest observable to be simulated.

The former result may be subject to changes upon prolongating to later times the simulations, and the use of different Hamiltonian points and models. The present results appear to indicate that temperature plays some role, but for the short times that have been simulated, potential transitory effects reflecting the geometry of the initial states may hide the true temperature dependence. If temperature would not be a defining factor, it would imply that in order to simulate long time observables, some initial states could be preferential due to their reduced complexity with respect to others lying on the same isothermal family in the Bloch sphere depicted at Fig. 2.3.

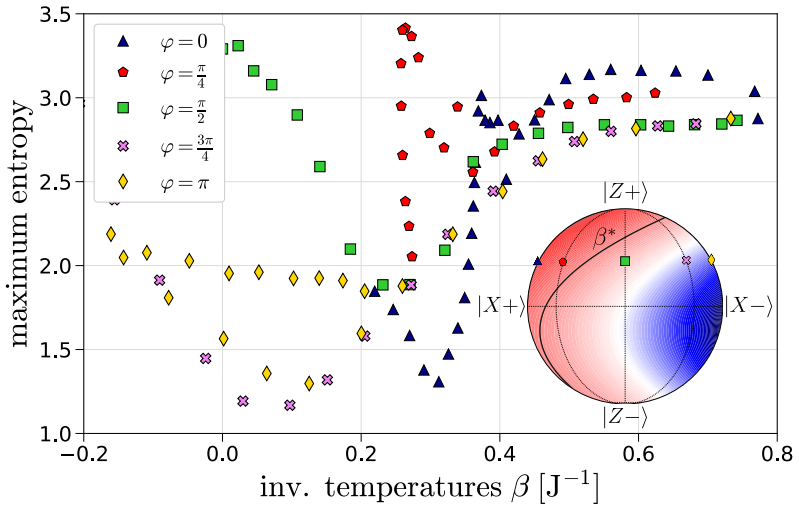

Figure 4.9: Maximal OWE complexity transition for σ^x. The simulations were run for the non-integrable Ising model at $\{\mathrm{J} = -1,\ g = -1,\ h = -0.5\}$. The TEBD parameters were $L = 32$, $|\mathrm{J}|\delta t = 0.02$ and $\chi = 384$; errorbars correspond to the difference with simulations at half the maximal bond dimension $\chi' = \frac{\chi}{2}$.

To conclude this section, we focus on the region where the complexity drop appears to occur, and simulate σ^x for states across other sagital cuts defined by $\varphi = 0,\ \frac{\pi}{4},\ \frac{\pi}{2},\ \frac{3\pi}{4},\ \pi$. In Fig. 4.9 we present the maximum OWE achieved in the time window $[0, 5]$ for these 5 families of states; as a guide to the eye, we plot the Bloch sphere as an inset with the 5 cuts (dotted black curves) containing $|0\rangle = |Z+\rangle$ and $|1\rangle = |Z-\rangle$ and the simulated states, together with the isothermal line (solid black curve) centered on the inverse temperature around which the drop appears to happen, $\beta^* \simeq 0.3|\mathrm{J}|^{-1}$.

Despite the short range of simulated times, it appears that β^* is associated with strong derivatives in the maximum OWE. Nevertheless, it is also visible that different states with equal temperatures reach different maximal OWEs; therefore we can not rule out the fact that the geometry of the states is a defining factor of the complexity of the simulation of σ^x for such states beyond their equilibration temperature. On top of that, it is unclear whether such a *transition* also occurs for the rest of observables. These results are subject to change upon further research in the long time regime.

4.3 Decoherence Assisted Operator Evolution.

In the former section we found evidence that the truncation of orthogonal PW could accurately generalize DAOE to initial PS, and we found a prescription for it in terms of the basis which diagonalizes a particular state. In this section, we implement the algorithm and test it, finding a definitive answer on the role of equilibration temperature on the Pauli Weight requirement of matrix elements of evolving local operators.

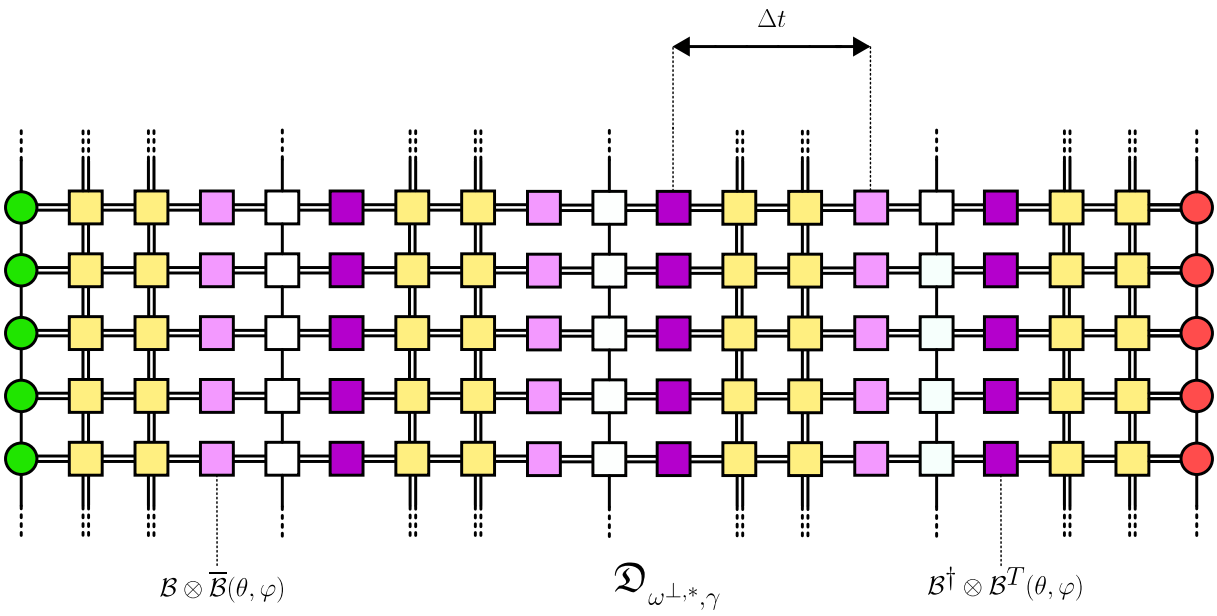

Figure 4.10: DecoAOE: truncating orthogonal PW. The 2D TN representing the folded dynamics is modified by introducing local rotations that set the operators into the parallel basis specified by the initial state, followed by the dissipation of the off-diagonals beyond $\omega^{\perp,*}$. This procedure is repeated with period Δt, and it is equivalent to generalized decoherence in the parallel magnetization basis.

4.3.1 Description of the method.

The structure of the algorithm is the same as the DAOE introduced in Sec. 4.1. This allows us to focus on the particularities of our modification in order to make it work for initial PS with arbitrary equilibration temperatures:

- In first place, the dissipator only eliminates strings with *too many mistakes*, i.e. it dissipates according to the orthogonal PW. As we explained in the former section, the elimination of $\omega^{\perp}$ is completely equivalent to the generalized decoherence of Ch. 2, $\sum_{m=0}^{n} \mathcal{C}_m \mathcal{F}_m$. This motivates us to dub our modification of the algorithm as DecoAOE, as a counterpart of DAOE, which should be rather called DepolAOE, since it corresponds to a generalized depolarization protocol eliminating any Pauli operator for strings with PW higher than ω^*. To see this last point clearly, recall Eq. 4.15: by setting $p^\alpha = \frac{1}{3}$, DAOE corresponds to a generalized depolarization scheme with a decay $\frac{\gamma}{3}$.

The MPO representing the dissipator $\mathfrak{D}_{\omega^\perp,\gamma}$ becomes:

$$W_{\mathfrak{D}}^{i_\ell \neq i_1, i_L} = \begin{pmatrix} \mathcal{P}_{\rm c}^{(1)} & \mathcal{P}_{\rm nc}^{(1)} & 0 & \cdots & 0 & 0 & 0 \\ 0 & \mathcal{P}_{\rm c}^{(1)} & \mathcal{P}_{\rm nc}^{(1)} & \cdots & 0 & 0 & 0 \\ 0 & 0 & \mathcal{P}_{\rm c}^{(1)} & \cdots & 0 & 0 & 0 \\ \vdots & \vdots & \vdots & \ddots & \vdots & \vdots & \vdots \\ 0 & 0 & 0 & \cdots & \mathcal{P}_{\rm c}^{(1)} & \mathcal{P}_{\rm c}^{(1)} & 0 \\ 0 & 0 & 0 & \cdots & 0 & \mathcal{P}_{\rm c}^{(1)} & \mathcal{P}_{\rm nc}^{(1)} \\ 0 & 0 & 0 & \cdots & 0 & 0 & \mathcal{P}_{\rm c}^{(1)} + e^{-\gamma}\mathcal{P}_{\rm nc}^{(1)} \end{pmatrix},$$

$$W_{\mathfrak{D}}^{i_1} = \begin{pmatrix} \mathcal{P}_{\rm c}^{(1)} & \mathcal{P}_{\rm nc}^{(1)} & 0 & \cdots & 0 & 0 & 0 \end{pmatrix}, \qquad W_{\mathfrak{D}}^{i_L} = \begin{pmatrix} \mathbb{1}_4 \\ \mathbb{1}_4 \\ \mathbb{1}_4 \\ \vdots \\ \mathbb{1}_4 \\ \mathbb{1}_4 \\ \mathcal{P}_{\rm c}^{(1)} + e^{-\gamma}\mathcal{P}_{\rm nc}^{(1)} \end{pmatrix}, \tag{4.24}$$

- The dissipation is performed in the basis $\mathcal{B}(\theta, \varphi)$ in which the local magnetization of the initial state is diagonal, so we introduce the appropriate rotations before and after the dissipator $\mathfrak{D}_{\omega^\perp,\gamma}$. The resulting 2D TN is depicted in Fig. 4.10.

- The reader could think that contracting the new network à la Schrödinger could also lead us to nice results, but there are small nuances that complicate that: in Ch. 2, the total decoherence was performed in the basis in which the coherence until $n = \omega^\perp$ spin-flips were diagonal, while generalized decoherence was performed without requiring rotation. These two styles tried to guarantee that several few-spin observables were saved from erasure.

  In particular, performing any decoherence in a basis diagonalizing the evolving local magnetization would preserve only the 3 components of the single-spin magnetization[5]. Therefore the protocol would bias the truncated density matrix to only represent correctly 1-spin-observables.

  Opposed to that, DecoAOE is acting on an operator taking a particular PS as a reference; as such, the rotation is not time dependent, and the Heisenberg evolution is biased to represent the overlap with just one state.

[5]This protocol would require finding the local observables at every step in time, and using them to determine the rotation that aligns with the running magnetization, which at least would protect the 1-spin-rdms from the dissipation.

Short after we devised this protocol and tested it, other group came up with the same idea of eliminating orthogonal PW, but they formulated their protocol by saving in memory a subset of the string components of the basis and solving the truncated hierarchy of equations of motion (Begušić and Chan (2025)). These Pauli-path methods have been proven to be able to simulate efficiently expectation values of unitary (Angrisani et al. (2024)) and noisy (Angrisani et al. (2025)) quantum circuits in arbitrary topologies.

4.3.2 Testing the method.

In this section we test the different hyperparameters that can be tuned in DecoAOE. As a first test, we compare the simulation of different local observables, $\sigma^{x,y,z}$ and the energy density in the middle of the chain for the normal Heisenebrg TEBD and DecoAOE.

In Fig. 4.11 we compare simulations for expectation values with the state $|0,0\rangle$. The fixed parameters of the simulation are $L = 32$, $|\mathrm{J}|\delta t = 0.1$, $\chi = 512$ (and errorbars for the difference with $\chi' = \frac{\chi}{2}$), decoherence period $|\mathrm{J}|\Delta t = 1$ and orthogonal PW threshold $\omega^{\perp} = 2$. We try two dissipation strengths, $\gamma = 0.1$ and 0.5. As a reference to the eye, the thermal values (obtained through Eq. 2.22 and converged for size $L = 10$) to which each observable should relax are included as solid horizontal black lines.

The results are coherent with our expectations: while the $\gamma = 0$ case (normal TEBD) struggles to converge with finite bond dimension (note the size of the errobars after time $|\mathrm{J}|t = 10$), the DecoAOE converges much faster in bond dimension, achieving smaller errorbars for stronger dissipation (error$_{\gamma=0}$>error$_{\gamma=0.1}$>error$_{\gamma=0.5}$). Nevertheless, the stronger the dissipation is, the more biased is the simulation towards a damped oscillation. The striking result is that even with the extra damping, the oscillations still occurs on top of the thermal values ($\sigma^{x,y}$ and $h_{\frac{L}{2},\frac{L}{2}+1}$), or stays close ($\sigma^{z}$) despite the low orthogonal PW threshold fixed for the simulations.

This result again means that thermal values are built soon in the Heisenberg picture, requiring only small amounts of orthogonal PW, pushing the complexity of the simulation towards determining the right fluctuations on top of it. As we analyzed in the former sections, these fluctuations originate from heavy strings, which we damp out through decoherence. In Sec. 4.4 we will analyze the spatial structure of the observable light-cone more closely, and we will find that these heavy strings inducing the oscillations (and therefore encoding the spectral quantities) actually live in the limit of the light-cone.

It is important to realize that these instances of DecoAOE, despite preserving the energy (see the fourth panel in Fig. 4.11), are still not accurate enough to encode the full dynamics. Most of the methods devised for TNs make a big emphasis on preserving the energy and other conserved quantities in presence of symmetries, but this is an example of a method where ensuring conservation laws is not a guarantee of accuracy (see the green solid line for $\gamma = 0.5$).

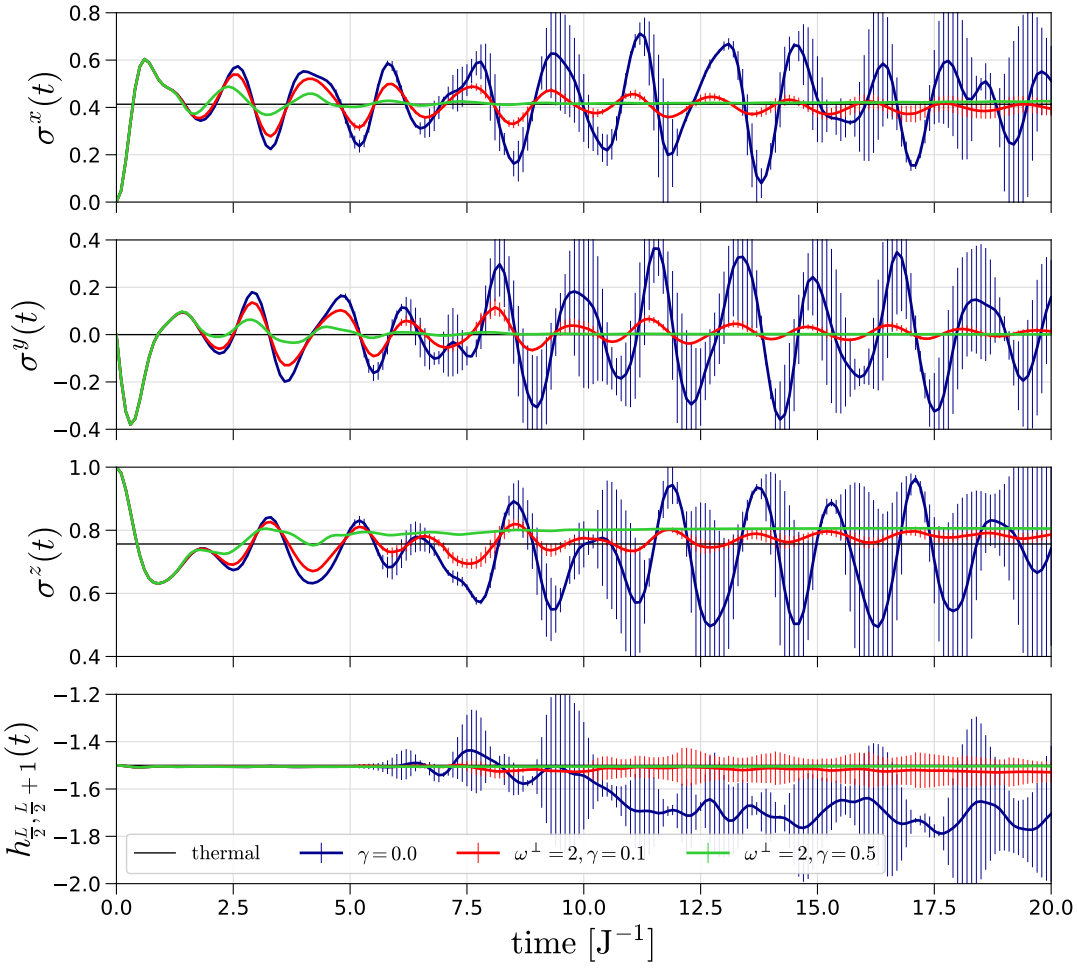

Figure 4.11: Heisenberg picture TEBD vs DecoAOE with varying dissipation strength. The simulations were run for $L = 32$, $|\mathrm{J}|\delta t = 0.1$, $\chi = 512$ (with errorbars for the difference with $\chi' = \frac{\chi}{2}$), decoherence period $|\mathrm{J}|\Delta t = 1$ and orthogonal PW threshold $\omega^\perp = 2$. The change of the dissipation intensity interpolates between the normal TEBD ($\gamma = 0$, solid blue lines) and the decoherence assisted simulations. The thermal values for each observable are included as a guide to the eye.

In Fig. 4.12 we present the different measures of error used in TEBD: the OSEE and the norm. It is clear that the later is not a proper measure of error, since most of the norm is in orthogonal subspaces, as seen in Sec. 4.2. Normal TEBD eliminates norm without paying attention to the subspaces being altered, while DecoAOE prunes the non-contributing norm; as it can be appreciated in the right column, the long-term norms for $\gamma = 0.1$ and 0.5 converge to the same curve, upper-bounded by the classical TEBD truncation.

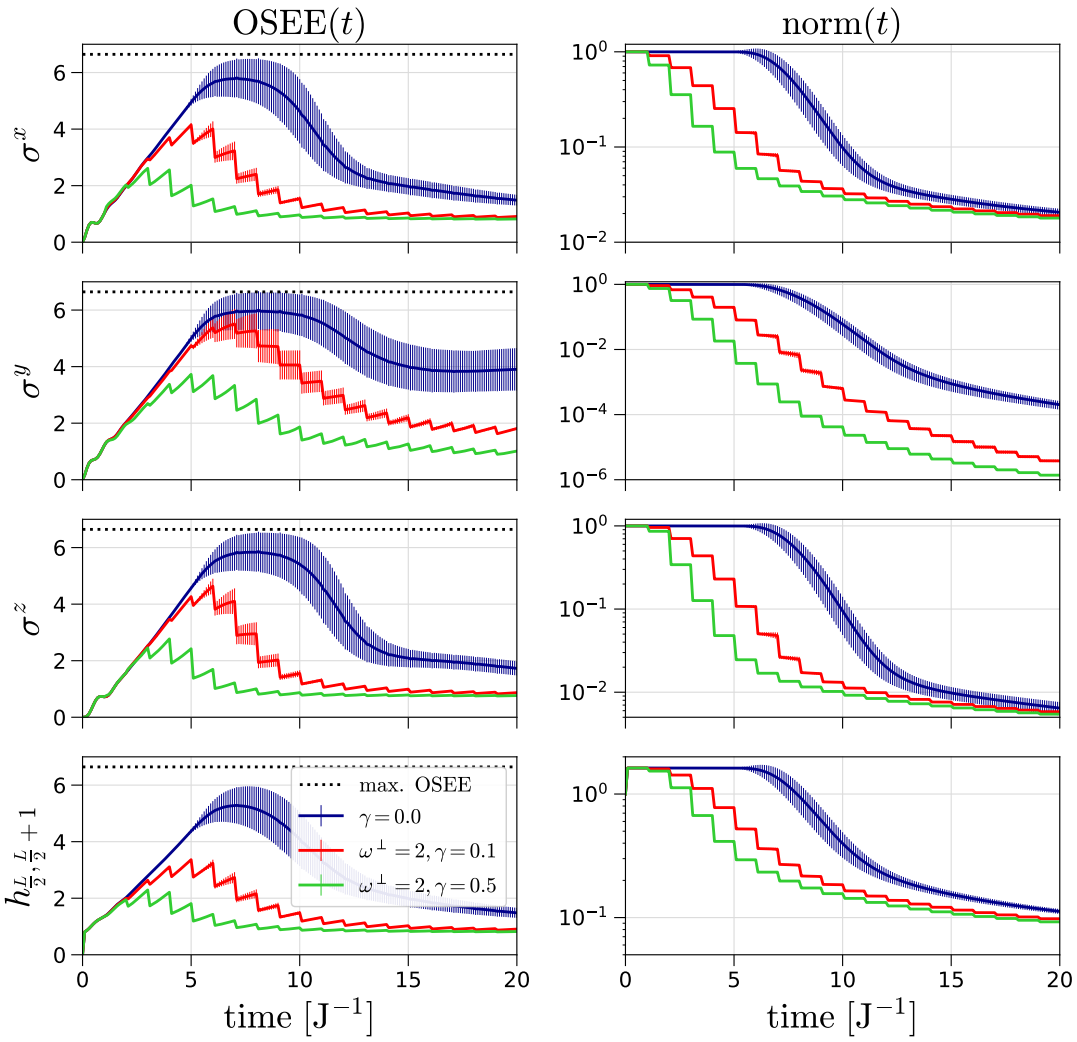

Figure 4.12: Heisenberg picture TEBD vs DecoAOE with varying dissipation strength: error measures. The simulations were run for $L = 32$, $|\mathrm{J}|\delta t = 0.1$, $\chi = 512$ (with errorbars for the difference with $\chi' = \frac{\chi}{2}$), decoherence period $|\mathrm{J}|\Delta t = 1$ and orthogonal PW threshold $\omega^{\perp} = 2$.

On the other hand, we already saw in Sec. 4.2 that the OSEE of the contributing superpositions appeared to fulfill an area law, so we expect that DecoAOE will converge OSEE to that area law value for any dissipation. Once again, the OSEE allowed by normal TEBD is above the DecoAOE one, but it does not necessarily represent the contributing subspaces faithfully.

In Fig. 4.13 we move towards tuning other hyperparameters. In the first panel we simulate σ^x for $|0, 0\rangle$ with fixed $L = 32$, $|\mathrm{J}|\delta t = 0.1$, $\chi = 512$, and $\omega^{\perp} = 2$, but we vary the decoherence period $|\mathrm{J}|\Delta t$ =1, 1.5, 2. As a reference, we compare the results with a converged simulation of the transverse light-cone algorithm with reflection-symmetric truncation introduced in Sec. 2.2.4.3; we assume that this algorithm is accurate and converged with $\chi = 256$ for all the simulated times.

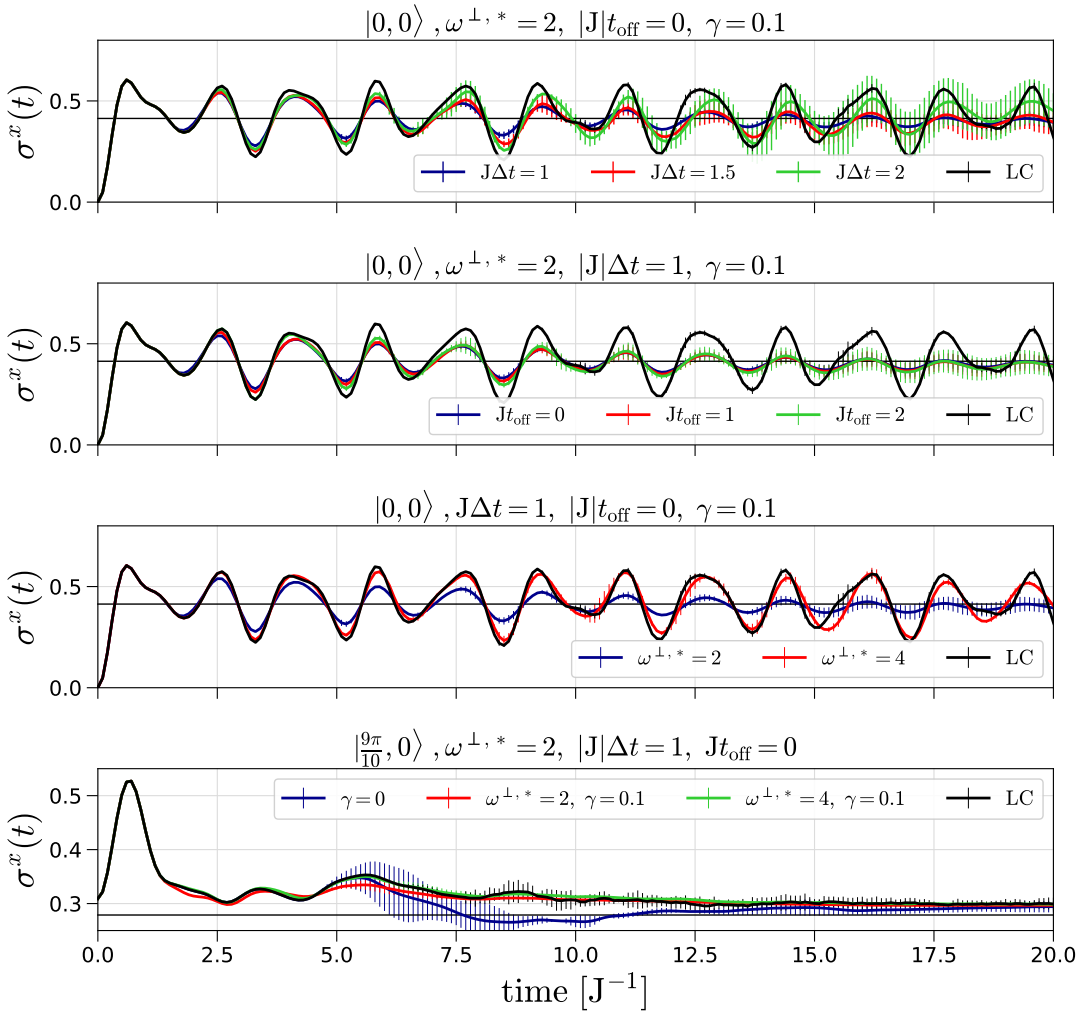

Figure 4.13: Tuning the hyperparameters of DecoAOE.. The simulations were run for $L = 32$, $|\mathrm{J}|\delta t = 0.1$, $\chi = 512$ (with errorbars for the difference with $\chi' = \frac{\chi}{2}$). The decoherence period $|\mathrm{J}|\Delta t = 1$ is varied on the first panel, the offset for decoherence in the second, and the orthogonal PW threshold $\omega^{\perp} = 2$ in the third for the operator and state combination σ^x and $|0,0\rangle$. The fourth panel proves that σ^x is simpler to simulate for $|\frac{9\pi}{10},0\rangle$.

The effect of this hyperparameter shows an interesting interplay: while shorter periods damp the oscillations more and accelerate convergence with bond dimension, longer periods delay convergence but do not show oscillations completely uncorrelated with the light-cone ones, as normal TEBD did in Fig. 4.11.

Another hyperparameter to be tuned is the offset time of dissipation: since we concluded that thermal values are settled at short times, probably starting the decoherence later will help the oscillation centering around the right value. This is indeed the case, and the increasing error bars are associated to lower decoherence frequencies.

The last hyperparameter which could be tuned is the orthogonal PW threshold. By increasing the value to $\omega^{\perp,*} = 4$ the results improve substantially as compared to the light-cone predictions. This was to be expected, since the limit $\omega^{\perp,*} \to L$ corresponds to the exact dynamics up to trotterization and truncation errors, but it is important to note that this intermediate dissipation regime converges fast to almost the correct oscillations, without drifting like normal TEBD.

Finally, we try our method for the *simple state* in terms of PW requirements from short times, $|\frac{9\pi}{10}, 0\rangle$. The reason why this state is simpler to simulate is now evident to bare eye: heavy strings hindering the simulation barely impact in the dynamics, i.e. no big amplitude oscillations are expected. Instead, a slowly relaxing behavior towards the thermal value occurs for all the simulations. It is interesting how the different DecoAOE simulations and light-cone predictions collapse together, while TEBD detaches between times 5 and 15. In this case, it seems that normal TEBD fails to predict the transitory dynamics but not the asymptotic one.

As a last check, it can be clarifying to apply the orthogonal PW truncation in the Schrödinger picture (removing the rotations!); this should amount to generalized decoherence as in Ch. 2. We report the results in Fig. 4.14 for the same numerical parameters, operators and state that we have used in Fig. 4.12.

In this case, despite the truncation threshold is the same $\omega^{\perp,*} = n = 2$, the results are not that good as in the Heisenberg picture. In fact, normal TEBD performs surprisingly well for σ^y, and slightly detaches from the light-cone results for $\sigma^{x,z}$; in contrast, TEBD rapidly breaks the preservation of the energy. These results are in contrast with the $\gamma > 0$ simulations, that fail to even approach the thermal values for the local observables, but manage to preserve the energy even with more ease than the light-cone predictions.

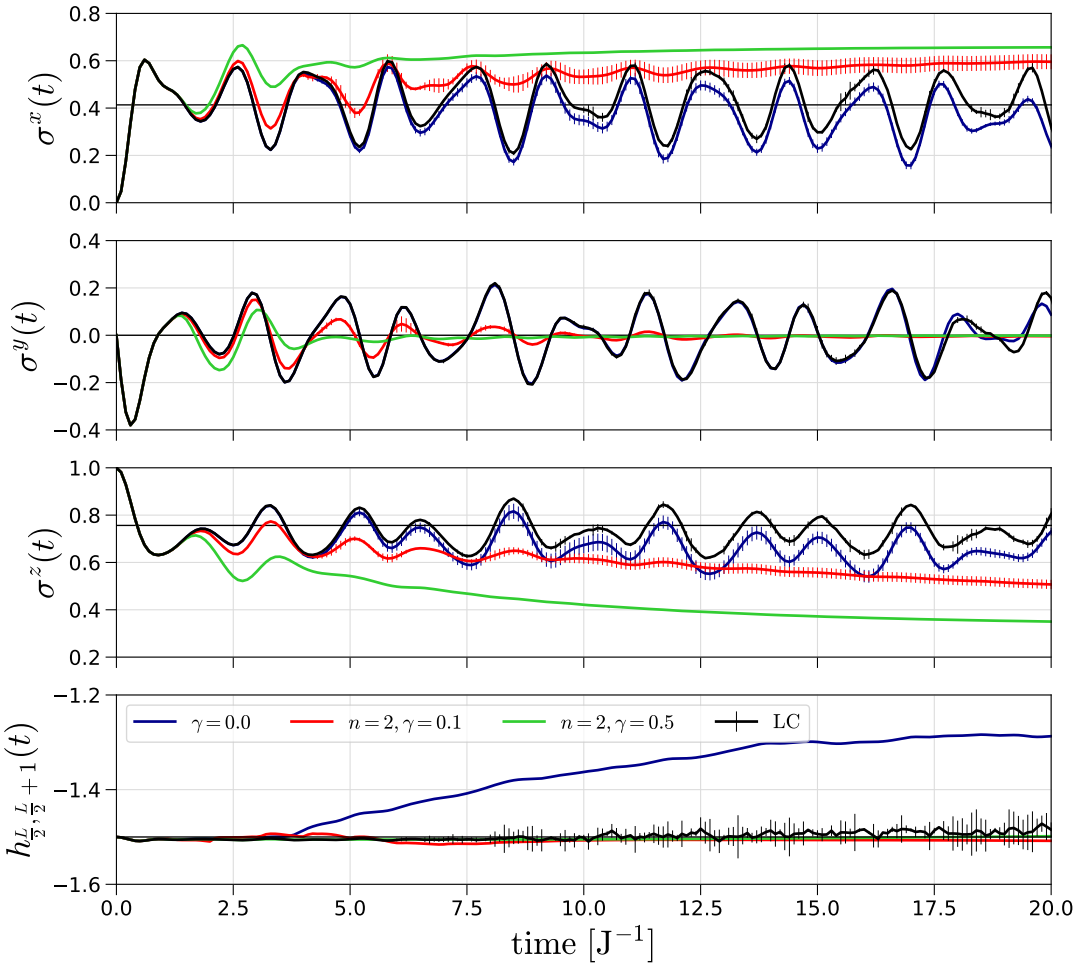

Figure 4.14: Schrödinger picture folded TEBD vs DecoAOE with varying dissipation strength. The simulations were run for $L = 32$, $|\mathrm{J}|\delta t = 0.1$, $\chi = 768$ (with errorbars for the difference with $\chi' = 512$), decoherence period $|\mathrm{J}|\Delta t = 1$ and orthogonal PW threshold $\omega^{\perp} = 2$. The change of the dissipation intensity interpolates between the normal TEBD ($\gamma = 0$, solid blue lines) and the decoherence assisted simulations. The thermal values for each observable are included as a guide to the eye.

Finally, we take a look at the *visible* sources of error of the Schrödinger picture DecoAOE simulations in Fig. 4.15. In this case, the quantity over which TEBD-style truncation occurs is the purity, as explained in Sec. 2.2.5, so we can see in the first panel how P is approximately preserved for times between generalized decoherences. As expected, the state norm, depicted in the second panel, does not necessarily follow the same trend as the purity in the intervals between dissipations.

The third and fourth panels evidence the errors of truncation; these results have been teased many times through indirect measures and discussions throughout the whole chapter, but here we present some quantitative results: for the transverse magnetization, at a given step when the dissipator is applied, we can check the expectation values *After the Unitary Evolution* layers (AUE), *After Truncating After the Unitarily Evolved* MPS (ATAUE), *After Generalized Decoherence* (AGD) and *After Truncating After Generalized Decoherence* (ATAGD). The expectation values after each of these intermediate steps of the algorithm are shown in the inset.

It can be clearly seen how finite jumps in the value occur only when truncation happens, and not after the dissipator is applied. This is a sanity check ensuring that the dissipator is well-coded, and that orthogonal PW truncation works in the way we are expecting. As a conclusion, the main issue with DecoAOE is the truncation itself performed after the dissipation.

The same impression can be made out of the fourth panel, where at each step in time of the energy presents visible jumps. This means that, despite DecoAOE destroys only non-contributing subspaces, after the application of the dissipator, contributing strings may descend down to the queue of singular values to be truncated. In future extensions of this work, it could be interesting to explore how to merge the DecoAOE with the Density Matrix Truncation (DMT) from *White et al.* (White et al. (2018)), where they merge the *dissipation* step with truncation in order to preserve the reduced density matrices of few neighboring spins.

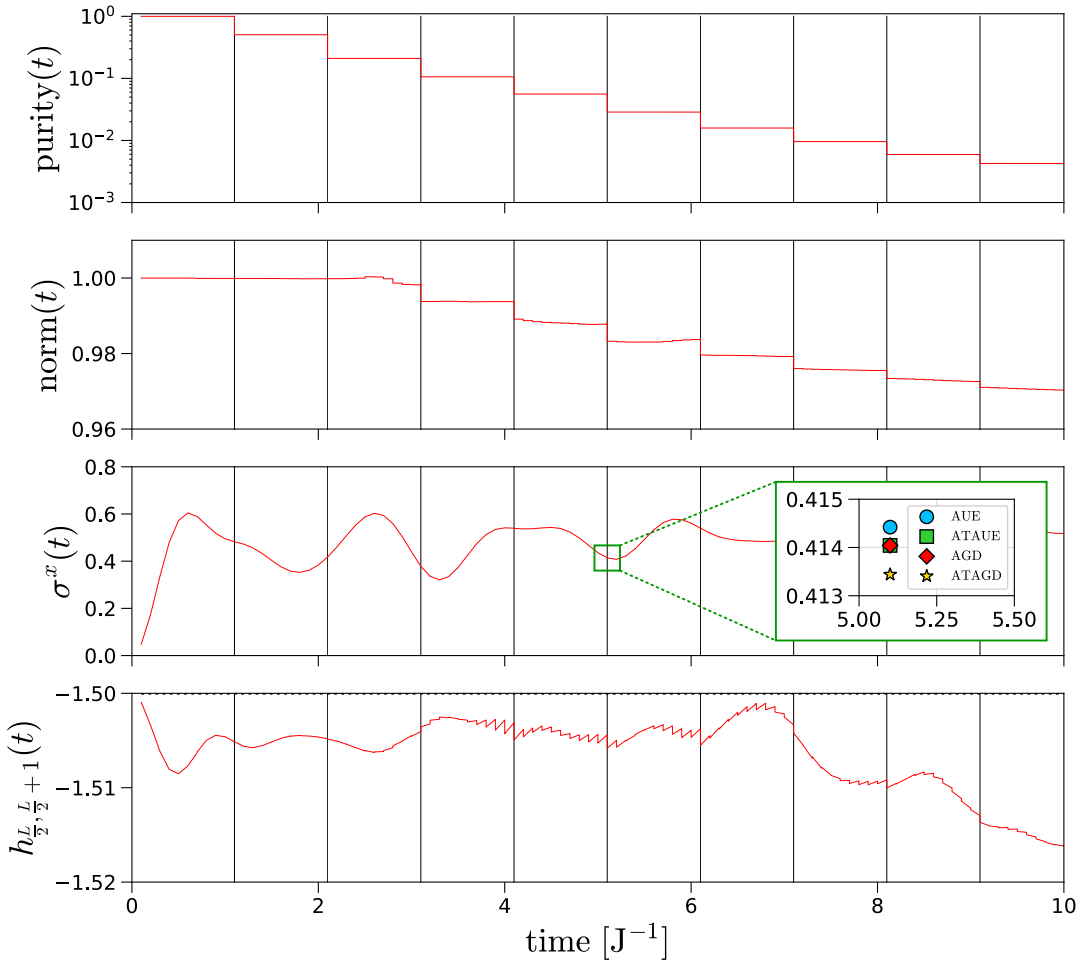

Figure 4.15: Usual Schrödinger picture folded TEBD vs DecoAOE with varying dissipation strength: error measures. The simulations were run for $L = 32$, $|\mathrm{J}|\delta t = 0.1$, $\chi = 768$, decoherence period $|\mathrm{J}|\Delta t = 1$, orthogonal PW threshold $\omega^{\perp} = 2$ and decoherence intensity $\gamma = 0.1$. The discontinuities in the observables, norm and purity of the evolving density matrix are evident upon zooming.

4.3.3 Long Time Simulation of Observables for States on Isothermal Families.

A proper benchmark for DecoAOE can be to compare its results for *good enough* hyperparameters with other converged methods. As we have already teased in the former section, the light-cone algorithm with symmetric truncation, studied in depth in Ch. 5, appears to converge much faster in bond dimension than classical Schrödinger/Heisenberg picture TEBD. Despite that, it is unclear whether the method biases the predictions or not; therefore, comparing DecoAOE and the light-cone algorithm would validate both, if they coincided *enough* on their predictions.

On top of that, this section is openly multipurpose, since we do not only seek to validate DecoAOE and the symmetrically truncated light-cone, but also answer for once and for all whether equilibration temperature of initial states is a complexity factor in terms of the amount of PS needed to accurately describe local dynamics.

With all these goals in mind, in this section we simulate the dynamics of σ^x for our favorite Ising Hamiltonian at the challenging point $\{\mathrm{J}=-1,\ g=-1,\ h=-0.5\}$ until $|\mathrm{J}|t=20$ for different initial states sharing the same energy density (or conversely, equilibration temperature). In the following we pick states lying in the intersection between an isothermal line in the Bloch sphere, defined by $\beta(\theta,\varphi)=\mathrm{const}$, and the sagital cuts $\varphi\in\{0,\ \frac{\pi}{4},\ \frac{\pi}{2},\ \frac{3\pi}{4},\ \pi\}$. The selected energy densities are $E\in\{-1.5|\mathrm{J}|,-|\mathrm{J}|,-0.5|\mathrm{J}|,0,+0.5|\mathrm{J}|,+|\mathrm{J}|\}$, and the corresponding equilibration temperatures are $\beta=\{0.75|\mathrm{J}|^{-1},0.43|\mathrm{J}|^{-1},0.21|\mathrm{J}|^{-1},0,-0.25|\mathrm{J}|^{-1},-0.7|\mathrm{J}|^{-1}\}$.

In the same style as in Ch. 3.4.2, we will compute the time averaged difference between the predictions of both methods

$$\langle\varepsilon(\sigma^\alpha)\rangle_t=\frac{1}{t}\int_0^t|\sigma^\alpha_{\mathrm{LC}}(s)-\sigma^\alpha_{\mathrm{DecoAOE}}(s)|\,ds=\frac{1}{n_{\mathrm{steps}}}\sum_{m=0}^{n_{\mathrm{steps}}}|\sigma^\alpha_{\mathrm{LC}}(m\delta t)-\sigma^\alpha_{\mathrm{DecoAOE}}(m\delta t)|. \tag{4.25}$$

This quantity contains two types of information: (1) if its value is small (say $\mathcal{O}(10^-2)$) we can safely conclude that both methods yield proper results up to their respective truncations; (2) if there is a clear trend of $\langle\varepsilon(\sigma^\alpha)\rangle_t$ with β independent of φ, then we can infer that equilibration temperature is determining in the PW requirement (and thus complexity) for simulating local expectation values until long times.

The results are gathered as follows: Figs. 4.16, 4.17, 4.18, 4.19, 4.20, 4.21 contain the simulations for all states matching the aforementioned conditions, and Fig. 4.22 summarize the average deviations $\langle\varepsilon(\sigma^\alpha)\rangle_t$ for all simulated states and temperatures.

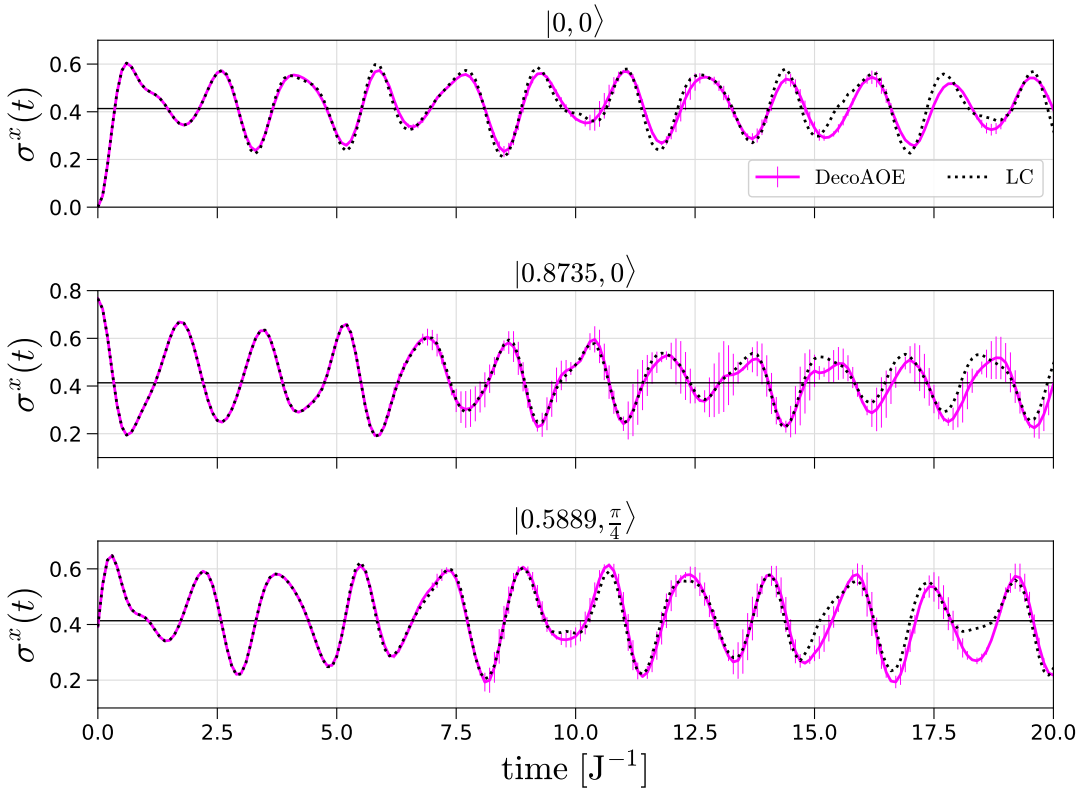

Figure 4.16: DecoAOE for $E=-1.5|\mathrm{J}|$ ($T=1.33|\mathrm{J}|^{-1}$). The first isothermal family is the one with lowest temperatures (in absolute value). This family contains the famously hard state $|0,0\rangle$ (first panel), and two siblings, equally (or more) complicated to converge in bond dimension. All the states in this family display persistent oscillations around the equilibrium magnetization $\langle\sigma^x(\beta)\rangle=0.41$, both for DecoAOE ($L=64$, $|\mathrm{J}|\delta t=0.1$, $\omega^*=4$, $|\mathrm{J}|\Delta t=1$, $\gamma=0.1$, $\chi=768$ and $\chi'=512$) and light-cone ($|\mathrm{J}|\delta t=0.1$ and $\chi=256$) algorithms. Despite the bond dimension is quite high, DecoAOE still has problems to converge for the second state, despite the error bars are overall small; both methods agree to a good extent until times ~ 15, when deviations start to take off.

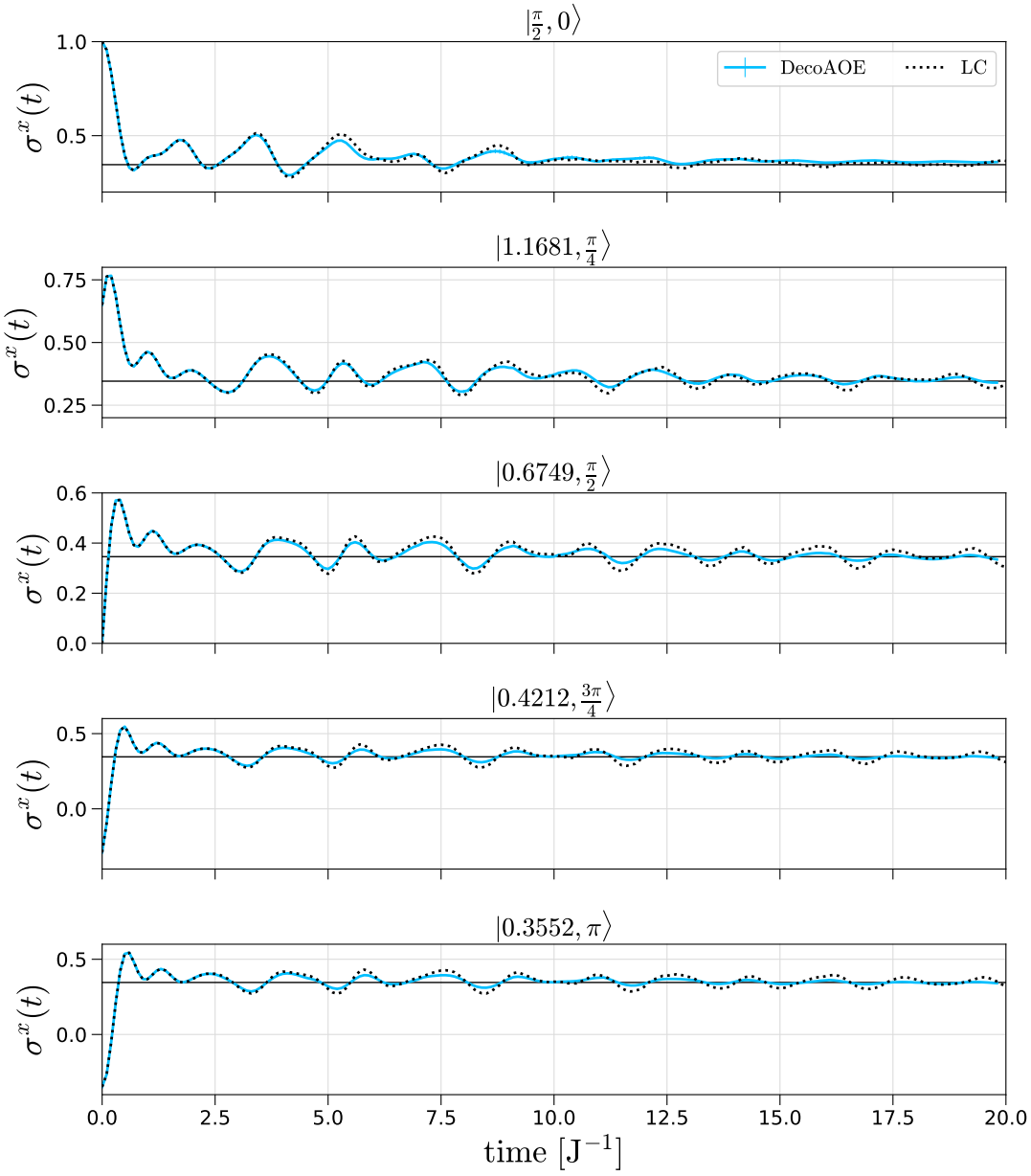

Figure 4.17: DecoAOE for $E = -|\mathrm{J}|$ ($T = 2.34|\mathrm{J}|^{-1}$). The second isothermal family is more numerous, and contains the state $|\frac{\pi}{2}, 0\rangle = |X+\rangle = |+\rangle$ (first panel). All the states in this family display persistent, lower-amplitude oscillations around the equilibrium magnetization $\langle\sigma^x(\beta)\rangle = 0.35$, both for DecoAOE ($L = 64$, $|\mathrm{J}|\delta t = 0.1$, $\omega^* = 4$, $|\mathrm{J}|\Delta t = 1$, $\gamma = 0.1$, $\chi = 768$ and $\chi' = 512$) and light-cone ($|\mathrm{J}|\delta t = 0.1$ and $\chi = 256$) algorithms. In this case, DecoAOE bond dimension convergence is much faster (as formerly predicted for lower amplitude oscillations), and both methods agree well; the main deviations are slight dampings with respect to the full amplitudes achieved by the light-cone algorithm.

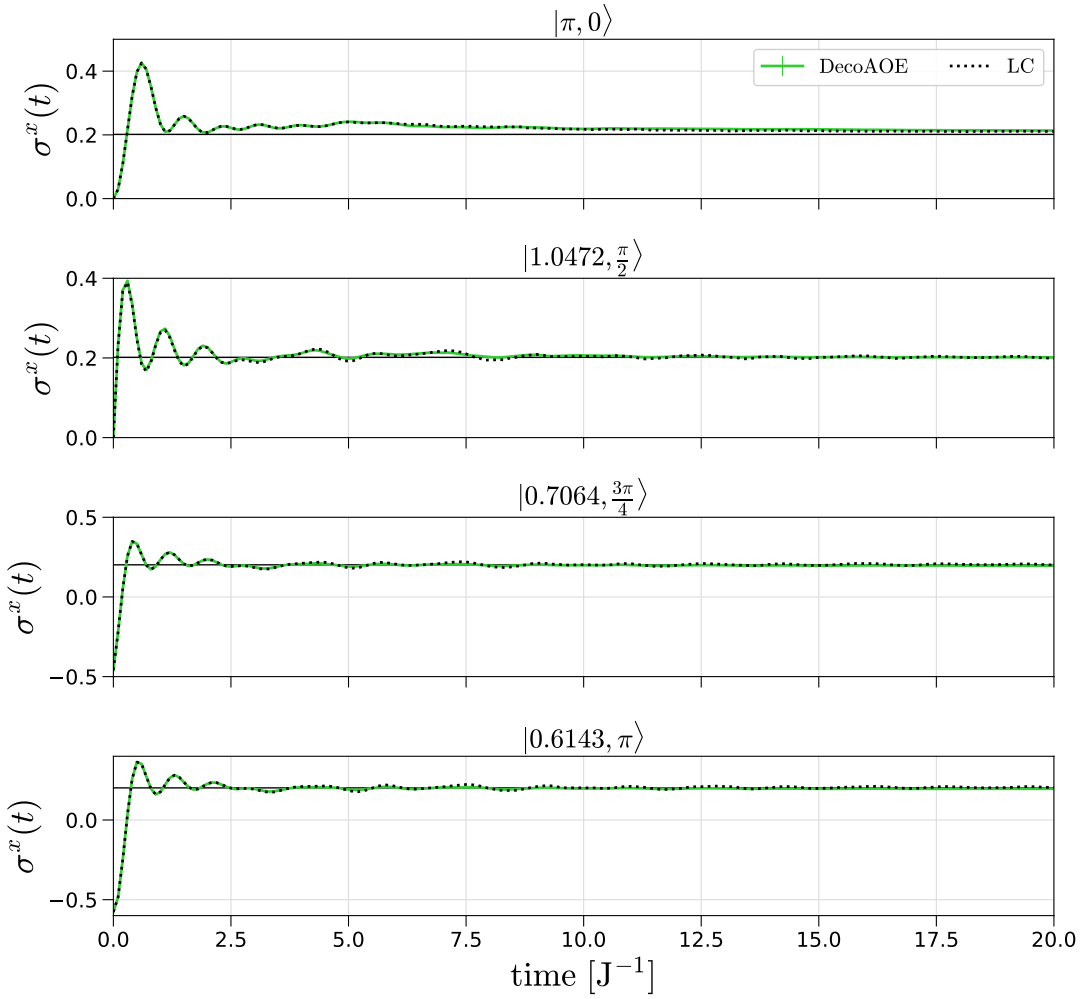

Figure 4.18: DecoAOE for $E = -0.5|\mathrm{J}|$ ($T = 4.71|\mathrm{J}|^{-1}$). The third isothermal family contains the state $|\pi, 0\rangle = |Z-\rangle = |1\rangle$ (first panel). Almost null amplitude oscillations occur on top of the equilibrium magnetization $\langle\sigma^x(\beta)\rangle = 0.2$, both for DecoAOE ($L = 64$, $|\mathrm{J}|\delta t = 0.1$, $\omega^* = 4$, $|\mathrm{J}|\Delta t = 1$, $\gamma = 0.1$, $\chi = 768$ and $\chi' = 512$) and light-cone ($|\mathrm{J}|\delta t = 0.1$ and $\chi = 256$) algorithms. Once more, DecoAOE bond dimension convergence is practically exact, and both methods agree well.

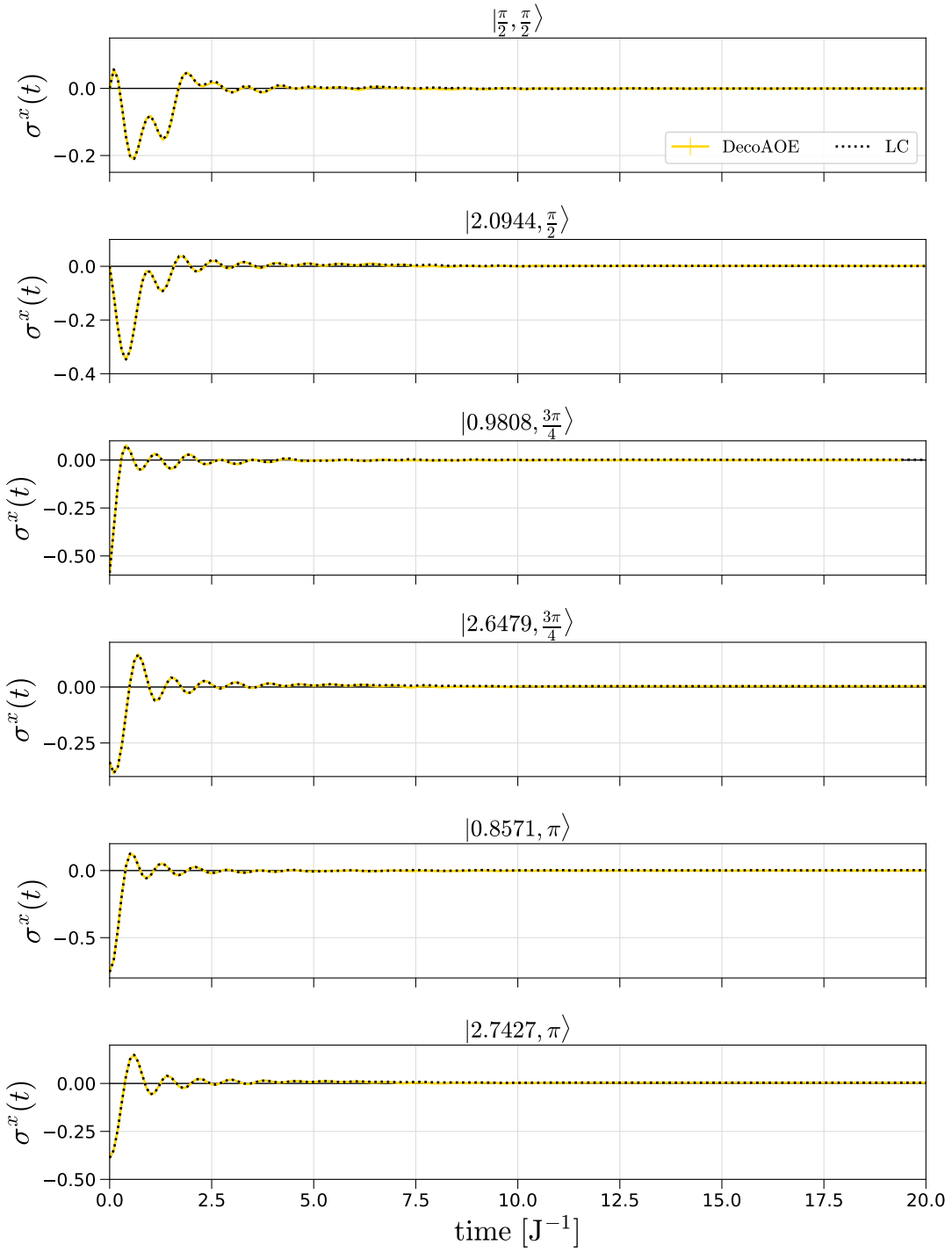

Figure 4.19: DecoAOE for $E = 0$ ($T = \pm\infty$). The fourth isothermal family is more numerous, and contains the state $|\frac{\pi}{2}, \frac{\pi}{2}\rangle = |Y+\rangle = |R\rangle$ (first panel). All the states in this family display fast damping oscillations to the equilibrium magnetization $\langle\sigma^x(\beta)\rangle = 0$, both for DecoAOE ($L = 64$, $|\mathrm{J}|\delta t = 0.1$, $\omega^* = 4$, $|\mathrm{J}|\Delta t = 1$, $\gamma = 0.1$, $\chi = 768$ and $\chi' = 512$) and light-cone ($|\mathrm{J}|\delta t = 0.1$ and $\chi = 256$) algorithms. DecoAOE bond dimension convergence exact.

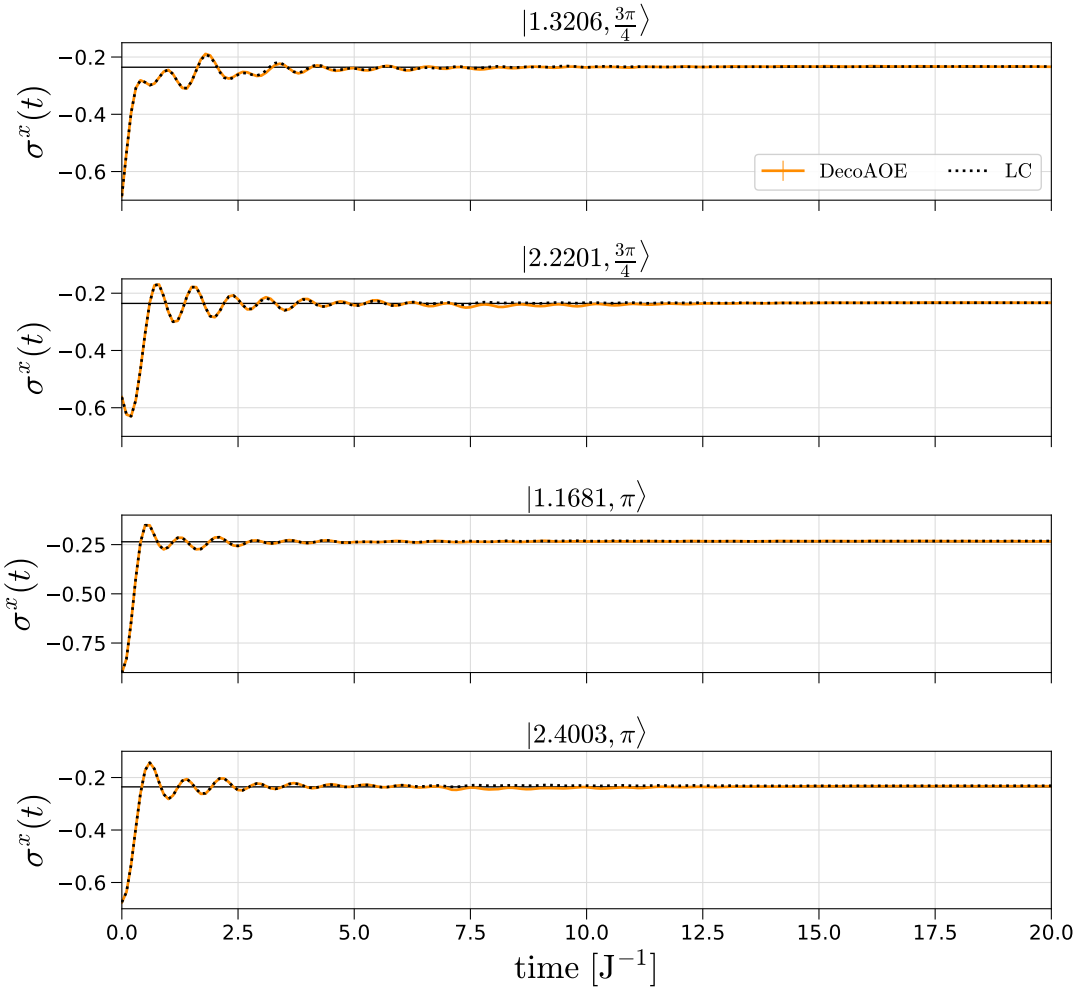

Figure 4.20: DecoAOE for $E = +|\mathrm{J}|$ ($T = -4|\mathrm{J}|^{-1}$). The fifth isothermal family does not contain any well-known state, but it is our first instance for negative temperatures. Low-amplitude oscillations around the equilibrium magnetization $\langle\sigma^x(\beta)\rangle = -0.24$ reignite, both for DecoAOE ($L = 64$, $|\mathrm{J}|\delta t = 0.1$, $\omega^* = 4$, $|\mathrm{J}|\Delta t = 1$, $\gamma = 0.1$, $\chi = 768$ and $\chi' = 512$) and light-cone ($|\mathrm{J}|\delta t = 0.1$ and $\chi = 256$) algorithms. DecoAOE bond dimension convergence is exact again, and the deviation corresponds to amplitude damping of the oscillations.

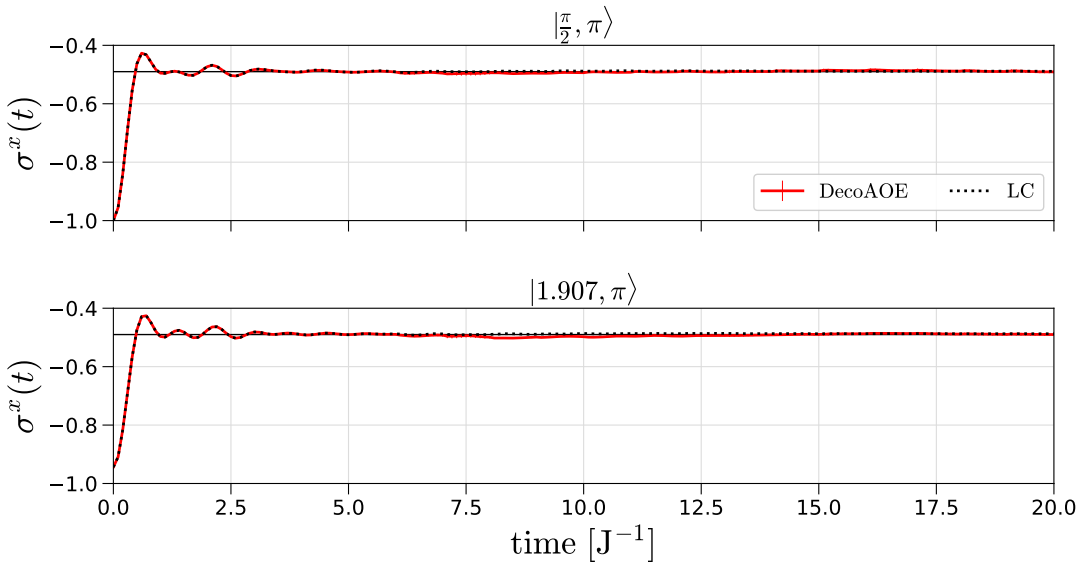

Figure 4.21: DecoAOE for $E = +|J|$ ($T = -1.44|\mathrm{J}|^{-1}$). The sixth and last isothermal family contains the state $|\frac{\pi}{2}, \pi\rangle = |X-\rangle = |-\rangle$ (first panel). Apparently uncorrelated low-amplitude oscillations emerge around the equilibrium magnetization $\langle\sigma^x(\beta)\rangle = -0.49$, both for DecoAOE ($L = 64$, $|\mathrm{J}|\delta t = 0.1$, $\omega^* = 4$, $|\mathrm{J}|\Delta t = 1$, $\gamma = 0.1$, $\chi = 768$ and $\chi' = 512$) and light-cone ($|\mathrm{J}|\delta t = 0.1$ and $\chi = 256$) algorithms. DecoAOE bond dimension convergence is good again, but deviations not related with oscillation damping cause an increase on $\langle\varepsilon(\sigma^\alpha)\rangle_t$.

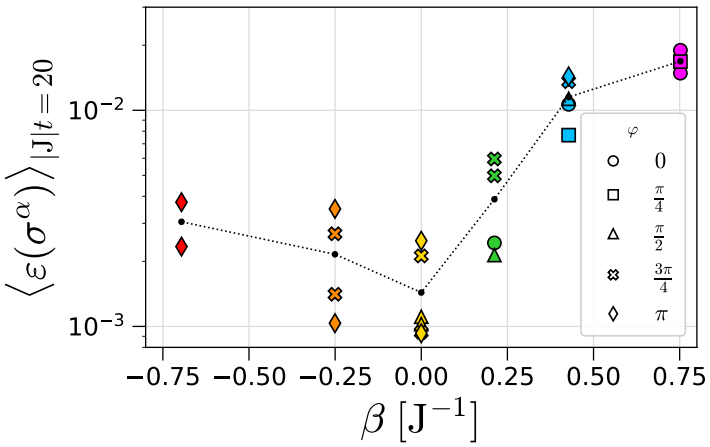

Figure 4.22: The Pauli Weight requirement of matrix elements depends only on the equilibration temperature in the long term evolution. When plotting $\langle \varepsilon(\sigma^{\alpha}) \rangle_t$ for all the states within each isothermal family (vertical lines with same marke color), a clear trend appears! Exactly at infinite temperature the deviation, provoked by orthogonal Pauli Weight truncation, reaches a minimum; at both sides of $\beta = 0$ there is an increase in the deviations between methods, and despite there exists some dispersion among states in the same family, the results appears to not be related to the value of φ (see for example the two diamonds and crosses for $\varphi = \frac{3\pi}{4}$). The Pauli Weight requirement appears no not be symmetric for both signs of temperature, suggesting that positive temperature equilibrating states are the hardest to simulate. Since the deviations range between $\mathcal{O}(10^{-}3)$ and $\mathcal{O}(10^{-}2)$ we conclude that both, DecoAOE and light-cone, can accurately predict the challenging non-integrable dynamics for a wide range of initial states, effectively dismantling their respective OSEE and TEE entanglement barriers.

4.4 Local Measures of Dispersion.

So far we have focused on the study of the PW requirement of matrix elements by itself, without paying much attention to how spread in space ω is. In order to develop a clearer picture of how the PW generation and propagation along the chain occurs, we introduce TN native strategies for the calculation of quantities that are also relevant in the field of **operator spreading**.

This field of research focuses on how the chaoticity of the underlying models induces particular types of transport for the operator norm, and how quantum information moves along the systems (Parker et al. (2019), Xu and Swingle (2020), Avdoshkin and Dymarsky (2020), Cao (2021), Srivatsa and von Keyserlingk (2024), Xu and Swingle (2024)). The accumulated knowledge existing on this field can be used to answer other questions, like how precise our TN simulations can be, and how the different spatial components of the spreading operator enter in such calculations.

4.4.1 Local Superposition Density.

In order to study the hydrodynamics of operators, a notion of local norm obeying some continuity equation must be introduced. In Khemani et al. (2018) such a quantity was presented as the norm of the superposition of strings starting/ending in a particular site of the lattice. The superposition ending at site ℓ is

$$|O(\ell,t)\rangle = \mathcal{P}_\ell |O(t)\rangle, \tag{4.26}$$

and the projector onto it acquires a simple product form ,with trivial bond dimension

$$\mathcal{P}_\ell = \Big(\bigotimes_{\ell'=1}^{\ell-1} \mathbb{1}_4\Big)\, \mathcal{P}_\omega^{(1)}\, \Big(\bigotimes_{\ell'=1}^{L-\ell} |\mathbb{1}_2\rangle\langle\mathbb{1}_2|\Big). \tag{4.27}$$

In Eq. 4.27 the $\mathbb{1}_4$ on the left of the ℓ-th site allows for any local operator to be inserted, while the $|\mathbb{1}_2\rangle\langle\mathbb{1}_2|$ filters out any component depositing PW in the region of the chain beyond ℓ. For a system with $L = 5$, an example of local superposition of strings ending at site $\ell = 3$ could be:

$$|O(\ell=3)\rangle = C_1|\mathbb{1}_2\mathbb{1}_2\sigma^\alpha\mathbb{1}_2\mathbb{1}_2\rangle + C_2|\mathbb{1}_2\sigma^\beta\sigma^\gamma\mathbb{1}_2\mathbb{1}_2\rangle + C_3|\sigma^\delta\sigma^\mu\sigma^\nu\mathbb{1}_2\mathbb{1}_2\rangle.$$

With this definition, the **(right-ending) local superposition norm** is

$$o(\ell,t) = \langle O(\ell,t)|O(\ell,t)\rangle, \qquad \text{with} \qquad \sum_{\ell=1}^{L} o(\ell,t) = 1. \tag{4.28}$$

Note that we could study also the left-ending local superposition density by exchanging the $\mathbb{1}_4$ and $|\mathbb{1}_2\rangle\langle\mathbb{1}_2|$ in Eq. 4.27, but since our problems will be reflection symmetric, there is no need for explicitly computing it. To the best of our knowledge, the study of these quantity has been limited to solvable models and small system sizes where exact diagonalization is viable ($L = 14$ in Khemani et al. (2018)). Introducing a way of studying it with TNs allows for studies of a variety of non-solvable models.

For random unitary circuits with and without local conservation laws, it has been reported (Gopalakrishnan et al. (2018); Khemani et al. (2018)) that the profile $o(\ell,t)$ splits into three well-defined spatial regions, according to the relation between the underlying strings and the generators of the dynamics. These regimes are depicted in Fig. 4.23, framed by the Trotter-Suzuki and physical light-cones within which the operator spreads, as discussed in Sec. 2.2.4.3 in the context of transverse contraction.

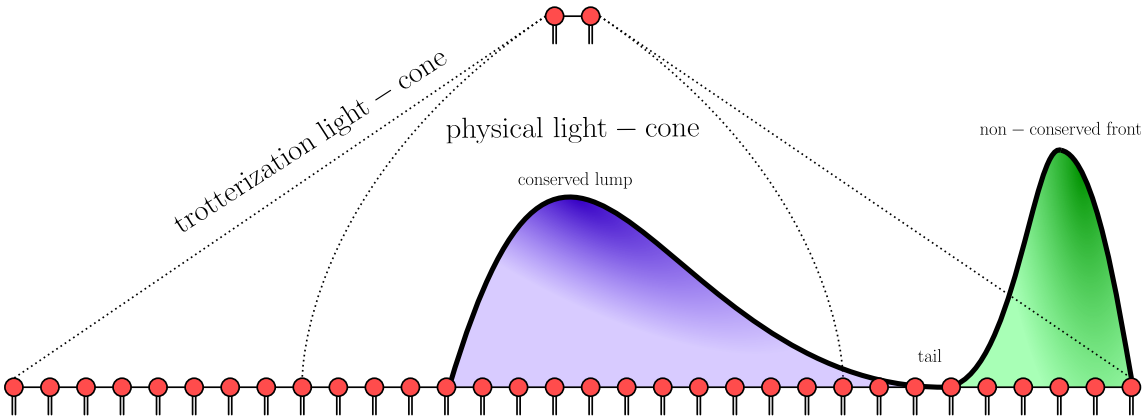

Figure 4.23: Right-ending local superposition norm in circuits with conservation.

The main region of $o(\ell, t)$ is a central **conserved lump**, where some operator norm is retained in presence of conservation laws; the existence of locally conserved quantities forces the lump to widen diffusively, since it contains those strings overlapping with the Hamiltonian and the rest of preserved quantities (like the longitudinal magnetization in the XY and XXZ models). This lump is connected through a **tail** to a **non-conserved front**, whose peak moves with butterfly velocity v_{B} away from the position where the original perturbation (the initial local Pauli operator) was; the width of such a front has been also found to spread diffusively, though with a different variance parameter than that of the central lump. The interpolating tail contains a suppressed amount of norm, decaying either polynomially $\sim |\ell - v_{\mathrm{B}} t|^{-\alpha}$ or exponentially $\sim \exp(-\alpha|\ell - v_{\mathrm{B}} t|^{\beta})$, depending on whether some quantity is conserved or not. The polynomial character is due to the constant radiation of non-conserved strings from the central lump at later times.

This spatial profile can be used to find a space-resolved splitting of the matrix elements representing the evolving expectation value:

$$O(\ell, t) = \langle \rho | O(\ell, t) \rangle, \qquad \sum_{\ell=1}^{L} O(\ell, t) = O(t). \tag{4.29}$$

In Fig. 4.24 we compute the norm and overlap profiles for the initial state $|0, 0\rangle$ and operator σ^x with the non-integrable Ising Hamiltonian at $\{\mathrm{J} = -1,\ g = -1,\ h = -0.5\}$, with and without channel decoherence. Despite the simulation was run for short times until $t|\mathrm{J}| = 6$, the detaching non-conserved front from the conserved lump in $o(\ell, t)$ can be perfectly visualized to bare eye in the closed system example (upper left panel, $\gamma = 0$) as time advances, but it disappears in presence of strong dissipation (upper right panel).

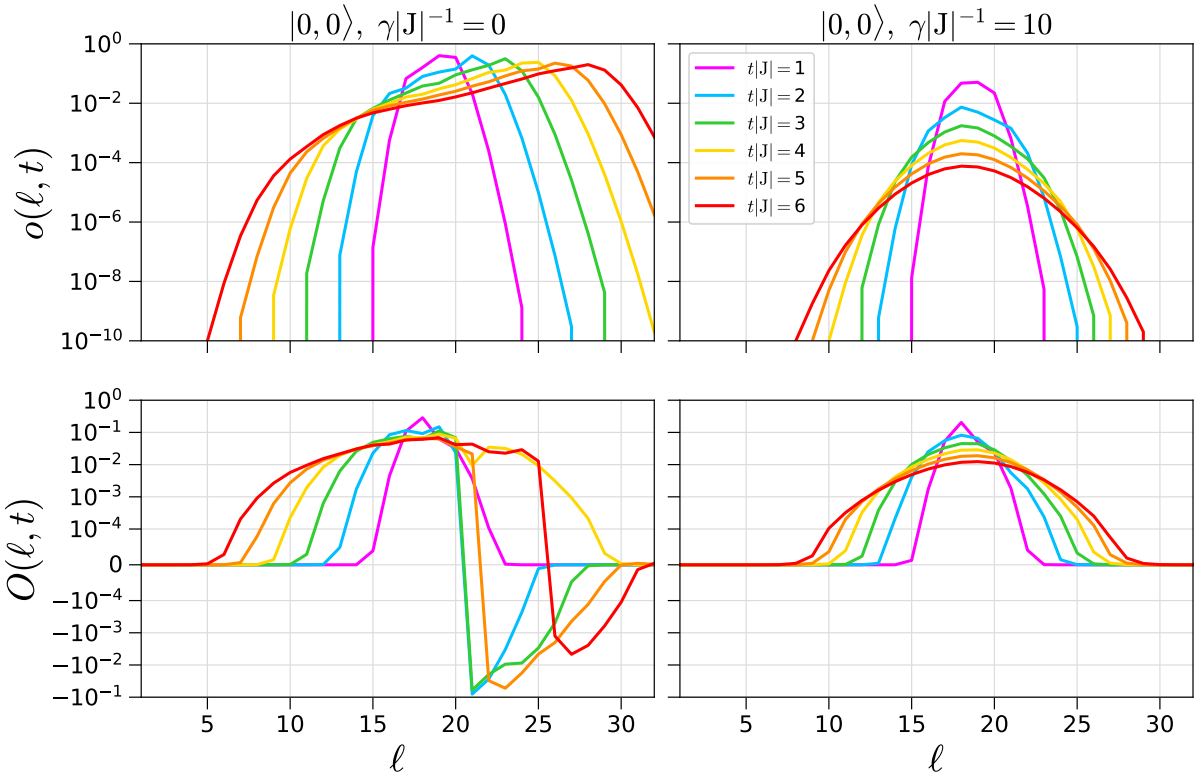

Figure 4.24: Spatial right-ending norm and overlap profiles. The simulations were run for the initial state $|0,0\rangle$ and non-integrable Ising model at $\{\mathrm{J}=-1,\ g=-1,\ h=-0.5\}$, without and with decoherence. TEBD parameters: $L=32$, $|\mathrm{J}|\delta t=0.02$ and $\chi=512$.

The overlap profile $O(\ell,t)$ contains more information for understanding the behavior of the local observable expectation value. As we could have foreseen, the contributions in the lump have a constant sign and spread diffusively with Gaussian envelope through the system, while the front contribution is subject to strong oscillations (see the change of sign between times $t|\mathrm{J}|=3$, 4 and 5). Again, the dissipative evolution does not show signatures of the unstable front.

These results give us another interpretative view on how different subspaces of the spreading operator feature in the expectation value: the oscillations seem to be originated from the non-conserved front! In former sections, we determined that those very same oscillations on top of the fast converging thermal values originate from long strings, and now we found that those strings must correspond to the non-conserved front. Therefore, it appears that thermal values can be predicted explicitly from the diffusive lump, while spectral properties shall be extracted from the ballistic front. This could be extremely useful for developing algorithms targeting either of both, thermal or spectral features from a system.

Moreover, the overlap profile is informative on the sizes of the underlying chain required to avoid finite size effects in simulations of restricted L. As expected from Lieb-Robinson bounds (Lieb and Robinson (1972), Frías-Pérez and Bañuls (2022)), the width of the spreading observable actually contributing (including the ballistic front) is narrower than the spread of norm, as distilled from comparing the panels on the right column of Fig. 4.24.

4.4.2 Average Local PW and End-to-End Length.

Finally, in order to settle down the combined picture including Pauli-Weight- and space-resolved contributions to the expectation value of local observables, we study the profiles of the average PW $\overline{\omega}$ and its spatial dispersion or end-to-end length $\overline{\xi}$ for local superpositions $|o(\ell,t)\rangle$.

To compute the **average PW** $\overline{\omega}$ of a string superposition $|Q\rangle$, we compute

$$\overline{\omega} = \lim_{\lambda\to 0} \frac{\partial}{\partial\lambda} \frac{\langle Q|\mathcal{Z}_{\mathrm{L,R}}(\lambda)|Q\rangle}{\langle Q|Q\rangle}, \tag{4.30}$$

where an MPO modifier $\mathcal{Z}_{\mathrm{W}}(\lambda)$ defined by the transfer tensor $W^{(\ell)}_{\overline{\omega}}(\lambda) = |\mathbb{1}\rangle\langle\mathbb{1}| + e^{\lambda}\mathcal{P}^{(1)}_{\omega}$ was applied. The rationale behind Eq. 4.30 can be easily understood with an example: consider the string superposition

$$|Q\rangle = \alpha|Q_1\rangle + \beta|Q_2\rangle + (1-\alpha-\beta)|Q_3\rangle$$

where

$$\begin{aligned} |Q_1\rangle &= |\mathbb{1}\sigma\mathbb{1}\mathbb{1}\mathbb{1}\sigma\mathbb{1}\rangle, \quad \omega_1 = 2 \\ |Q_2\rangle &= |\mathbb{1}\mathbb{1}\mathbb{1}\mathbb{1}\sigma\mathbb{1}\sigma\rangle, \quad \omega_2 = 2 \\ |Q_3\rangle &= |\sigma\mathbb{1}\mathbb{1}\mathbb{1}\sigma\mathbb{1}\sigma\rangle, \quad \omega_3 = 3. \end{aligned}$$

The modifier $\mathcal{Z}_{\mathrm{W}}(\lambda)$ acts as a marker, inducing a factor e^{λ} on each Pauli insertion

$$\alpha|\mathbb{1}\sigma\mathbb{1}\mathbb{1}\mathbb{1}\sigma\mathbb{1}\rangle + \beta|\mathbb{1}\mathbb{1}\mathbb{1}\mathbb{1}\sigma\mathbb{1}\sigma\rangle + (1-\alpha-\beta)|\sigma\mathbb{1}\mathbb{1}\mathbb{1}\sigma\mathbb{1}\sigma\rangle \xrightarrow{\mathcal{Z}_{\mathrm{W}}(\lambda)}$$

$$\alpha e^{2\lambda}|\mathbb{1}\sigma\mathbb{1}\mathbb{1}\mathbb{1}\sigma\mathbb{1}\rangle + \beta e^{2\lambda}|\mathbb{1}\mathbb{1}\mathbb{1}\mathbb{1}\sigma\mathbb{1}\sigma\rangle + (1-\alpha-\beta)e^{3\lambda}|\sigma\mathbb{1}\mathbb{1}\mathbb{1}\sigma\mathbb{1}\sigma\rangle \xrightarrow{\partial_\lambda}$$

After this, the derivative with respect to λ (which can be carried out numerically for few and small values of λ) yields

$$\alpha(2\cdot e^{2\lambda})|\mathbb{1}\sigma\mathbb{1}\mathbb{1}\mathbb{1}\sigma\mathbb{1}\rangle + \beta(2\cdot e^{2\lambda})|\mathbb{1}\mathbb{1}\mathbb{1}\mathbb{1}\sigma\mathbb{1}\sigma\rangle + (1-\alpha-\beta)(3\cdot e^{3\lambda})|\sigma\mathbb{1}\mathbb{1}\mathbb{1}\sigma\mathbb{1}\sigma\rangle \xrightarrow{\lim_{\lambda\to 0}}$$

and the limit for $\lambda \to 0$ eliminates the exponents, leaving a prefactor on each string equal to its PW. A final overlap and renormalization retrieves the average PW of the superposition:

$$2\alpha|\mathbb{1}\sigma\mathbb{1}\mathbb{1}\mathbb{1}\sigma\mathbb{1}\rangle + 2\beta|\mathbb{1}\mathbb{1}\mathbb{1}\mathbb{1}\sigma\mathbb{1}\sigma\rangle + 3(1-\alpha-\beta)|\sigma\mathbb{1}\mathbb{1}\mathbb{1}\sigma\mathbb{1}\sigma\rangle \xrightarrow{\text{overlap+normalization}}$$

$$\overline{\omega}(|Q\rangle) = \frac{2\alpha^2 + 2\beta^2 + 3(1-\alpha-\beta)^2}{\alpha^2 + \beta^2 + (1-\alpha-\beta)^2}.$$

This recipe can be applied both to the whole superposition or to the local projections with right-ending strings, as we do in Fig. 4.25. We delay the discussion of these results until we discuss another interesting average: the end-to-end length.

Throughout this chapter, we have focused on measuring ω without caring about how spread it is within each string. We can define the **end-to-end length** ξ of a string, or its average $\overline{\xi}$ in a superposition, as the distance (in sites) between the first and last Pauli matrices appearing in it. Computing such a quantity for the right-ending projections informs us on the **Pauli Weight density** profile

$$\rho_\omega(\ell) = \frac{\overline{\omega}(\ell)}{\overline{\xi}(\ell)}. \tag{4.31}$$

This quantity is of extreme interest, since it can be used as a proxy on the rank required on a particular bond for the faithful prediction of observables: if the local superposition is heavy (high ω) but very long (higher ξ) then the PW density is sparse; in this case we expect a combinatorial increase on the subspace explored by the local superposition, corresponding to distributing ω Pauli matrices on a long range ξ.

The study of this density could even be connected to Schrödinger picture works, that identified and eliminated long-range entanglement structures in evolving density matrices (Frías-Pérez et al. (2024)).

In a similar style, as introduced for the average PW, we compute the average end-to-end length of a superposition with a similar protocol: given some string superposition $|Q\rangle$, we can compute the average distances from both edges to the first Pauli matrix of the string: $\overline{\xi}_{\mathrm{L}}$ from the left and $\overline{\xi}_{\mathrm{R}}$ from the right

$$\overline{\xi}_{\mathrm{L,R}} = \lim_{\lambda\to 0} \frac{\partial}{\partial\lambda} \frac{\langle Q|\mathcal{Z}_{\mathrm{L,R}}(\lambda)|Q\rangle}{\langle Q|Q\rangle}, \tag{4.32}$$

with the left/right modifier MPOs $\mathcal{Z}_{\mathrm{L,R}}(\lambda)$, defined through the bulk transfer tensors

$$W_{\mathrm{L}}^{(\ell)}(\lambda) = \begin{pmatrix} e^{\lambda}|\mathbb{1}\rangle\langle\mathbb{1}| & \mathcal{P}_\omega^{(1)} \\ 0 & \mathbb{1}_4 \end{pmatrix}, \qquad W_{\mathrm{R}}^{(\ell)}(\lambda) = \begin{pmatrix} e^{\lambda}|\mathbb{1}\rangle\langle\mathbb{1}| & 0 \\ \mathcal{P}_\omega^{(1)} & \mathbb{1}_4 \end{pmatrix}, \tag{4.33}$$

and compute

$$\overline{\xi} = L - \overline{\xi}_{\mathrm{L}} - \overline{\xi}_{\mathrm{R}}. \tag{4.34}$$

This calculus can be further simplified if $|Q\rangle$ is a right-ending profile $|O(\ell,t)\rangle$, since one of the edges is known: $\overline{\xi}\big(|O(\ell,t)\rangle\big) = \overline{\xi}(\ell) = \ell - \overline{\xi}_{\mathrm{L}}$.

For illustrative reasons, we propose another example: consider the superposition

$$|Q\rangle = \alpha|Q_1\rangle + \beta|Q_2\rangle + (1-\alpha-\beta)|Q_3\rangle$$

with

$$\begin{aligned} |Q_1\rangle &= |\mathbb{1}\sigma\mathbb{1}\mathbb{1}\mathbb{1}\sigma\mathbb{1}\rangle, \quad \xi_1 = 5 = 7-1-1, \quad \xi_{\mathrm{L},1} = 1, \quad \xi_{\mathrm{R},1} = 1, \\ |Q_2\rangle &= |\mathbb{1}\mathbb{1}\mathbb{1}\mathbb{1}\sigma\mathbb{1}\sigma\rangle, \quad \xi_2 = 3 = 7-4-0, \quad \xi_{\mathrm{L},2} = 4, \quad \xi_{\mathrm{R},2} = 0 \\ |Q_3\rangle &= |\sigma\mathbb{1}\mathbb{1}\mathbb{1}\sigma\mathbb{1}\sigma\rangle, \quad \xi_3 = 7 = 7-0-0, \quad \xi_{\mathrm{L},3} = 0, \quad \xi_{\mathrm{R},3} = 0. \end{aligned} \tag{4.35}$$

We find the average left edge as:

$$\alpha|\mathbb{1}\sigma\mathbb{1}\mathbb{1}\mathbb{1}\sigma\mathbb{1}\rangle + \beta|\mathbb{1}\mathbb{1}\mathbb{1}\mathbb{1}\sigma\mathbb{1}\sigma\rangle + (1-\alpha-\beta)|\sigma\mathbb{1}\mathbb{1}\mathbb{1}\sigma\mathbb{1}\sigma\rangle \xrightarrow{\mathcal{Z}_{\mathrm{L}}(\lambda)}$$

$$\alpha e^{\lambda}|\mathbb{1}\sigma\mathbb{1}\mathbb{1}\mathbb{1}\sigma\mathbb{1}\rangle + \beta e^{4\lambda}|\mathbb{1}\mathbb{1}\mathbb{1}\mathbb{1}\sigma\mathbb{1}\sigma\rangle + (1-\alpha-\beta)|\sigma\mathbb{1}\mathbb{1}\mathbb{1}\sigma\mathbb{1}\sigma\rangle \xrightarrow{\partial_\lambda}$$

$$\alpha(1\cdot e^{\lambda})|\mathbb{1}\sigma\mathbb{1}\mathbb{1}\mathbb{1}\sigma\mathbb{1}\rangle + \beta(4\cdot e^{4\lambda})|\mathbb{1}\mathbb{1}\mathbb{1}\mathbb{1}\sigma\mathbb{1}\sigma\rangle \xrightarrow{\lim_{\lambda\to 0}}$$

$$\alpha|\mathbb{1}\sigma\mathbb{1}\mathbb{1}\mathbb{1}\sigma\mathbb{1}\rangle + 4\beta|\mathbb{1}\mathbb{1}\mathbb{1}\mathbb{1}\sigma\mathbb{1}\sigma\rangle \xrightarrow{\text{overlap+normalization}}$$

$$\overline{\xi}_{\mathrm{L}}(|Q\rangle) = \frac{\alpha^2 + 4\beta^2}{\alpha^2 + \beta^2 + (1-\alpha-\beta)^2}.$$

In Fig. 4.25 we find $\overline{\omega}(\ell, t)$ and $\overline{\xi}(\ell, t)$ for the same cases as in Fig. 4.24. As expected for the unitary evolving case (left column), the average PW of the superpositions finishing on sites far to the right of the initial perturbation grow fast to average weights around value $15 \gg 1$; on top of this, this average weight is clearly distributed on longer segments of the chain, as indicated by the average PW density $\frac{\overline{\omega}}{\overline{\xi}}$: around a 20% of the spatial support of their PW is empty (only $\mathbb{1}_2$'s). This contrasts with the sites to the left of the initial perturbation, showing tight packing of the PW into short strings.

For the dissipative case, the average PW does not grow at the same rate as the unitary case; in fact, it is reduced as the time passes, and this is not surprising, as the structure of local channels correspond to PW dissipation. In spite of that, the PW density does show an interesting structure: the results suggest that the PW density is able to track the non-conserved front, which could not be resolved anymore by the local norm or the local expectation value in Fig. 4.24. This result therefore equips us with another strategy for studying the operator hydrodynamics and the extent of the light-cone in presence of dissipation, and informs us on the regions of low PW density, where the bond dimension of evolving MPS may grow faster.

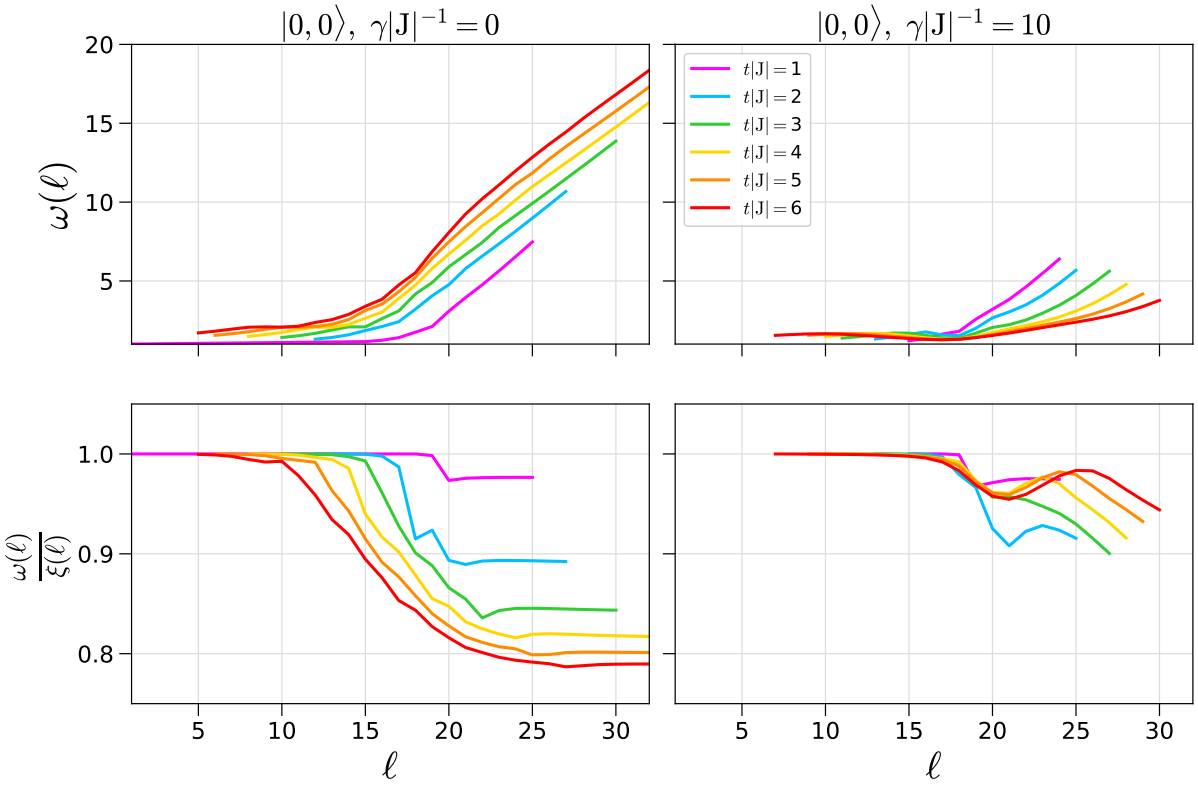

Figure 4.25: Average Pauli Weight and density profiles of right-ending superpositions. The simulations were run for the initial state $|0,0\rangle$ and non-integrable Ising model at $\{\mathrm{J}=-1,\ g=-1,\ h=-0.5\}$, without and with decoherence. TEBD parameters: $L=32$, $|\mathrm{J}|\delta t=0.02$ and $\chi=512$. In the left column the dynamics is unitary, and the strings reaching the right boundary are heavy ($\omega \gg 1$) and sparse $\rho_\omega \simeq 0.8$. Opposed to that, dissipative dynamics on the right column shows a decrease of PW as the front arrives to the right edge of the chain. Despite former measures like the superposition norm lost the footprints of the front in presence of decoherence, the Pauli density is able to measure the position of the non-conserved front.

4.5 Outlook in the Heisenberg Picture.

In this chapter we built a clear picture on how the amount of Pauli Weight and its spatial distribution contribute to expectation values of local observables through Heisenberg picture evolution. The study of the PW alone was enough to motivate a reformulation of TEBD (built on top of DAOE) that is able to accurately predict $O(t)$ in time regimes not accessible by simple evolution methods.

In future studies, we would be interested on giving a layer of analytical insight on our the numerical results, landing our present findings in mathematically solid grounds. In particular, we would like to elaborate on the separation between conserved and non-conserved strings, and how it can be used for determining thermal expectation values and spectral form factors, respectively.

The interplay between the character of the underlying Hamiltonian and both PW requirement and spreading is also an interesting direction for extending these studies: What would happen in other Hamiltonian regimes? Do these results hold when approaching integrable points (Ising with $h \to 0$, XX and XY models)? Would interactions change the operator spreading at the integrable point (XXZ)? What is the matter at critical values for (non-)integrable models?

On top of that, all the techniques which we have introduced here can be reused for carrying out similar studies on **magic**, in the spirit of works like Dowling et al. (2025); Turkeshi et al. (2025) (magic spreading) and Masot-Llima and Garcia-Saez (2024) (magic-based improvements of TEBD). Finally, perturbative schemes in terms of the Pauli Weight, magic and their densities could be proven useful, like in Begušić et al. (2025).

5

Explorations in the Transverse Folded Picture: Computational Time Entropy

In this last chapter we turn our attention (and the network to be contracted) to the transverse style contraction. Here we aim to make a lower-level characterization of the hybrid truncation scheme used by Hastings and Mahajan (2015), in combination with the light-cone growth algorithm (Frías-Pérez and Bañuls (2022)). In particular, we want to know how the rank of the trimmed matrices and the associated entropy behave for different models of closed and open dynamics.

5.1 Specifications of the Implementation.

This first section is devoted to clarifying the setup we will be using, with a focus on the truncation scheme of the rotated MPS along time (tMPS). In Fig. 5.1 we recall the light-cone simplification of the 2D TN representing the evolving expectation value of some observable, as introduced by Frías-Pérez and Bañuls (2022) and Lerose et al. (2023). This folded version was introduced to allow for an iterative construction of the cone (as explained in Sec. 2.2.4.3), accelerating the previously tested transverse contraction by Bañuls et al. (2009) and Müller-Hermes et al. (2012a).

Note that we intentionally left the upmost leg exposed, without a local operator connected to it. As mentioned in Ch. 2, this produces an evolved reduced density matrix when the left tMPS $\langle\mathcal{L}(t)|$ is contracted with the right tMPS $|\mathcal{R}(t)\rangle$. By fixing the orthogonality center at a particular bond representing time t ($t = 2\delta t$ in the figure), its environment matrix $\mathcal{M}_{t,T-t}$ to be truncated is the evolved reduced density matrix $\rho_{\ell(t)}(t)$, with support on the width of the trotterized light-cone $\ell(t) = v_{\text{Trotter}}\frac{T-t}{\delta t}$ at that selected time[1]. In other words, when the light-cone is cut horizontally, the environment matrix coincides with the cone stem/log.

[1]For even-odd trotterization the **Trotter velocity** v_{Trotter} is 2.

Nevertheless, the full physical dimensionality $4^{\ell(t)}$ associated to that spatial support, is reduced upon erasure of the tail of the distribution produced by eigenvalues or singular values of $\rho_{\ell(t)}(t)$. Therefore any truncation scheme in the transverse picture reducing $\chi \to \chi'$ at a particular time is effectively compressing the light-cone by narrowing its width down to $\ell_{\text{eff}}(t) = 2\log_4 \chi'(t)$. Therefore, bond compression substitutes the cone stem $\rho_{\ell(t)}(t)$ by $\tilde{\rho}_{\ell_{\text{eff}}(t)}(t)$ with $\ell_{\text{eff}}(t) \leq \ell(t)$.

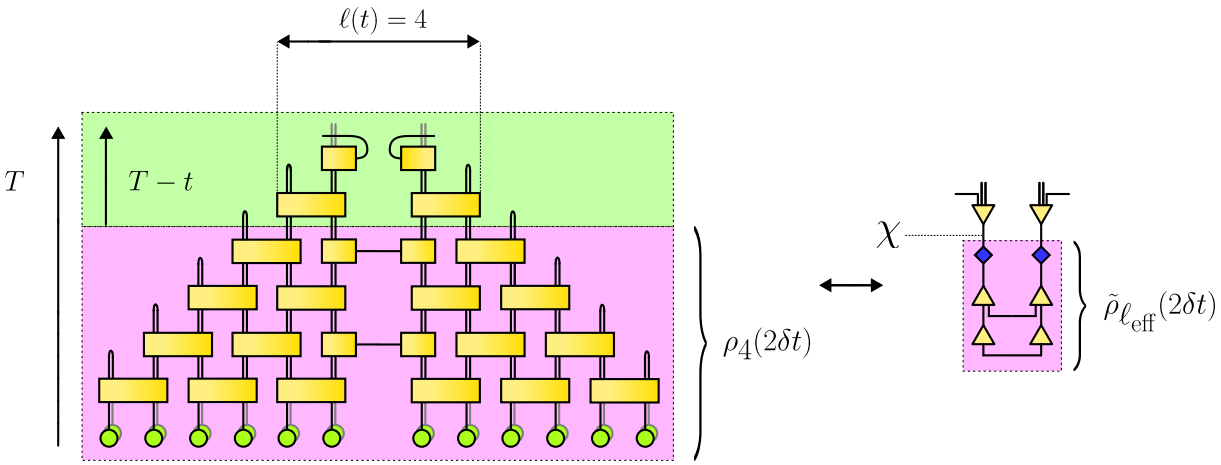

Figure 5.1: Truncating tMPS. The natural Trotter light-cone structure induced by local observables allows us to identify the new virtual bonds at time t with the physical indices of evolved reduced density matrices on a support fixed by the light-cone. Truncating these bonds corresponds to compressing the support of that light-cone to a narrower one.

The truncation of the column tMPS could be carried out in the same manner as for density matrices and operators, i.e. by diagonalizing the environment matrix arising from the zip-up contraction until time t; nevertheless, using SVD decomposition and truncating over the distribution of squared singular values made special sense when working with the state vector or with hermitian operators. Isometrizing with simple QR decompositions to fix a center of orthogonality, and truncating afterwards with SVDs had a clear connection with the probability normalization (in the case of the state vector $|\Psi\rangle$), purity ($|\rho\rangle$) and Frobenius norm ($|O\rangle$).

Opposed to that, for our reflection-symmetric models, the tMPS is contracted with itself (without the intermediate conjugation operation!). This leaves room for an improvement of the truncation scheme, profiting that $\rho_{\ell(t)}(t)$ is symmetric when split into two equal halves, as indicated by Hastings and Mahajan (2015), and executed by Frías-Pérez and Bañuls (2022). This property allows us to use the symmetric Autonne-Takagi factorization (Eq. 2.55) splitting of the matrices, rather than the eigendecomposition[2]. This truncation scheme was proven to produce a slower rate of increase of the bond dimensions for long-time simulations with respect to the classical SVD program.

[2]In fact $\rho_{\ell(t)}(t)$, as reorganized to split its spatial legs in left and right sites, is a complex symmetric matrix, and there is no guarantee that upon diagonalization with $\mathcal{B}$, the inverse transformation $\mathcal{B}^{-1}$ will coincide with the conjugate transpose $\mathcal{B}^{\dagger}$.

To sum up, we will use tMPS with the operator boundary open, and truncate them by first setting the operator-to-state canonical form (isometries pointing towards the state) and truncate in a symmetric style from state to the operator. We optimize the overlap $\langle\mathcal{L}(t)|\mathcal{L}(t)\rangle$, rather than $\langle\mathcal{L}(t)|\mathcal{L}^\dagger(t)\rangle$ (SVD truncation), or non-reflection-symmetric overlaps $\langle\mathcal{L}(t)|\mathcal{R}(t)\rangle$ (which we introduced in Carignano et al. (2024)).

For this particular set of prescriptions, we define the **computational time entanglement entropy** (cTEE) in the same way as the OSEE:

$$\mathrm{cTEE}_{t,T-t} = -\sum_k s_k^{(t)} \log s_k^{(t)}, \tag{5.1}$$

where the singular values are not squared, since the SVD is performed on $\rho_{\ell(t)}(t)$, rather than on one of its halves; i.e. we replace the position of the typical eigenvalues of the environment matrices by their symmetric factorization singular values. This quantity may be slightly different if the aforementioned prescriptions changed (tMPS with closed edge, truncating from the opposite direction or optimizing $\langle\mathcal{L}(t)|\mathcal{L}^\dagger(t)\rangle$ to reduce χ).

Note that we have added the word *computational* before TEE to distinguish this measure from other proposals, motivated from quantum field theory (Milekhin et al. (2025)). In their study, *Milekhin et at.* define TEE as a complex valued quantity, derived from plugging the eigenvalues of generalized density matrices ρ_{gen} into Eq. 5.1. These density matrices are defined such that their local indices refer to different instants in time:

$$\langle O_{\ell_1}(0) Q_{\ell_2}(t)\rangle = \mathrm{Tr}\{\rho_{\mathrm{gen}}(0,t) O_{\ell_1} Q_{\ell_2}\}, \tag{5.2}$$

where O and Q are single spin operators acting at different sites $\ell_{1,2}$, and at different times 0 and t.

In Fig. 5.2 we show the different elements involved in the computation of cTEE that can help us measuring the complexity of a simulation with our prescription. For this example we evolved state $|+\rangle$ with the non-integrable Ising Hamiltonian at point $\{\mathrm{J}=-1,\ g=-1,\ h=-0.5\}$, time step $|\mathrm{J}|\delta t = 0.1$ and cutoff 10^{-10}.

In the upper left panel of Fig. 5.2 we show a stacked plot of the cTEE profiles on the open edge tMPS as its length (physical time) is increased. On the state edge (total times $T \to \delta t$) the cTEE is always minimum, while on the operator edge the open bond retains some remnant entanglement. Between these edges, a double-hump structure appears in the profile for long enough times (see $|\mathrm{J}|T > 2$ in Fig. 5.2). At early times, an operator edge hump corresponding to the open bond dominates the cTEE, as marked with colored circles (dark blue). Some time later, a bulk (in time) hump emerges and surpasses the edge hump (white and red markers).

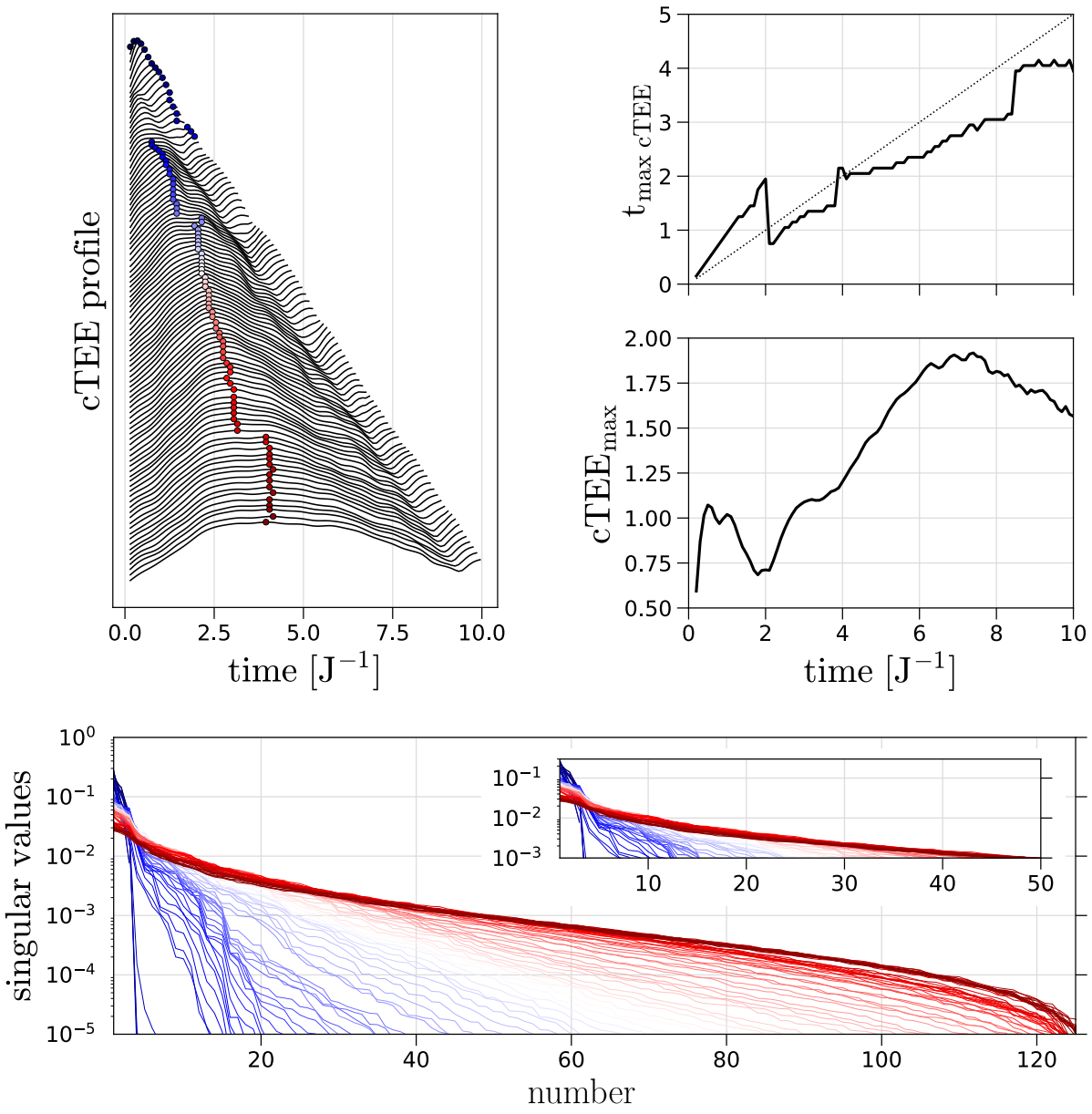

Figure 5.2: Analyzing the cTEE. This example evolved state $|+\rangle$ with the non-integrable Ising Hamiltonian at point $\{\mathrm{J} = -1,\ g = -1,\ h = -0.5\}$, time step $|\mathrm{J}|\delta t = 0.1$ and cutoff 10^{-10}. The cTEE profile starts from a null value on the state edge and finishes in a non-zero value on the operator edge; in the middle, a main hump grows, containing the maximum value for longer times. The position of the maximum jumps from the operator edge hump to the main one at short times, and may keep jumping when a plateau shape is reached. The value of the maximum is not well converged unless higher bond dimensions are reached, so the true behavior only reaches $|\mathrm{J}|t = 6$. The sigular value distribution generating the entropy displays a head with few singular values, and an exponentially decaying tail, synthesized for long times (red).

This is the reason why the time slice at which cTEE is maximum displays discontinuous jumps (see the upper right panel displaying $\mathrm{t}_{\max\ \mathrm{cTEE}}$), while the value of the maximum cTEE at a particular time shows a complex structure (panel displaying $\mathrm{cTEE}_{\max}$). Importantly enough, comparing both the position of the maximum and its value in time informs us whether we are visualizing a stable maximum or whether it jumped to neighboring maxima. When we analyze the behavior of the maximum cTEE in terms of the integrability of the model in Sec. 5.2, we will follow the behavior of the bulk hump, hosting the maximum after short times ($|\mathrm{J}|T > 2$ in Fig. 5.2).

On the bottom panel we plot the distribution of singular values from early times (blue) to later times (red), displaying an exponential decay. Importantly, by zooming in the first 50 singular values, we detect that only 10 of them are leading. This behavior was already detected by Foligno et al. (2023) when simulating chaotic circuits with the transverse contraction, concluding that the tMPS has a strong overlap with Product States along time.

The next question we want to answer is how does this algorithm converge with bond dimension. For the same parameters as in Fig. 5.2, in Fig. 5.3 we show the transverse magnetization σ^x, the energy density h, the logarithmic bond dimension (equivalent to the effective width of the light-cone ℓ_{eff}) and the maximum value of cTEE.

We observe that, for the simulated times, the observable quantities are well converged for a maximum bond dimension $\chi = 256$, and the conservation of energy only shows small fluctuations on top of the correct value $h(t) = -1$. Opposed to that, cTEE appears to require bigger bond dimensions to converge, deviating from its monotonously increasing trend after a time $|\mathrm{J}|\Delta t = 2$ from the saturation of the bond dimension; this is striking, since cTEE did not reach the maximum allowed $\log 128 \simeq 4.85$ value by χ. We accuse this apparent mismatch to the fact that the singular value spectrum is dominated by few values out of a long exponential tail.

It is important to note that *there appears to exist some numerical instability bugging the smoothness of the predictions*, despite it disappears as the bond dimension is increased. This could mean that our implementation could be further optimized.

For this particular implementation and example, the behavior of the bond dimension is clearly exponential, but determining its exact shape is not easy for the converged times: fitting the effective light-cone width ℓ_{eff} for $\chi_{\max} = 512$ to a power law in the time window $|\mathrm{J}|t \in [1, 6]$ yields an almost perfect square root (black dotted curve) growth

$$\ell_{\text{eff}} = 2 \log_4 \chi(t) = (3.54 \pm 0.03)\, t^{0.505 \pm 0.007}$$

which, in connection to the interpretation of the logarithmic bond dimension reflecting the size of the effective light-cone seen by the algorithm, suggests that converged simulations reflect the diffusive underlying spreading of correlations. Nevertheless, this could be mere interpretation, since the exponent of the scaling with time becomes

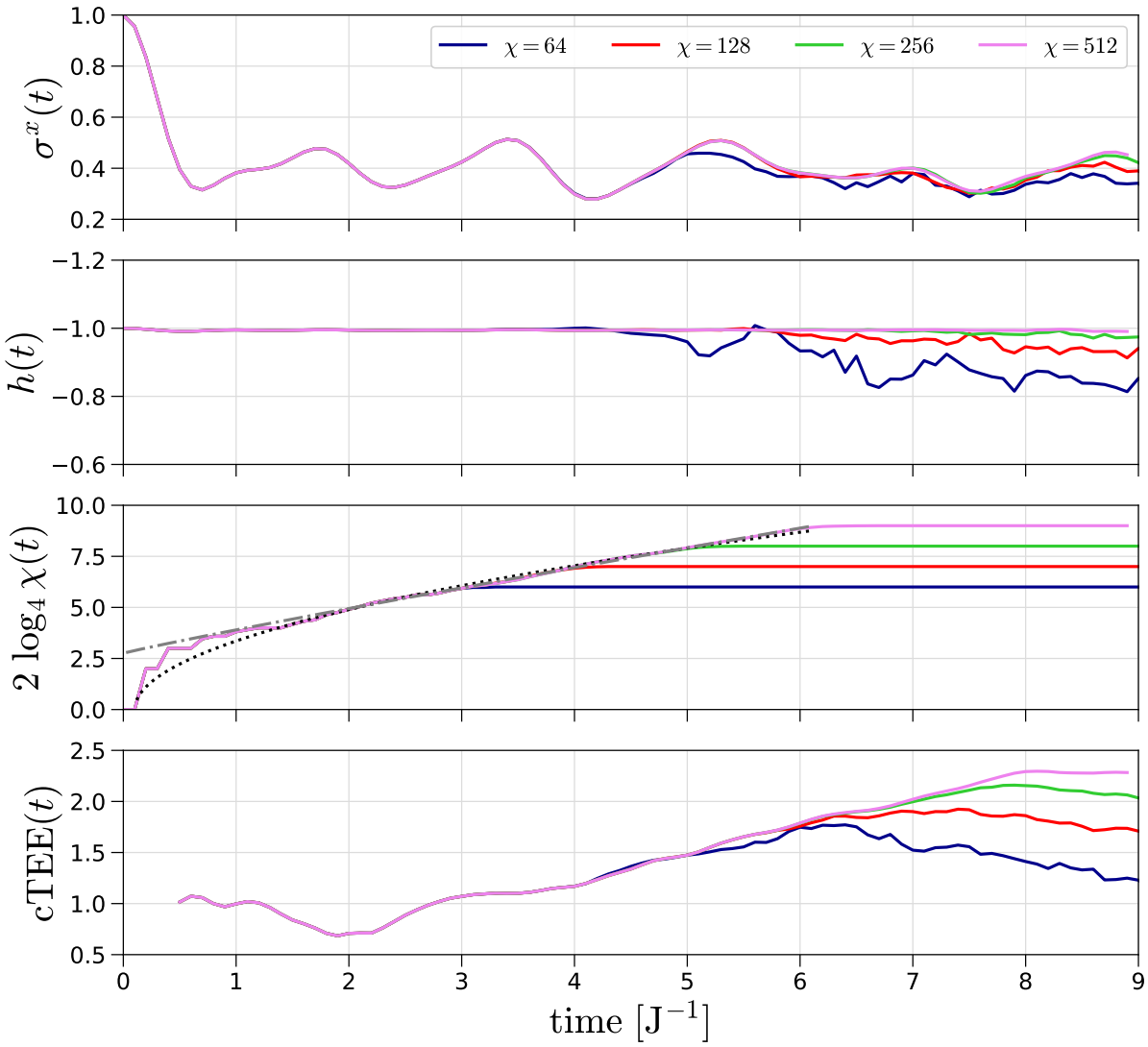

Figure 5.3: Convergence of tMPS predictions with χ. We show the transverse magnetization and energy density for the same parameters as in Fig. 5.2, together with the logarithmic bond dimension and the cTEE. Despite observables converge around $\chi = 256$, cTEE requires increasing χ to unveil an apparently linear growth, matching the exponential one of $\chi(t)$.

compatible with a straight line (gray dash-dotted line) when fitting in the window $|\mathrm{J}|t \in [2, 6]$:

$$\ell_{\text{eff}} = 2\log_4\chi(t) = (2.8 \pm 0.2) + (1.15 \pm 0.14)\, t^{0.94\pm0.05}$$

For the explored times, it is unclear which is the right exponent of time. On top of that, it could be that eliminating the numerical instability of the implementation would lead to a faster convergence of the observables and the cTEE without growing χ that much. In the following section, we aim at connecting the rank growth of the environment matrices with the one known in Heisenberg and Schrödinger pictures.

5.2 Connecting the Space and Time Complexity Measures.

This section is based on our article Carignano et al. (2024). If a matrix $\mathcal{M}$ can be decomposed in several factor matrices m_i with $i > 1$, the number of singular values of $\mathcal{M}$ is upper bounded by the smallest of the ranks of the matrices m_i. In particular, the tMPS overlap $\langle \mathcal{L}(T)|OQ|\mathcal{L}(T)\rangle = \langle OQ(T)\rangle$, corresponding to the time evolution of two neighboring local operators O and Q, is computed by contracting the full 2D TN (left hand side of Fig. 5.4). A horizontal cut, splitting the its total length T into t and $T-t$, partitions the network into an early lower half, corresponding to the Schrödinger picture evolved density matrix $\langle \rho(t)|$, and a late upper half, identified as the Heisenberg evolution $|OQ(T-t)\rangle$.

When an environment matrix $\mathcal{M}$ is composed for performing its singular value decomposition and subsequent truncation, the particular bond we are trimming is set as the center of orthogonality. Therefore, the spectrum of $\mathcal{M}$ is the same as that of

$$\sqrt{O(T-t)}\rho(t)\sqrt{Q(T-t)}, \tag{5.3}$$

as it can be seen in the right hand side of Fig. 5.4.

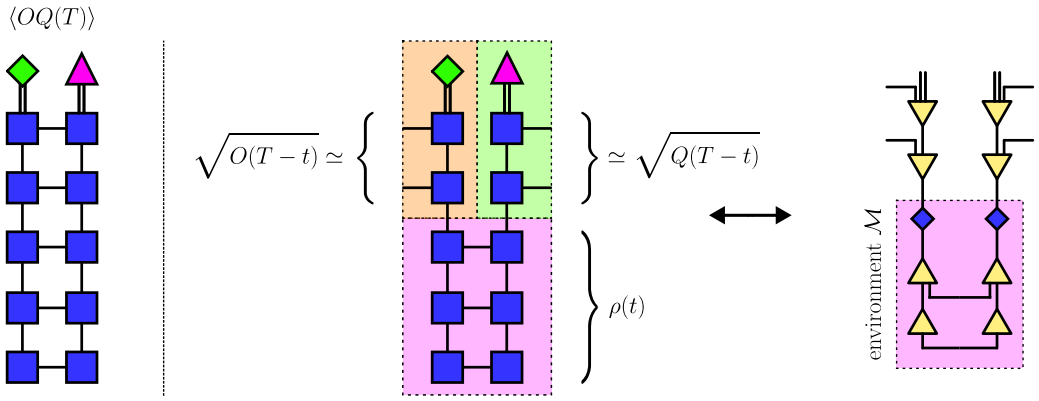

Figure 5.4: Matrices involved in the truncation of the environments of a bond.

Therefore, for our reflection-symmetric setup ($O = Q$), the rank of $\mathcal{M}$ fulfills

$$\mathfrak{R}(\mathcal{M}) \leq \min\Big\{\mathfrak{R}\big(O(T-t)\big), \mathfrak{R}\big(\rho(t)\big)\Big\}. \tag{5.4}$$

Actually, in our open legged implementation, it is not the Heisenberg evolution of operators what enters the rank discussion, but the tip of the light-cone without the central Pauli operator O, as in Fig. 5.1; this is the same as considering de rank growth of an arbitrary local operator à la Heisenberg.

Recovering the results from the table with which we finished Ch. 2, we conclude that the smallest rank is associated with the results of *Prosen, Znidaric* and *Pizorn* on Heisenberg evolved local operators. Their results were the following: in models that can be mapped to fermions, local operators with finite fermion index, like σ^x required a finite bond dimension (area law), while local operators with infinite index, like σ^z, showed $\chi(t) \propto t$ (log law). This implies that, for integrable Hamiltonians, the cTEE should be upper bounded by an area/log law, and for non-integrable systems by a volume law.

This would mean that transverse contraction could behave as badly as Schrödinger/Heisenberg contraction for challenging non-integrable dynamics. Nevertheless, there must be a twist to this argument, since we have already witnessed high quality simulations of local observables for this method in Sec. 4.3.3 from Ch. 4, matching the results of orthogonal Pauli Weight truncation; this twist is related to temperature and the pre-discussion we have made in the former section.

As we illustrated in Fig. 5.1, when trimming the bond dimension of an index in the middle of the tMPS, we are narrowing the support of the reduced density matrix entering the rank discussion in Eq. 5.4. Such a reduced density matrix, defined on a support $\ell_{\text{eff.}}$ of order $\mathcal{O}(\log \chi(t))$, may and will thermalize as the evolution progresses. As we commented in Ch. 2, equilibrium thermal density matrices display an area law OSEE. This opens a window for the smallest rank featuring in Eq. 5.4 being the one associated with the reduced system Schrödinger picture, corresponding to a bounded entanglement when equilibration is reached, rather than the volume law displayed by non-integrable Heisenberg evolved local operators!

In the remaining of this chapter we devote ourselves to confirm these analytical arguments with numeric results. We want to note that other authors have developed other bounds for the cTEE in terms of the purity of underlying density matrices (Foligno et al. (2023)).

5.2.1 Unitarily Evolved Nearest-Neighbor Models.

In this section we systematically study the behavior of the cTEE for different toy models in terms of the underlying integrability.

The first case of study is the Ising model at the integrable point $\mathrm{J} = -1,\ g = -0.5$, with initial state $|0\rangle$ evolved with second order trotterization and time step $|\mathrm{J}|\delta t = 1$. As for the rest of simulations of this thesis, the truncation threshold of singular values is set to 10^{-10}. In Fig. 5.5 we present the evolution of the contributions to the cTEE for each singular value $s_k^{(t)}$, i.e. $-s_k^{(t)} \log s_k^{(t)}$ (in thin black curves), together with their global sum (the cTEE, in the thicker red curve).

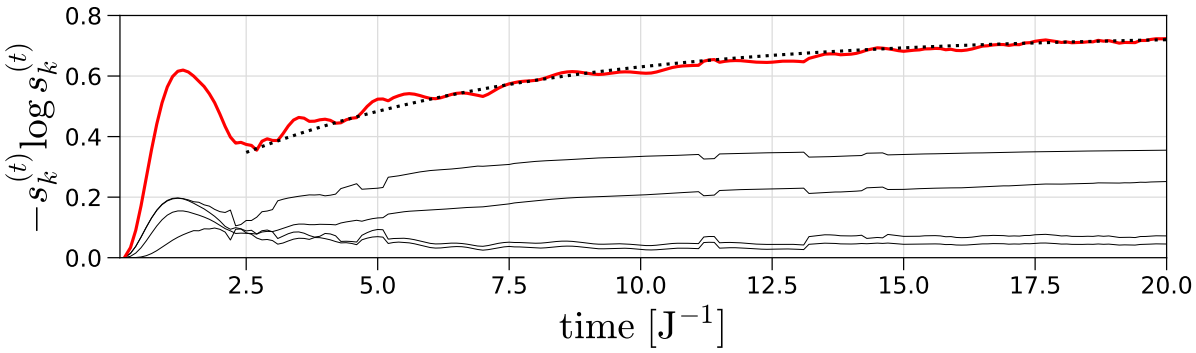

Figure 5.5: cTEE in the integrable Ising model. Initial state: $|0\rangle$; Hamiltonian: Ising with $\mathrm{J} = -1,\ g = -0.5$; trotterization: second order, $|\mathrm{J}|\delta t = 0.1$. The cTEE saturates, as required by the rank of local Heisenberg operators with finite fermion index.

Interestingly, we only see 4 dominant singular values[3], out of which 2 saturate fast, and the other 2 take longer. An exponential saturation fit (black dotted curve), results in

$$(0.79 \pm 0.03) - (0.59 \pm 0.02)e^{-(0.17 \pm 0.04)t}$$

which appears to indicate an area law behavior. This result appears to be consistent with the findings by Prosen and Pižorn (2007a): in this case the cTEE could be upper bounded by the OSEE of local Heisenberg operators, particularly those with lower fermion index (σ^x, inducing an exact bond dimension $\chi = 4$). Nevertheless, since our setup is that of an open leg, it is unclear which of the local operators is bounding the behavior, whether those with finite index or those with infinite one. Therefore, the best we can say from Fig. 5.5 is that cTEE grows sublinearly.

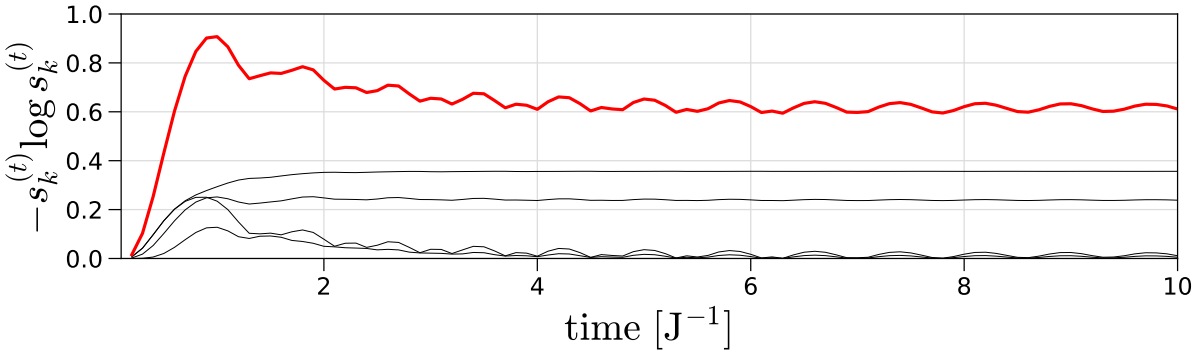

Figure 5.6: cTEE in in the integrable critical Ising model. Initial state: $|0\rangle$; Hamiltonian: Ising with $\mathrm{J} = -1,\ g = -1$; trotterization: second order, $|\mathrm{J}|\delta t = 0.1$. The cTEE saturates, as required by the rank of local Heisenberg operators with finite fermion index.

[3]There is an exponentially suppressed tail with around 2 orders of magnitude that collapse in the linear scale plot. We do not know whether this tail is to be expected, or whether it forms part of the implementation instability we have previously mentioned.

More stringent results are obtained by shifting to the critical point $\mathrm{J} = -1,\ g = -1$ in Fig. 5.6, where saturation of the cTEE becomes clear already for short times. This result is curious, since we would expect a log law for this particular point, while we detect a clear area law.

The case of the XY model is less obvious, since a cascade of singular values appears during the evolution, as reflected by Fig. 5.7; for this model we simulated the evolution of the initial state $|\frac{\pi}{4}, 0\rangle$ with first order even-odd trotterization, and time step $|\mathrm{J}_x|\delta t = 0.025$.

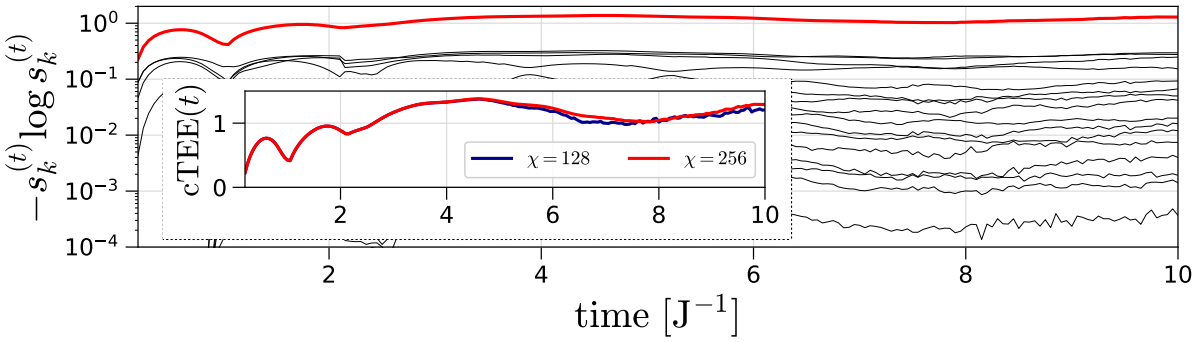

Figure 5.7: cTEE in the XY model. Initial state: $|\frac{\pi}{4}, 0\rangle$; Hamiltonian: XY with $\mathrm{J}_x = -0.5,\ \mathrm{J}_y = -0.75$; trotterization: first order, $|\mathrm{J}_x|\delta t = 0.025$. The cTEE saturates, despite a cascade of pairing-induced singular values is synthesized along evolution.

Interestingly, the instability of the numerical algorithm is witnessed by the smaller singular values; in order to draw clear conclusions, we display $\chi = 256$ in the main panel, and the comparison with $\chi = 128$ in the inset. We conclude that the cTEE appears to oscillate around a constant value, being compatible with an area law behavior.

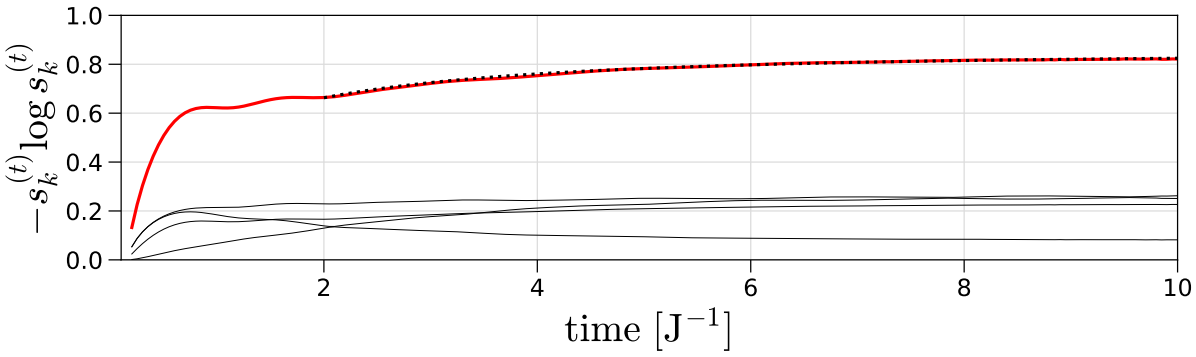

Figure 5.8: cTEE in the XX model. Initial state: $|\frac{\pi}{4}, 0\rangle$; Hamiltonian: XX with $\mathrm{J}_x = -0.5,\ \mathrm{J}_y = -0.5$; trotterization: first order, $|\mathrm{J}|\delta t = 0.025$. The cTEE is compatible with an exponential relaxation and with a logarithmic growth for the explored window of times.

The appearance of the cascade of singular values could be related to the presence of non-zero pair creation/annihilation (recall the hard-core boson mapping of this model in Ch. 2), since when shifting to the XX model in Fig. 5.8, the 4 dominant singular value structure is recovered.

The example run for the XX model with the same initial state and numerical parameters could be compatible with saturation of cTEE or with a log law. In order to check this, we could profit the fact that few singular values dominate and simulate until long times; nevertheless, a tail of exponentially small singular values effectively increases the bond dimension until out threshold $\chi = 256$. Once more, we delay drawing conclusions on whether this model shows an area or log law for cTEE to future works with more stable instances of the algorithm.

The last model we want to comment on is the XXZ. We check both phases, the critical Luttinger liquid phase with $|\mathrm{J}_z| < |\mathrm{J}| = |\mathrm{J}_{x,y}|$ in Fig. 5.9, and the ferromagnetic phase with $|\mathrm{J}_z| > |\mathrm{J}|$ in Fig. 5.10. The mapping to hard-core bosons or fermions for this model includes an interaction between neighboring site densities; on the critical regime, this interaction is not strong enough to drive the physics of the excitations, while on the ferromagnetic phase interactions dominate the physics. The difference between the underlying physical scenarios is clearly translated into a difference of the singular value spectra contributing to the cTEE, despite both regimes are integrable.

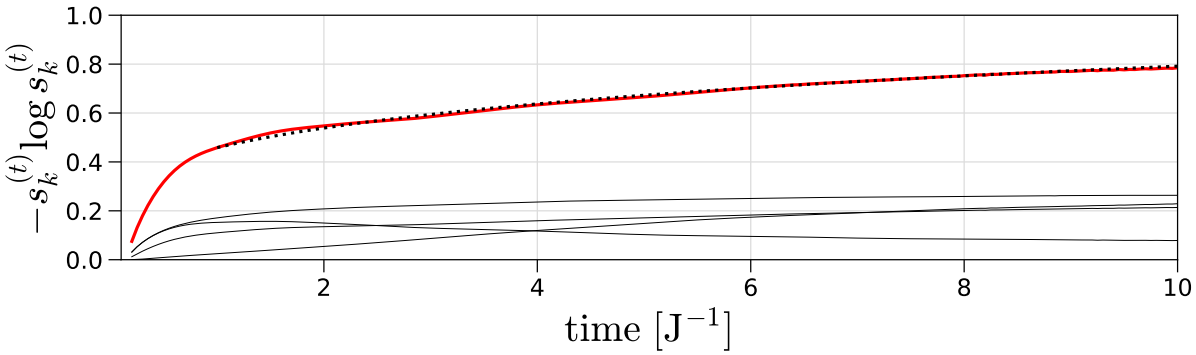

Figure 5.9: cTEE in the critical XXZ model. Initial state: $|\frac{\pi}{4}, 0\rangle$; Hamiltonian: XXZ with $\mathrm{J}_x = -0.5,\ \mathrm{J}_y = -0.5,\ \mathrm{J}_z = -0.25$; trotterization: first order, $|\mathrm{J}|\delta t = 0.025$. The cTEE is compatible with an exponential relaxation and with a logarithmic growth for the explored window of times.

For the critical phase we find the same structure as the XX model, as it could be expected from the proximity in parameter space (the unique difference is $\mathrm{J}_z = 0 \to -0.25$). A fit to an exponential relaxation appears to yield results compatible with an area law

$$(1.218 \pm 0.016) - e^{-(0.275 \pm 0.016) t^{(0.491 \pm 0.009)}}$$

as depicted in Fig. 5.9, but in the same style as for the XX model, it would be necessary to reach longer times to ensure that this curve is an area law rather than a log law.

In the ferromagnetic phase, an intense cascade of singular values is generated along evolution (with corresponding bond dimension increase much steeper than for the XY model). The difference between XXZ and XY lies on their underlying physics: the first is a clearly interacting model with density-density energy penalties after boson/fermion mapping, while the second is considered non-interacting despite the presence of pairing (double creation/annihilation of particles).

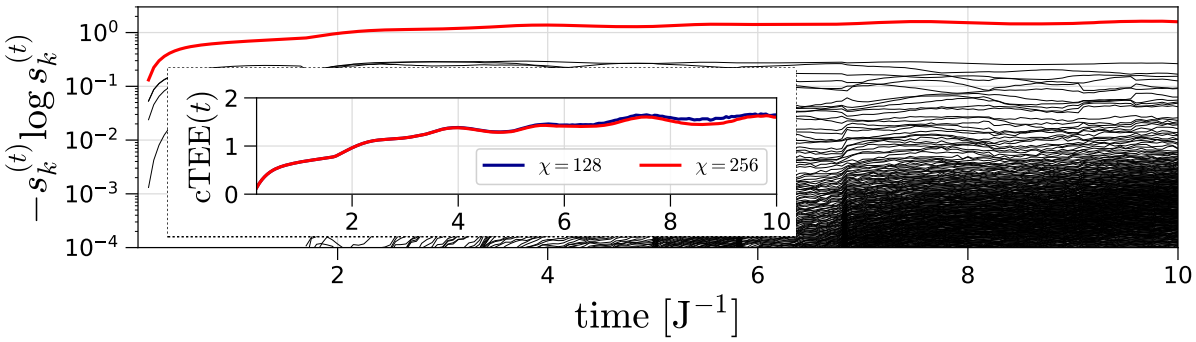

Figure 5.10: cTEE in the ferromagnetic XXZ model. Initial state: $|\frac{\pi}{4}, 0\rangle$; Hamiltonian: XXZ with $\mathrm{J}_x = -0.5,\ \mathrm{J}_y = -0.5,\ \mathrm{J}_z = -1$; trotterization: first order, $|\mathrm{J}|\delta t = 0.025$. The cTEE saturates, despite the underlying interactions between fermions/hard-core bosons generate an intense cascade of singular values.

The behavior of cTEE at a non-integrable point was shown to be connected with an exponential scaling of the bond dimension in Fig. 5.3, suggesting a volume law growth. Since we are suspicious of the potential breakdown of such behavior for longer times depending on the equilibration temperatures, we delay our discussion on this matter to Sec. 5.2.3.

5.2.2 Dissipatively Evolved Nearest-Neighbor Models.

For the case of dissipatively evolved systems together with non-integrable Hamiltonians, we suspect that cTEE will be upper bounded, since we already saw that any kind of dissipation of Pauli Weight efficiently reduces the maximum bond dimension to that of the subspace with few Pauli matrices. In Fig. 5.11 we expose the initial state $|0\rangle$ to channel decoherence and Hamiltonian unitary evolution at the point $\mathrm{J} = -1,\ g = -1\ h = -0.5$. The parameters of the second-order trotterized simulations are $|\mathrm{J}|\delta t = 0.1$ and $\chi = 256$.

The results are consistent with our expectations: in all the cases, despite the decoherence rates are low, the observables and cTEE decay with time, implying that classical simulation of these Lindblad type evolutions is efficient. Despite that, there appears to exist a particular intermediate rate for which the cTEE rapidly converges to a constant value. This means that there exist different cTEE scalings between that of the fully unitary evolution (volume law) and that of strong dissipation (going to 0).

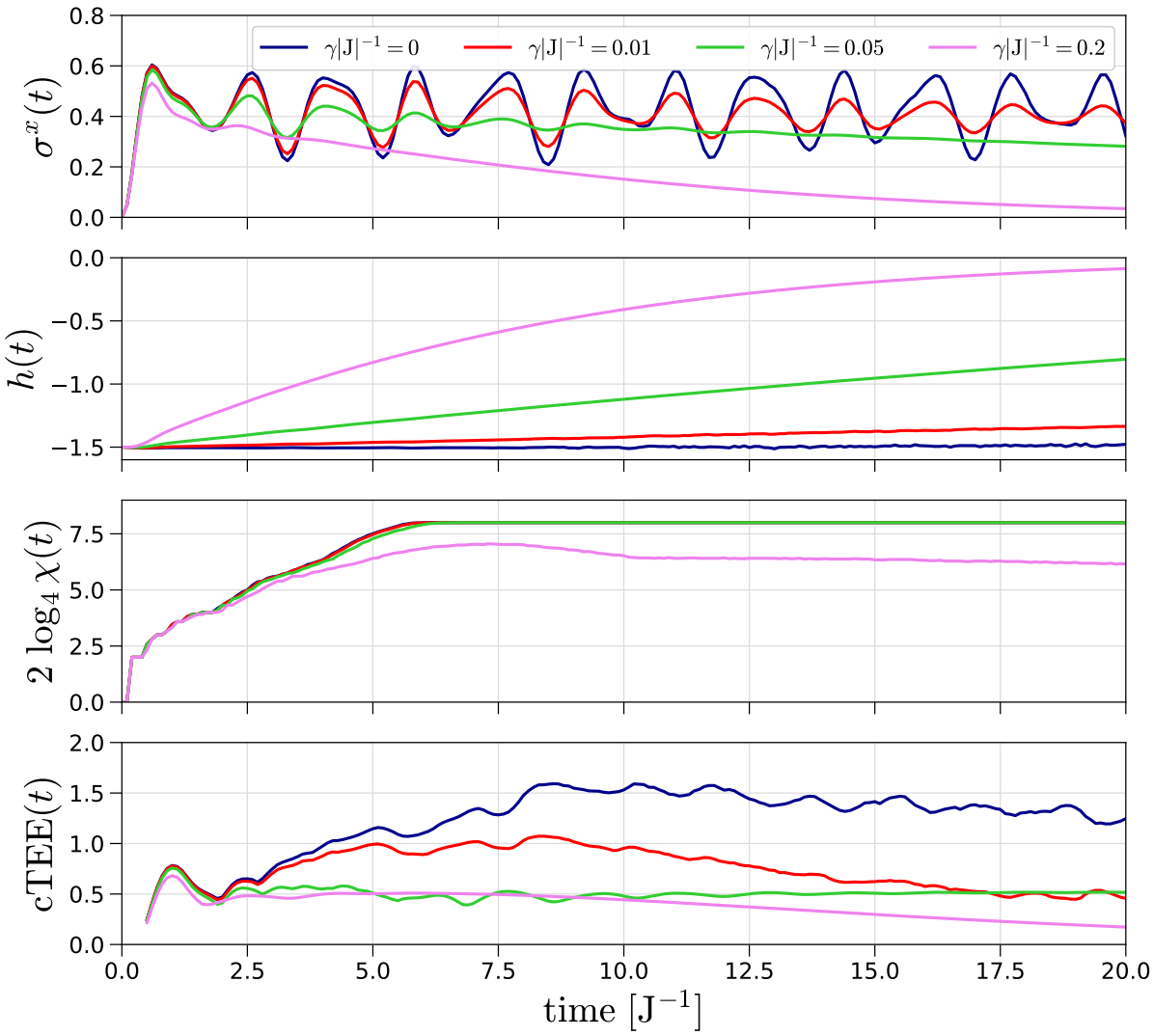

Figure 5.11: cTEE behavior for the decoherent non-integrable Ising model. Initial state: $|0\rangle$; Hamiltonian: Ising with $\mathrm{J}=-1$, $g=-1$, $h=-0.5$; trotterization: second order, $|\mathrm{J}|\delta t=0.1$; maximal bond dimension: $\chi=256$. The cTEE behavior is lowered with respect to the fully unitary case (dark blue curve); for any of the intensities of dissipation the observables decay towards their infinite temperature expectation values.

5.2.3 Connection between β and cTEE.

In this last section we would like to focus on a challenging non-integrable model, and understand whether there exist differences on the complexity (as indicated by the cTEE) for simulating local physics. In particular, we suspect that equilibration temperatures may play again some role, as for DecoAOE, since:

- tMPS represent the influence of the system on itself, i.e. how it behaves as a bath. Knowing that non-integrable systems thermalize, it is possible that a signatures of temperature are visible in the cTEE.

- The rank of the environments at given times t, yielding the singular values that enter the definition of cTEE, is upper bounded by either the OSEE of local operators evolved until $T - t$ (which grows linearly for non-integrable Hamiltonians) or by the OSEE of the effective density matrix evolved until that time t.

  If our thoughts are correct, the support of these density matrices is effectively reduced by the limited bond dimension at a fixed truncation threshold. Baring in mind that density matrices of small subsystems tend to approach their thermal ensemble counterparts, which are characterized by a bounded OSEE, it is possible that cTEE displays an early linear increase, followed by a decay to a steady, temperature-dependent value.

In Fig. 5.12 we recover representative states equilibrating within the same range of temperatures explored in Sec. 4.3.3 at Ch. 4 for our favorite non-integrable Ising model point $\mathrm{J} = -1,\ g = -1\ h = -0.5$. Despite we know that cTEE is not well converged for $\chi = 256$, we identify clear differences among the accessed temperature regimes:

- Negative temperatures (red and orange-red curves) do not show the polynomial growth of the main cTEE hump, rapidly stabilizing to an constant value.

- Positive temperatures (violet to green) transition from the operator edge hump to a *linearly* rising of the maximum cTEE, corresponding to the time bulk hump explained in Fig. 5.2. The slope of this apparently linear growth tilts up as temperature decreases (from green to violet[4]).

- A peak is reached by positive temperature cases, followed by a decay. The height of the peak appears to increase as temperatures fall, and the decay is also delayed for these *colder* states. The cases close to high temperature, with $\beta|\mathrm{J}| \in [-0.2, 0.2]$, reach a converged temperature-dependent value, with a clear minimum at $\beta = 0$. To ease the 3D visualization of this V-shape, we plotted black markers at the cuts corresponding to $|\mathrm{J}|T = 15$ and 20.

[4]It is true that the lowest temperatures simulated here appear to escape this trend, but we also saw in Fig. 5.3 that higher bond dimensions are required for cTEE to converge, and that $\chi = 512$ delayed the decay for the initial state $|+\rangle$. This invites us to think that the use of more computational resources would match the expectations of an increasing slope $\propto |\beta|$.

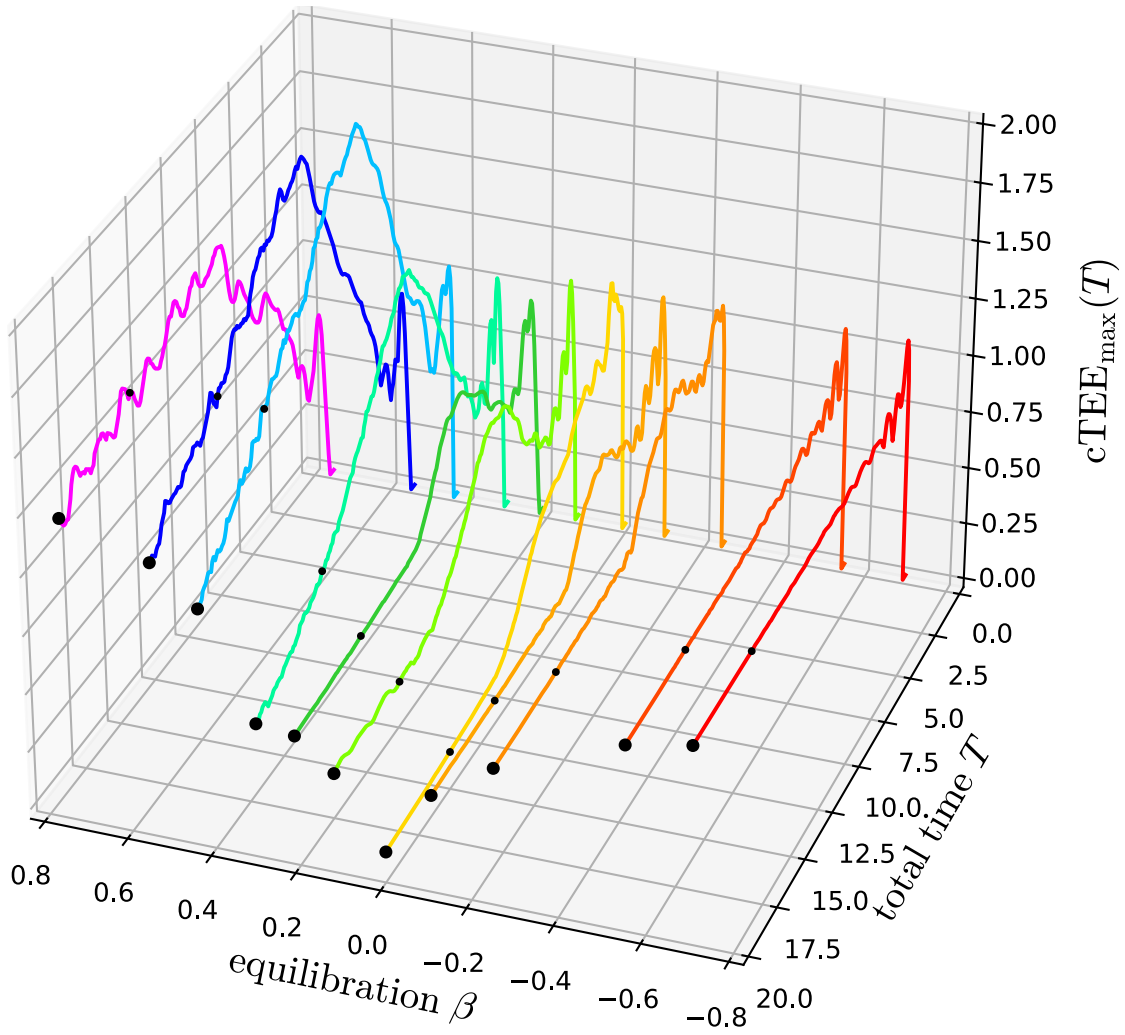

Figure 5.12: Connection between cTEE and temperature in non-integrable Hamitlonians. For the non-integrable point $\mathrm{J} = -1,\ g = -1\ h = -0.5$ we evolve different initial states with equilibration temperatures within the range $\beta|\mathrm{J}| \in [-0.8, 0.8]$. We detect (1) the saturation of cTEE to constant for negative temperatures; (2) an early increase of the cTEE for positive temperatures, steeper as the temperature decreases; (3) a decay to saturating value dependent on temperature with V-shape profile centered at $\beta = 0$.

The V-shape centered at $\beta = 0$, is consistent with that observed for the Pauli Weight requirement in Sec. 4.3.3 at Ch. 4. Thus we conclude that, up to proving convergence of these results for bigger bond dimensions, our intuition on the thermalization of the effective density matrices at intermediate times of the light-cone imposes a stringent upper bound on the rank of the environments, forcing the initially volume law growth of cTEE to fall down to a temperature-dependent constant. Such a constant is minimum for density matrices converging to infinite temperature states, as observed in Fig. 5.12 for the yellow curve.

We receive this result as the potential *icing on the cake* of this thesis: it seems that the light-cone algorithm implements the transition to an area law imposed by thermalization that Dubail (2017) had foreseen, and that colleagues have searched for in the past (Surace et al. (2019), Frías-Pérez et al. (2024)). The transverse contraction could be effectively trading entanglement by mixture, or in other words recovering the scaling of complexity for thermal matrices in the long time limit.

This brings us to conjecture that Bañuls et al. (2009); Müller-Hermes et al. (2012a) already gave the prescription to overcome the entanglement barrier in the transverse picture. This barrier is possibly not anymore an indefinitely increasing linear ramp of an entanglement measure; it could rather be a mountain, with finite height and width, that could be crossed (provided one counted with enough resources to climb up the summit).

5.3 Outlook in the Transverse Picture.

In future work we would like to land all these predictions on analytical grounds by performing calculations for quadratic fermion models like XY and XXZ for the influence functional for integrable Hamiltonians. If possible, analyzing the dependence on temperature with robust tools like QFT at finite temperature would be enlightening, together with stabilizing our algorithm implementations to clearly show bond dimension convergence on the temperature behavior outlined in the last section.

In connection with the former, understanding the effect of truncation on unequal-time correlations between local operators (i.e. the impact of compression on the memory of the system) could open interesting bridges with other studies like that of Sonner et al. (2025).

6

Summary and Conclusions

In this thesis we studied three different approaches for optimally contracting the 2-dimensional Tensor Network representing the evolution of local observables for initial unentangled states. Such a task is known to be challenging when the Hamiltonian inducing the unitary evolution is non-integrable, which translates in a volume law growth of the Operator Space Entanglement Entropy in both Schrödinger and Heisenberg pictures. With the purpose of overcoming this entanglement barrier, we explored modifications of the Time Evolving Block Decimation algorithm for density matrices in Ch. 3, observables in Ch. 4 and influence functionals in Ch. 5.

In Chapter 2 we introduced the basic notions required to understand the problem tackled throughout the thesis: the dynamics of many-body quantum systems after a quench. Since predicting this dynamics exactly requires an exponentially growing amount of memory and computation time resources, we introduced Tensor Networks as a means to open a window through which these computations could be rendered amenable (provided the amount of entanglement generated during the evolution was bounded).

As expected from classical thermodynamics, generic systems thermalize, producing extensive amounts of entropy, which translates into an exponential growth of the dimensions of the tensors in which our physical objects are decomposed. In Tensor Network language, this growth of complexity is known as a volume law behavior of the entropy; the issue it poses, hindering the simulation of long time dynamics in non-integrable systems, is dubbed as the entanglement barrier.

In Chapter 3 we aimed at introducing a gap in the folded evolution Matrix Product Operator while saving the information on local observables; these are expected to clearly witness thermalization in generic Hamiltonians, and are easily accessible in experiments. The prescription of introducing a gap is believed to indirectly control the growth of entropy by bounding the accessible Hilbert space. In order to open a gap in the spectrum of the evolution, we first developed a means to address arbitrary matrix elements through Tensor Networks.

After that, we constructed two variants of a dissipative evolution imitating the unitary one: (1) total decoherence in an optimally chosen basis, and (2) generalized unphysical decoherence. The total decoherence scheme was especially interesting, as it gave a prescription for mapping quantum dynamics to the classical stochastic variable language. Nevertheless, to the best of our knowledge, finding the optimal basis in which the off-diagonals had to be eliminated required diagonalizing subspaces of big matrices, which could become a difficult variational task.

To avoid such a caveat, we shifted to generalized decoherence, finding a way to address the density matrix entries not contributing to local observables, and designing a decoherer superoperator that could be interspersed with unitary evolution. Despite the successful results for small systems, we detected that generalized decoherence induced unphysical negativity on the density matrix, since it cannot be written as a channel (Completely Positive and Trace Preserving map).

Nevertheless, generalized decoherence served as a bridge with Ch. 4, since the decoherers written in Pauli string language are operators truncating orthogonal Pauli Weight (the number of Pauli matrices spanning the off-diagonal for a fixed computational basis). This connection allowed us to study whether the Dissipation Assisted Operator Evolution algorithm could be extended to initial states different from infinite temperature ones.

This study consisted on characterizing the Pauli Weight requirement of the evolving expectation values for local observables in terms of contributing and non-contributing strings, and Pauli Weight ω (the number of Pauli matrices on a basis element). We found that expectation values with some initial Product States are simpler to simulate, since heavy strings ($\omega \gg 1$) contributed marginally to the observable, while others required more and more Pauli Weight. The same splitting between easy and hard initial states was found in terms of backflow, i.e. the amount of norm flowing back to contributing subspaces from non-contributing ones.

These results motivated an early-time characterization of this Pauli Weight requirement in terms of the Operator Weight Entropy, measuring through a single parameter how uneven the contribution from subspaces with different Pauli Weight was. This extensive study concluded that, for short times, not only the equilibration temperature of the states played a role on the Pauli Weight requirement, but also their geometry.

These preliminary results would be confirmed by the long time simulation of local observables through our modification of DAOE, the Decoherence Assisted Operator Evolution, truncating orthogonal Pauli Weight from a fixed threshold; our findings, appart of controlling the Operator Space Entanglement Entropy growth, wiped out any dependence further than equilibration temperature in the long term evolution when comparing to other converged algorithms like the light-cone. We concluded that initial pure states locally equilibrating to high temperature ensembles can be simulated with less Pauli Weight.

A final spatial characterization endowed us with a holistic picture of which Pauli Weight subspaces correspond to the thermal values in the overlap with the state, and which contain the spectral properties (oscillations). In the spreading of operators, a central diffusively spreading conserved lump of light strings yielded non-oscillating values to the observable, which we identify as the thermal contribution; a non-conserved front radiated from the lump contained heavier and heavier strings as time advanced, and this Pauli Weight growth was accompanied of strong oscillations, leading to the spectral properties.

Finally, in Ch. 4, we studied the transverse contraction of the 2-dimensional Tensor Network by characterizing the light-cone algorithm, with symmetric factorization of the environments and an open edge on the operator side. The measure of complexity for this method is the computational Time Entanglement Entropy, and we successfully upper bounded its behavior by connecting the rank of the truncated environments with that of Schrödinger and Heisenberg style contractions. Since the Operator Space Entanglement Entropy showed a better scaling with time (logarithmic or area laws), we concluded that in the transverse picture, the environment matrices should scale similarly or better than that.

By simulating several integrable Hamiltonians, we found agreement with our upper bound, obtaining results in all cases compatible with area and logarithmic laws for the growth of the computational Time Entanglement Entropy with time. For the case of dissipative evolution, the decay of the rank of the environments already present in Schrödinger and Heisenberg pictures was inherited in the transverse picture. Interestingly, a deeper study for the non-integrable Ising Hamiltonian with initial states thermalizing to different temperatures unveiled a structure with β, suggesting that high temperature states are also simpler to simulate in the transverse picture.

These results were obtained for non-converged simulations of the states, but the long-term Time Entanglement Entropy still reflected a temperature-dependent V-shape centered at infinite temperature. This inspired us to revisit the upper bounds established through the former rank discussion, and realize that it is not the rank of the global pure density matrix the one potentially upper bounding the rank of transverse contraction environments, but the reduced density matrices after some time, which are expected to thermalize. Since thermal equilibrium density matrices display a bounded Operator Space Entanglement Entropy, the results are coherent with former studies and the new insights studied throughout the thesis.

Potential continuations of this work could consist on performing deeper studies on the points that have been tangentially commented, like finding ways to diagonalize the local subspaces of density matrices and mapping the quantum dynamics to a classical stochastic process, or the applying the spatial characterization of Pauli Weight and operator spreading to the design of new algorithms targeting spectral properties.

Bibliography

D. A. Abanin, W. De Roeck, and F. Huveneers. Exponentially Slow Heating in Periodically Driven Many-Body Systems. *Physical Review Letters*, 115(25):256803, Dec. 2015. doi: 10.1103/PhysRevLett.115.256803. (Cited on page 2.)

V. Alba and P. Calabrese. Entanglement and thermodynamics after a quantum quench in integrable systems. *Proceedings of the National Academy of Sciences*, 114(30):7947–7951, July 2017. doi: 10.1073/pnas.1703516114. (Cited on page 39.)

A. Altland and B. D. Simons. *Condensed Matter Field Theory*. Cambridge University Press, Cambridge, 2 edition, 2010. doi: 10.1017/CBO9780511789984. (Cited on page 1.)

P. W. Anderson. More Is Different. *Science*, 177(4047):393–396, Aug. 1972. doi: 10.1126/science.177.4047.393. (Cited on page 1.)

A. Angrisani, A. Schmidhuber, M. S. Rudolph, M. Cerezo, Z. Holmes, and H.-Y. Huang. Classically estimating observables of noiseless quantum circuits, Sept. 2024. (Cited on page 104.)

A. Angrisani, A. A. Mele, M. S. Rudolph, M. Cerezo, and Z. Holmes. Simulating quantum circuits with arbitrary local noise using Pauli Propagation, Jan. 2025. (Cited on page 104.)

A. Avdoshkin and A. Dymarsky. Euclidean operator growth and quantum chaos. *Physical Review Research*, 2(4):043234, Nov. 2020. doi: 10.1103/PhysRevResearch.2.043234. (Cited on page 119.)

M. C. Bañuls, M. B. Hastings, F. Verstraete, and J. I. Cirac. Matrix Product States for Dynamical Simulation of Infinite Chains. *Physical Review Letters*, 102(24):240603, June 2009. doi: 10.1103/PhysRevLett.102.240603. (Cited on pages 32, 129, and 144.)

M. C. Bañuls, J. I. Cirac, and M. B. Hastings. Strong and Weak Thermalization of Infinite Nonintegrable Quantum Systems. *Physical Review Letters*, 106(5):050405, Feb. 2011. doi: 10.1103/PhysRevLett.106.050405. (Cited on page 76.)

J. A. Barandes. The Stochastic-Quantum Correspondence, Sept. 2023a. (Cited on page 51.)

J. A. Barandes. The Stochastic-Quantum Theorem, Sept. 2023b. (Cited on page 51.)

D. Barcons Ruiz, N. C. H. Hesp, H. Herzig Sheinfux, C. Ramos Marimón, C. M. Maissen, A. Principi, R. Asgari, T. Taniguchi, K. Watanabe, M. Polini, R. Hillenbrand, I. Torre, and F. H. L. Koppens. Experimental signatures of the transition from acoustic plasmon to electronic sound in graphene. *Science Advances*, 9(39):eadi0415, Sept. 2023. ISSN 2375-2548. doi: 10.1126/sciadv.adi0415. (Cited on page 2.)

J. H. Bardarson, F. Pollmann, and J. E. Moore. Unbounded Growth of Entanglement in Models of Many-Body Localization. *Physical Review Letters*, 109(1):017202, July 2012. doi: 10.1103/PhysRevLett.109.017202. (Cited on page 41.)

R. Barends, L. Lamata, J. Kelly, L. García-Álvarez, A. G. Fowler, A. Megrant, E. Jeffrey, T. C. White, D. Sank, J. Y. Mutus, B. Campbell, Y. Chen, Z. Chen, B. Chiaro, A. Dunsworth, I.-C. Hoi, C. Neill, P. J. J. O'Malley, C. Quintana, P. Roushan, A. Vainsencher, J. Wenner, E. Solano, and J. M. Martinis. Digital quantum simulation of fermionic models with a superconducting circuit. *Nature Communications*, 6(1):7654, July 2015. ISSN 2041-1723. doi: 10.1038/ncomms8654. (Cited on page 3.)

T. Barthel. Precise evaluation of thermal response functions by optimized density matrix renormalization group schemes. *New Journal of Physics*, 15(7):073010, July 2013. ISSN 1367-2630. doi: 10.1088/1367-2630/15/7/073010. (Cited on page 61.)

T. Barthel and Y. Zhang. Optimized Lie–Trotter–Suzuki decompositions for two and three non-commuting terms. *Annals of Physics*, 418:168165, July 2020. ISSN 0003-4916. doi: 10.1016/j.aop.2020.168165. (Cited on page 30.)

T. Barthel, U. Schollwöck, and S. R. White. Spectral functions in one-dimensional quantum systems at finite temperature using the density matrix renormalization group. *Physical Review B*, 79(24):245101, June 2009. doi: 10.1103/PhysRevB.79.245101. (Cited on page 61.)

T. Begušić and G. K.-L. Chan. Real-Time Operator Evolution in Two and Three Dimensions via Sparse Pauli Dynamics. *PRX Quantum*, 6(2):020302, Apr. 2025. doi: 10.1103/PRXQuantum.6.020302. (Cited on page 104.)

T. Begušić, K. Hejazi, and G. K.-L. Chan. Simulating quantum circuit expectation values by Clifford perturbation theory. *The Journal of Chemical Physics*, 162(15):154110, Apr. 2025. ISSN 0021-9606. doi: 10.1063/5.0269149. (Cited on page 127.)

G. Benenti, G. Casati, T. Prosen, D. Rossini, and M. Žnidarič. Charge and spin transport in strongly correlated one-dimensional quantum systems driven far from equilibrium. *Physical Review B*, 80(3):035110, July 2009. doi: 10.1103/PhysRevB.80.035110. (Cited on page 78.)

J. Berges, Sz. Borsányi, and C. Wetterich. Prethermalization. *Physical Review Letters*, 93 (14):142002, Sept. 2004. doi: 10.1103/PhysRevLett.93.142002. (Cited on page 2.)

H. Bernien, S. Schwartz, A. Keesling, H. Levine, A. Omran, H. Pichler, S. Choi, A. S. Zibrov, M. Endres, M. Greiner, V. Vuletić, and M. D. Lukin. Probing many-body

dynamics on a 51-atom quantum simulator. *Nature*, 551(7682):579–584, Nov. 2017. ISSN 1476-4687. doi: 10.1038/nature24622. (Cited on page 2.)

A. V. Bezvershenko, C.-M. Halati, A. Sheikhan, C. Kollath, and A. Rosch. Dicke Transition in Open Many-Body Systems Determined by Fluctuation Effects. *Physical Review Letters*, 127(17):173606, Oct. 2021. doi: 10.1103/PhysRevLett.127.173606. (Cited on page 3.)

M. Binder and T. Barthel. Minimally entangled typical thermal states versus matrix product purifications for the simulation of equilibrium states and time evolution. *Physical Review B*, 92(12):125119, Sept. 2015. doi: 10.1103/PhysRevB.92.125119. (Cited on page 61.)

R. Blatt and C. F. Roos. Quantum simulations with trapped ions. *Nature Physics*, 8(4): 277–284, Apr. 2012. ISSN 1745-2481. doi: 10.1038/nphys2252. (Cited on page 3.)

I. Bloch, J. Dalibard, and W. Zwerger. Many-body physics with ultracold gases. *Reviews of Modern Physics*, 80(3):885–964, July 2008. doi: 10.1103/RevModPhys.80.885. (Cited on page 3.)

I. Bloch, J. Dalibard, and S. Nascimbène. Quantum simulations with ultracold quantum gases. *Nature Physics*, 8(4):267–276, Apr. 2012. ISSN 1745-2481. doi: 10.1038/nphys2259. (Cited on page 3.)

O. Bohigas, M. J. Giannoni, and C. Schmit. Characterization of Chaotic Quantum Spectra and Universality of Level Fluctuation Laws. *Physical Review Letters*, 52(1):1–4, Jan. 1984. doi: 10.1103/PhysRevLett.52.1. (Cited on page 13.)

P. Bordia, H. Lüschen, U. Schneider, M. Knap, and I. Bloch. Periodically driving a many-body localized quantum system. *Nature Physics*, 13(5):460–464, May 2017. ISSN 1745-2481. doi: 10.1038/nphys4020. (Cited on page 2.)

T. Bourdel, L. Khaykovich, J. Cubizolles, J. Zhang, F. Chevy, M. Teichmann, L. Tarruell, S. J. J. M. F. Kokkelmans, and C. Salomon. Experimental Study of the BEC-BCS Crossover Region in Lithium 6. *Physical Review Letters*, 93(5):050401, July 2004. doi: 10.1103/PhysRevLett.93.050401. (Cited on page 3.)

C. Brahms, L. Zhang, X. Shen, U. Bhattacharya, M. Recasens, J. Osmond, T. Grass, R. W. Chhajlany, K. A. Hallman, R. F. Haglund, S. T. Pantelides, M. Lewenstein, J. C. Travers, and A. S. Johnson. Decoupled few-femtosecond phase transitions in vanadium dioxide. *Nature Communications*, 16(1):3714, Apr. 2025. ISSN 2041-1723. doi: 10.1038/s41467-025-58895-z. (Cited on page 2.)

H.-P. Breuer and F. Petruccione. *The Theory of Open Quantum Systems*. Oxford University Press, Oxford ; New York, 2002. ISBN 978-0-19-852063-4. (Cited on pages 7, 15, and 26.)

A. Browaeys and T. Lahaye. Many-body physics with individually controlled Rydberg atoms. *Nature Physics*, 16(2):132–142, Feb. 2020. ISSN 1745-2481. doi: 10.1038/s41567-019-0733-z. (Cited on page 3.)

T. A. Brun. A simple model of quantum trajectories. *American Journal of Physics*, 70(7): 719–737, July 2002. ISSN 0002-9505. doi: 10.1119/1.1475328. (Cited on page 16.)

S. Buob, J. Höschele, V. Makhalov, A. Rubio-Abadal, and L. Tarruell. A Strontium Quantum-Gas Microscope. *PRX Quantum*, 5(2):020316, Apr. 2024. doi: 10.1103/PRXQuantum.5.020316. (Cited on page 3.)

C. R. Cabrera, L. Tanzi, J. Sanz, B. Naylor, P. Thomas, P. Cheiney, and L. Tarruell. Quantum liquid droplets in a mixture of Bose-Einstein condensates. *Science*, 359(6373): 301–304, Jan. 2018. doi: 10.1126/science.aao5686. (Cited on page 3.)

P. Calabrese. Introductory lecture on thermalization, Feb. 2024. (Cited on pages 12 and 13.)

P. Calabrese and J. Cardy. Entanglement entropy and quantum field theory. *Journal of Statistical Mechanics: Theory and Experiment*, 2004(06):P06002, June 2004. ISSN 1742-5468. doi: 10.1088/1742-5468/2004/06/P06002. (Cited on page 39.)

P. Calabrese and J. L. Cardy. Evolution of entanglement entropy in one-dimensional systems. *J. Stat. Mech.*, 0504:P04010, 2005. doi: 10.1088/1742-5468/2005/04/P04010. (Cited on page 39.)

X. Cao. A statistical mechanism for operator growth. *Journal of Physics A: Mathematical and Theoretical*, 54(14):144001, Mar. 2021. ISSN 1751-8121. doi: 10.1088/1751-8121/abe77c. (Cited on page 119.)

S. Carignano, C. R. Marimón, and L. Tagliacozzo. Temporal entropy and the complexity of computing the expectation value of local operators after a quench. *Physical Review Research*, 6(3):033021, July 2024. ISSN 2643-1564. doi: 10.1103/PhysRevResearch.6.033021. (Cited on pages 131 and 135.)

D. M. Ceperley. Path integrals in the theory of condensed helium. *Reviews of Modern Physics*, 67(2):279–355, Apr. 1995. doi: 10.1103/RevModPhys.67.279. (Cited on page 1.)

S. Cerezo-Roquebrún, A. Bou-Comas, J. T. Schneider, E. López, L. Tagliacozzo, and S. Carignano. Spatio-temporal tensor-network approaches to out-of-equilibrium dynamics bridging open and closed systems, Feb. 2025. (Cited on page 36.)

A. M. Chebotarev and A. E. Teretenkov. Singular value decomposition for the Takagi factorization of symmetric matrices. *Applied Mathematics and Computation*, 234:380–384, May 2014. ISSN 0096-3003. doi: 10.1016/j.amc.2014.01.170. (Cited on page 30.)

C. S. Chisholm, A. Frölian, E. Neri, R. Ramos, L. Tarruell, and A. Celi. Encoding a one-dimensional topological gauge theory in a Raman-coupled Bose-Einstein condensate. *Physical Review Research*, 4(4):043088, Nov. 2022. doi: 10.1103/PhysRevResearch.4.043088. (Cited on page 3.)

J. I. Cirac and P. Zoller. Quantum Computations with Cold Trapped Ions. *Physical Review Letters*, 74(20):4091–4094, May 1995. doi: 10.1103/PhysRevLett.74.4091. (Cited on page 3.)

P. Coleman. *Introduction to Many-Body Physics*. Cambridge University Press, Cambridge, 2015. ISBN 978-0-521-86488-6. doi: 10.1017/CBO9781139020916. (Cited on page 1.)

J. Cui, J. I. Cirac, and M. C. Bañuls. Variational Matrix Product Operators for the Steady State of Dissipative Quantum Systems. *Physical Review Letters*, 114(22):220601, June 2015. doi: 10.1103/PhysRevLett.114.220601. (Cited on page 78.)

L. D'Alessio, K. , Yariv, P. , Anatoli, and M. and Rigol. From quantum chaos and eigenstate thermalization to statistical mechanics and thermodynamics. *Advances in Physics*, 65(3):239–362, May 2016. ISSN 0001-8732. doi: 10.1080/00018732.2016.1198134. (Cited on pages 14 and 51.)

A. J. Daley, C. Kollath, U. Schollwöck, and G. Vidal. Time-dependent density-matrix renormalization-group using adaptive effective Hilbert spaces. *Journal of Statistical Mechanics: Theory and Experiment*, 2004(04):P04005, Apr. 2004a. ISSN 1742-5468. doi: 10.1088/1742-5468/2004/04/P04005. (Cited on page 31.)

A. J. Daley, C. Kollath, U. Schollwöck, and G. Vidal. Time-dependent density-matrix renormalization-group using adaptive effective Hilbert spaces. *Journal of Statistical Mechanics: Theory and Experiment*, 2004(04):P04005, Apr. 2004b. ISSN 1742-5468. doi: 10.1088/1742-5468/2004/04/P04005. (Cited on page 61.)

J. M. Deutsch. Quantum statistical mechanics in a closed system. *Physical Review A*, 43 (4):2046–2049, Feb. 1991. doi: 10.1103/PhysRevA.43.2046. (Cited on page 13.)

M. H. Devoret and R. J. Schoelkopf. Superconducting Circuits for Quantum Information: An Outlook. *Science*, 339(6124):1169–1174, Mar. 2013. doi: 10.1126/science.1231930. (Cited on page 3.)

S. Diehl, A. Micheli, A. Kantian, B. Kraus, H. P. Büchler, and P. Zoller. Quantum states and phases in driven open quantum systems with cold atoms. *Nature Physics*, 4(11): 878–883, Nov. 2008. ISSN 1745-2481. doi: 10.1038/nphys1073. (Cited on page 16.)

N. Dowling, P. Kos, and X. Turkeshi. Magic of the Heisenberg Picture, Apr. 2025. (Cited on page 127.)

J. Dubail. Entanglement scaling of operators: A conformal field theory approach, with a glimpse of simulability of long-time dynamics in 1 + 1d. *Journal of Physics A: Mathematical and Theoretical*, 50(23):234001, May 2017. ISSN 1751-8121. doi: 10.1088/1751-8121/aa6f38. (Cited on pages 40, 41, 43, 44, and 144.)

C. Eckart and G. Young. The Approximation of One Matrix by Another of Lower Rank. *Psychometrika*, 1(3):211–218, Sept. 1936. ISSN 0033-3123, 1860-0980. doi: 10.1007/BF02288367. (Cited on page 36.)

T. Enss and J. Sirker. Light cone renormalization and quantum quenches in one-dimensional Hubbard models. *New Journal of Physics*, 14(2):023008, Feb. 2012. ISSN 1367-2630. doi: 10.1088/1367-2630/14/2/023008. (Cited on page 61.)

G. Evenbly. Tensors.net. (Cited on page 37.)

M. Fagotti and F. H. L. Essler. Reduced density matrix after a quantum quench. *Physical Review B*, 87(24):245107, June 2013. doi: 10.1103/PhysRevB.87.245107. (Cited on page 15.)

D. Fausti, R. I. Tobey, N. Dean, S. Kaiser, A. Dienst, M. C. Hoffmann, S. Pyon, T. Takayama, H. Takagi, and A. Cavalleri. Light-Induced Superconductivity in a Stripe-Ordered Cuprate. *Science*, 331(6014):189–191, Jan. 2011. doi: 10.1126/science.1197294. (Cited on page 2.)

A. E. Feiguin and G. A. Fiete. Spectral properties of a spin-incoherent Luttinger liquid. *Physical Review B*, 81(7):075108, Feb. 2010. doi: 10.1103/PhysRevB.81.075108. (Cited on page 61.)

R. P. Feynman. Simulating physics with computers. *International Journal of Theoretical Physics*, 21(6):467–488, June 1982. ISSN 1572-9575. doi: 10.1007/BF02650179. (Cited on page 3.)

R. P. Feynman and F. L. Vernon. The theory of a general quantum system interacting with a linear dissipative system. *Annals of Physics*, 24:118–173, Oct. 1963. ISSN 0003-4916. doi: 10.1016/0003-4916(63)90068-X. (Cited on page 36.)

A. Foligno, T. Zhou, and B. Bertini. Temporal Entanglement in Chaotic Quantum Circuits. *Physical Review X*, 13(4):041008, Oct. 2023. doi: 10.1103/PhysRevX.13.041008. (Cited on pages 43, 133, and 136.)

M. Frías-Pérez and M. C. Bañuls. Light cone tensor network and time evolution. *Physical Review B*, 106(11):115117, Sept. 2022. doi: 10.1103/PhysRevB.106.115117. (Cited on pages 34, 36, 123, 129, and 130.)

M. Frías-Pérez, L. Tagliacozzo, and M. C. Bañuls. Converting Long-Range Entanglement into Mixture: Tensor-Network Approach to Local Equilibration. *Physical Review Letters*, 132(10):100402, Mar. 2024. doi: 10.1103/PhysRevLett.132.100402. (Cited on pages 44, 124, and 144.)

G. Giudice, G. Giudici, M. Sonner, J. Thoenniss, A. Lerose, D. A. Abanin, and L. Piroli. Temporal Entanglement, Quasiparticles, and the Role of Interactions. *Physical Review Letters*, 128(22):220401, June 2022. doi: 10.1103/PhysRevLett.128.220401. (Cited on page 43.)

C. Gogolin and J. Eisert. Equilibration, thermalisation, and the emergence of statistical mechanics in closed quantum systems. *Reports on Progress in Physics*, 79(5):056001, Apr. 2016. ISSN 0034-4885. doi: 10.1088/0034-4885/79/5/056001. (Cited on pages 12 and 14.)

C. Gogolin, M. P. Müller, and J. Eisert. Absence of Thermalization in Nonintegrable Systems. *Physical Review Letters*, 106(4):040401, Jan. 2011. doi: 10.1103/PhysRevLett.106.040401. (Cited on page 15.)

S. Gopalakrishnan, D. A. Huse, V. Khemani, and R. Vasseur. Hydrodynamics of operator spreading and quasiparticle diffusion in interacting integrable systems. *Physical Review B*, 98(22):220303, Dec. 2018. doi: 10.1103/PhysRevB.98.220303. (Cited on pages 89 and 120.)

M. Grady. Infinite set of conserved charges in the Ising model. *Physical Review D*, 25(4):1103–1113, Feb. 1982. doi: 10.1103/PhysRevD.25.1103. (Cited on page 15.)

M. Greiner, O. Mandel, T. Esslinger, T. W. Hänsch, and I. Bloch. Quantum phase transition from a superfluid to a Mott insulator in a gas of ultracold atoms. *Nature*, 415(6867):39–44, Jan. 2002. ISSN 1476-4687. doi: 10.1038/415039a. (Cited on page 3.)

M. Gring, M. Kuhnert, T. Langen, T. Kitagawa, B. Rauer, M. Schreitl, I. Mazets, D. A. Smith, E. Demler, and J. Schmiedmayer. Relaxation and Prethermalization in an Isolated Quantum System. *Science*, 337(6100):1318–1322, Sept. 2012. doi: 10.1126/science.1224953. (Cited on page 2.)

X. Gu, A. F. Kockum, A. Miranowicz, Y.-x. Liu, and F. Nori. Microwave photonics with superconducting quantum circuits. *Physics Reports*, 718–719:1–102, Nov. 2017. ISSN 0370-1573. doi: 10.1016/j.physrep.2017.10.002. (Cited on page 3.)

J. Haegeman, J. I. Cirac, T. J. Osborne, I. Pižorn, H. Verschelde, and F. Verstraete. Time-Dependent Variational Principle for Quantum Lattices. *Physical Review Letters*, 107(7):070601, Aug. 2011. doi: 10.1103/PhysRevLett.107.070601. (Cited on page 4.)

J. C. Halimeh, M. Aidelsburger, F. Grusdt, P. Hauke, and B. Yang. Cold-atom quantum simulators of gauge theories. *Nature Physics*, 21(1):25–36, Jan. 2025. ISSN 1745-2481. doi: 10.1038/s41567-024-02721-8. (Cited on page 3.)

M. J. Hartmann, J. Prior, S. R. Clark, and M. B. Plenio. Density Matrix Renormalization Group in the Heisenberg Picture. *Physical Review Letters*, 102(5):057202, Feb. 2009. doi: 10.1103/PhysRevLett.102.057202. (Cited on page 31.)

M. B. Hastings. An area law for one-dimensional quantum systems. *Journal of Statistical Mechanics: Theory and Experiment*, 2007(08):P08024, Aug. 2007. ISSN 1742-5468. doi: 10.1088/1742-5468/2007/08/P08024. (Cited on pages 4 and 39.)

M. B. Hastings and R. Mahajan. Connecting entanglement in time and space: Improving the folding algorithm. *Physical Review A*, 91(3):032306, Mar. 2015. doi: 10.1103/PhysRevA.91.032306. (Cited on pages 129 and 130.)

M. B. Hastings, I. González, A. B. Kallin, and R. G. Melko. Measuring Renyi Entanglement Entropy in Quantum Monte Carlo Simulations. *Physical Review Letters*, 104(15):157201, Apr. 2010. doi: 10.1103/PhysRevLett.104.157201. (Cited on page 40.)

M. Heyl, A. Polkovnikov, and S. Kehrein. Dynamical Quantum Phase Transitions in the Transverse-Field Ising Model. *Physical Review Letters*, 110(13):135704, Mar. 2013. doi: 10.1103/PhysRevLett.110.135704. (Cited on page 1.)

T. Holstein and H. Primakoff. Field Dependence of the Intrinsic Domain Magnetization of a Ferromagnet. *Physical Review*, 58(12):1098–1113, Dec. 1940. doi: 10.1103/PhysRev.58.1098. (Cited on page 23.)

E. Ilievski, M. Medenjak, T. Prosen, and L. Zadnik. Quasilocal charges in integrable lattice systems. *Journal of Statistical Mechanics: Theory and Experiment*, 2016(6):064008, June 2016. ISSN 1742-5468. doi: 10.1088/1742-5468/2016/06/064008. (Cited on page 15.)

R. Islam, R. Ma, P. M. Preiss, M. Eric Tai, A. Lukin, M. Rispoli, and M. Greiner. Measuring entanglement entropy in a quantum many-body system. *Nature*, 528(7580):77–83, Dec. 2015. ISSN 1476-4687. doi: 10.1038/nature15750. (Cited on page 40.)

S. Jesenko and M. Žnidarič. Finite-temperature magnetization transport of the one-dimensional anisotropic Heisenberg model. *Physical Review B*, 84(17):174438, Nov. 2011. doi: 10.1103/PhysRevB.84.174438. (Cited on page 78.)

J. Jordan, R. Orús, G. Vidal, F. Verstraete, and J. I. Cirac. Classical Simulation of Infinite-Size Quantum Lattice Systems in Two Spatial Dimensions. *Physical Review Letters*, 101(25):250602, Dec. 2008. doi: 10.1103/PhysRevLett.101.250602. (Cited on page 17.)

P. Jordan and E. Wigner. Über das Paulische Äquivalenzverbot. *Zeitschrift für Physik*, 47 (9):631–651, Sept. 1928. ISSN 0044-3328. doi: 10.1007/BF01331938. (Cited on page 23.)

C. Karrasch, J. H. Bardarson, and J. E. Moore. Finite-Temperature Dynamical Density Matrix Renormalization Group and the Drude Weight of Spin-$1/2$ Chains. *Physical Review Letters*, 108(22):227206, May 2012. doi: 10.1103/PhysRevLett.108.227206. (Cited on page 61.)

C. Karrasch, D. M. Kennes, and F. Heidrich-Meisner. Spin and thermal conductivity of quantum spin chains and ladders. *Physical Review B*, 91(11):115130, Mar. 2015. doi: 10.1103/PhysRevB.91.115130. (Cited on page 61.)

D. M. Kennes and C. Karrasch. Extending the range of real time density matrix renormalization group simulations. *Computer Physics Communications*, 200:37–43, Mar. 2016. ISSN 0010-4655. doi: 10.1016/j.cpc.2015.10.019. (Cited on page 61.)

V. Khemani, A. Vishwanath, and D. A. Huse. Operator Spreading and the Emergence of Dissipative Hydrodynamics under Unitary Evolution with Conservation Laws. *Physical Review X*, 8(3):031057, Sept. 2018. doi: 10.1103/PhysRevX.8.031057. (Cited on pages 89 and 120.)

H. Kim and D. A. Huse. Ballistic Spreading of Entanglement in a Diffusive Nonintegrable System. *Physical Review Letters*, 111(12):127205, Sept. 2013. doi: 10.1103/PhysRevLett.111.127205. (Cited on page 39.)

T. Kinoshita, T. Wenger, and D. S. Weiss. A quantum Newton's cradle. *Nature*, 440(7086):900–903, Apr. 2006. ISSN 1476-4687. doi: 10.1038/nature04693. (Cited on page 3.)

M. Kliesch, D. Gross, and J. Eisert. Matrix-Product Operators and States: NP-Hardness and Undecidability. *Physical Review Letters*, 113(16):160503, Oct. 2014. doi: 10.1103/PhysRevLett.113.160503. (Cited on page 78.)

B. Kloss, J. Thoenniss, M. Sonner, A. Lerose, M. T. Fishman, E. M. Stoudenmire, O. Parcollet, A. Georges, and D. A. Abanin. Equilibrium quantum impurity problems via matrix product state encoding of the retarded action. *Physical Review B*, 108(20):205110, Nov. 2023. doi: 10.1103/PhysRevB.108.205110. (Cited on pages 34 and 43.)

F. H. L. Koppens, D. E. Chang, and F. J. García de Abajo. Graphene Plasmonics: A Platform for Strong Light–Matter Interactions. *Nano Letters*, 11(8):3370–3377, Aug. 2011. ISSN 1530-6984. doi: 10.1021/nl201771h. (Cited on page 2.)

P. Krantz, M. Kjaergaard, F. Yan, T. P. Orlando, S. Gustavsson, and W. D. Oliver. A quantum engineer's guide to superconducting qubits. *Applied Physics Reviews*, 6(2):021318, June 2019. ISSN 1931-9401. doi: 10.1063/1.5089550. (Cited on page 26.)

E.-J. Kuo, B. Ware, P. Lunts, M. Hafezi, and C. D. White. Energy diffusion in weakly interacting chains with fermionic dissipation assisted operator evolution. *Physical Review B*, 110(7):075149, Aug. 2024. doi: 10.1103/PhysRevB.110.075149. (Cited on page 84.)

B. Ladewig, S. Diehl, and M. Buchhold. Monitored open fermion dynamics: Exploring the interplay of measurement, decoherence, and free Hamiltonian evolution. *Physical Review Research*, 4(3):033001, July 2022. doi: 10.1103/PhysRevResearch.4.033001. (Cited on page 16.)

J. I. Latorre, E. Rico, and G. Vidal. Ground state entanglement in quantum spin chains, Mar. 2004. (Cited on page 17.)

A. Lerose, M. Sonner, and D. A. Abanin. Influence Matrix Approach to Many-Body Floquet Dynamics. *Physical Review X*, 11(2):021040, May 2021a. doi: 10.1103/PhysRevX.11.021040. (Cited on pages 36 and 42.)

A. Lerose, M. Sonner, and D. A. Abanin. Scaling of temporal entanglement in proximity to integrability. *Physical Review B*, 104(3):035137, July 2021b. doi: 10.1103/PhysRevB.104.035137. (Cited on pages 36 and 43.)

A. Lerose, M. Sonner, and D. A. Abanin. Overcoming the entanglement barrier in quantum many-body dynamics via space-time duality. *Physical Review B*, 107(6):L060305, Feb. 2023. doi: 10.1103/PhysRevB.107.L060305. (Cited on pages 34, 43, and 129.)

E. H. Lieb and D. W. Robinson. The finite group velocity of quantum spin systems. *Communications in Mathematical Physics*, 28(3):251–257, Sept. 1972. ISSN 1432-0916. doi: 10.1007/BF01645779. (Cited on pages 36 and 123.)

N. Linden, S. Popescu, A. J. Short, and A. Winter. Quantum mechanical evolution towards thermal equilibrium. *Physical Review E*, 79(6):061103, June 2009. doi: 10.1103/PhysRevE.79.061103. (Cited on page 12.)

J. Lloyd, T. Rakovszky, F. Pollmann, and C. von Keyserlingk. Ballistic to diffusive crossover in a weakly interacting Fermi gas. *Physical Review B*, 109(20):205108, May 2024. doi: 10.1103/PhysRevB.109.205108. (Cited on page 84.)

U. Marzolino and T. Prosen. Computational complexity of nonequilibrium steady states of quantum spin chains. *Physical Review A*, 93(3):032306, Mar. 2016. doi: 10.1103/PhysRevA.93.032306. (Cited on page 78.)

E. Mascarenhas, H. Flayac, and V. Savona. Matrix-product-operator approach to the nonequilibrium steady state of driven-dissipative quantum arrays. *Physical Review A*, 92(2):022116, Aug. 2015. doi: 10.1103/PhysRevA.92.022116. (Cited on page 78.)

S. Masot-Llima and A. Garcia-Saez. Stabilizer Tensor Networks: Universal Quantum Simulator on a Basis of Stabilizer States. *Physical Review Letters*, 133(23):230601, Dec. 2024. doi: 10.1103/PhysRevLett.133.230601. (Cited on page 127.)

N. Metropolis, A. W. Rosenbluth, M. N. Rosenbluth, A. H. Teller, and E. Teller. Equation of State Calculations by Fast Computing Machines. *The Journal of Chemical Physics*, 21 (6):1087–1092, June 1953. ISSN 0021-9606. doi: 10.1063/1.1699114. (Cited on page 1.)

A. Milekhin, Z. Adamska, and J. Preskill. Observable and computable entanglement in time, Feb. 2025. (Cited on page 131.)

C. Monroe, W. C. Campbell, L.-M. Duan, Z.-X. Gong, A. V. Gorshkov, P. W. Hess, R. Islam, K. Kim, N. M. Linke, G. Pagano, P. Richerme, C. Senko, and N. Y. Yao. Programmable quantum simulations of spin systems with trapped ions. *Reviews of Modern Physics*, 93 (2):025001, Apr. 2021. doi: 10.1103/RevModPhys.93.025001. (Cited on page 3.)

A. Müller-Hermes, J. I. Cirac, and M. C. Bañuls. Tensor network techniques for the computation of dynamical observables in one-dimensional quantum spin systems. *New Journal of Physics*, 14(7):075003, July 2012a. ISSN 1367-2630. doi: 10.1088/1367-2630/14/7/075003. (Cited on pages 42, 129, and 144.)

A. Müller-Hermes, J. Ignacio Cirac, and M. C. Bañuls. Tensor network techniques for the computation of dynamical observables in one-dimensional quantum spin systems. *New Journal of Physics*, 14(7):075003, July 2012b. ISSN 1367-2630. doi: 10.1088/1367-2630/14/7/075003. (Cited on page 32.)

M. A. Nielsen and I. L. Chuang. *Quantum Computation and Quantum Information*. Cambridge University Press, Cambridge ; New York, 2000. ISBN 978-0-521-63235-5 978-0-521-63503-5. (Cited on pages 7, 15, and 26.)

T. Nishino. Density Matrix Renormalization Group Method for 2D Classical Models. *Journal of the Physical Society of Japan*, 64(10):3598–3601, Oct. 1995. ISSN 0031-9015. doi: 10.1143/JPSJ.64.3598. (Cited on page 4.)

T. Nishino and K. Okunishi. Corner Transfer Matrix Renormalization Group Method. *Journal of the Physical Society of Japan*, 65(4):891–894, Apr. 1996. ISSN 0031-9015. doi: 10.1143/JPSJ.65.891. (Cited on page 4.)

K. Noh, L. Jiang, and B. Fefferman. Efficient classical simulation of noisy random quantum circuits in one dimension. *Quantum*, 4:318, Sept. 2020. doi: 10.22331/q-2020-09-11-318. (Cited on page 91.)

R. Orús. A practical introduction to tensor networks: Matrix product states and projected entangled pair states. *Annals of Physics*, 349:117–158, Oct. 2014. ISSN 0003-4916. doi: 10.1016/j.aop.2014.06.013. (Cited on page 17.)

R. Orús and G. Vidal. Infinite time-evolving block decimation algorithm beyond unitary evolution. *Physical Review B*, 78(15):155117, Oct. 2008. doi: 10.1103/PhysRevB.78.155117. (Cited on pages 31 and 36.)

D. E. Parker, X. Cao, A. Avdoshkin, T. Scaffidi, and E. Altman. A Universal Operator Growth Hypothesis. *Physical Review X*, 9(4):041017, Oct. 2019. doi: 10.1103/PhysRevX.9.041017. (Cited on page 119.)

D. Perez-Garcia, F. Verstraete, M. M. Wolf, and J. I. Cirac. Matrix product state representations. *Quantum Info. Comput.*, 7(5):401–430, July 2007. ISSN 1533-7146. (Cited on page 18.)

B. Pirvu, V. Murg, J. I. Cirac, and F. Verstraete. Matrix product operator representations. *New Journal of Physics*, 12(2):025012, Feb. 2010. ISSN 1367-2630. doi: 10.1088/1367-2630/12/2/025012. (Cited on pages 30 and 35.)

I. Pižorn and T. Prosen. Operator space entanglement entropy in XY spin chains. *Physical Review B*, 79(18):184416, May 2009a. doi: 10.1103/PhysRevB.79.184416. (Cited on page 41.)

I. Pižorn and T. Prosen. Operator space entanglement entropy in XY spin chains. *Physical Review B*, 79(18):184416, May 2009b. doi: 10.1103/PhysRevB.79.184416. (Cited on page 78.)

I. Pižorn, V. Eisler, S. Andergassen, and M. Troyer. Real time evolution at finite temperatures with operator space matrix product states. *New Journal of Physics*, 16(7):073007, July 2014. ISSN 1367-2630. doi: 10.1088/1367-2630/16/7/073007. (Cited on pages 31 and 78.)

A. Polkovnikov, K. Sengupta, A. Silva, and M. Vengalattore. Colloquium: Nonequilibrium dynamics of closed interacting quantum systems. *Reviews of Modern Physics*, 83(3):863–883, Aug. 2011. doi: 10.1103/RevModPhys.83.863. (Cited on page 14.)

J. Preskill. Quantum Computing in the NISQ era and beyond. *Quantum*, 2:79, Aug. 2018. doi: 10.22331/q-2018-08-06-79. (Cited on page 26.)

T. Prosen and I. Pižorn. Operator space entanglement entropy in a transverse Ising chain. *Physical Review A*, 76(3):032316, Sept. 2007a. doi: 10.1103/PhysRevA.76.032316. (Cited on pages 41 and 137.)

T. Prosen and I. Pižorn. Operator space entanglement entropy in a transverse Ising chain. *Physical Review A*, 76(3):032316, Sept. 2007b. doi: 10.1103/PhysRevA.76.032316. (Cited on page 78.)

T. Prosen and I. Pižorn. Quantum Phase Transition in a Far-from-Equilibrium Steady State of an XY Spin Chain. *Physical Review Letters*, 101(10):105701, Sept. 2008. doi: 10.1103/PhysRevLett.101.105701. (Cited on page 78.)

T. Prosen and M. Žnidarič. Is the efficiency of classical simulations of quantum dynamics related to integrability? *Physical Review E*, 75(1):015202, Jan. 2007. doi: 10.1103/PhysRevE.75.015202. (Cited on page 41.)

T. Prosen and M. Žnidarič. Matrix product simulations of non-equilibrium steady states of quantum spin chains. *Journal of Statistical Mechanics: Theory and Experiment*, 2009 (02):P02035, Feb. 2009. ISSN 1742-5468. doi: 10.1088/1742-5468/2009/02/P02035. (Cited on page 78.)

T. Prosen and M. Žnidarič. Diffusive high-temperature transport in the one-dimensional Hubbard model. *Physical Review B*, 86(12):125118, Sept. 2012. doi: 10.1103/PhysRevB.86.125118. (Cited on page 78.)

T. Rakovszky, F. Pollmann, and C. W. von Keyserlingk. Diffusive Hydrodynamics of Out-of-Time-Ordered Correlators with Charge Conservation. *Physical Review X*, 8(3):031058, Sept. 2018. doi: 10.1103/PhysRevX.8.031058. (Cited on pages 83 and 85.)

T. Rakovszky, C. W. von Keyserlingk, and F. Pollmann. Dissipation-assisted operator evolution method for capturing hydrodynamic transport. *Physical Review B*, 105(7):075131, Feb. 2022. doi: 10.1103/PhysRevB.105.075131. (Cited on pages 81 and 85.)

C. Ramos-Marimón, S. Carignano, and L. Tagliacozzo. Pauli weight requirement of the matrix elements in time-evolved local operators: Dependence beyond the equilibration temperature. *Physical Review B*, 111(9):094301, Mar. 2025. doi: 10.1103/PhysRevB.111.094301. (Cited on page 86.)

S.-J. Ran, E. Tirrito, C. Peng, X. Chen, L. Tagliacozzo, G. Su, and M. Lewenstein. *Tensor Network Contractions: Methods and Applications to Quantum Many-Body Systems*, volume 964 of *Lecture Notes in Physics*. Springer International Publishing, Cham, 2020. ISBN 978-3-030-34488-7 978-3-030-34489-4. doi: 10.1007/978-3-030-34489-4. (Cited on page 17.)

B. Rauer, S. Erne, T. Schweigler, F. Cataldini, M. Tajik, and J. Schmiedmayer. Recurrences in an isolated quantum many-body system. *Science*, 360(6386):307–310, Apr. 2018. doi: 10.1126/science.aan7938. (Cited on page 2.)

M. Rigol, V. Dunjko, and M. Olshanii. Thermalization and its mechanism for generic isolated quantum systems. *Nature*, 452(7189):854–858, Apr. 2008. ISSN 1476-4687. doi: 10.1038/nature06838. (Cited on page 14.)

M. Saffman, T. G. Walker, and K. Mølmer. Quantum information with Rydberg atoms. *Reviews of Modern Physics*, 82(3):2313–2363, Aug. 2010. doi: 10.1103/RevModPhys.82.2313. (Cited on page 3.)

U. Schollwöck. The density-matrix renormalization group in the age of matrix product states. *Annals of Physics*, 326(1):96–192, Jan. 2011. ISSN 0003-4916. doi: 10.1016/j.aop.2010.09.012. (Cited on page 4.)

M. Schreiber, S. S. Hodgman, P. Bordia, H. P. Lüschen, M. H. Fischer, R. Vosk, E. Altman, U. Schneider, and I. Bloch. Observation of many-body localization of interacting fermions in a quasirandom optical lattice. *Science*, 349(6250):842–845, Aug. 2015. doi: 10.1126/science.aaa7432. (Cited on page 2.)

N. Schuch, M. M. Wolf, F. Verstraete, and J. I. Cirac. Entropy Scaling and Simulability by Matrix Product States. *Physical Review Letters*, 100(3):030504, Jan. 2008. doi: 10.1103/PhysRevLett.100.030504. (Cited on page 39.)

M. Serbyn, Z. Papić, and D. A. Abanin. Universal Slow Growth of Entanglement in Interacting Strongly Disordered Systems. *Physical Review Letters*, 110(26):260601, June 2013. doi: 10.1103/PhysRevLett.110.260601. (Cited on page 42.)

M. Serbyn, D. A. Abanin, and Z. Papić. Quantum many-body scars and weak breaking of ergodicity. *Nature Physics*, 17(6):675–685, June 2021. ISSN 1745-2481. doi: 10.1038/s41567-021-01230-2. (Cited on page 2.)

Y.-Y. Shi, L.-M. Duan, and G. Vidal. Classical simulation of quantum many-body systems with a tree tensor network. *Physical Review A*, 74(2):022320, Aug. 2006. doi: 10.1103/PhysRevA.74.022320. (Cited on page 17.)

A. J. Short. Equilibration of quantum systems and subsystems. *New Journal of Physics*, 13 (5):053009, May 2011. ISSN 1367-2630. doi: 10.1088/1367-2630/13/5/053009. (Cited on page 12.)

J. Smith, A. Lee, P. Richerme, B. Neyenhuis, P. W. Hess, P. Hauke, M. Heyl, D. A. Huse, and C. Monroe. Many-body localization in a quantum simulator with programmable random disorder. *Nature Physics*, 12(10):907–911, Oct. 2016. ISSN 1745-2481. doi: 10.1038/nphys3783. (Cited on page 2.)

M. Sonner, A. Lerose, and D. A. Abanin. Influence functional of many-body systems: Temporal entanglement and matrix-product state representation. *Annals of Physics*,

435:168677, Dec. 2021. ISSN 0003-4916. doi: 10.1016/j.aop.2021.168677. (Cited on pages 36 and 43.)

M. Sonner, V. Link, and D. A. Abanin. Semi-group influence matrices for non-equilibrium quantum impurity models, Jan. 2025. (Cited on page 144.)

M. Srednicki. Chaos and quantum thermalization. *Physical Review E*, 50(2):888–901, Aug. 1994. doi: 10.1103/PhysRevE.50.888. (Cited on page 14.)

M. Srednicki. The approach to thermal equilibrium in quantized chaotic systems. *Journal of Physics A: Mathematical and General*, 32(7):1163, Feb. 1999. ISSN 0305-4470. doi: 10.1088/0305-4470/32/7/007. (Cited on page 14.)

N. S. Srivatsa and C. von Keyserlingk. Operator growth hypothesis in open quantum systems. *Physical Review B*, 109(12):125149, Mar. 2024. doi: 10.1103/PhysRevB.109.125149. (Cited on page 119.)

J. Surace, M. Piani, and L. Tagliacozzo. Simulating the out-of-equilibrium dynamics of local observables by trading entanglement for mixture. *Physical Review B*, 99(23):235115, June 2019. doi: 10.1103/PhysRevB.99.235115. (Cited on pages 44 and 144.)

M. Suzuki. Generalized Trotter's formula and systematic approximants of exponential operators and inner derivations with applications to many-body problems. *Communications in Mathematical Physics*, 51(2):183–190, June 1976. ISSN 1432-0916. doi: 10.1007/BF01609348. (Cited on pages 28 and 29.)

R. H. Swendsen and J.-S. Wang. Nonuniversal critical dynamics in Monte Carlo simulations. *Physical Review Letters*, 58(2):86–88, Jan. 1987. doi: 10.1103/PhysRevLett.58.86. (Cited on page 1.)

J. Thoenniss, A. Lerose, and D. A. Abanin. Nonequilibrium quantum impurity problems via matrix-product states in the temporal domain. *Physical Review B*, 107(19):195101, May 2023a. doi: 10.1103/PhysRevB.107.195101. (Cited on page 43.)

J. Thoenniss, M. Sonner, A. Lerose, and D. A. Abanin. Efficient method for quantum impurity problems out of equilibrium. *Physical Review B*, 107(20):L201115, May 2023b. doi: 10.1103/PhysRevB.107.L201115. (Cited on pages 34 and 43.)

A. C. Tiegel, S. R. Manmana, T. Pruschke, and A. Honecker. Matrix product state formulation of frequency-space dynamics at finite temperatures. *Physical Review B*, 90(6):060406, Aug. 2014. doi: 10.1103/PhysRevB.90.060406. (Cited on page 61.)

H. F. Trotter. On the product of semi-groups of operators. *Proceedings of the American Mathematical Society*, 10(4):545–551, 1959. ISSN 0002-9939, 1088-6826. doi: 10.1090/S0002-9939-1959-0108732-6. (Cited on page 28.)

X. Turkeshi, E. Tirrito, and P. Sierant. Magic spreading in random quantum circuits. *Nature Communications*, 16(1):2575, Mar. 2025. ISSN 2041-1723. doi: 10.1038/s41467-025-57704-x. (Cited on page 127.)

C. J. Turner, A. A. Michailidis, D. A. Abanin, M. Serbyn, and Z. Papić. Quantum scarred eigenstates in a Rydberg atom chain: Entanglement, breakdown of thermalization, and stability to perturbations. *Physical Review B*, 98(15):155134, Oct. 2018a. doi: 10.1103/PhysRevB.98.155134. (Cited on page 2.)

C. J. Turner, A. A. Michailidis, D. A. Abanin, M. Serbyn, and Z. Papić. Weak ergodicity breaking from quantum many-body scars. *Nature Physics*, 14(7):745–749, July 2018b. ISSN 1745-2481. doi: 10.1038/s41567-018-0137-5. (Cited on page 2.)

F. Verstraete and J. I. Cirac. Renormalization algorithms for Quantum-Many Body Systems in two and higher dimensions, July 2004. (Cited on page 17.)

F. Verstraete and J. I. Cirac. Matrix product states represent ground states faithfully. *Physical Review B*, 73(9):094423, Mar. 2006. doi: 10.1103/PhysRevB.73.094423. (Cited on page 39.)

F. Verstraete, J. J. García-Ripoll, and J. I. Cirac. Matrix Product Density Operators: Simulation of Finite-Temperature and Dissipative Systems. *Physical Review Letters*, 93 (20):207204, Nov. 2004. doi: 10.1103/PhysRevLett.93.207204. (Cited on page 78.)

F. Verstraete, M. M. Wolf, and J. Ignacio Cirac. Quantum computation and quantum-state engineering driven by dissipation. *Nature Physics*, 5(9):633–636, Sept. 2009. ISSN 1745-2481. doi: 10.1038/nphys1342. (Cited on page 16.)

G. Vidal. Efficient Simulation of One-Dimensional Quantum Many-Body Systems. *Physical Review Letters*, 93(4):040502, July 2004a. doi: 10.1103/PhysRevLett.93.040502. (Cited on page 4.)

G. Vidal. Efficient Simulation of One-Dimensional Quantum Many-Body Systems. *Physical Review Letters*, 93(4):040502, July 2004b. doi: 10.1103/PhysRevLett.93.040502. (Cited on pages 28 and 31.)

G. Vidal. Classical Simulation of Infinite-Size Quantum Lattice Systems in One Spatial Dimension. *Physical Review Letters*, 98(7):070201, Feb. 2007a. doi: 10.1103/PhysRevLett.98.070201. (Cited on page 17.)

G. Vidal. Entanglement Renormalization. *Physical Review Letters*, 99(22):220405, Nov. 2007b. doi: 10.1103/PhysRevLett.99.220405. (Cited on page 17.)

G. Vidal. Class of Quantum Many-Body States That Can Be Efficiently Simulated. *Physical Review Letters*, 101(11):110501, Sept. 2008. doi: 10.1103/PhysRevLett.101.110501. (Cited on page 17.)

G. Vidal, J. I. Latorre, E. Rico, and A. Kitaev. Entanglement in Quantum Critical Phenomena. *Physical Review Letters*, 90(22):227902, June 2003. doi: 10.1103/PhysRevLett.90.227902. (Cited on pages 17 and 39.)

L. Vidmar and M. Rigol. Generalized Gibbs ensemble in integrable lattice models. *Journal of Statistical Mechanics: Theory and Experiment*, 2016(6):064007, June 2016. ISSN 1742-5468. doi: 10.1088/1742-5468/2016/06/064007. (Cited on page 15.)

C. von Keyserlingk, F. Pollmann, and T. Rakovszky. Operator backflow and the classical simulation of quantum transport. *Physical Review B*, 105(24):245101, June 2022. doi: 10.1103/PhysRevB.105.245101. (Cited on page 84.)

C. W. von Keyserlingk, T. Rakovszky, F. Pollmann, and S. L. Sondhi. Operator Hydrodynamics, OTOCs, and Entanglement Growth in Systems without Conservation Laws. *Physical Review X*, 8(2):021013, Apr. 2018. doi: 10.1103/PhysRevX.8.021013. (Cited on page 83.)

D. Wellnitz, G. Preisser, V. Alba, J. Dubail, and J. Schachenmayer. Rise and Fall, and Slow Rise Again, of Operator Entanglement under Dephasing. *Physical Review Letters*, 129(17):170401, Oct. 2022. doi: 10.1103/PhysRevLett.129.170401. (Cited on page 42.)

A. H. Werner, D. Jaschke, P. Silvi, M. Kliesch, T. Calarco, J. Eisert, and S. Montangero. Positive Tensor Network Approach for Simulating Open Quantum Many-Body Systems. *Physical Review Letters*, 116(23):237201, June 2016. doi: 10.1103/PhysRevLett.116.237201. (Cited on page 61.)

C. D. White. Effective dissipation rate in a Liouvillian-graph picture of high-temperature quantum hydrodynamics. *Physical Review B*, 107(9):094311, Mar. 2023. doi: 10.1103/PhysRevB.107.094311. (Cited on page 84.)

C. D. White, M. Zaletel, R. S. K. Mong, and G. Refael. Quantum dynamics of thermalizing systems. *Physical Review B*, 97(3):035127, Jan. 2018. doi: 10.1103/PhysRevB.97.035127. (Cited on page 110.)

S. R. White. Density matrix formulation for quantum renormalization groups. *Physical Review Letters*, 69(19):2863–2866, Nov. 1992. doi: 10.1103/PhysRevLett.69.2863. (Cited on pages 4 and 39.)

S. R. White and A. E. Feiguin. Real-Time Evolution Using the Density Matrix Renormalization Group. *Physical Review Letters*, 93(7):076401, Aug. 2004. doi: 10.1103/PhysRevLett.93.076401. (Cited on pages 4 and 31.)

J. F. Wienand, S. Karch, A. Impertro, C. Schweizer, E. McCulloch, R. Vasseur, S. Gopalakrishnan, M. Aidelsburger, and I. Bloch. Emergence of fluctuating hydrodynamics in chaotic quantum systems. *Nature Physics*, 20(11):1732–1737, Nov. 2024. ISSN 1745-2481. doi: 10.1038/s41567-024-02611-z. (Cited on page 3.)

M. M. Wolf and J. I. Cirac. Dividing Quantum Channels. *Communications in Mathematical Physics*, 279(1):147–168, Apr. 2008. ISSN 1432-0916. doi: 10.1007/s00220-008-0411-y. (Cited on pages 27 and 52.)

U. Wolff. Collective Monte Carlo Updating for Spin Systems. *Physical Review Letters*, 62 (4):361–364, Jan. 1989. doi: 10.1103/PhysRevLett.62.361. (Cited on page 1.)

S. Xu and B. Swingle. Accessing scrambling using matrix product operators. *Nature Physics*, 16(2):199–204, Feb. 2020. ISSN 1745-2481. doi: 10.1038/s41567-019-0712-4. (Cited on page 119.)

S. Xu and B. Swingle. Scrambling Dynamics and Out-of-Time-Ordered Correlators in Quantum Many-Body Systems. *PRX Quantum*, 5(1):010201, Jan. 2024. doi: 10.1103/PRXQuantum.5.010201. (Cited on page 119.)

Y. Yang, S. Iblisdir, J. I. Cirac, and M. C. Bañuls. Probing Thermalization through Spectral Analysis with Matrix Product Operators. *Physical Review Letters*, 124(10):100602, Mar. 2020. doi: 10.1103/PhysRevLett.124.100602. (Cited on page 76.)

J. Yao and P. W. Claeys. Temporal entanglement barriers in dual-unitary Clifford circuits with measurements. *Physical Review Research*, 6(4):043077, Oct. 2024. doi: 10.1103/PhysRevResearch.6.043077. (Cited on page 43.)

S. Yi-Thomas, B. Ware, J. D. Sau, and C. D. White. Comparing numerical methods for hydrodynamics in a one-dimensional lattice spin model. *Physical Review B*, 110(13): 134308, Oct. 2024. doi: 10.1103/PhysRevB.110.134308. (Cited on page 84.)

Y. Yoo, C. D. White, and B. Swingle. Open-system spin transport and operator weight dissipation in spin chains. *Physical Review B*, 107(11):115118, Mar. 2023. doi: 10.1103/PhysRevB.107.115118. (Cited on page 84.)

M. P. Zaletel, R. S. K. Mong, C. Karrasch, J. E. Moore, and F. Pollmann. Time-evolving a matrix product state with long-ranged interactions. *Physical Review B*, 91(16):165112, Apr. 2015. doi: 10.1103/PhysRevB.91.165112. (Cited on page 30.)

L. Zhang, U. Bhattacharya, M. Recasens, T. Grass, R. W. Chhajlany, M. Lewenstein, and A. S. Johnson. Tensor network study of the light-induced phase transitions in vanadium dioxide. *npj Quantum Materials*, 10(1):1–10, Mar. 2025. ISSN 2397-4648. doi: 10.1038/s41535-025-00751-w. (Cited on page 2.)

T. Zhou and D. J. Luitz. Operator entanglement entropy of the time evolution operator in chaotic systems. *Physical Review B*, 95(9):094206, Mar. 2017. doi: 10.1103/PhysRevB.95.094206. (Cited on page 41.)

M. Žnidarič. Solvable quantum nonequilibrium model exhibiting a phase transition and a matrix product representation. *Physical Review E*, 83(1):011108, Jan. 2011. doi: 10.1103/PhysRevE.83.011108. (Cited on page 78.)

M. Žnidarič, T. Prosen, and I. Pižorn. Complexity of thermal states in quantum spin chains. *Physical Review A*, 78(2):022103, Aug. 2008a. doi: 10.1103/PhysRevA.78.022103. (Cited on pages 41 and 78.)

M. Žnidarič, T. Prosen, and P. Prelovšek. Many-body localization in the Heisenberg XXZ magnet in a random field. *Physical Review B*, 77(6):064426, Feb. 2008b. doi: 10.1103/PhysRevB.77.064426. (Cited on pages 41 and 78.)

M. Zwolak and G. Vidal. Mixed-State Dynamics in One-Dimensional Quantum Lattice Systems: A Time-Dependent Superoperator Renormalization Algorithm. *Physical Review Letters*, 93(20):207205, Nov. 2004. doi: 10.1103/PhysRevLett.93.207205. (Cited on pages 31 and 36.)